2011

Effect of Process Variables on the Microstructural Features for As-Cast Magnesium Alloys

Indranil Basu

Effect of Process Variables on the Microstructural Features for As-Cast Magnesium Alloys

(Spine title: Process-Structure Relationships in Mg Alloys)

(Thesis format: Monograph)

by

Indranil Basu

Graduate Program in Engineering Science
Department of Mechanical and Materials Engineering

A thesis submitted in partial fulfillment
of the requirements for the degree of
Master of Engineering Science

The School of Graduate and Postdoctoral Studies
The University of Western Ontario
London, Ontario, Canada

Abstract

The solidification pattern for a material is strongly dependent on the process parameters, such as cooling rate, thermal gradient, solidification time, mold shape and dimensions, mold filling rate, superheat temperature etc. Thus, the obtained microstructural features have a direct functional relation with these initial variables.

In this study, two commercial Mg alloys (AM60B and AZ91D) were studied under different solidification conditions to characterize the influence of cooling rate, thermal gradient, growth velocity, Niyama criterion, solidification time and mold dimensions on microstructural features such as secondary and tertiary dendrite arm spacing, grain size, porosity, pore shape and size, local morphological and phase variations.

Porosity, grain size and dendrite arm spacing were measured and correlated with the process variables recording during the casting process. It was determined that the process of mold filling and solidification are simultaneous in nature and they significantly affect the development of microstructure and its dependency on the process parameters. This significantly affects the obtained porosity values and their variation along the casting. These results clearly indicate that rate of filling, nature of flow of liquid and shape of the mold greatly affect the solidification process and thereby the microstructure. Any predictive solidification model, treating these factors singularly wouldn't be appropriate to pre-determine the microstructure and properties of the casted component.

Keywords: magnesium, solidification, microstructural features, cooling rate, thermal gradient, mold filling rate, Niyama criterion, dendrite arm spacing, grain size, porosity, morphological and phase variations, solidification model, microstructure development

Acknowledgements

First, I would like to thank Meridian Lightweight Technologies Inc., for access to the materials, equipment and facilities that made this work possible and the Resource for the Innovation of Engineering Materials (RIEM) program funded by CANMET (Canada Centre for Mineral and Energy Technology), a Natural Resources Canada laboratory.

Second, this research was also partly funded by the AUTO21 Network of Centres of Excellence, an automotive research and development program focusing on issues relating to the automobile in the 21st century. AUTO21, a member of the Networks of Centres of Excellence of Canada program is funded by the Natural Sciences and Engineering Research Council (NSERC), the Social Science and Humanities Research Council (SSHRC) and multiple industry and government partners.

Third, I would like to gratefully acknowledge the significant contributions of Mr. Junning Li and Dr. Mohammad Aljarrah, in performing the casting experiments.

Fourth, I would also like to acknowledge the invaluable inputs and guidance provided by Dr. Jon Weiler, during the course of this study. I would also like to thank Mr. A.Z.M Ariful Islam, for providing me with valuable inputs, during the period of writing my thesis.

Finally, I would like to express my deep sense of gratitude to my advisor, Dr. Jeffrey. T. Wood for his tremendous patience, guidance and generosity over the tenure of this research. His constant support and encouragement were indispensible factors behind the successful completion of this research.

Dedications

To my beloved parents, who have stood behind me during thick and thin and whose constant moral support and encouragement helped me overcome every hardship I faced.

I would also like to dedicate the writing of this thesis to my colleagues: Charu Chawla, Pathikrit Bhattacharya, Ajit Mishra, Mahadevan Balakrishnan and Sneha Lele, who have become my significant others, over the period of my stay in London. I would always be grateful to them for keeping my spirits high and making my stay an extremely pleasant experience.

Finally, my gratitude to God, the father of all, for giving us this invaluable gift called 'life' and the ability to think and innovate.

Contents

List of Figures

List of Tables

Nomenclature

SYMBOL	PARAMETER
E_Q	Activation energy (J/kJ)
Q	Activation energy (J/kJ)
k	Boltzmann constant ($m^2kg\ s^{-2}K^{-1}$)
R	Cooling rate (°C/s)
ΔP_{cr}	Critical pressure drop (N/m^2)
ρ	Density (kg/m^3)
ρ_l	Density of liquid metal (kg/m^3)
ρ_s	Density of solidified metal (kg/m^3)
x,y,z	Distance (m/mm)
d	Distance from cooling end (mm)
μ	Dynamic viscosity ($kg\ s/m^2$)
ΔS_f	Entropy for freezing (J/K)
t_{exp}	Experimentally measured local solidification time (s)
ΔG_f	Free energy for solidification (J/mole)
ΔT	Freezing range of the alloy (°C)
R_g	Gas constant (J/mol K)

$G.D.$	Grain size (μm/mm)
V_0	Hypothetical maximum growth velocity (m/s or mm/s)
L	Latent heat of freezing (J)
μ_l	Liquid dynamic viscosity (kg s/m^2)
$g_{l,s}$	Liquid or solid fraction
T_L	Liquidus temperature (°C)
t_{sol}	Local solidification time (s)
C_λ	Material constant
N_y	Niyama criterion (°C$^{0.5}$mm^{-1}s$^{0.5}$)
p	Partial pressure of gas (N/m^2)
P	Pressure (N/m^2)
$SDAS$	Secondary dendrite arm spacing (μm/mm)
ΔT_{st}	Solidification temperature range (°C)
T_S	Solidus temperature (°C)
V_s/V	Solidus velocity/Solidification velocity (m/s or mm/s)
c_g	Solubility of gas
c	Specific heat (J/kg K)
t_{stat}	Statistically calculated local solidification time (s)

ΔT_{sh}	Superheat temperature (°C)
A	Surface area (m^2)
σ	Surface energy (J)
T	Temperature (°C)
$TDAS$	Tertiary dendrite arm spacing (μm/mm)
G	Thermal gradient (°C/m or °C/mm)
t	Time (s)
β	Total solidification shrinkage
μ_o	Viscosity for extremely dilute gas (kg s/m^2)
V	Volume (m^3)
σ_y	Yield stress (N/m^2)

Chapter 1

Introduction

Lately, efforts are being concentrated towards reduced fuel consumption and environmental effects of the automotive sector. One of the primary suggested solutions to tackle these issues has been vehicle weight reduction. Magnesium alloys, being lightweight and having a high strength to weight ratio, comparable to currently used automotive materials, stand as a befitting candidate for the above purpose. Their excellent castability and machinability further encourage their employment in commercial applications.

Magnesium alloys are 75% lighter than steel and 33% lighter than aluminum. High pressure die cast Mg-Al alloys are being increasingly used in the automotive sector, showing an annual usage growth of 15-20% over the last decade and their use is expected to grow at a rate of 10-15% over the next decade [1,2]. The primary alloys used for automotive applications are AZ91D, AM60B and AM50. AZ91D is the most commonly used alloy for die casting. It offers good strength to weight ratio, high toughness and corrosion resistance. The alloy is mainly used for power-train and mechanical components.

AM60B automotive components are typically used as safety components such as instrument panel structures and seat frames. AM60B is specifically used for its excellent ductility and energy absorption properties. AM50 has a lower Al content, thus offering higher ductility but has reduced strength and castability. It is therefore used in applications requiring greater elongation than AM60B.

The research presented here represents a portion of a larger project that was initiated to understand the local variation in the mechanical properties as a function of the casting process parameters for high-pressure die cast components. The primary application of these components is in the automotive sector. This project has been conducted with the

collaboration of industrial partners, Meridian Lightweight Technologies, Inc. Strathroy, Ontario, Canada. The first phase of the project dealt with the understanding of the influence of microstructural features on the resultant mechanical properties. Consequently, the current study aims at obtaining a correlation between the process parameters and the as-cast microstructure of the material.

The microstructure of an alloy has a strong influence on the resultant mechanical properties. High pressure die cast magnesium alloys contain non-uniformly distributed porosity leading to drastic variations in the mechanical properties throughout the casting. The rate of filling in HPDC is very high, ranging around 2000-2500cm/s. Such high filling rates lead to droplet formation in the metal entering the mold gradually becoming more laminar as the mold fills. The droplets lead to entrapment and oxidation of metal leading to defects such as porosity, oxide inclusions and knit lines [3].

The variation in the grain size and non-uniform microstructure compromises the part reliability, leading to production inefficiency and degrading vehicle safety. It is therefore important to understand the correlation between the process variables, microstructure and properties of the cast alloy.

The work presented here is an effort to understand the correlation between process parameters and the microstructural features (Figure 1.1) during casting of Magnesium alloys. The approach of the study deals with the investigation of the solidification phenomenon of the commercially used alloys at different cooling rates and thermal gradients. The variations in these parameters have been achieved using the following solidification techniques:

1. Gravity Sand Casting – AM60B
2. Wedge Casting – AM60B and AZ91D

Microstructural features such as porosity, dendrite arm spacing and grain size were measured and their dependence upon the solidification parameters- cooling rate, thermal gradient, interface velocity, Niyama criterion- has been characterized. The study has been segregated into six primary sections. Chapter 2 describes the physical properties

and their manufacturing process. It furthers discusses the established theories and studies regarding the influence of process variables on the main structural features namely, grain size, dendrite arm spacing and porosity.

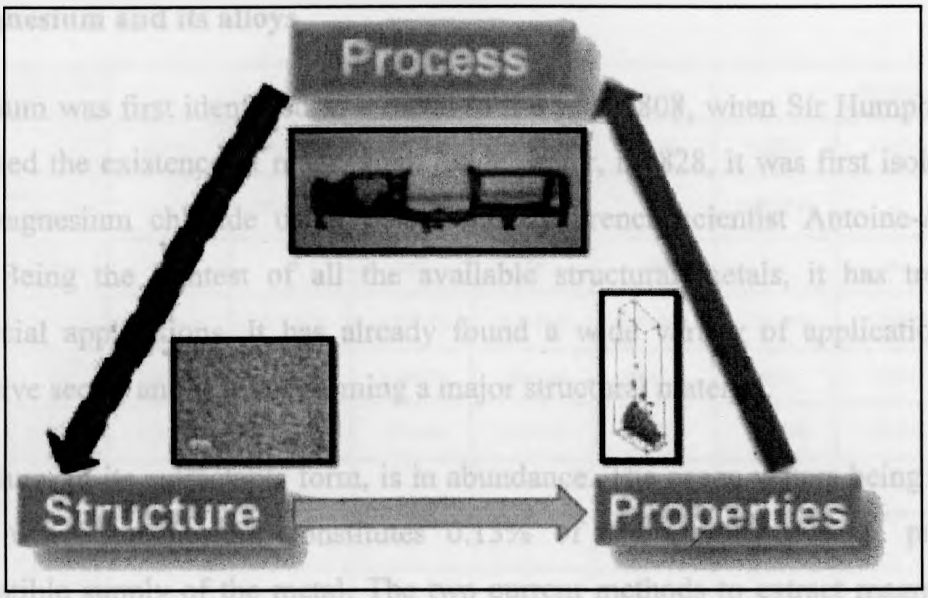

Figure 1.1 Process-Structure-Property relationship.

Chapters 3 and 4 present the various experimental procedures carried out during the study and the obtained experimental data. Chapter 3 describes the various casting methods used and the subsequent characterization methods. Similarly, Chapter 4 presents the experimentally obtained data and how they vary as a function of the standard independent variables namely, distance and time.

Chapters 5 and 6 analyze the obtained experimental data and discuss the dependence of the various structural features on the process parameters. Empirical fitting methods and correlations with established theories have been presented in these two chapters.

Finally, Chapter 7 provides a closure to the complete study by presenting the obtained conclusions and summarizing the results. It also provides the scope for future work required to further understand the relationship between the process parameters and the structural features.

Chapter 2

Literature Review

2.1 Magnesium and its alloys

Magnesium was first identified as a metal in the year 1808, when Sir Humphrey Davy established the existence of magnesium oxide. Later, in1828, it was first isolated from fused magnesium chloride using potassium, by French scientist Antoine-Alexander Bussy. Being the lightest of all the available structural metals, it has tremendous commercial applications. It has already found a wide variety of applications in the automotive sector and is fast becoming a major structural material.

Magnesium, in its extractable form, is in abundance. The ocean waters being the major source, where magnesium constitutes 0.13% of the world's oceans, provide an inexhaustible supply of the metal. The two current methods to extract magnesium are electrolysis of fused magnesium chloride in an anhydrous state, obtained from magnesite, brine and seawater, and thermal reduction of magnesium oxide by ferrosilicon derived from carbonate ores [4]. Magnesium is extremely light-weight, with a density ranging from 1.77 g/cc to 1.83 g/cc at 20 °C. It is a silvery-white metal with a lustrous surface. It has a moderate melting point of 650 °C. At room temperature, it shows a tendency for brittleness due to intercrystalline and local transcrystalline failure, due to twinning and basal slip {0001}. Above 225 °C, secondary slip or pyramidal planes {1011} become active and deformation is extremely easy. It has an elastic modulus of 44.8 GPa (Table 2.1(b)), yield strength in the range of 80 – 180 MPa and an elongation of 1– 12% [5].

Pure magnesium is extremely reactive with a high affinity for oxygen and sulphur (and is used as a desulphurizer for the same reason) [4]. It crystallizes into a hexagonal closed packed (HCP) structure, making it noncompliant to forming and rolling processes. This is due to preferred crystallographic orientation of the basal planes or strong texture, leading to large mechanical anisotropy [6,7].Pure magnesium is hardly used in its unalloyed state, for engineering applications, due to its low mechanical pro-

Table 2.1 a) Chemical composition of common die casting magnesium alloy ingots b) Physical properties of magnesium, as compared to other common structural metals.

CHEMICAL COMPOSITIONS OF DIE CASTING MAGNESIUM ALLOY INGOTS(%)

Alloy composition		MgAlZn					MgAlMn		
Type		AZ81A	AZ81S	AZ91D	AZ91S	AZ63A	AS21S	AS41B	AS41S
The numeric symbol corresponding to EN1753		-	MB21110	MB21120	MB21121	-	MB21310	-	MB21320
Chemical composition,%	Mg	Bal	Bal	Bal	Bal	Bal	Bal	Bal	Bal
	Al	7.20-8.80	7.20-8.20	8.50-9.50	8.80-10.0	5.80-6.80	1.90-2.50	3.70-4.80	3.70-4.80
	Zn	0.50-0.90	0.45-0.90	0.45-0.90	0.30-1.00	2.70-3.30	<0.20	<0.10	<0.20
	Mn	0.15-0.35	0.17-0.40	0.17-0.40	0.10-0.30	0.15-0.35	0.20-0.60	0.35-0.60	0.20-0.60
	Si	-	-	-	-	-	-	-	-
	Zr	-	-	-	-	-	-	-	-
	Ag	-	-	-	-	-	-	-	-
	Y	-	-	-	-	-	-	-	-
	Li	-	-	-	-	-	-	-	-
	Be	0.0005-0.0015	-	0.0005-0.003	-	0.0005-0.0015	-	0.0005-0.003	-
	Ni	<0.20	<0.02	<0.03	<0.10	<0.05	0.70-1.20	0.40-1.40	0.70-1.20
	Fe	-	<0.004	<0.004	<0.01	<0.005	<0.004	<0.0035	<0.004
	Cu	<0.10	<0.025	<0.025	<0.20	<0.015	<0.008	<0.0015	<0.008
	Na	<0.010	<0.001	<0.001	<0.010	<0.001	<0.001	<0.001	<0.001
	Each	-	<0.01	<0.01	<0.05	-	<0.01	<0.01	<0.01
	Total	<0.30	-	-	-	<0.30	-	-	-

		Mg	Al	Ti	Fe	Cu
Lattice Structure		HCP	FCC	HCP	BCC	FCC
Density	(g/cm^3)	1.74	2.70	4.51	7.87	8.93
Melting Point	(℃)	650	660	1668	1535	1083
Specific Heat	(cal/g ℃)	0.24	0.22	0.13	0.11	0.09
Young's Modulus	(GPa)	45	76	114	198	136

-perties. Aluminum and zinc (Table 2.1(a)) are the two most common alloying elements that are added to magnesium. Every alloying element has a significant effect on the properties of the resultant alloy, depending upon the amount added. Discussed below are few of the major alloying elements added to magnesium and their effects on the resulting alloy.

a) **Aluminum** has a maximum solid solubility of 12.7%, by weight, at the eutectic point (437 °C) as per the binary aluminum-magnesium phase diagram. However, commercial alloys generally have aluminum content less than 10%. It has the most favorable effect on magnesium as compared to any other alloying element. It increases the tensile strength and hardness of the metal. This is primarily as a result of precipitation of the intermetallic phase, $Mg_{17}Al_{12}$, observed only upto 120 °C. It provides excellent corrosion resistance and significantly improves the alloy castability, by widening the freezing range of the alloy. However, this effect also has a tendency to induce micro-porosity in the casting.
b) **Zinc** is another effective alloying addition. It is preferably used along with aluminum, as this combination offers excellent properties such as a high tensile strength, excellent castability, good corrosion resistance and high hardness. However, addition of zinc over 2% leads to micro-porosity and hot cracking in the alloy.
c) **Manganese** increases the yield strength of the alloy. One of its biggest advantages is that it mitigates the effect of iron on magnesium (iron significantly reduces the corrosion resistance of magnesium alloys), by removing it and other heavy metal impurities into relatively harmless intermetallic compounds. Its alloying content in commercial alloys is generally below 1.5%.
d) **Silicon** addition in magnesium castings increases the fluidity of the molten metal and also increases its creep resistance, by forming Mg_2Si particles that pin grain boundaries. However, it also reduces the castability and adversely affects the corrosion resistance in the presence of iron.
e) **Rare earth** elements are added as misch metal (50% cerium along with lanthanum and neodymium) or didymium (mixture of neodymium and praseodymium). They increase the strength and the hardness of alloy by formation of precipitates. They

also reduce the freezing range of the alloy; hence, lessen the porosity content in it [4,5].

The most commonly used commercial alloys of magnesium are AM60, AZ91, AE44 and AM50.

2.2 Casting of magnesium alloys

Casting begins with the melting of a metal, followed by its pouring into a mold, which is a hollow cavity of desired shape and geometry. The metal is then allowed to solidify inside the mold. Heat transfer takes place through the mold walls. Sometimes a chill metal (material with high thermal conductivity) is incorporated at one end of the mold to achieve a directional solidification pattern. The material that solidifies is generally separated from the mold, either by the process of mold breaking or using an ejection technique. Magnesium alloys are cast by several different casting techniques including sand casting, permanent mold casting, squeeze casting and die casting.

Magnesium alloys melt in the temperature range of 615 - 650 °C. Molten magnesium tends to oxidize and burn unless care is taken to protect the molten metal surface against oxidation. Magnesium oxides tend to form a discontinuous, porous film possessing low protective properties. Oxides in magnesium alloys form a loose, permeable oxide coating on the molten metal surface. This allows oxygen to pass through and support burning below the oxide at the surface [8]. Protection of the molten alloy, using either a flux or a protective gas cover to exclude oxygen, is therefore necessary. The most common cover gas used is a mixture of CO_2 and SF_6.

In commercial high pressure die casting techniques, cover gas is sprayed onto surface of molten magnesium in a melting furnace at a constant rate so as to prevent high temperature combustion by exposure to air.

Oxidation can also occur during pouring of melt during the casting, hence the need of filters to remove oxides. Steel wool filters [9] are typically used during sand casting of magnesium alloys. Alternatives, such as ceramic filters are also being considered.

However, very little work, analyzing the use of ceramic filters for magnesium alloy castings, has been completed. Bakke et al. [10] investigated the use of ceramic foam filters with AZ91 although with more emphasis on bath filtration. It was found that a ceramic foam filter is capable of only capturing a given number of oxide particles of a given distribution.

During the sand casting process, mold additives and coatings (such as MgO) are used to produce a smooth casting surface. The mold coating (or additive) material should not react with the melt. It should collapse after solidification and shake-out without cracking the casting. It is also necessary to have a controlled mold filling process without any oxidation and induced turbulence. Mechanical/electrical pumping systems can produce a controlled metal flow and hence effectively mitigate the above mentioned problems.

The process of pouring varies, depending on the type of casting and mold geometry. Pouring techniques are of mainly two kinds, namely simple dip ladling from bale out crucibles for sand and permanent mold castings and automated systems as in the case of high pressure die castings. Oxidation and burning of the melt is highly possible while pouring. It is therefore necessary to use some protection in the form of flux or cover gas to minimize this. Another important precaution that needs attention is the absence of moisture. The hydrogen in the moisture reacts with magnesium and the reaction can be extremely explosive in nature. During pouring, the ladle should never be completely emptied as it might allow oxide and flux residues to enter the melt.

2.3 Solidification microstructure in as- cast magnesium alloys

The majority of magnesium alloys, used commercially are primarily magnesium-aluminum alloys. A eutectic phase, between primary magnesium (α-Mg) and the intermetallic phase ($Mg_{17}Al_{12}$ or β-Mg), forms at a temperature of437 °C with the Al content at approximately 33% by weight (Figure 2.1).

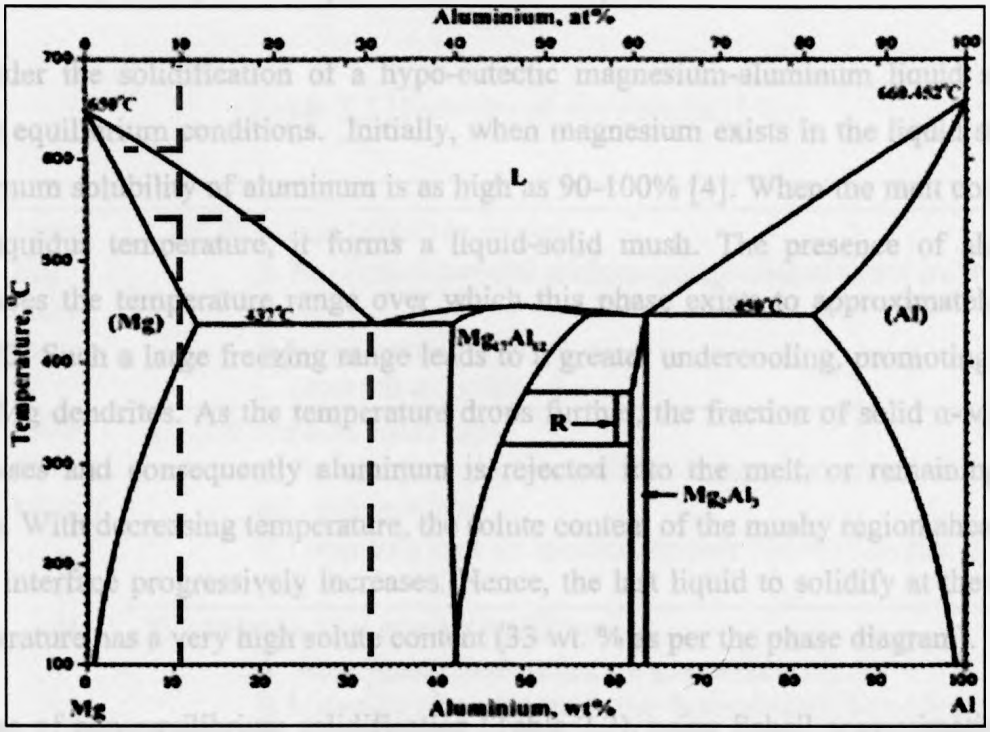

Figure 2.1 Magnesium-aluminum phase diagram, showing eutectic and Mg-Al (10 wt. %) compositions [11].

Liquid →α-Mg (solid solution) + $Mg_{17}Al_{12}$ ($T_{reaction}$ = 437 °C) .....(2.1)

Equation 2.1 represents the eutectic reaction. Since most of the commercial magnesium-aluminum alloys have aluminum content less than 10%, the equilibrium solidification microstructure of these alloys will consist of 100% primary magnesium (Figure 2.1) or α-Mg (a homogenous solid solution of aluminum in a magnesium matrix). The observation of eutectic structures in castings indicates meta-stable or non-equilibrium solidification. The eutectic phases formed are in a metastable state, which on age hardening and solution heat-treatment result in the dissolution of the β-Mg phase, producing a super-saturated solid solution of aluminum in magnesium. Due to non-equilibrium solidification conditions, eutectic structures are observed for alloys with

aluminum content as low as 2%. However, for aluminum contents above 20%, permanent and stable eutectic phases are observed [11].

Consider the solidification of a hypo-eutectic magnesium-aluminum liquid solution, under equilibrium conditions. Initially, when magnesium exists in the liquid state, the maximum solubility of aluminum is as high as 90-100% [4]. When the melt cools from the liquidus temperature, it forms a liquid-solid mush. The presence of aluminum increases the temperature range over which this phase exists to approximately 100 – 150 °C. Such a large freezing range leads to a greater undercooling, promoting growth of α-Mg dendrites. As the temperature drops further, the fraction of solid α-Mg phase increases and consequently aluminum is rejected into the melt, or remaining liquid phase. With decreasing temperature, the solute content of the mushy region ahead of the solid interface progressively increases. Hence, the last liquid to solidify at the eutectic temperature has a very high solute content (33 wt. % as per the phase diagram).

In case of non-equilibrium solidification (Table 2.2), using Scheil approximations [12] and assuming no diffusion in the solid, it can be shown that the average composition of aluminum in the solid phase is lower than the equilibrium solidus composition. Non equilibrium solidification occurs at solidification rates greater than the equilibrium value. Higher solidification rates increase the tendency of undercooling in the melt. Consequently, an overall downward shift of the liquidus and solidus lines in the magnesium-aluminum phase diagram (Figure 2.2) is observed. The formation of eutectic phases is observed for alloys with aluminum content lower than that of the eutectic composition as a result of solute segregation (Figure 2.3). Thus, Mg-Al alloys solidify under non equilibrium conditions, producing a cored α-Mg dendritic structure with a lower overall aluminum content than predicted by the equilibrium phase diagram [11,13].

Table 2.2 Hierarchy of equilibrium [14].

Increasing undercooling or solidification velocity ↓	I. Full diffusional (global) equilibrium A. No chemical potential gradients (composition of phases are uniform) B. No temperature gradients C. Lever rule applicable
	II. Local interfacial equilibrium A. Phase diagram gives compositions and temperatures only at liquid - solid interface B. Corrections made for interface curvature (Gibbs - Thomson effect)
	III. Metastable local interface equilibrium A. Stable phase cannot nucleate or grow sufficiently fast B. Metastable phase diagram (a true thermodynamic phase diagram missing the stable phase or phases) gives the interface conditions
	IV. Interface non-equilibrium A. Phase diagram fails to give temperature and compositions at the interface B. Chemical potentials are not equal at the interface C. Free energy functions of phases still lead to criteria for impossible reactions

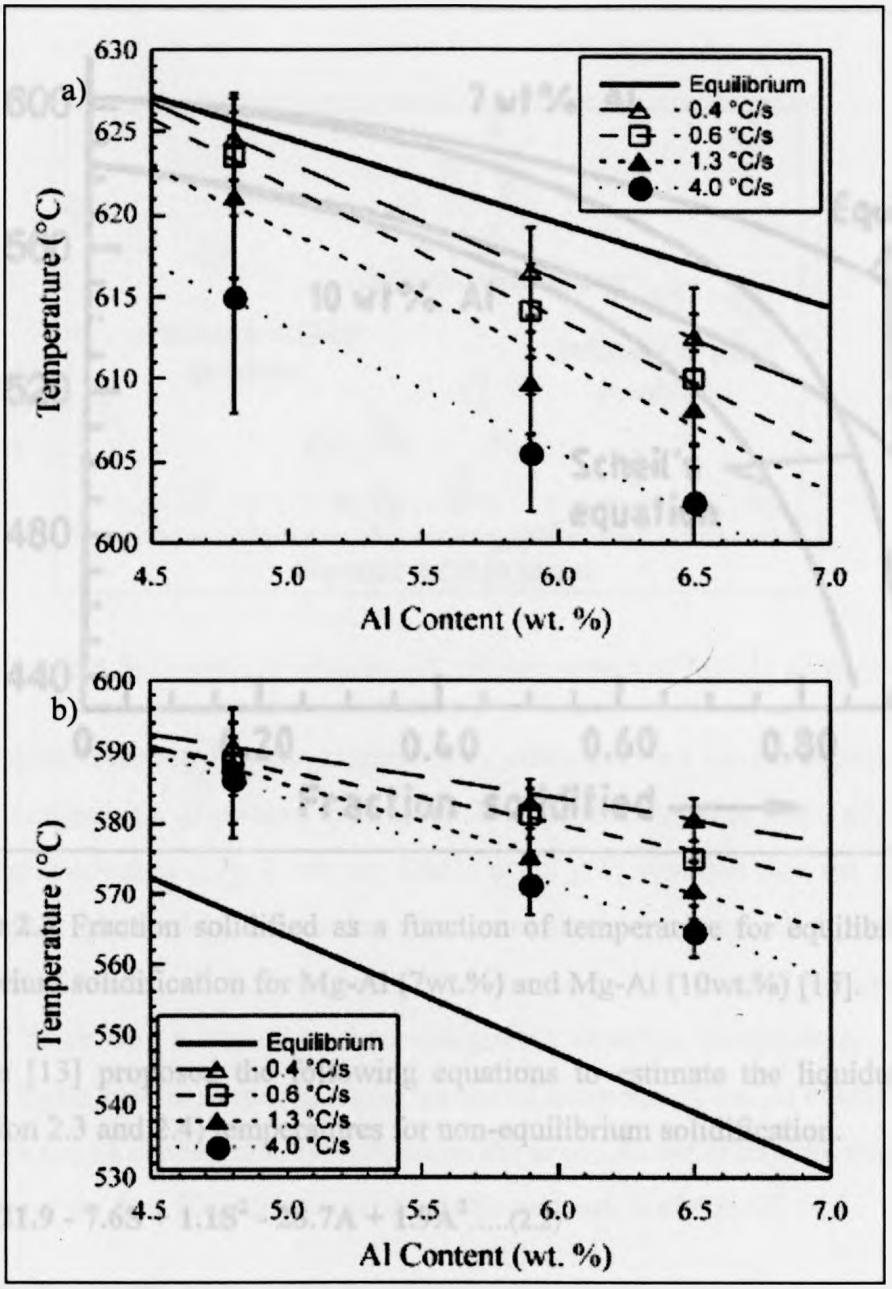

Figure 2.2 a) Liquidus and b) Solidus temperatures for Mg-Al alloys as a function of cooling rate and Al content [13].

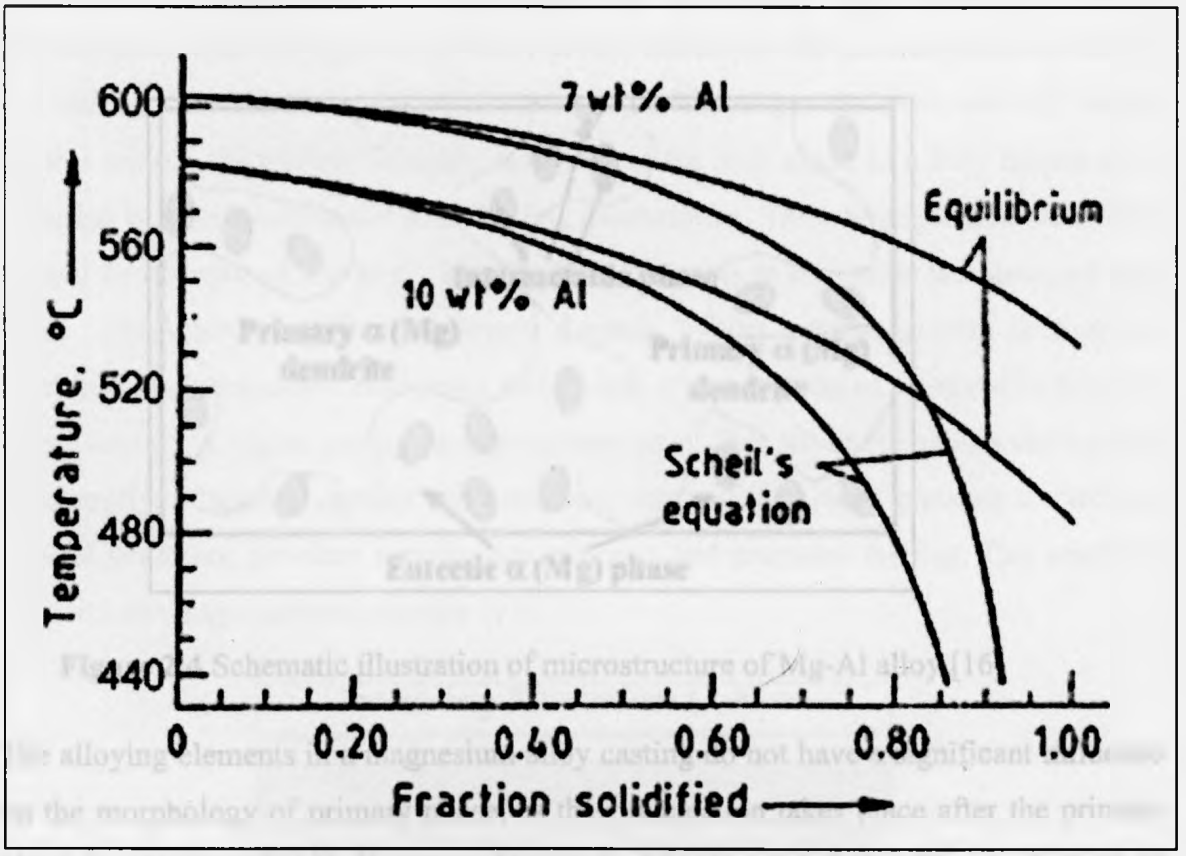

Figure 2.3 Fraction solidified as a function of temperature for equilibrium and non-equilibrium solidification for Mg-Al (7wt.%) and Mg-Al (10wt.%) [15].

Carlson [13] proposed the following equations to estimate the liquidus and solidus (Equation 2.3 and 2.4) temperatures for non-equilibrium solidification.

$$T_L = 721.9 - 7.6S + 1.1S^2 - 28.7A + 1.9A^2 \quad \text{.....(2.2)}$$

$$T_S = 621.2 + 2.2S^2 - 5.6A - 2.1AS \quad \text{.....(2.3)}$$

where, A = aluminum content (wt. %) and S = solidification rate (°°C/s)

Han et.al [16] found that for the AZ91D alloy, the average aluminum content at the edge of the dendrites, prior to intermetallic (β-phase) precipitation (Figure 2.4), is approximately 4-5 times greater than that in the center.

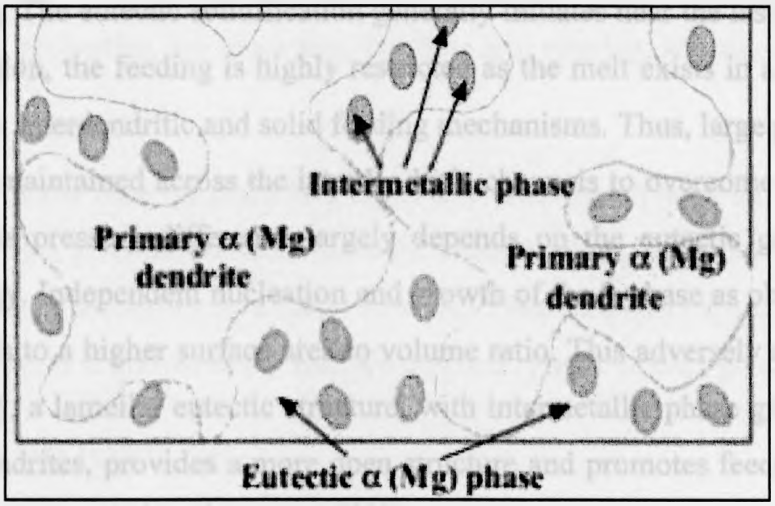

Figure 2.4 Schematic illustration of microstructure of Mg-Al alloy [16]

The alloying elements in a magnesium alloy casting do not have a significant influence on the morphology of primary phase, as their nucleation takes place after the primary phase has nucleated [17]. However, Dahle et. al [11] reported that the morphology of the primary phase depends on the aluminum content of the solid solution. At low aluminum content, cellular structures were observed. With an increase in the aluminum content, there was a transition from cellular to dendritic morphology. The dendrites initially had a rosette shaped globular equiaxed morphology (at Al content of 5 wt. %), with high solute concentrations in between the arms. As the aluminum content increases to around 9 wt. % a fully developed dendritic network is obtained.

Alloying elements have a strong influence on the eutectic morphology. Nave, Dahle and coworkers [18,19] studied the effect of cooling rate, aluminum and zinc content on the eutectic morphology (Figure 2.5). They report that with increasing aluminum content the eutectic formation tends towards a lamellar morphology. However, with an increasing cooling rate and increasing zinc content, there is segregation of the eutectic constituents (α-Mg and β-$Mg_{17}Al_{12}$), producing partially and fully divorced eutectic structures.

The formation and morphology of eutectic plays a major role in the final as-cast microstructure development. It influences the size, shape and distribution of the intermetallic phase (β-$Mg_{17}Al_{12}$), which in turn influences the mechanical properties of the casting. The eutectic solidification generally initiates near the last-to-solidify region. At this region, the feeding is highly restricted as the melt exists in a fully mushy state, resulting in interdendritic and solid feeding mechanisms. Thus, large pressure difference should be maintained across the interdendritic channels to overcome the restricted melt flow. This pressure difference largely depends on the eutectic growth fashion and morphology. Independent nucleation and growth of the β-phase as observed in divorced forms leads to a higher surface area to volume ratio. This adversely affects the feeding. Conversely, a lamellar eutectic structure, with intermetallic phase growing towards the core of dendrites, provides a more open structure and promotes feeding. This results in reduced shrinkage induced porosity [11].

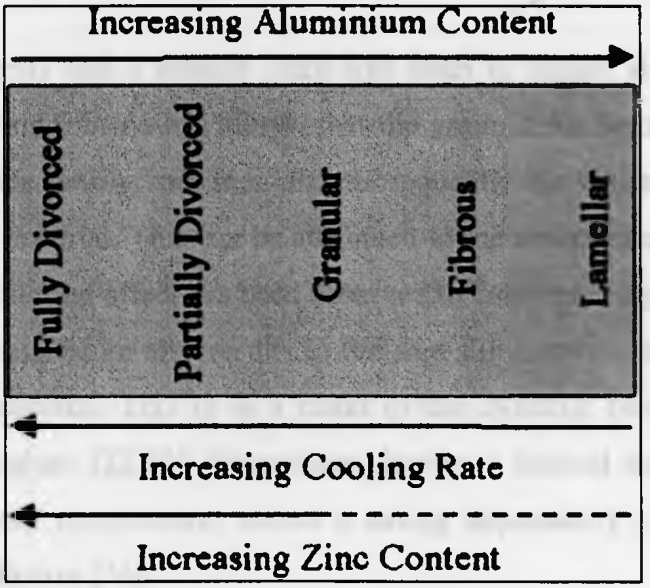

Figure 2.5 Variation of the eutectic morphology as a function of cooling rate, aluminum and zinc content [11].

2.4 Structure-Property relationships

The mechanical properties of magnesium alloys are strongly affected by the obtained microstructure. The primary structural features, which strongly influence the mechanical properties, are grain size, dendrite arm spacing, and size and distribution of porosity.

Effect of Grain Size: A grain is a small enclosed region with all the crystal lattices aligned along a given orientation inside the domain. Grain size has a strong influence on the mechanical properties of a metal or alloy. Yield strength depends on the grain size and this relation is known as the Hall-Petch [20,21] relationship, given as:

$$\sigma_y = \sigma_{y_0} + \lambda(G.D.)^{-0.5} \quad \text{..... (2.4)}$$

where, σ_y= Yield strength (kg/mm^2) and $G.D.$= Grain size (mm)

Equation 2.4 suggests that a smaller grain size leads to higher yield strength (Figure 2.6). It has been found, in Al-Mg alloys, that the grain size affects the propagation of Lüder's bands in the tensile specimen and subsequently the resistance to initiation of plastic flow in the material. This can be attributed to the dislocation pile up at the grain boundaries. The Lüdering effect has been observed to vary inversely with the grain size. The presence of magnesium also results in the free slip distance being independent of the strain in the material. This is as a result of the dynamic recovery effects in the presence of magnesium [22,23]. Magnesium, having a limited number of active slip systems at the room temperature, shows a strong dependency of the elongation to fracture on the grain size [24].

In the case of die-castings it has been observed that the variable rate of heat transfer produces a non-uniform microstructure. Variable grain sizes with extremely fine grains near the walls and coarse grains in the core region are obtained. The section of the casting region with fine grains is called the skin region, exhibiting superior mechanical properties [3].

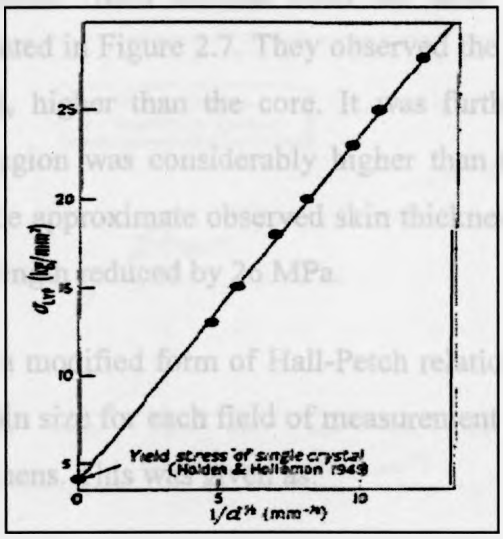

Figure 2.6 Variation of yield stress with respect to grain size$^{-0.5}$ for mild steel [20].

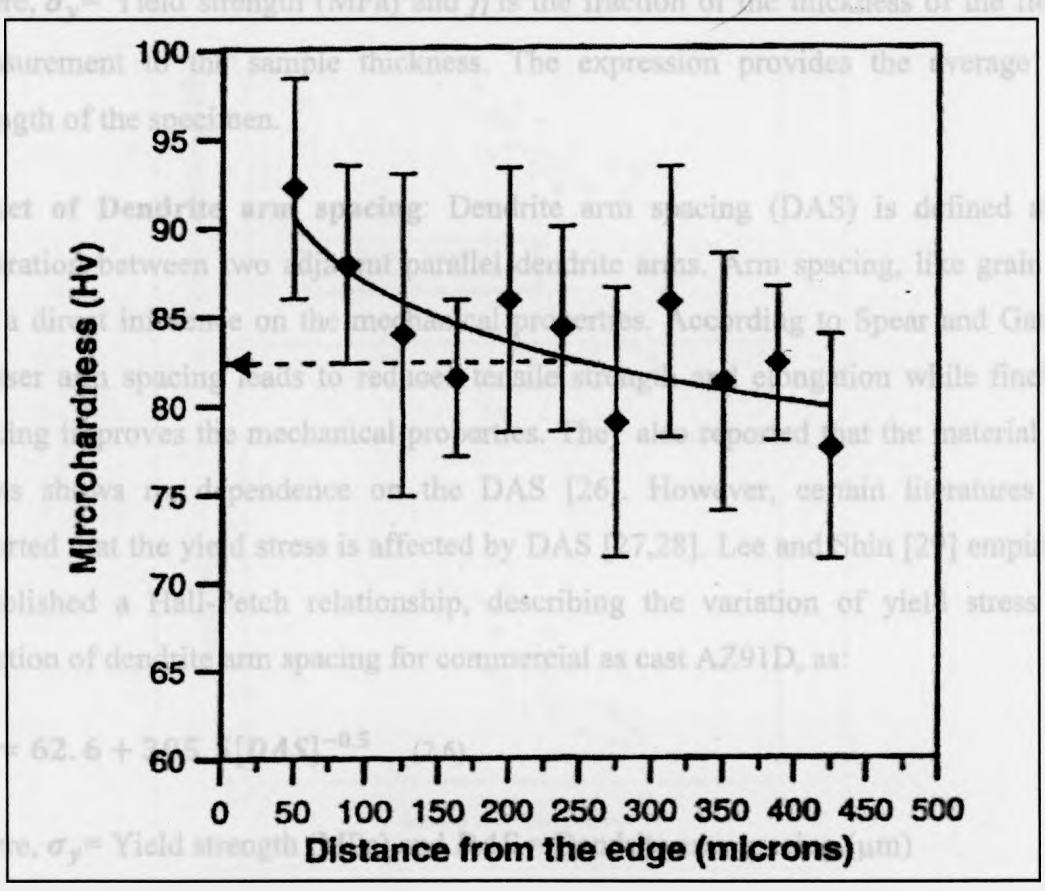

Figure 2.7 Variation of microhardness from skin to core for die-cast AZ91D [25].

Sequeira et. al. [25] observed a reduction in surface hardness of die-cast AZ91D magnesium alloy castings when moving from the skin to the core region. Their observations are presented in Figure 2.7. They observed the hardness values in the skin region to be 15-20 H_v higher than the core. It was further observed that the yield strength in the skin region was considerably higher than in the core region. On the removal of 125 μm (the approximate observed skin thickness), from a casting of 1 mm thickness, the yield strength reduced by 26 MPa.

Weiler proposed [24] a modified form of Hall-Petch relationship, which accounted for the variation in the grain size for each field of measurement across the thickness of die-cast magnesium specimens. This was given as:

$$\sigma_y = \sum f_i \, (\sigma_{y_o} + k(G.D.)^{-0.5}) \quad \text{.....(2.5)}$$

where, σ_y= Yield strength (MPa) and f_i is the fraction of the thickness of the field of measurement to the sample thickness. The expression provides the average yield strength of the specimen.

Effect of Dendrite arm spacing: Dendrite arm spacing (DAS) is defined as the separation between two adjacent parallel dendrite arms. Arm spacing, like grain size, has a direct influence on the mechanical properties. According to Spear and Gardner, coarser arm spacing leads to reduced tensile strength and elongation while finer arm spacing improves the mechanical properties. They also reported that the material yield stress shows no dependence on the DAS [26]. However, certain literatures have reported that the yield stress is affected by DAS [27,28]. Lee and Shin [29] empirically established a Hall-Petch relationship, describing the variation of yield stress as a function of dendrite arm spacing for commercial as cast AZ91D, as:

$$\sigma_y = 62.6 + 305.5[DAS]^{-0.5} \quad \text{.....(2.6)}$$

where, σ_y= Yield strength (MPa) and DAS = Dendrite arm spacing (μm)

Figures 2.8 and 2.9 show the variation of yield strength, elongation and ductility as a function of DAS as observed by Lee and Shin.

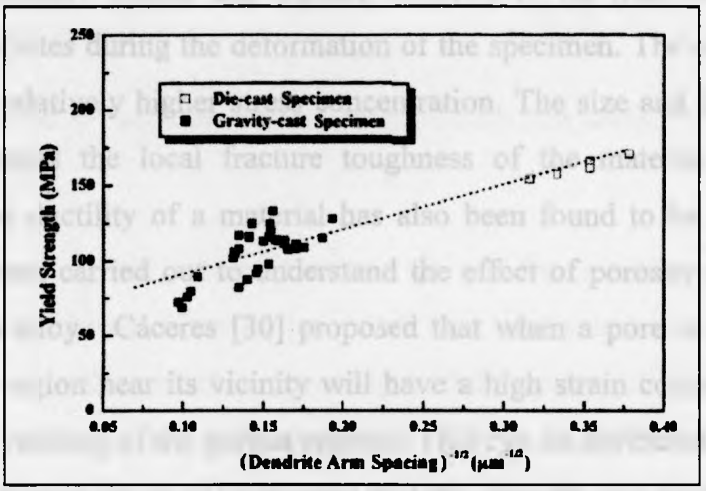

Figure 2.8 Variation of yield stress with respect to $DAS^{-0.5}$ for AZ91D [29].

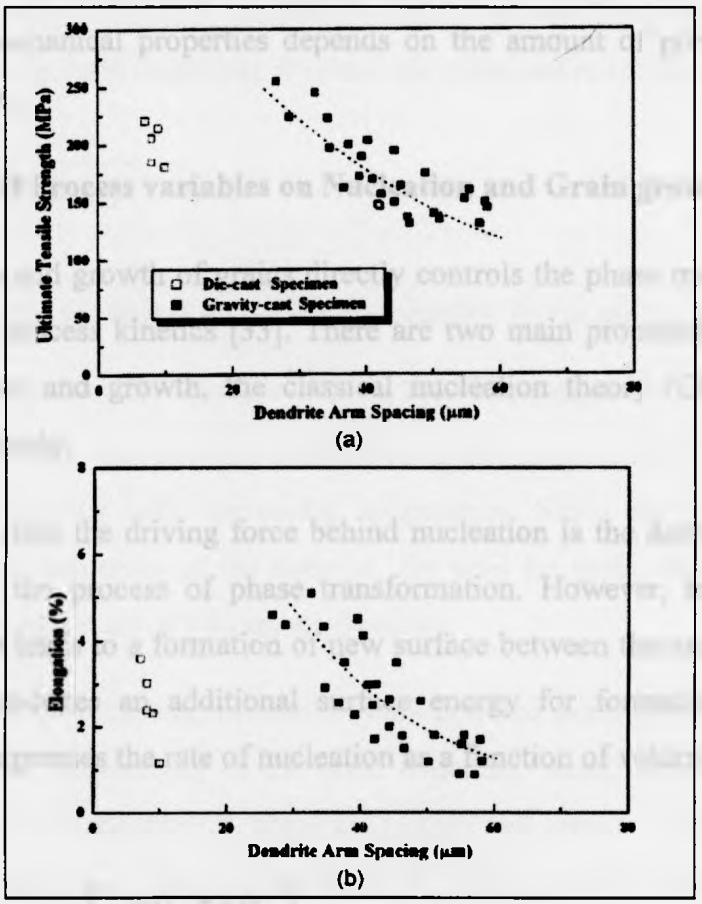

Figure 2.9 Variation of a) UTS and b) Elongation with respect to DAS for AZ91D [29].

Effect of Porosity: Volume defects such as porosity greatly affect the local mechanical properties, especially fatigue and fracture behavior of the material. The pores act as crack initiation sites during the deformation of the specimen. The region around a pore experiences a relatively higher stress concentration. The size and distribution of pores greatly determines the local fracture toughness of the material. The influence of porosity on the ductility of a material has also been found to be significant. Several studies have been carried out to understand the effect of porosity on the strength and ductility of an alloy. Cáceres [30] proposed that when a pore is present in a tensile specimen, the region near its vicinity will have a high strain concentration, leading to the premature yielding of the porous regions. This can be attributed to the reduced load bearing area. Surrapa et. al. [31] reported that the strength and ductility of the material depends on the size of the macropore rather than the volume fraction of the porosity in the specimen. Gokhale and Patel [32] conducted studies and concluded that the variation in mechanical properties depends on the amount of porosity on the tensile fracture surface.

2.5 Influence of Process variables on Nucleation and Grain growth

The nucleation and growth of grains directly controls the phase transformation and re-crystallization process kinetics [33]. There are two main proposed theories to explain grain nucleation and growth, the classical nucleation theory (CNT) and the Zener theory, respectively.

CNT proposes that the driving force behind nucleation is the decrease in volume free energy during the process of phase transformation. However, the process of grain nucleation also leads to a formation of new surface between the nuclei and the original phase. This produces an additional surface energy for formation of the interface. Equation 2.7 expresses the rate of nucleation as a function of volume free energy, as per CNT.

$$\frac{dN}{dt} \propto (1-f)kT \exp\left[-\frac{\Delta G_f^* + Q_D}{kT}\right] \quad \text{.....(2.7)}$$

Here parameter $(1-f)$ represents the decrease in the number of potential nucleation sites. $\Delta G_f{}^*$ can be expressed as $\psi / \Delta g_v{}^2$, where Δg_v is the free energy for phase transformation and ψ accounts for the energy of the new surface formed and the shape of the nucleus [33].

Nucleation can occur via two mechanisms: progressive nucleation and instantaneous nucleation. In progressive nucleation (PN), the nucleation processes occurs on a continuous basis, with nucleation occurring in the presence of nucleated grains. Thus, the nucleated grains are of different sizes. On the other hand, in instantaneous nucleation (IN) a fixed number of grains nucleate and are of the same size, growing at the same rate [34].

The classical Zener model [35] predicts a parabolic growth for a spherical grain under a diffusion limited growth condition. It relates the grain radius to time as the equation as:

$$\left(\frac{G.D.}{2}\right) = \chi\sqrt{D_C^{\gamma}(t-t_s)} \quad \text{.....(2.8)}$$

χ is a parameter dependent on the solute solubility in the matrix; t_s is the time value at which the grain nucleates, whereas D_C^{γ} is the diffusion coefficient in the bulk melt. With increasing time there is also a decrease in the temperature. This implies that the grain radius increases with decreasing temperature. Since the grain size has direct influence on the properties of the material, the need for grain refinement is of utmost importance during industrial casting applications.

For high pressure die casting, nucleation initiation and grain refinement occurs due to the high thermal conductivity of the mold materials, which ensures that many small grains of the primary magnesium phase are formed and carried. Grain refinement can be defined as a process of inoculation so as to induce grain boundary strengthening. However, for sand casting, the grain refinement needs to be introduced by the addition of alloying elements and nucleants (a grain refiner) before or during the casting process.

Unlike aluminum alloys, there are not many commercially well-established grain refiners available for magnesium alloys [36].

The following discusses several of the grain refining techniques for Magnesium alloys:

a) Superheating

This technique deals with heating the alloy to a temperature above its liquidus and holding it there for a short time, followed by cooling. The superheat range is around 150-260 °C. Al (more than 1 wt. %), Fe and Mn significantly affect the process of grain refinement. Increasing the Al content leads to an increase in the grain refining tendency. Excess of manganese retards the process, while Zn shows negligible effect. The interplay of superheating range and the holding time decides the resultant grain size.

The grain refinement mechanism during superheating is still subject to discussion. Wood proposed [37] that the solubility of Fe is highly sensitive to temperature and decreases with decreasing temperature. Fe thus precipitates out, acting as a nucleating agent leading to higher nucleation and consequently lower growth rate. Al restricts the solubility of Fe and Mn, thus increasing the tendency for grain refinement.

Another theory explains the phenomenon as due to oxide formation, where the solute particles Al, Mn and Fe form oxides that act as nucleants. The probability of oxide formation is higher at higher temperatures. However, this fails to explain the appropriate temperature range for superheating.

The temperature-solubility-nucleation theory deals with the change in the particle size with the change in temperature. For coarse particles at low temperature, heating would lead to their dissolution and subsequent precipitation as finer particles that act as nuclei.

b) Elfinal Process

In this process, ferric chloride addition takes place at 750 °C. They require lower superheat temperatures and can also be held for a longer duration at the pouring temperature without compromising on the grain refinement efficiency. This process is effective in the presence of Mn and Al (greater than 3 wt. %). Nucleation occurs by formation of Al-Mn-Fe ternary compounds. However, the presence of Fe reduces corrosion resistance of the alloy, thereby limiting its use.

c) Addition of carbon

This method involves inoculation of the melt by carbon particles obtained from paraffin, wax, lampblack and other organic compounds. They have attractive advantages such as a lower operating temperature, larger melt volumes and less fading of the effect on grain refinement with longer hold times. It is used extensively as a magnesium grain refinement technique. The presence of Al in the alloy further promotes nucleation by formation of aluminum carbide (Al_4C_3) as the nucleating agent.

It has been proposed that grain refinement works by two major undercooling mechanisms, namely, thermal undercooling near the mold walls encouraging nucleation and the presence of solute particle in the constitutionally undercooled, to be discussed in section 2.6, region acting as nucleants [36].

Grain size has been typically observed to depend on the rate of heat extraction in the casting [38,39]. It is reported to follow an inverse power law relationship (Equation 2.9 and Figure 2.10) with the cooling rate, as:

$$G.D. \propto R^{-a} \quad \text{.....(2.9)}$$

where, R is the cooling rate (°C/s). R is numerically defined (Equation 2.10) as the negative of the rate of change of temperature with respect to time during solidification.

$$\mathbf{R} = \left[-\frac{\mathbf{dT}}{\mathbf{dt}} \right]_{\mathbf{x,P,V}} \quad \text{..... (2.10)}$$

Equation 2.9 is true under certain conditions. The primary parameter influencing grain size is the degree of undercooling (U_c). The undercooling determines the rate of nucleation. However, nucleation does not take place until a certain degree of undercooling, called critical undercooling, is reached. The critical undercooling is found to be dependent on the rate of heat extraction [40].

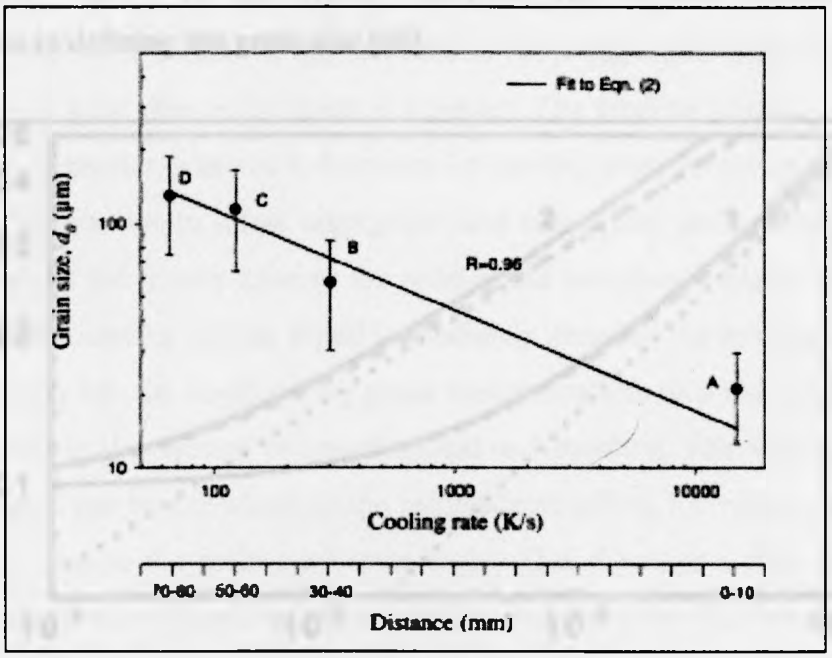

Figure 2.10 Variation of grain size with cooling rate [36].

Kashchiev et. al. [34] described the variation of undercooling, with respect to the cooling rate, as:

$$\ln R = \ln R_o + (1/m)\ln[U_c^{(n+1)m} - U_o^{(n+1)m}] \quad \text{..... (2.11)}$$

where, R_o is the quantity linking the process parameters for instantaneous nucleation and subsequent growth (K/s), R is the cooling rate (K/s), U_o is the relative undercooling value at which instantaneous nucleation occurs and U_c is the critical undercooling for crystallization and **n** and **m** are growth exponents, (1<n<2) and (0<m<1).

If $U_c^{(n+1)m} >> U_o^{(n+1)m}$ then Equation 2.11 can be simplified into

$$ln\left\{\frac{R}{R_o}\right\} = (1+n)ln[U_c] \quad \text{..... (2.12)}$$

Figure 2.11 is a graphical representation of Equation 2.11 and Equation 2.12 with growth exponents 'n' and 'm' assumed to be 1 and 2, respectively. When the undercooling rate is above the critical value, the rate of heat extraction plays a prominent role in defining the grain size [40].

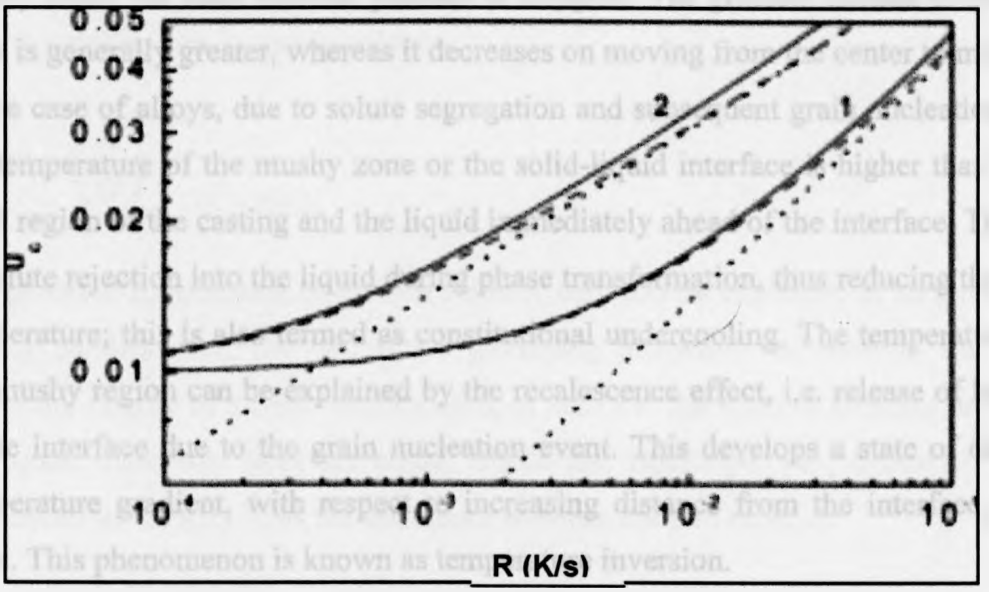

Figure 2.11 Undercooling as a function of cooling rate: The straight lines represent Equation 2.11 and the curved lines signify Equation 2.12. '1' and '2' are the growth exponent values of 'n' [34].

2.6 Influence of Process variables on dendrite growth and coarsening

Before understanding the formation of dendrites and the subsequent growth and coarsening mechanisms, it is essential to introduce two new process parameters namely, thermal gradient and solidification velocity that play an elementary role in the solidification process. These variables have been briefly discussed here.

The thermal gradient (***G***) is a physical quantity (Equation 2.13) that describes the direction in which the rate of change of temperature is most rapid. The gradient is a

vector field and always operates onto a scalar function, which should be an intensive quantity.

$$T = T(x, y, z)$$

$$G = \nabla T = \left(\hat{x}\frac{\partial}{\partial x} + \hat{y}\frac{\partial}{\partial y} + \hat{z}\frac{\partial}{\partial z} \right)_{t,P,V} \bullet T(x, y, z) \quad \text{.....(2.13)}$$

The gradient is always normal to the level curve [41]. The mold shape and geometry greatly affect the local thermal gradient in a region. The gradient normal to the solidus front is generally greater, whereas it decreases on moving from the center to mold walls. In the case of alloys, due to solute segregation and subsequent grain nucleation effects, the temperature of the mushy zone or the solid-liquid interface is higher than both the solid region of the casting and the liquid immediately ahead of the interface. This is due to solute rejection into the liquid during phase transformation, thus reducing the melting temperature; this is also termed as constitutional undercooling. The temperature rise in the mushy region can be explained by the recalescence effect, i.e. release of latent heat at the interface due to the grain nucleation event. This develops a state of decreasing temperature gradient, with respect to increasing distance from the interface, on both sides. This phenomenon is known as temperature inversion.

High gradient values are observed at the mold walls and the thin sections of the casting, while low values are found in the thicker sections. The thermal gradient has a strong influence over the active feeding mechanisms in a region. Feeding is always in the direction of the gradient, since the gradient in a region governs the local pressure differences, which in turn decides the direction of flow of melt. Regions with high gradient and high temperature experience good feeding conditions, as a high gradient enhances the feeding pressure. However, in case of interdendritic feeding, the mechanism is based on capillary pressure, since flow occurs through thin dendrite channels. For this case, it is preferential to have low gradients and high temperatures. High gradients and low temperatures promote solid feeding. As a result, the thermal gradient has a direct influence on the macro and micro-porosity in the region.

Solidification or growth velocity (V_s or V) is the rate of displacement of the solidus front along the casting. It is calculated as the difference between the average rates of atoms joining and leaving the solid phase, since the exchange of atoms between solid and liquid is a continuous process. It has a direction opposite to the heat flow, but a magnitude directly proportional to the rate of heat extraction. Hence, it has a strong dependence on the thermal gradient and generally the combined influence of both parameters affects the solidification microstructure. The rate of movement is directly proportional to the rate of undercooling at the interface. At a macro-scale analysis, the growth velocity can be expressed by:

$$V_s = \left(\frac{R}{G}\right) \quad \text{..... (2.14) [42]}$$

The physical significance of growth velocity can also be explained at an atomic scale. During solidification, the two active governing processes are freezing and melting. When the degree of kinetic undercooling is zero i.e. the rates of freezing and melting are equal, these two rates are equal. Biloni and Boettinger [43] defined the overall solidification velocity V_s as the difference between the two rates, as:

$$V_s = V_0\left(1 - \exp\left(\frac{-\Delta G_f}{RT}\right)\right) \quad \text{..... (2.15)}$$

where, ΔG_f = free energy for solidification (J/mole) and V_0 is the hypothetical maximum growth velocity at infinite driving force. The above relation is based on the assumption that the rate of forward movement (incorporation of atom into solid) is same as the rate of backward movement.

Dendrite growth is primarily an outcome of temperature inversion (Figures 2.12 and 2.13). Thus, a temperature gradient normal to the interface is set up on both sides of the interface. The net direction of heat flow is though, from liquid to solid.

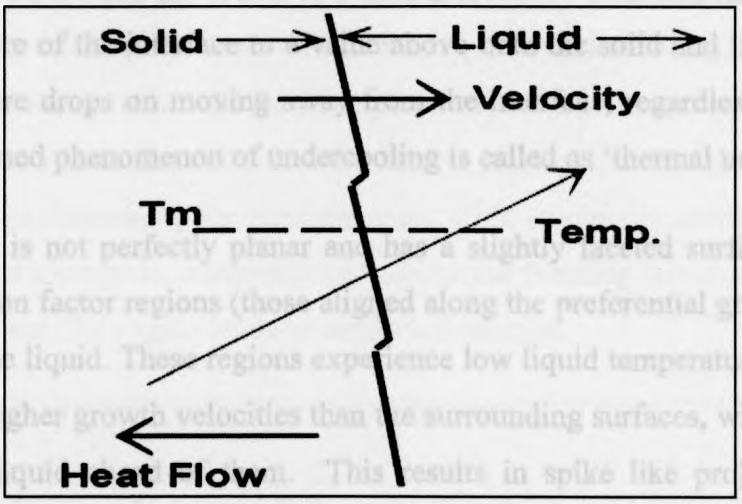

Figure 2.12 Schematic of a moving solid-liquid interface.

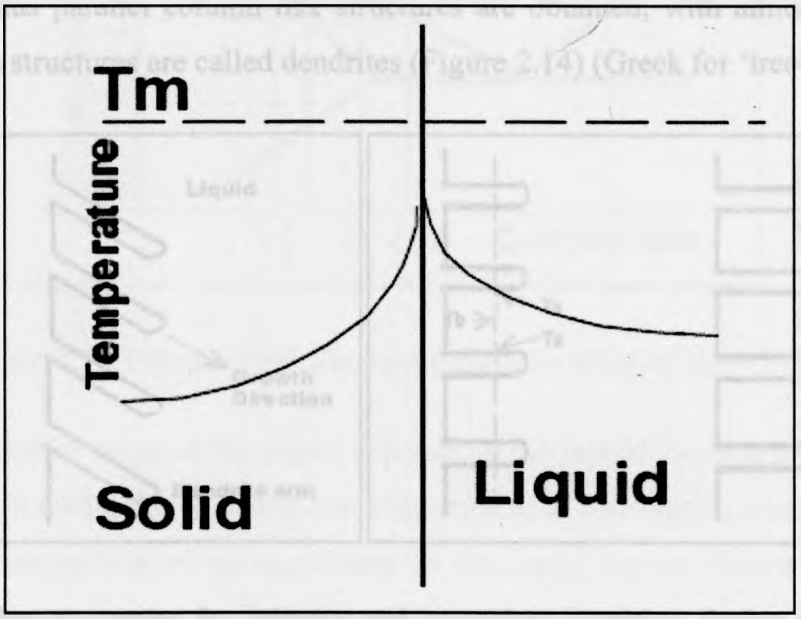

Figure 2.13 Schematic showing the temperature profile, at the interface, during temperature inversion [39].

Considering the solidification of pure metal or a eutectic alloy, the interface moves away from the chill zone as solidification proceeds. During the entire process, there will be a constant heat flow away from the interface through the solid region. Now, if the liquid is in an undercooled state, then the liquid ahead of the interface will exist in a

temperature below its melting point. When phase transformation occurs at the interface, then a certain amount of latent heat of fusion is released. This heat release will increase the temperature of the interface to a value above both the solid and liquid region. Thus the temperature drops on moving away from the interface, regardless of the side. The above mentioned phenomenon of undercooling is called as 'thermal undercooling' [44].

The interface is not perfectly planar and has a slightly faceted surface, with the high accommodation factor regions (those aligned along the preferential growth orientations) jutting into the liquid. These regions experience low liquid temperatures ahead and thus will exhibit higher growth velocities than the surrounding surfaces, which have a higher temperature liquid ahead of them. This results in spike like projections, from the interface into the liquid. These projections accompany with them release of latent heat, thus heating up the surrounding liquid and retarding further growth of similar projections. Thus parallel column like structures are obtained, with almost equivalent spacing. These structures are called dendrites (Figure 2.14) (Greek for 'tree-like').

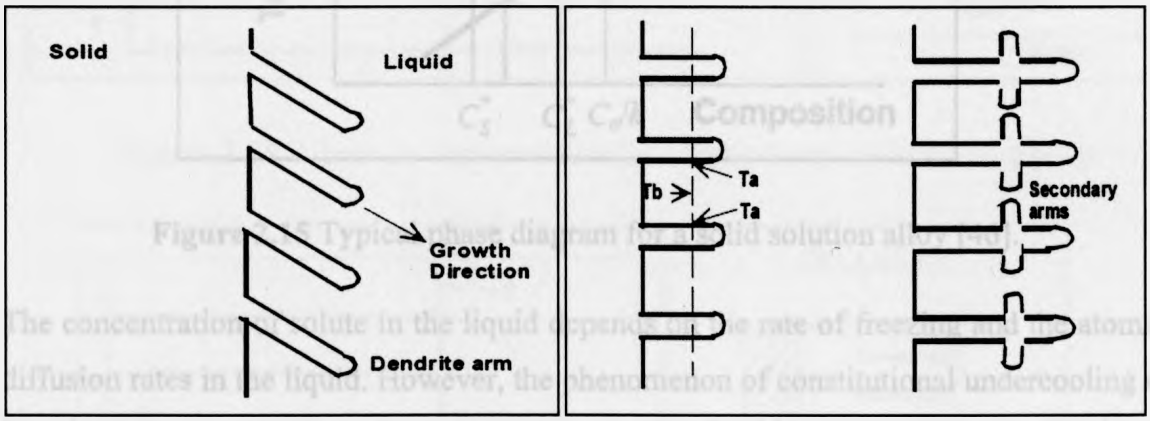

Figure 2.14 Growth modes for primary and secondary dendrites during solidification [44].

The region lying between the dendrite arms also has a decreasing temperature gradient (by a similar analogy given to explain the growth of primary arms) due to the release of latent heat during the arm growth in the surrounding liquid. This promotes the growth of secondary arms and in a similar fashion the growth of tertiary arms. Dendrite arms usually grow both in thickness and length [44].

In the case of solidification of normal alloy systems, the major contributing factor is the effect of constitutional undercooling/supercooling [45]. The difference in the solid and liquid solubility is the main cause behind this type of undercooling. The solid contains less amount of solute, while the liquid region is rich in solute content (Figure 2.15). As solidification proceeds, the solid forming rejects more solute into the liquid just ahead of the interface, increasing its concentration. This eventually reaches a steady state condition. This change in concentration lowers the freezing temperature of the liquid near the interface. This again leads to dendrite formation.

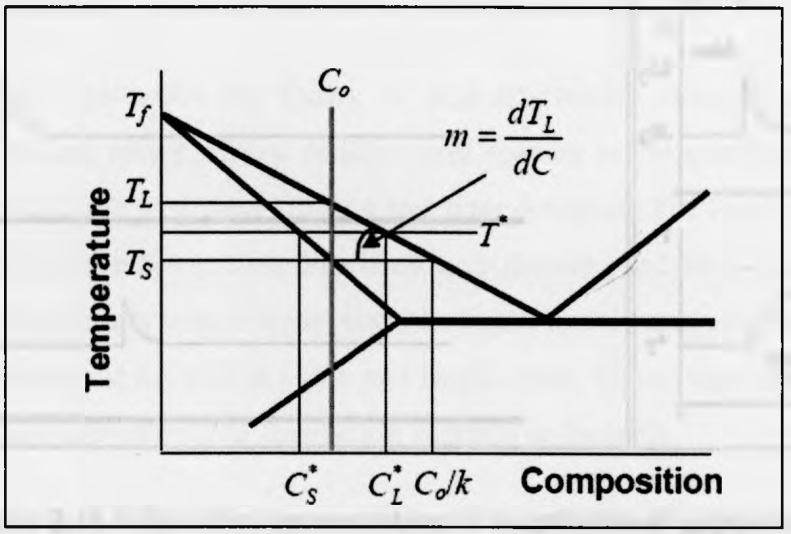

Figure 2.15 Typical phase diagram for a solid solution alloy [46].

The concentration of solute in the liquid depends on the rate of freezing and the atomic diffusion rates in the liquid. However, the phenomenon of constitutional undercooling is based on the assumption of no convection in the liquid region; otherwise the large concentrations experienced at the interface are not possible.

The distance of the supercooled zone, as shown in Figure 2.16, decides the dendritic growth morphology. If the distance is large, then dendritic growth is expected. On the other hand, for small distance values, a cellular growth will be expected. Cellular growth arises as a result of limited depth of undercooled layer (Figure 2.17), forming small oval projections on the interface. This kind of interface moves along with the undercooled region and micro-segregation is observed at the cusp formations in-

between the projections. The temperature of the solid on the oval tips furthest to the right (T_1) is higher than the temperature at the cusp region (T_2). This results in higher solute content in the liquid freezing at the cusps, thus explaining the micro-segregation in this region. These are called the 'cell walls'. [44]

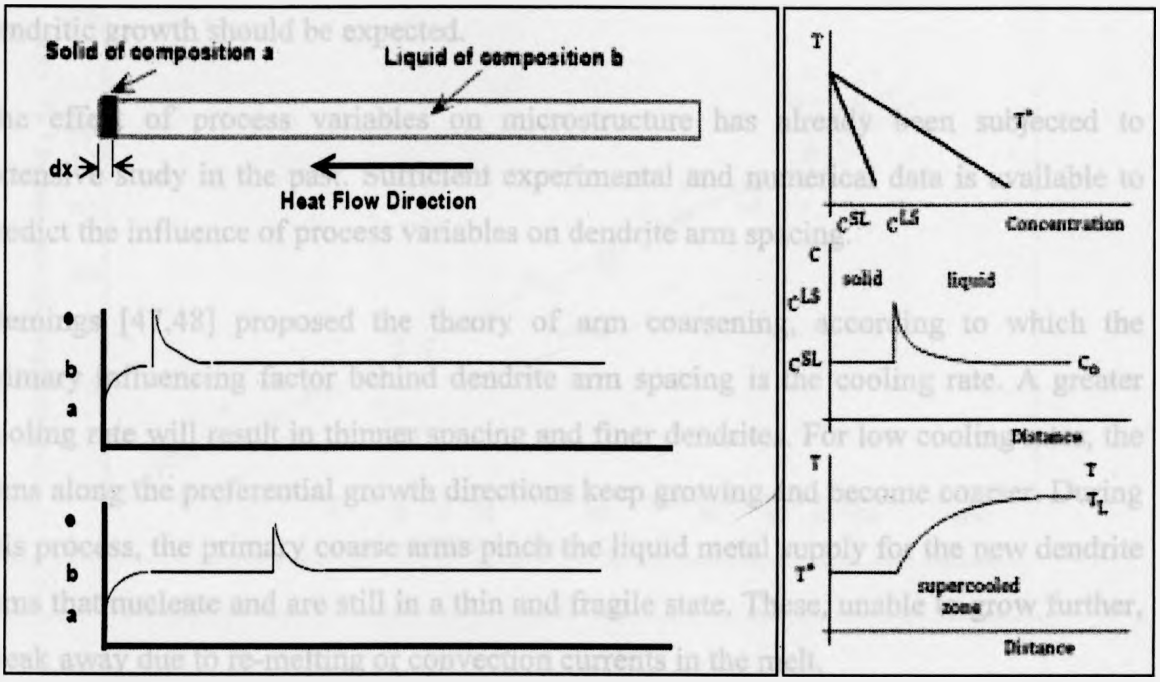

Figure 2.16 Schematic representation of constitutional undercooling [44].

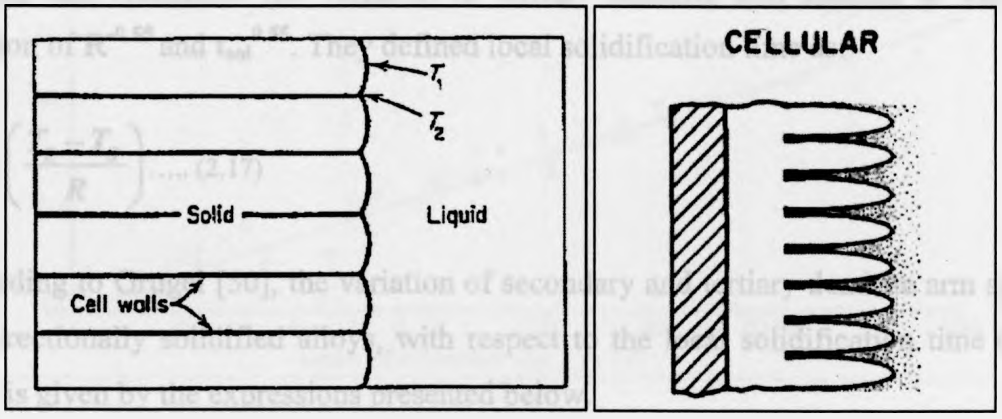

Figure 2.17 Schematic representation of cellular growth [44,47].

The interface stability can also be determined by the desorption probability. Desorption probability for a molecule is defined as:

$$P_{desorption} \propto \exp\left(-\frac{\Delta S_f}{k}\right) \ldots\ldots (2.16)$$

For higher values of $\frac{\Delta S_f}{k}$, we obtain a planar interface; whereas for lower values a dendritic growth should be expected.

The effect of process variables on microstructure has already been subjected to extensive study in the past. Sufficient experimental and numerical data is available to predict the influence of process variables on dendrite arm spacing.

Flemings [47,48] proposed the theory of arm coarsening, according to which the primary influencing factor behind dendrite arm spacing is the cooling rate. A greater cooling rate will result in thinner spacing and finer dendrites. For low cooling rates, the arms along the preferential growth directions keep growing and become coarser. During this process, the primary coarse arms pinch the liquid metal supply for the new dendrite arms that nucleate and are still in a thin and fragile state. These, unable to grow further, break away due to re-melting or convection currents in the melt.

Sá et. al. [49] studied the effect of cooling rate and local solidification time on arm spacing and concluded the variation of tertiary dendrite arm spacing to vary as a function of $R^{-0.55}$ and $t_{sol}^{0.55}$. They defined local solidification time as:

$$t_{sol} = \left(\frac{T_L - T_S}{R}\right) \ldots\ldots (2.17)$$

According to Grugel [50], the variation of secondary and tertiary dendrite arm spacing, for directionally solidified alloys, with respect to the local solidification time (Figure 2.18) is given by the expressions presented below.

$$\mathbf{SDAS} = \mathbf{k}t_{sol}^{(1/2)} \ldots\ldots (2.18)$$

$$\mathbf{TDAS} = \mathbf{k}t_{sol}^{(1/3)} \ldots\ldots (2.19)$$

Hunt, Lu et. al. in 1996 [51] and Kurz-Fisher [52,53], postulated an expression representing dendrite arm spacing (λ) as a function of G, V, where,

$$\lambda \propto V^{-a} G^{-b} \ldots\ldots (2.20)$$

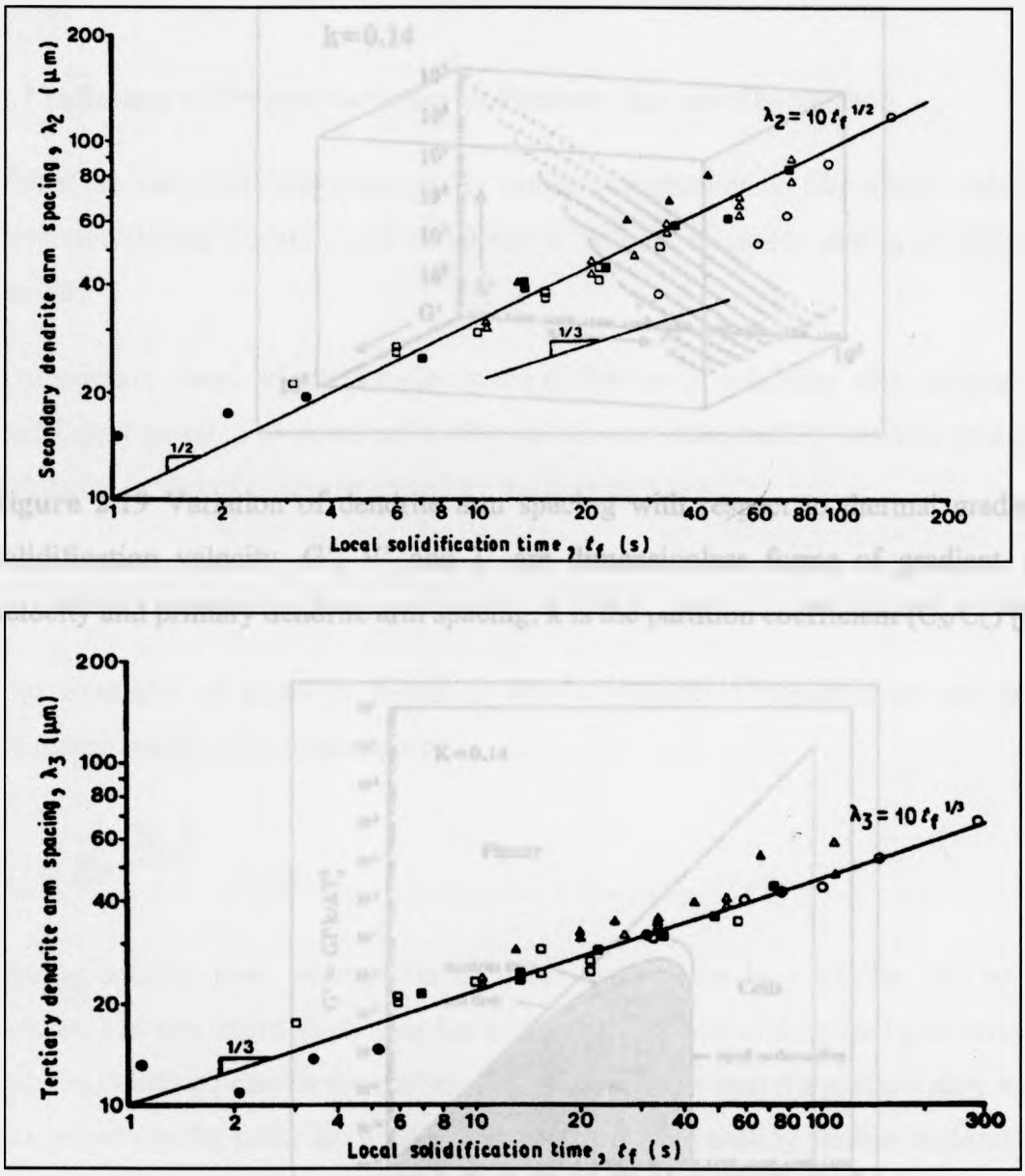

Figure 2.18 Variation of SDAS and TDAS with respect to local solidification time for Al-Si alloys (for diff. Si concentrations (wt. %) – 4, 6, 8, 10 at G=5 K/mm; Si – 6 wt. % at G=15 K/mm) [50].

They proposed that the variation of primary dendrite arm spacing is a function of gradient and solidification velocity (Figure 2.19), as:

$$\lambda \propto V^{-0.25} G^{-0.5} \quad \text{.....(2.21)}$$

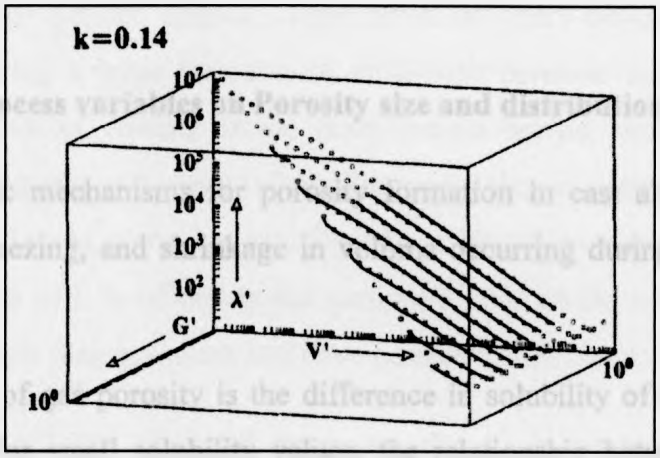

Figure 2.19 Variation of dendrite arm spacing with respect to thermal gradient and solidification velocity. G', V' and λ' are dimensionless forms of gradient, growth velocity and primary dendrite arm spacing; k is the partition coefficient (C_S/C_L) [51].

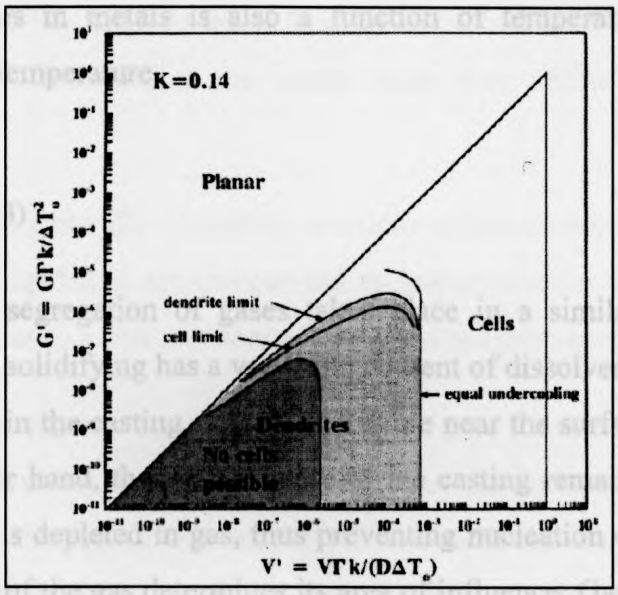

Figure 2.20 Influence of G and V on the solidification front morphology. ΔT_o is the degree of constitutional undercooling; D is the solute diffusivity and **Γ** is the Gibbs-Thomson coefficient [51].

The Hunt-Lu model [51] further states that the stability and morphology of the solidification front (Figure 2.20) is determined by the variation of G and V. G and V directly influence the degree of undercooling ahead of the interface, which predominantly decides whether the solidification front is planar, cellular or dendritic in nature.

2.7 Influence of Process variables on Porosity size and distribution

There are two basic mechanisms for porosity formation in cast alloys, namely, gas evolution during freezing, and shrinkage in volume occurring during solidification of metals.

The primary cause of gas porosity is the difference in solubility of hydrogen in solid and liquid metal. For small solubility values, the relationship between pressure and solubility in metals is approximated by the Sievert's law:

$$c_g = k\sqrt{p} \quad \text{..... (2.22)}$$

The solubility of gases in metals is also a function of temperature and generally increases rapidly with temperature.

$$c_g = Be^{-\left(Q/RT\right)} \quad \text{..... (2.23)}$$

During solidification, segregation of gases takes place in a similar way to that of solutes. The last liquid solidifying has a very high content of dissolved gas, which forms bubble- creating pores in the casting. If the bubbles are near the surface, they escape as gas pores. On the other hand, those at the core of the casting remain as porosity. The area around gas pores is depleted in gas, thus preventing nucleation of other gas pores. The diffusion distance of the gas determines its area of influence. Gas pores are usually spherical in shape, due to formation of bubbles and are distributed uniformly along the casting. Gas solubility has been shown to be affected significantly by the applied pressure; gas solubility can be prevented by carrying out freezing processes under high pressure conditions [44].

In the case of shrinkage, the liquid freezing to solid causes a pressure drop in the melt and feeding of the shrinkage zone, by liquid metal, is restricted. Eventually, a pool of liquid gets surrounded by a shell of solid metal. This liquid then cools to solid and the accompanying shrinkage becomes shrinkage porosity. Shrinkage pores have long irregular arms and no defined shapes. These pores are more common in long range freezing alloys (having a large temperature difference between liquidus and solidus temperatures), as lack of feeding is the main reason behind shrinkage. A single shrinkage pore may appear as a cluster of smaller pores lying on a plane, when observed in a two-dimensional scale, since it is actually a large irregular central pore through the volume of the casting with its offshoots and sections visible on the surface. They have a larger area of influence than gas pores and have a random distribution [54].

In practical cases [55], the observed pores are due to a combination of gas and shrinkage. When a shrinkage pore forms around a gas pore, it is facilitated by the gas pores. Lee and Gokhale termed this category as gas induced shrinkage porosity (GISP). The air in the gas pore acts as a heat insulating medium and thus the chemical pressure inside the gas pores, being proportional to the gas concentration, can reduce the heat transfer rate in the melt. This leads to lower local solidification rates inducing shrinkage porosity. GISP are not connected to the central main pore unlike normal shrinkage porosity.

Porosity in a casting is generally classified as micro or macro-porosity. Large pores, with diameters exceeding 5 mm are categorized as macro-porosity, while pores in the size range of few microns to a few millimeters is termed as micro-porosity [56].

The effect of process parameters on the phenomenon of pore formation has been subject to extensive studies. However, it has been observed that the formation mechanisms are governed by a combined effect of the various process variables. The basic mechanism determining the local pore formation is the rate of feeding in the mushy region. It is especially necessary to understand shrinkage induced porosity since it is the primary cause behind formation of macroporosity, which deteriorates material ductility and fracture toughness. Various criterions and parameters have been defined to quantify the feeding in a region and subsequently the resultant shrinkage.

Niyama, Uchida et. al, in 1982 [57], reported that the porosity is dependent on the ratio of thermal gradient to the square root of cooling rate. They initially carried out experiments on steel castings with different types of risers. Both were step plates with a circular riser in one and a plate shaped riser in the other. Solidification time was proposed as the criterion for shrinkage. A modified form of heat content was defined initially on the basis of Chvorinov's rule [58], which relates the solidification time for a simple casting to the volume and surface area of the casting.

$$t_f = kH\left(\frac{V}{A}\right) \quad \text{..... (2.24)}$$

where, $\mathbf{H=\rho\ (L + c\ \Delta T_{sh} + c\ \Delta T_{st})}$

They applied this rule on both the cylindrical and plate risers (Equation 2.25) and compared them, obtaining the following equation.

$$H_c\left(\frac{V}{A}\right)_c = H_p\left(\frac{V}{A}\right)_p \quad \text{..... (2.25)}$$

Subscript 'C' represents the cylindrical riser and 'P' is for the plate riser. H_p is known as the modified heat content [59]. The solidification time parameter provided crude approximations regarding the prediction of shrinkage porosity in a casting. Thus, Niyama et.al further proposed using the temperature gradient as the defining parameter for shrinkage in a casting. It was found that at low temperature gradients the shrinkage was at a greater level. Hence, temperature gradient was proposed to be a powerful tool for shrinkage prediction. It was also found that for cylindrical steel castings of different diameters, the diameter was inversely proportional to the temperature gradient. The use of temperature gradient to predict shrinkage was based on the application of Darcy's law for interdendritic fluid flow. However, both thermal gradient and solidification time were completely empirical and did not account for the variations and effect due to casting size. Thus, a new parameter was defined as an accurate measure of shrinkage porosity and this was termed as the '**Niyama**' criterion.

$$N_y = \left(\frac{G}{\sqrt{R}}\right) \quad \text{..... (2.26) [57]}$$

This criterion has proved to be a useful prediction criterion and is used for industrial castings at a large scale. In 2008, Carlson and Beckermann [60] defined a dimensionless form of Niyama (Equation 2.27), proposing it to be a more accurate prediction for porosity.

$$N_y^* = C_\lambda \frac{G}{R^{5/6}} \sqrt{\frac{\Delta P_{cr}}{\mu_l \beta \Delta T}} \quad \text{..... (2.27)}$$

Carlson et.al [61] also reported that at higher Niyama values, lower porosity levels are observed. For Niyama values greater than 2.0 the porosity levels are very low and there is a greater presence of micro-pores rather than macro-pores, which is generally gas induced shrinkage type in nature. For Niyama values less than 2.0 there is a sudden increase in porosity levels indicating formation of large gas induced shrinkage pores throughout the structure (Figure 2.21).

For $\mathbf{N_y \geq 2.0}$: Sound Casting

For $\mathbf{1.6 \leq N_y < 2.0}$: Microporosity in the casting

For $\mathbf{N_y \leq 1.0}$: Macroporosity mostly due to inter-connected gas induced shrinkage porosity [61]

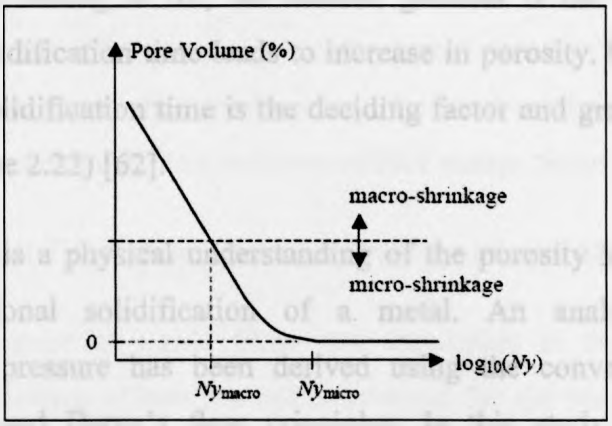

Figure 2.21 Relationship between porosity values and Niyama criterion [61].

Another porosity prediction criterion is the **feeding efficiency parameter**. The feeding efficiency parameter is defined as the ratio of the product of thermal gradient and cube root of the square of the solidification time to the solidification velocity (Equation 2.28). It was first proposed by Lee, Chang et. al [62], based on empirical analysis.

One of the major underlying factors behind pore formation is the interdendritic fluid flow. Poirier et. al [63] reported increase in interdendritic feeding and reduction in porosity with increasing gradient and cooling rate. This disagrees with the predicted Niyama criterion. Following this, Pathak and Prabhakar [64] provided the theory of FET (feeding efficiency due to solidification time during the last stage) and FEP (feeding efficiency due to the pasty zone). The Niyama criterion can be explained by the FET theory, since it generally applies to the end of the solidification process, where the solute content approaches the eutectic compositions. The FET theory states that for a greater solidification time or lower cooling rate, there is a larger amount of time for interdendritic feeding to take place and subsequently less shrinkage. Conversely, the FEP theory depends upon a high thermal gradient and a high cooling rate, resulting in lower solidification times. Combining both the FET and FEP, the feeding efficiency parameter was proposed to account for both the effects.

$$FEP = \frac{G * t^{2/3}}{V_s} \quad \text{..... (2.28)}$$

This accounts for both the effects of thermal gradient and solidification time. In the first regions of the casting to fill, the thermal gradient is the dominating factor and an increase in solidification time leads to increase in porosity. However, at the end of the castings the solidification time is the deciding factor and greater values result in lower porosity (Figure 2.22) [62].

Shown below is a physical understanding of the porosity formation due to shrinkage during directional solidification of a metal. An analytical expression of the interdendritic pressure has been derived using the conventional mass and energy conservation, and Darcy's flow principles. In this study, the interdendritic region between the tertiary dendrite arms has been considered as the proposed region for pore

nucleation. This assumption is based on the fact that secondary dendrite arms are saddle shaped, when observed in three dimensions. They have a low solid-liquid interfacial energy leading to a small contact angle. This retards the process of pore nucleation [65].

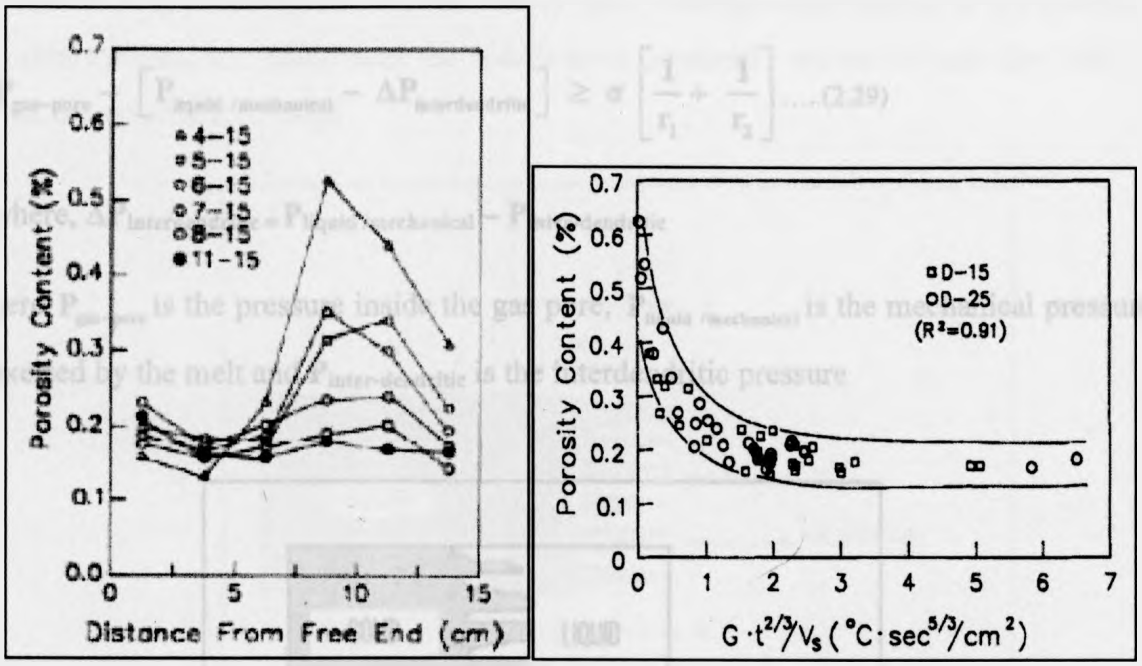

Figure 2.22 Porosity variation along the casting and its dependence on the *FEP* [62].

For Gas Induced Shrinkage Porosity:

The primary factors contributing to porosity formation are: a) heat transfer and alloy solidification rate, b) gas redistribution during solidification, c) fluid flow and mass transfer between liquid and solid phases.

Pores form in a solidifying metal when the partial pressure of the gas corresponding to its concentration within the liquid exceeds the local mechanical pressure in the mushy zone by an amount needed to overcome surface energy forces [66].

Criteria for Pore Formation: Chemical Pressure ≥Local Mechanical pressure

Since the presence of oxide films and impurities in the melt, act as nucleating substrates, nucleation effects are not considered for the porosity model. To accurately quantify the porosity (specifically microporosity) the pore growth phenomenon and the

liquid feeding in the interdendritic region are considered [67]. The feeding in the interdendritic region is strongly dependent on the interdendritic pressure.

Neglecting nucleation and diffusion effects–

$$P_{gas-pore} - \left[P_{liquid\ /mechanical} - \Delta P_{interdendritic}\right] \geq \sigma\left[\frac{1}{r_1} + \frac{1}{r_2}\right] \quad .....(2.29)$$

where, $\Delta P_{interdendritic} = P_{liquid\ /mechanical} - P_{inter\text{-}dendritic}$

here, $P_{gas-pore}$ is the pressure inside the gas pore, $P_{liquid\ /mechanical}$ is the mechanical pressure exerted by the melt and $P_{inter\text{-}dendritic}$ is the interdendritic pressure

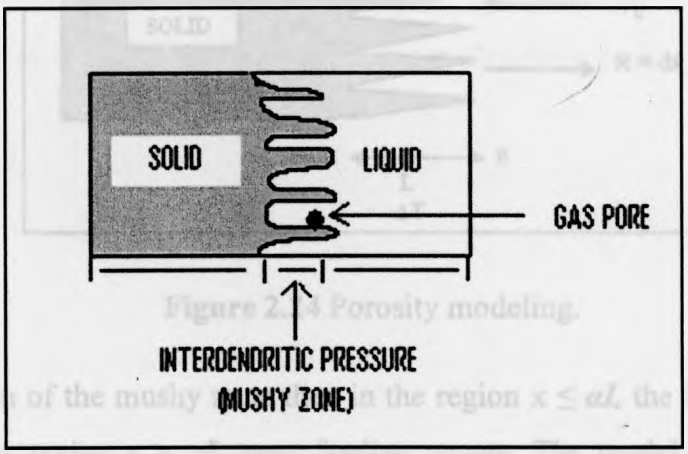

Figure 2.23 Schematic illustration of a pore formation.

So to validate the stability of pore,

$$P_{gas-pore} \geq P_{interdendritic} + \sigma\left[\frac{1}{r_1} + \frac{1}{r_2}\right] \quad ..... (2.30)$$

If there were no gas pores present, then

$$P_{gas\text{-}pore} = 0 \text{ and } P_{interdendritic} \geq -\sigma\left[\frac{1}{r_1} + \frac{1}{r_2}\right] \quad .....(2.31)$$

This accounts for the formation of shrinkage porosity only.

Porosity Modeling:

Zone AB (Figure 2.24) is called the Mushy zone. During solidification, as the interface moves forward, the liquid near the mushy zone constantly moves towards the solid to feed the volume shrinkage.

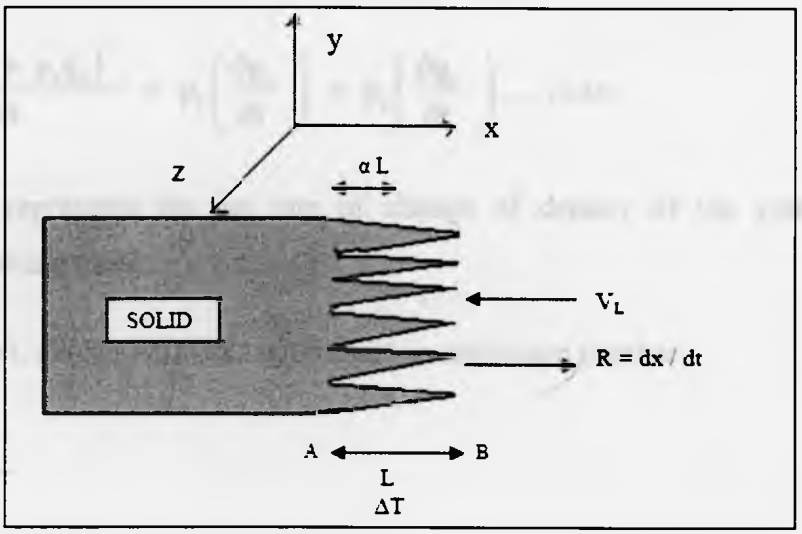

Figure 2.24 Porosity modeling.

If L is the length of the mushy zone then in the region $x \leq \alpha L$ the feeding is restricted. However for the region $x > \alpha L$ mass feeding occurs. The model assumes directional solidification conditions. Therefore, the liquid volume fraction varies linearly along x only i.e. no variation along the y and z axes [66].

So,

$$g_l = \frac{x}{L} \quad \text{..... (2.32) [53]}$$

Applying mass conservation to the whole system:

$\rho_o = \rho_l g_l + \rho_s g_s$ (Neglecting the specific mass of gas)

$$\nabla.(\rho_l g_l V_l)+\frac{\partial \rho_o}{\partial t}=0 \quad \text{..... (2.33)}$$

where, V_l is the volume flow rate of melt (m^3/s) and ρ_l is the specific gravity of melt

Equation (2.33) is applied before the formation of porosity

Therefore,

$$\frac{\partial \rho_o}{\partial t} = \frac{\partial\left(\rho_l g_l + \rho_s g_s\right)}{\partial t} = \rho_l\left(\frac{\partial g_l}{\partial t}\right) + \rho_s\left(\frac{\partial g_s}{\partial t}\right) \quad \text{..... (2.34)}$$

Equation (2.34) represents the net rate of change of density of the system while solidification is taking place.

Sigworth, Wang et. al [68] defined a solidification shrinkage number,

$$\beta = \frac{(\rho_s - \rho_l)}{\rho_s}$$

Also, $g_s + g_l = 1$

Hence,

$$\rho_l = \rho_s(1-\beta) \quad \text{..... (2.35)}$$

Substituting relation (2.35) in equation (2.34)

$$\frac{\partial \rho_o}{\partial t} = \rho_s \beta\left(\frac{\partial g_s}{\partial t}\right) \quad \text{..... (2.36)}$$

Let the rate of solidification be

$$V_s = \frac{dx}{dt} = -\frac{d\left(Lg_l\right)}{dt} = -L\frac{\left(\partial\left(1-g_s\right)\right)}{\partial t}$$

So,

$$V_s = L\frac{dg_s}{dt} \quad \text{..... (2.37)}$$

$$\text{Therefore } \frac{\partial \rho_o}{\partial t} = \frac{(\rho_s \beta V_s)}{(L)} = \frac{(\rho_l \beta V_s)}{(1-\beta)L} \quad \text{.....(2.38)}$$

Thus, substituting equation (2.38) into equation (2.33) gives

$$\frac{\rho_l \partial (g_l V_l)}{\partial x} = -\frac{\rho_l \beta V_s}{(1-\beta) L}$$

Integrating both sides

$$\rho_l \int_0^{g_l V_l} d(g_l V_l) = -\int_0^x \left(\rho_l \beta V_s / (1-\beta) L \right) dx$$

This gives

$$V_l = -\frac{\beta V_s}{(1-\beta)} \quad \text{..... (2.39)}$$

V_l is numerically equal to the volume flow rate (m^3/s) in case of a unit area cross-section. Applying 1- dimensional forms of Darcy's Law at the mushy zone we get,

$$V_l = -\left(K/\mu\right) \nabla \left(P_{inter-dendritic}\right) \text{.... .(2.40)}$$

Now it can be assumed that in the mushy region the flow of the liquid is analogous to the flow through a packed bed of solid since the dendritic structure resembles an interlocked type of structure (Figure 2.25) [63]. The equation of flow through a packed bed of solid is given by Kozeny – Carmen equation,

$$\frac{\partial P}{\partial x} = -\frac{180 \mu (1-e)^2 [v]}{(e^3 d_s^2)} \quad \text{..... (2.41)}$$

where, e is the bed porosity and d_s is the diameter of the solid particles.,

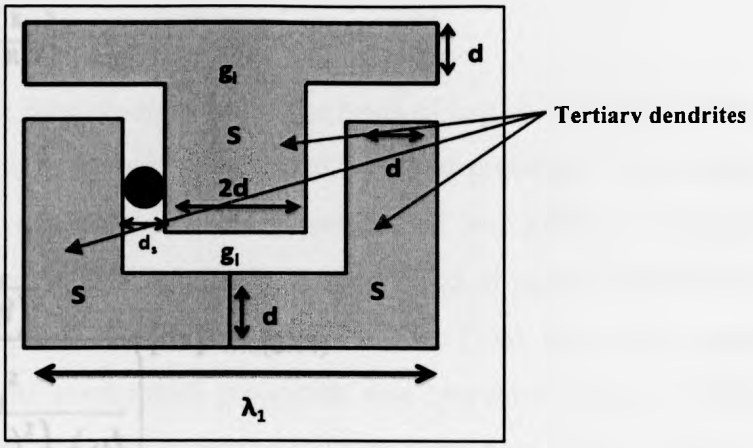

Figure 2.25 Interlocked dendrite structure.

Comparing equation (2.40) and (2.41)

$$K = \frac{e^3 d_s^2}{180\,(1-e)^2}$$

The packed bed of solids is analogous to the mushy region consisting of a dense interdendritic network. Therefore $e = g_l$ and $d_s = \lambda_1 g_l / 2$ ..... [63,69,70]

where, λ_1 is the tertiary dendrite arm spacing (TDAS)

Therefore,

$$K = \frac{g_l^5 \lambda_1^2}{\left(720\,(1-g_l)^2\right)} \quad \text{..... (2.42)}$$

Using (2.39) and (2.42) in Darcy's Law for 1 Dimensional Flow

$$-\frac{\beta R}{(1-\beta)} = -\left(\frac{g_l^5 \lambda_1^2}{\left(720\,(1-g_l)^2\right)(\mu)}\right)\left[\frac{dp}{dx}\right] \quad \text{..... (2.43)}$$

where, μ is the dynamic viscosity, which is dependent on temperature

This implies, $\mu = \mu_0 e^{\left(\frac{E_\mu}{R_g T}\right)}$

Therefore,

$$[dp] = \frac{\frac{\beta V_s}{(1-\beta)}}{\left(\frac{g_l^5 \lambda_1^2}{\left(720\ (1-g_l)^2\right)(\mu)}\right)}[dx] \quad .....(2.44)$$

Let $C = \frac{720\ \beta\ \mu_0}{\left((1-\beta)\ \lambda_1^2\right)}$

Therefore,

$$\Delta P_{inter-dendritic} = CLV_s\ e^{\left(\frac{E_\mu}{R_g T}\right)} \int_0^{g_l} \left(\frac{(1-g_l)^2}{g_l^5}\right) dg_l \quad .....(2.45)$$

Solving the above equation and using $g_s + g_l = 1$,

$$\int_0^{g_l} \frac{\left((1-g_l)^2\right)}{g_l^5}\, dg_l = I\ (g_s,\ \alpha)$$ (where, I is a polynomial function of g_s and α)

Now, $VG = R$

$$\Delta P_{inter-dendritic} = -C'\Delta T R\ e^{(E_\mu/RT)} \frac{I\ (g_s,\ \alpha)}{(G^2)} = Constant * \left(\frac{R}{G^2}\right) ..... (2.46)$$

'-' sign signifies pressure drop.

The above analytical expression validates the Niyama criterion, which states $N_y = G/\sqrt{R}$ as the criterion for quantifying the shrinkage during solidification.

2.8 Summary

This chapter provided a brief description of the basis of our research. It first introduced the important properties along with basic manufacturing processes for magnesium and its alloys. It further discussed the development of solidification microstructure, primarily from the point of view of the thermodynamics of phase transformations and the effect of alloy composition on the as-cast structure. Then, a layout of the effect of structural features on the mechanical properties was presented so as to introduce the need of understanding the process-structure relationships. This was followed by a brief description of various microstructural features and their dependence on the process variables.

Chapter 2 thus concludes that the basic microstructural features namely, grain size, dendrite arm spacing and porosity are greatly influenced by variables such as cooling rate, thermal gradient, solidification velocity, solidification time, and prediction criteria namely, Niyama and feeding efficiency parameter. The next sections will primarily discuss the effect of the above mentioned variables on the as-cast microstructure of commercial magnesium alloys.

Chapter 3

Experimental Techniques

3.1 Casting Procedure

3.1.1 Gravity Sand Casting

The alloy used for the sand casting was AM60B. A simplified step-shaped plate casting geometry (Figures 3.1 and 3.2) was designed with step heights of 4, 8, and 12 mm. The sand mold is designed to promote directional solidification by incorporating a copper chill at the thin end (4mm) of the cavity. Sand was used to keep the mold walls adiabatic. The mold was coated with MgO powder (using spray coating method) to ensure a smooth casting surface and prevent the melt from reacting with its surroundings.

For each casting plate, 3 or 7 thermocouples (K-type; chromel-alumel) were inserted into the pattern to measure the cooling rate and solidification time. The thermocouples report the local temperature at intervals of 1.0 second. During the casting process the thermocouples are connected to a data acquisition system. In total, 36 step-shaped plate castings were produced. The pouring temperature of the melt was maintained at 730 ± 20 °C.

The casting was carried out at room temperature. After completion, the casting was cut into 13 rectangular coupons (12mm*12mm*3mm) along its length.

3.1.2 Wedge Casting

The wedge shaped castings were carried out at the CANMET – Materials Technology Facility in Ottawa. The alloys casted were commercially used AM60B and AZ91D. The ingots were melted and degassing was carried out with hexachloroethane (C_2Cl_6) tablets.

Figure 3.1 Sand Casting Set-up.

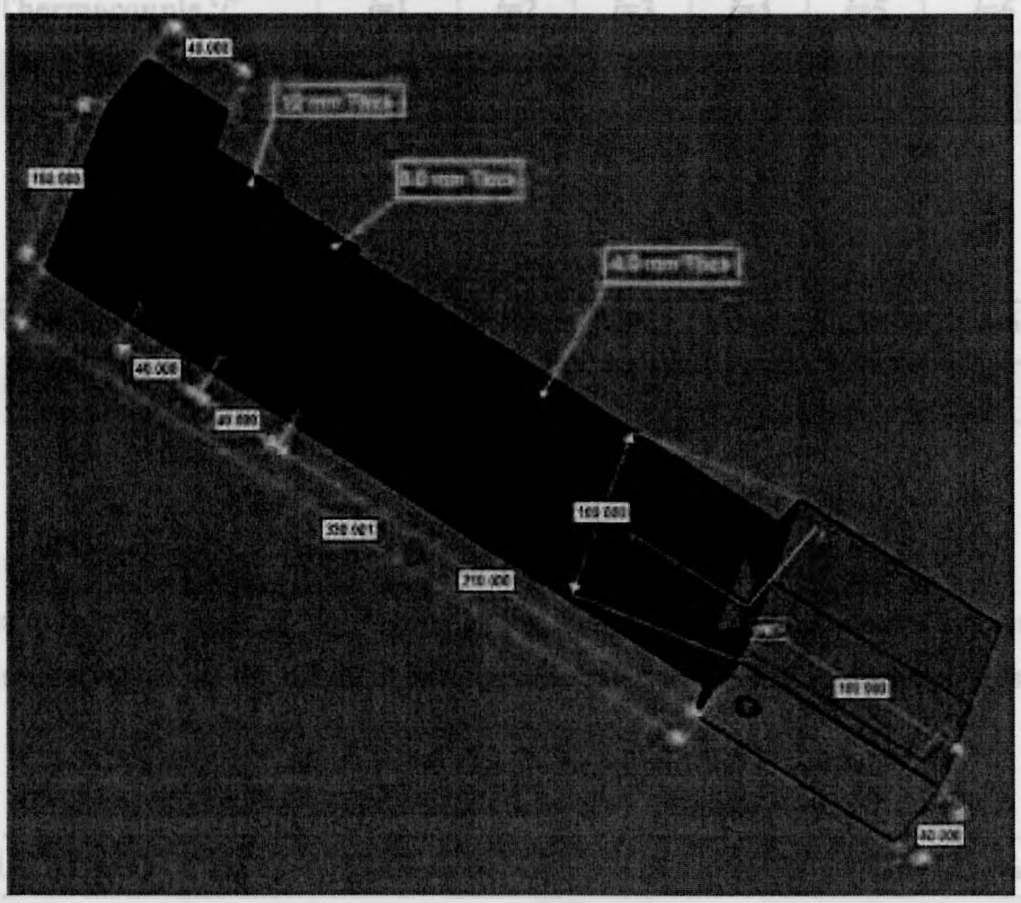

Figure 3.2 Step-shaped mold dimensions.

Argon gas was used to purge the melt. Purging was carried out for around 20 minutes. Spectrographic analysis techniques were used to obtain the chemical composition of the wedge casting. Tables 3.2 and 3.3present the obtained chemical compositions for the AM60B and AZ91D alloys

The mold was wedge-shaped (Figure 3.3) with base dimensions of 200mm x 75mm and a height of 140mm (tip to base). The mold walls were made of water-cooled copper along the longer dimension and of steel along the smaller dimension. 6 K-type thermocouples were positioned along the height of the casting, at the centerline of the mold, as per the distances in Table 3.1.

Table 3.1 Table showing the thermocouple locations for AM60B and AZ91D.

AM60B WEDGE CAST

Thermocouple '*i*'	***i*=1**	***i*=2**	***i*=3**	***i*=4**	***i*=5**	***i*=6**
Location from tip (mm)	13	19	26	37	51	69

AZ91D WEDGE CAST

Thermocouple '*i*'	***i*=1**	***i*=2**	***i*=3**	***i*=4**	***i*=5**	***i*=6**
Location from tip (mm)	12	19	26	39	52	71

The steel walls weren't water cooled. The metal was poured in the mold at a temperature of 1000 °K or 723 °C. After the completion of solidification coupons, at regular intervals along the height of casting, were cut out for metallographic analysis.

Table 3.2 Table showing chemical composition of AM60B.

MELT ALLOY	**%Al**	**%Zn**	**%Mn**	**%Si**	**%Cu**	**%Fe**	**%Ni**
AM60 B	**5.7**	**0.022**	**0.29**	**0.012**	**<0.005**	**<0.005**	**<0.002**

Table 3.3 Table showing chemical composition of AZ91D.

MELT ALLOY	%Al	%Zn	%Mn	%Si	%Cu	%Fe	%Ni
AZ91D	8.70	0.73	0.34	0.015	<0.005	<0.005	<0.002

3.2 Specimen Preparation and Metallographic analysis

The specimens were hot mounted using a phenolic resin compound, so as to make the sample fit for further grinding and polishing. A hot mounting press was used. A pressure of 4200 lbf/in^2 was applied during the mounting process. The mounted samples were subjected to grinding.

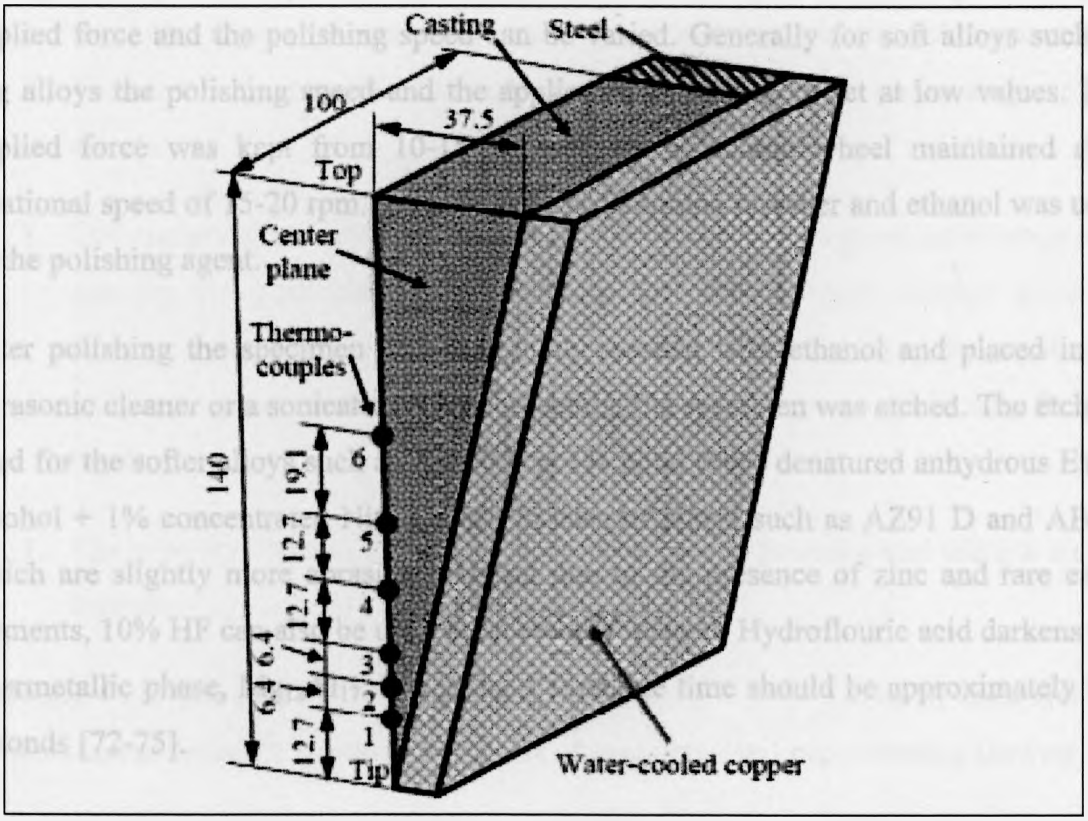

Figure 3.3 Wedge-shaped mold dimensions [71].

Only wet grinding processes were employed in this study since magnesium has a very high affinity for oxygen. A slight increase in temperature of the alloy during the grinding process can lead to burning of the sample, ruining the as-cast microstructure.

After an initial round of coarse grinding on an automatic grinding belt to smooth out any discernable irregularities in the sample, fine grinding using grit paper was carried out.

Silicon carbide papers of the following grades were used: 180, 320, 400, 600, 1200 and 4000. The grinding was done in the presence of a water jet, in a direction perpendicular to the grinding motion.

Once the grinding stage was over the specimen was washed using ethanol. (Mg is a highly reactive metal with a high oxygen affinity hence it can react with water too when kept under prolonged contact).

The specimen was then polished on a manual cloth wheel or an automatic polisher. The applied force and the polishing speed can be varied. Generally for soft alloys such as Mg alloys the polishing speed and the applied force should be set at low values. The applied force was kept from 10-15 N, with the polishing wheel maintained at a rotational speed of 15-20 rpm. A combination of alumina in water and ethanol was used as the polishing agent.

After polishing the specimen was thoroughly washed with ethanol and placed in an ultrasonic cleaner or a sonicator. After sonicating, the specimen was etched. The etchant used for the softer alloys such as AM60 B is 1% Nital (99% denatured anhydrous Ethyl alcohol + 1% concentrated Nitric acid). In case of alloys such as AZ91 D and AE44, which are slightly more abrasion resistant due to the presence of zinc and rare earth elements, 10% HF can also be used as an etching reagent. Hydroflouric acid darkens the intermetallic phase, $Mg_{12}Al_{17}$. The etchant exposure time should be approximately 3-5 seconds [72-75].

After the etchant was applied to the surface, the sample was washed with ethanol and subject to drying using an air gun. The specimen is now suitable to be studied under an optical microscope.

The image obtained was then analyzed using SimplePCI (Hamamatsu Corp.) digital image analysis software and ImageJ image processing program. The purpose of the software is to quantify the porosity, grain size, dendrite arm spacing etc. in the microstructure. Parameters such as the average pore area and percentage porosity were determined and their variation was studied throughout the sample. The grain size variation was studied in both the transverse and longitudinal directions.

a) Determination of grain size (G.D.), average pore area (P_A) and porosity fraction (P_F)

1. Using the image analysis software the region of interest is marked (Figure 3.4). The software selects similar regions on the basis of intensity, color and lightness. An RGB color pattern is used as the images reproduced are digital.

2. Once the region of interest is marked, the software carries out the area and diameter measurements for individual pores or grains (depending on the selection).

3. The numerical average of all the pore area measurements gives the average pore area for that particular image. Similarly the grain diameter average gives the average grain size. These values are furthered averaged over the number of images to produce the total average pore area or average grain size for that region.

4. The porosity fraction for the particular region can be calculated using a simple formula :

Porosity Fraction (%) = Total Pore Area$^{\#}$ (pixels^2) * 100 / (Area of each field of measurement (pixels^2) * number of fields of measurement representing the region)

Total Pore Area = Sum of area values of all the pores in that region.

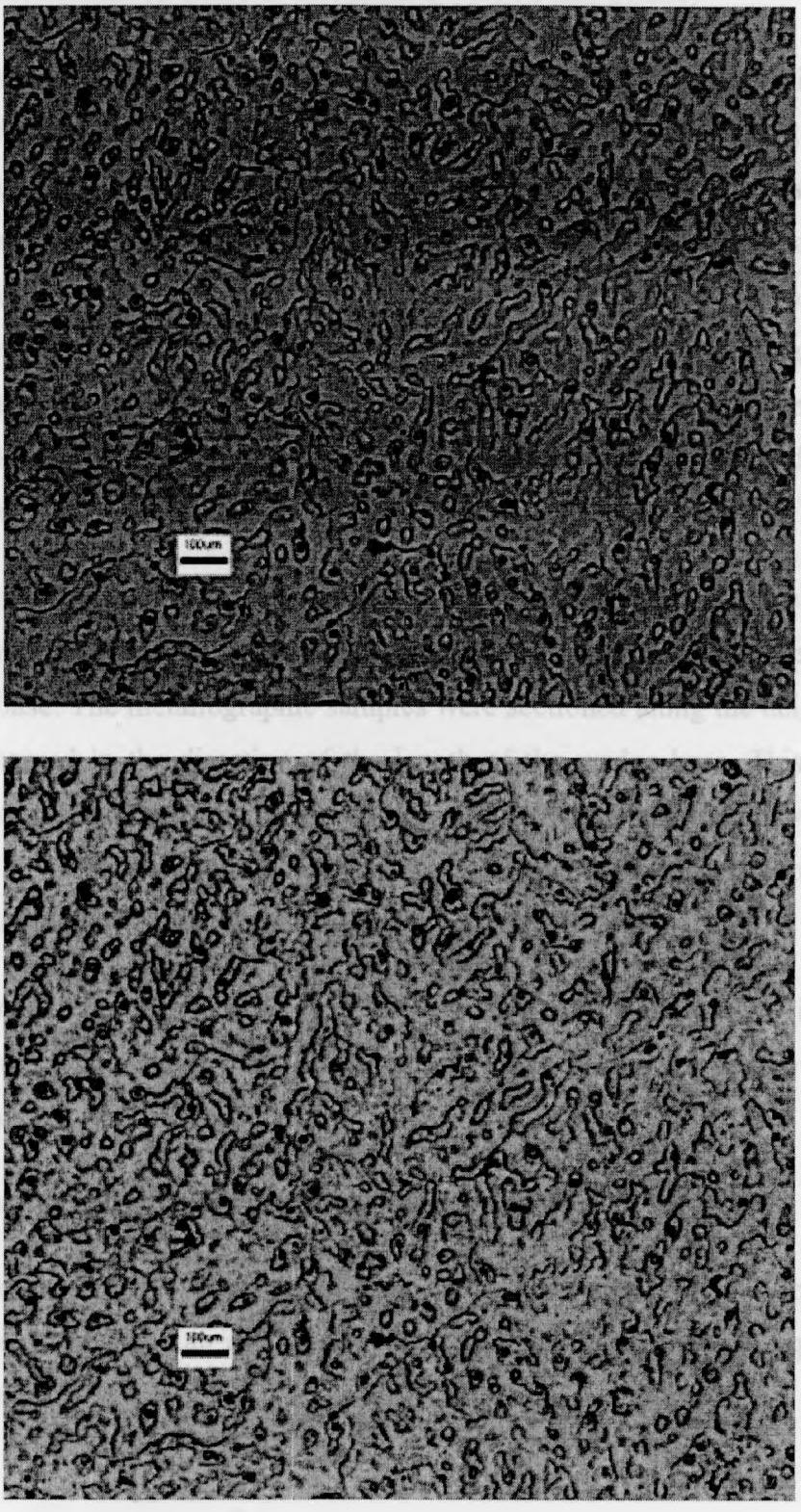

Figure 3.4 a) Optical micrograph of AZ91D wedge casting (as obtained from metallography) b) Same micrograph showing grain size as the selected region of interest.

b) Determination of dendrite arm spacing (SDAS and TDAS)

The dendrites were identified by visual investigation of the optical micrographs. In the case of the sand casting the solidification was in the longitudinal direction, along increasing step heights (See Figure 3.2). The metallographic studies were carried on samples cut along the length. The solidification being directional in nature, the primary dendrites grew parallel to the casting length, directed towards the core of the casting. The secondary and tertiary arms projected along the six crystallographic directions from the primary and secondary dendrites, respectively. Hence, any planar section observed from the transverse direction would reveal the secondary and tertiary dendrites.

However, in case of the wedge casting (Figure 3.3) the dendrites grew away from the mold walls towards the center of the wedge, with the their tips directed towards the wedge base. The metallographic samples were sectioned along the height of the casting and observed in the direction of the length of the wedge base. This implies that the obtained micrographs, for these sections, would display the secondary arms growing in the six crystallographic directions along with the tertiary arms projecting from the secondary dendrites.

The distance between the arm spacing was measured using ImageJ image processing software and an average of 10 measurements for each micrograph, provided the average arm spacing.

c) Density measurements using Archimedes principle

The specimen density is obtained using the Archimedes principle. In this the mass of specimen is found in air and then in water and using force balance equations we arrive at the result:

$$\rho_{\text{specimen}} = \frac{\mathbf{W}}{\mathbf{W}-\mathbf{W}_{\alpha}} \rho_{\text{water}} \quad \text{..... (3.1)}$$

where, ρ is the Density (g/cc), W is the weight of specimen in air and W_a is the apparent weight of the specimen

3.3 SEM/EDX analysis

Phase studies were carried out using LEO 440 SEM (ZEISS Ltd.) setup equipped with a Quartz X1 EDX system. A 20kV electron beam was used and the methods of analysis were BSE (back scattered electron) imaging and SE (secondary electron imaging).

3.4 Summary

The experimental techniques discussed in this section were used to obtain the pre-processed data. This data was further analyzed, both numerically and statistically, to develop empirical correlations between the process variables and the structural features. This has been discussed in the forthcoming sections.

Chapter 4

Thermal and Microstructural analysis

This chapter presents the thermal and microstructural data obtained from the aforementioned experimental procedures. The thermocouples positioned in the castings were used to record temperature values at each location at regular time intervals. The subsequent metallographic analysis gave the corresponding microstructural data.

4.1 Sand Casting – AM60B

4.1.1 Thermal Analysis

The temperature-time data, obtained from the thermocouples, provided the following cooling curves.

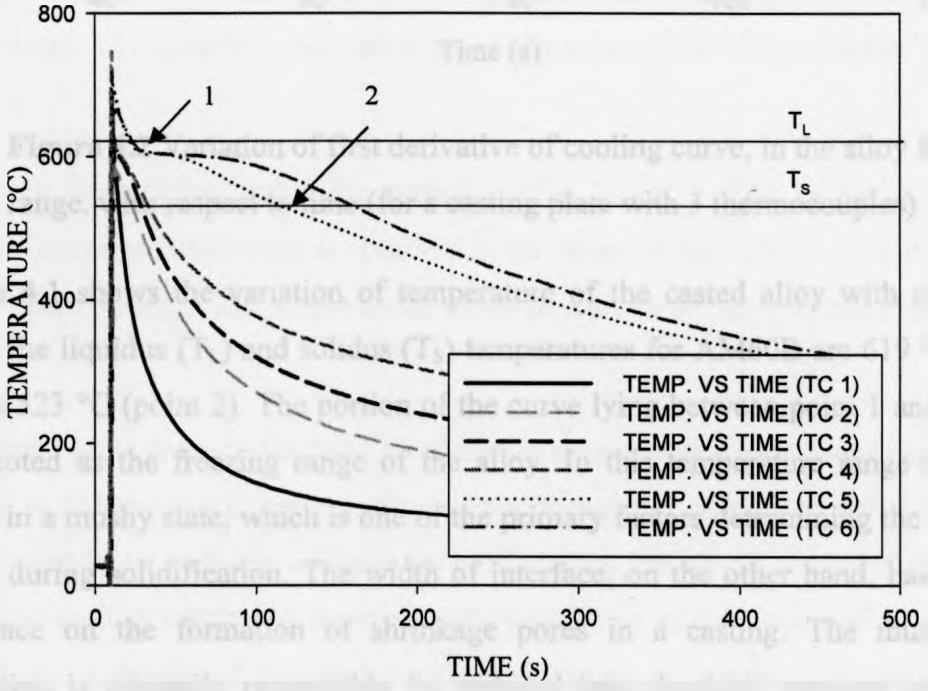

Figure 4.1 Temperature-time curves at different thermocouple locations (for a casting plate with 6 thermocouples).

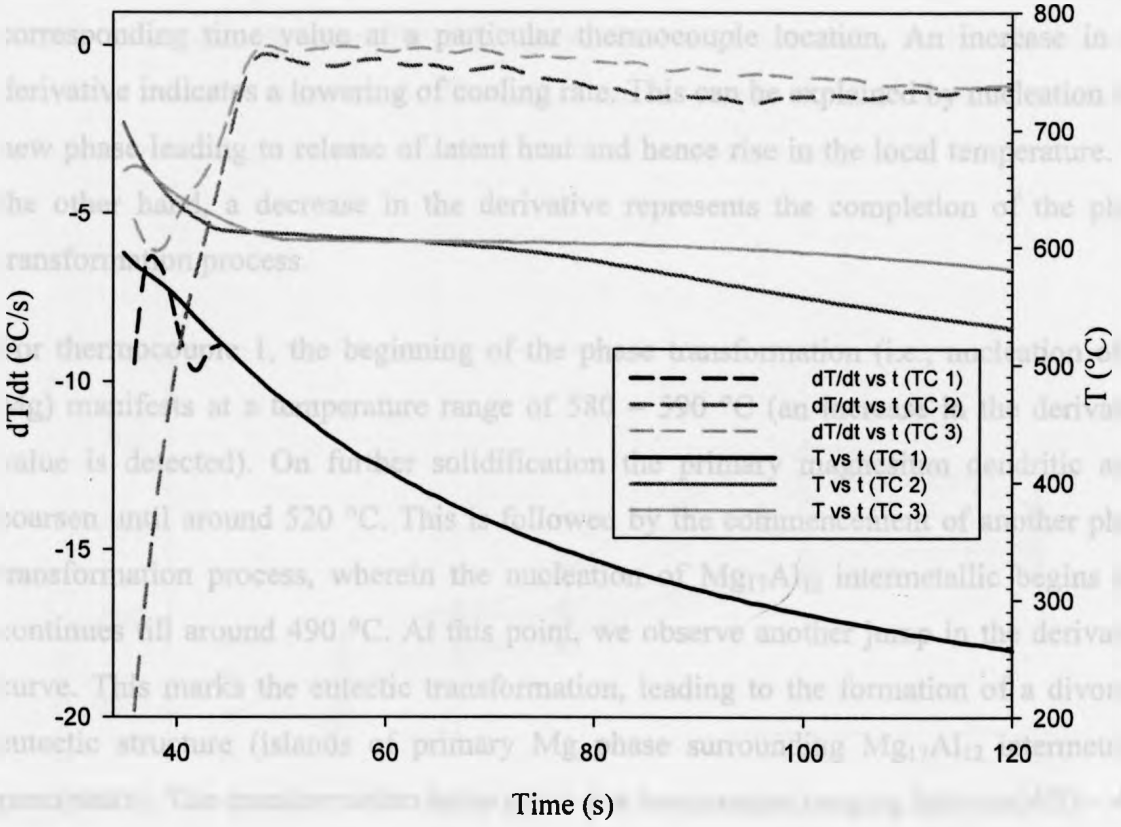

Figure 4.2 Variation of first derivative of cooling curve, in the alloy freezing range, with respect to time (for a casting plate with 3 thermocouples).

Figure 4.1 shows the variation of temperature of the casted alloy with respect to time. The liquidus (T_L) and solidus (T_S) temperatures for AM60B are 619 °C (point 1) and 523 °C (point 2). The portion of the curve lying between point 1 and point 2 is denoted as the freezing range of the alloy. In this temperature range the alloy exists in a mushy state, which is one of the primary factors determining the interface width during solidification. The width of interface, on the other hand, has a direct influence on the formation of shrinkage pores in a casting. The mushy zone formation is primarily responsible for reduced inter-dendritic pressure and hence restricted feeding. The larger the freezing range of the alloy, the greater the width of the interface and greater is the probability of shrinkage porosity.

Figure 4.2 shows the variation of derivative of the cooling curve, in the freezing range, as a function of time. At each point of the derivative curve, the ordinate value represents the instantaneous cooling rate (instantaneous slope of the cooling curve), for the corresponding time value at a particular thermocouple location. An increase in the derivative indicates a lowering of cooling rate. This can be explained by nucleation of a new phase leading to release of latent heat and hence rise in the local temperature. On the other hand, a decrease in the derivative represents the completion of the phase transformation process.

For thermocouple 1, the beginning of the phase transformation (i.e., nucleation of α-Mg) manifests at a temperature range of 580 – 590 °C (an increase in the derivative value is detected). On further solidification the primary magnesium dendritic arms coarsen until around 520 °C. This is followed by the commencement of another phase transformation process, wherein the nucleation of $Mg_{17}Al_{12}$ intermetallic begins and continues till around 490 °C. At this point, we observe another jump in the derivative curve. This marks the eutectic transformation, leading to the formation of a divorced eutectic structure (islands of primary Mg phase surrounding $Mg_{17}Al_{12}$ intermetallic precipitate). The transformation takes place at a temperature ranging between 450 – 460 °C [76].

A similar explanation holds for thermocouples 2 and 3. The beginning of primary magnesium phase nucleation is observed in the range of 610-620 °C for both the 2nd and the 3rd thermocouple. The phase transformation ends as the temperature approaches 560 °C.

The above plots describe the local temperature dependence on time intervals and can be related to subsequent phase transformations during the process of solidification. It is also important to study the temperature profile along the length of casting to understand the local cooling trends and the temperature variation as a function of distance. Figure 4.3 shows a family of temperature-distance curves at regular intervals (1.0 second intervals) for the sand cast AM60B alloy. The vertical spacing between the points, for a particular thermocouple location, is proportional to the instantaneous local cooling rate. Thermocouple 1 (i.e. d= 20mm) shows a uniform cooling rate as the ordinate points are

nearly evenly spaced with respect to each other. Moving to thermocouples 2 and 3, the distance between the ordinate points reduce (distribution is more clustered), indicating lowering in cooling rate. For the 4th and 5th thermocouple, high cooling rate values are initially observed. However, the cooling rate decreases drastically as the solidification proceeds towards completion. Similarly, thermocouple 6 also shows a constant reduction in cooling rate with time, but the trend is much more gradual.

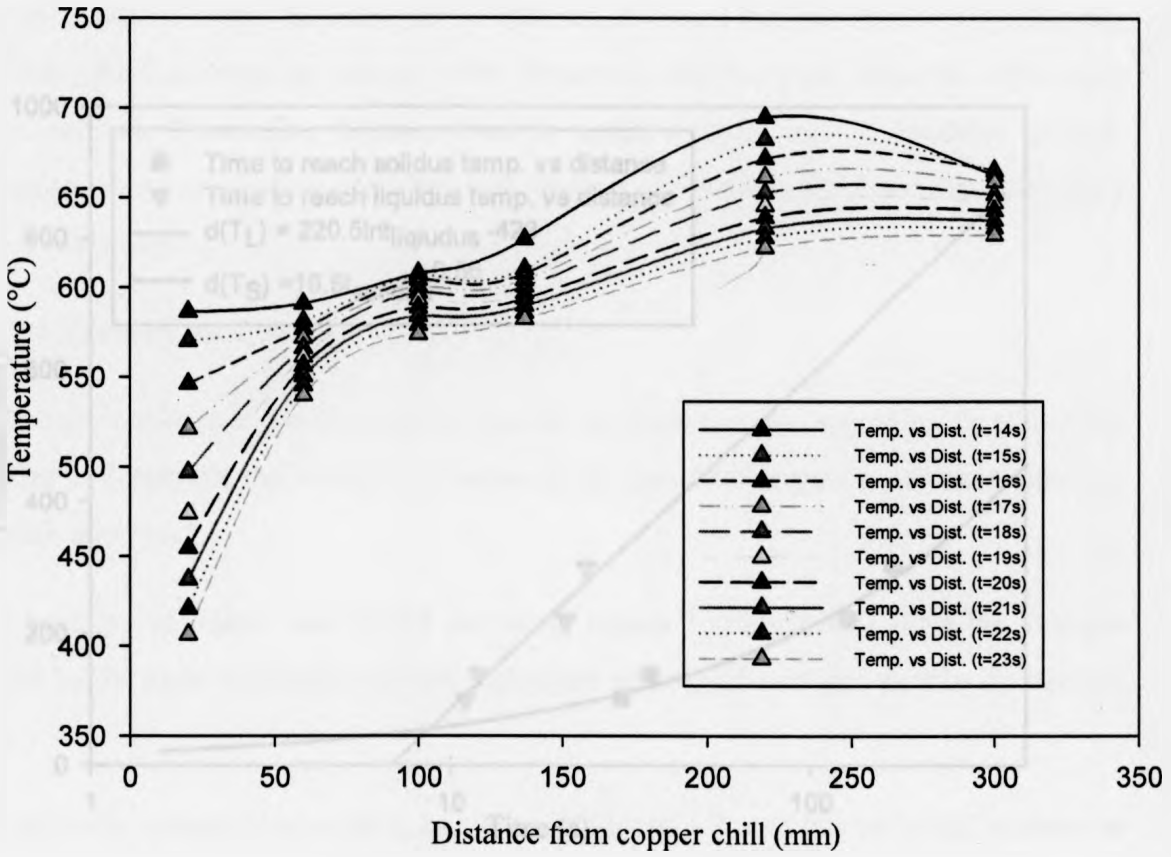

Figure 4.3 Temperature with respect to distance along the casting (at regular time intervals).

During the process of casting, solid and liquid fronts proceed from the chill zone to the feeding region. The movement of the solid front determines the rate of solidification. The region bounded by the solid and the liquid front is called as the mushy or pasty

zone. Here the alloy exists in a partly liquid, partly solid phase. As mentioned before, this region is prone to the maximum amount of shrinkage. Thus the position of the liquid and the solid front, as a function of time, provides valuable information regarding the rate of solidification and the mushy zone formation.

The variation of the position of the liquidus and the solidus fronts with respect to time, (Figure 4.4) suggests interesting conclusions. Both the plots increase monotonically with time. The empirical relationships (Equation 4.1 and 4.2) established for the liquidus and solidus fronts can be differentiated to obtain the interface velocity.

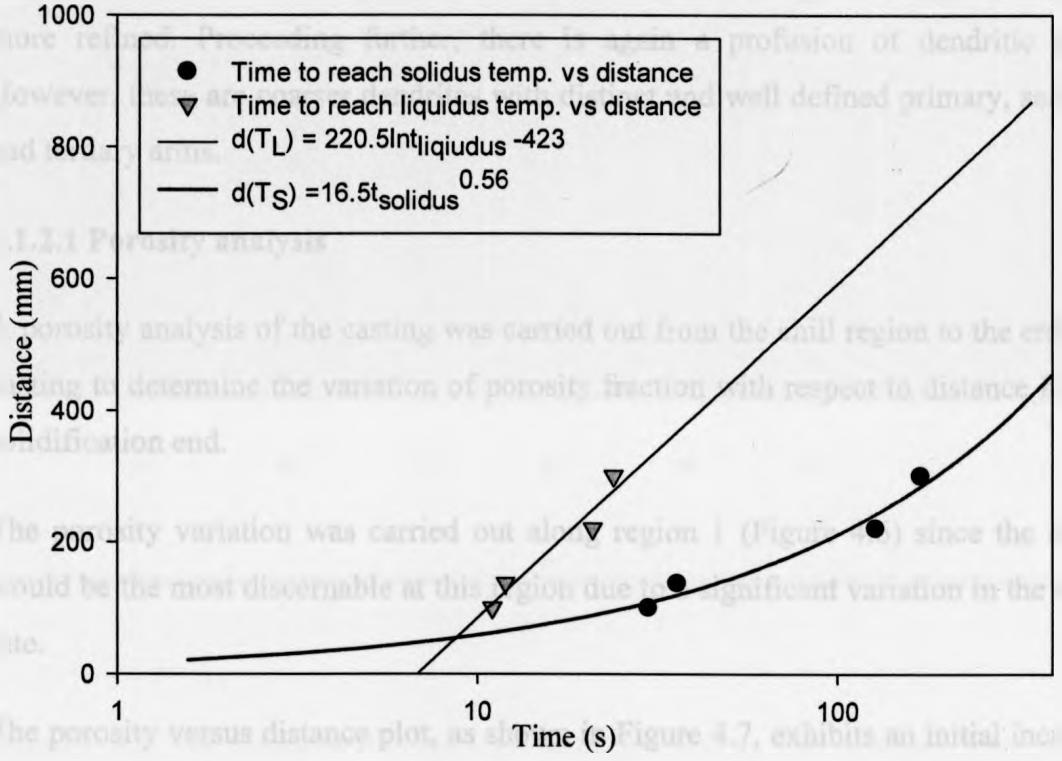

Figure 4.4 Distance versus time plot for the solidus and liquidus interface.

$$\mathbf{d(T_L) = 220.5lnt_{liquidus} - 423} \quad \text{.....(4.1)}$$

$$\mathbf{d(T_S) = 16.5t_{solidus}^{0.56}} \quad \text{.....(4.2)}$$

4.1.2 Microstructural Analysis

Figure 4.5 shows the variation of microstructure with distance from the cooling end. The corresponding distance values from the cooling end for each micrograph are given in the figure. The direction of solidification is from left to right. Equiaxed grains are observed at a distance of 12mm from the copper chill. On moving away from the cooling end the grains coarsen and elongate giving rise to dendritic structures. Growth was primarily observed from the walls to the center of the casting in an angular fashion. The dendrites become coarser as the interface proceeds further and structure resembles that of a cellular array. At a distance of 120mm, divorced eutectic structures (alpha-Mg and $Mg_{17}Al_{12}$intermetallic phases) were observed and the grain structure was much more refined. Proceeding further, there is again a profusion of dendritic growth. However, these are coarser dendrites with distinct and well defined primary, secondary and tertiary arms.

4.1.2.1 Porosity analysis

A porosity analysis of the casting was carried out from the chill region to the end of the casting to determine the variation of porosity fraction with respect to distance from the solidification end.

The porosity variation was carried out along region 1 (Figure 4.6) since the changes would be the most discernable at this region due to a significant variation in the cooling rate.

The porosity versus distance plot, as shown in Figure 4.7, exhibits an initial increase in porosity with distance from the cooling end. However, unlike the expected porosity trends [48,65,77], where the pore fraction increases as the distance from the cooling end increases, there is a drastic drop in the porosity values after the 96mm mark and the porosity values decrease much below the value observed at 96mm from the cooling end.

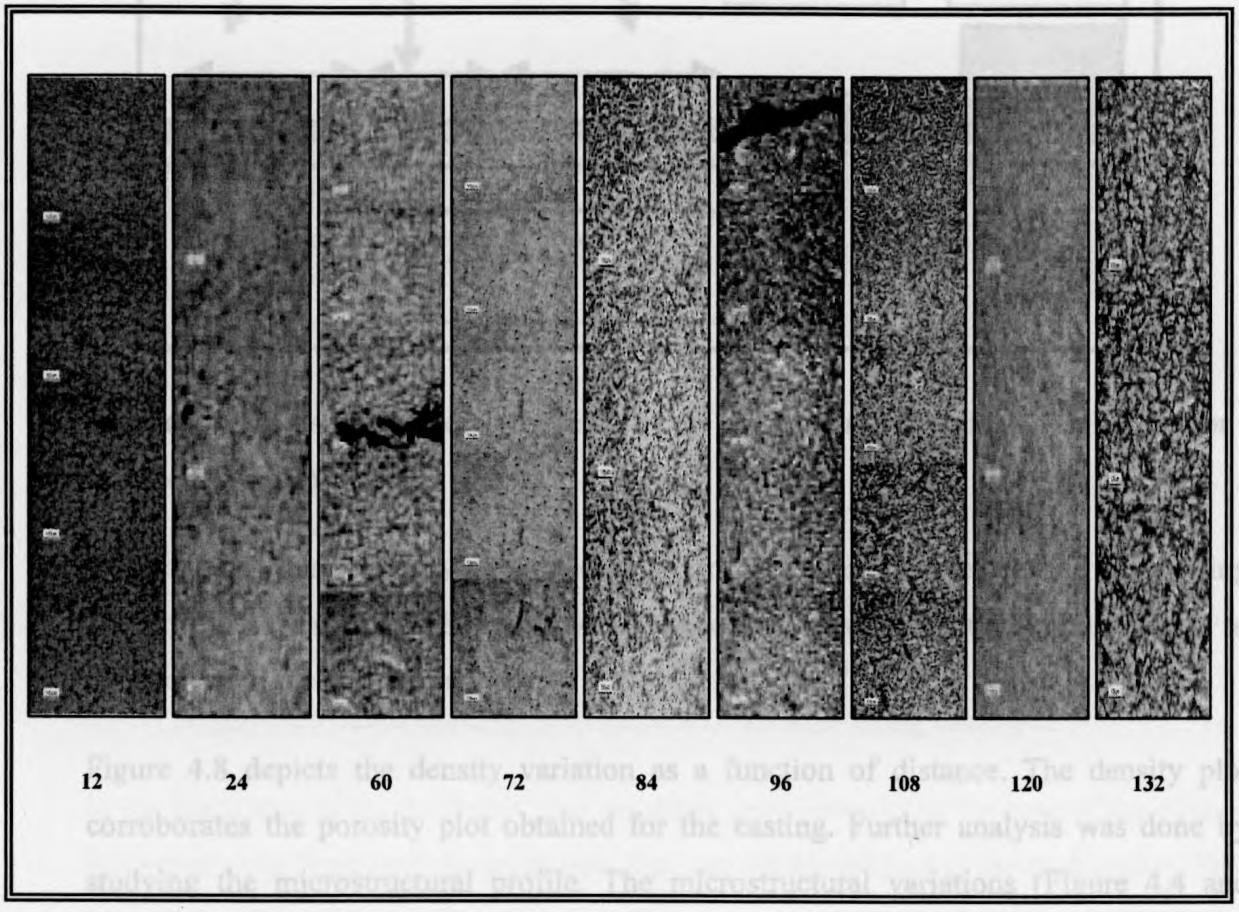

Figure 4.5 Microstructural variations with respect to the distance from the cooling end/copper chill. Micrographs, from left to right, are along the direction of solidification (distance values are indicated below the micrographs with units in millimeters).

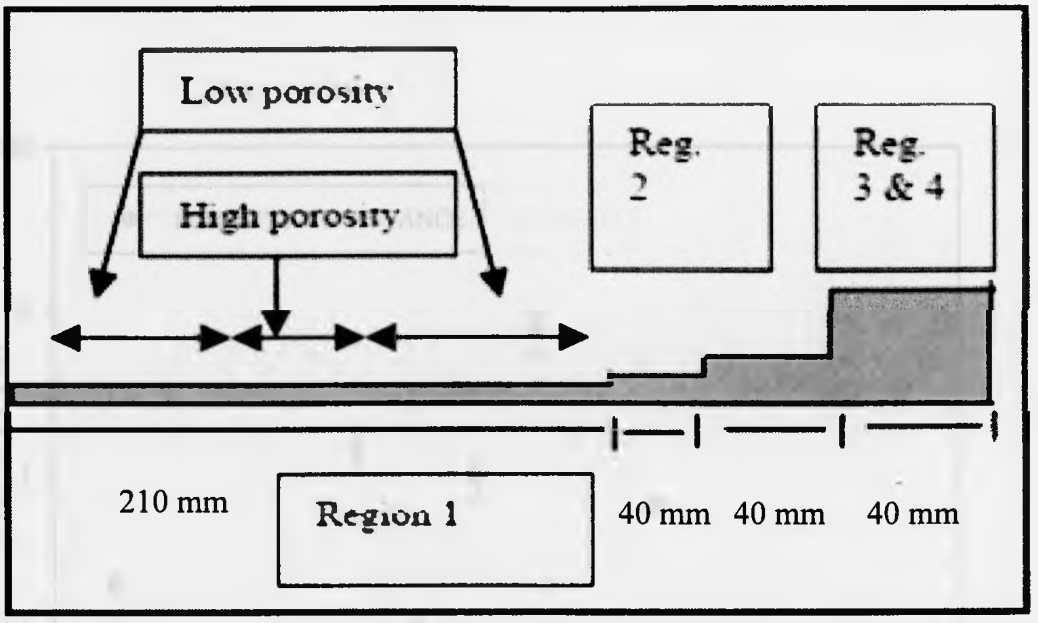

Figure 4.6 Porosity profile along region 1 of the casting (direction of solidification is from left to right).

To validate this porosity trend, density measurements were carried out using Archimedes' principle. The density values obtained were plotted with respect to distance from the cooling end.

Figure 4.8 depicts the density variation as a function of distance. The density plot corroborates the porosity plot obtained for the casting. Further analysis was done by studying the microstructural profile. The microstructural variations (Figure 4.4 and Figure 4.9(a)) were analyzed along the length of the casting. The growth patterns suggested equiaxed grains near the copper chill. On further progression, these equiaxed grains transform into columnar grains giving rise to dendrites. Dendritic growth initiated from the mold walls and at an oblique angle (roughly 45°) to the centerline of the casting. As we move away from the cooling end, the dendritic branching becomes coarser and thicker in shape thus cutting off feeding by liquid metal. This most likely explains the high porosity observed at the mid area of region 1 (90-100 mm). However, the region next to it (110-125 mm) showed a sudden drop in porosity along with a fine grained structure. This can be explained by the pinching of inter-dendritic feeding due

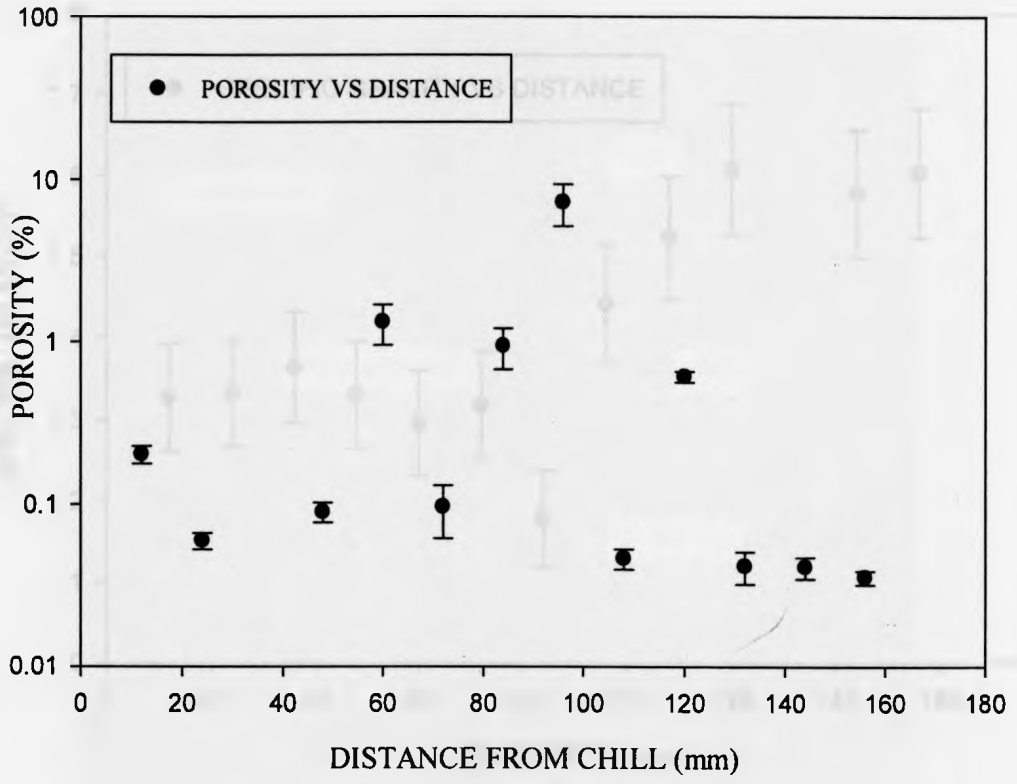

Figure 4.7 Areal porosity with respect to distance along casting.

to the branching of the dendrites. The dendrites grow inwards to the core of the casting and when arms from both the ends meet they cut off the feeding in the core region. This leads to the formation of a large amount of shrinkage porosity in the core region. Figure 4.9(b) shows an SEM image of an observed shrinkage pore in the 96mm region. However, the region immediately adjacent to this high porosity zone still has access to feeding from melt source, resulting in a decreased amount of porosity. The substantially low porosity can also be attributed to the phenomenon of grain nucleation. With the commencement of solidification the solid continuously rejects solute particles into the melt, until the content of solute is significantly high. The metal at this region is still at a temperature above the liquidus temperature. As per the temperature time data, when the metal at a distance of 20mm from the chill solidifies, the region around 125-137 mm from the chill is still above the liquidus temperature.

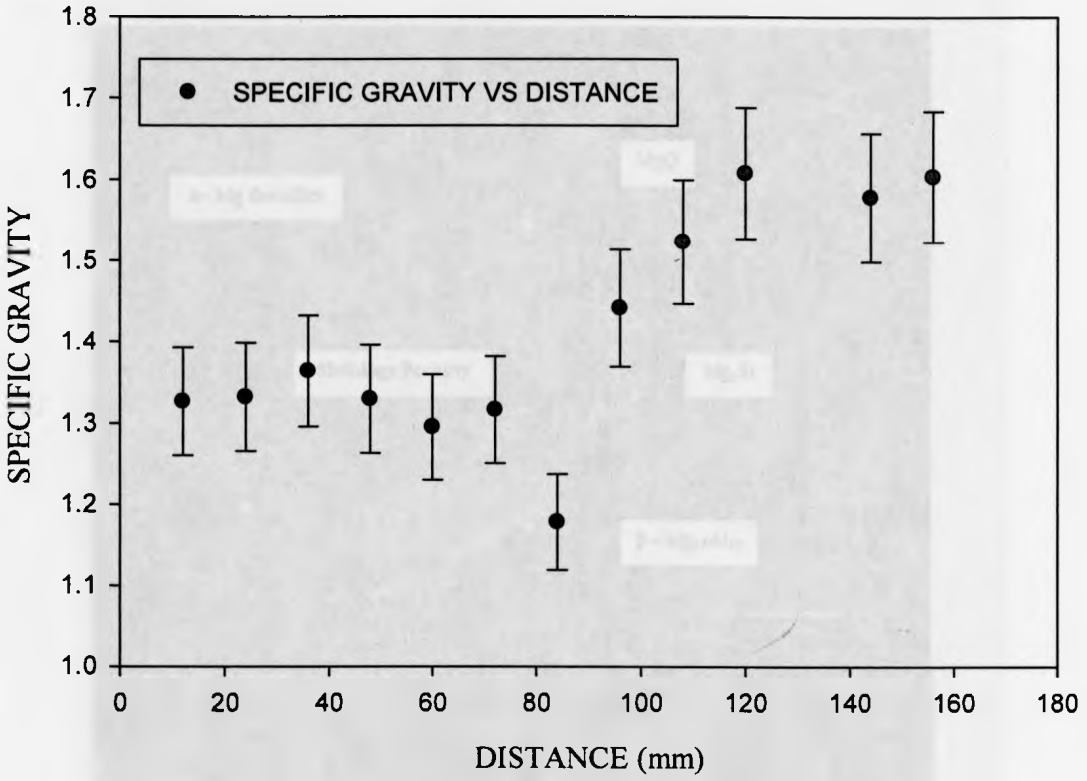

Figure 4.8 Specific gravity with respect to distance along casting.

The presence of Al, the major alloying element in the melt reduces the solubility of Mn. Thus with the decrease in the temperature, the solubility of both manganese and aluminum decreases significantly, leading to their precipitation. These insoluble precipitates (Al, Mn) act as nuclei for grains during solidification [36,78]. Hence, the nucleation rate is increased considerably giving a refined grain structure and consequently low porosity. Figure 4.10 and 4.11 show the SEM images for the 120mm region, and the corresponding EDX spectrum. Table 4.1 presents the related elemental composition data. They show a high concentration of Al and Mn phases in the 120 mm region, corroborating the above proposed explanation.

Moving ahead, dendritic growth is observed again as the region gets substantial feeding by the melt from the broader portion of the casting. However, due to very low cooling rates and temperature gradients coarse dendrites (Figure 4.5) are observed, but with

distinct secondary and tertiary branches. Also, a high local solidification time makes the feeding extremely slow, leading to further coarsening of arms.

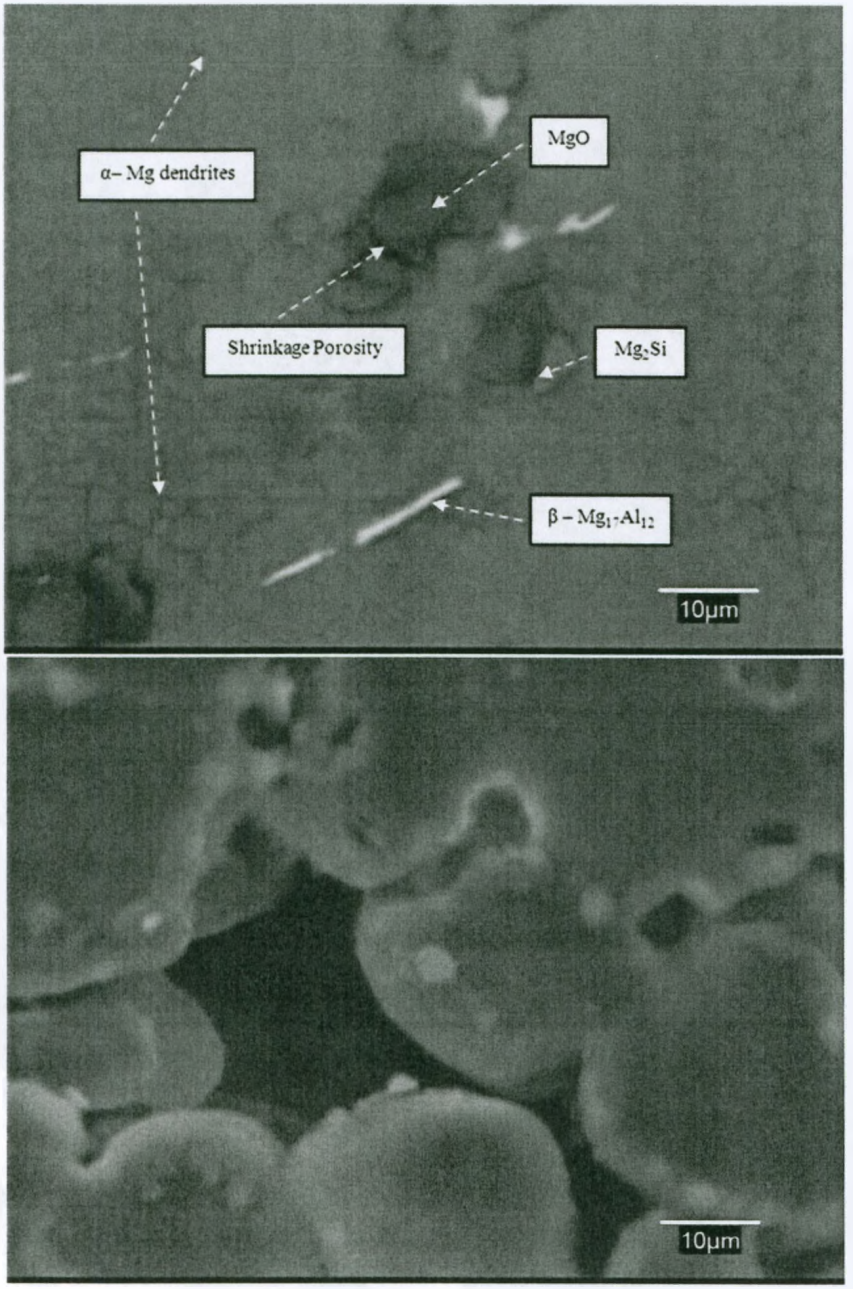

Figure 4.9 a) SEM image of AM60B sand cast alloy at a location 80-90mm from the chill zone b) A shrinkage pore observed (in the 96 mm region) in the as-cast structure of AM60B.

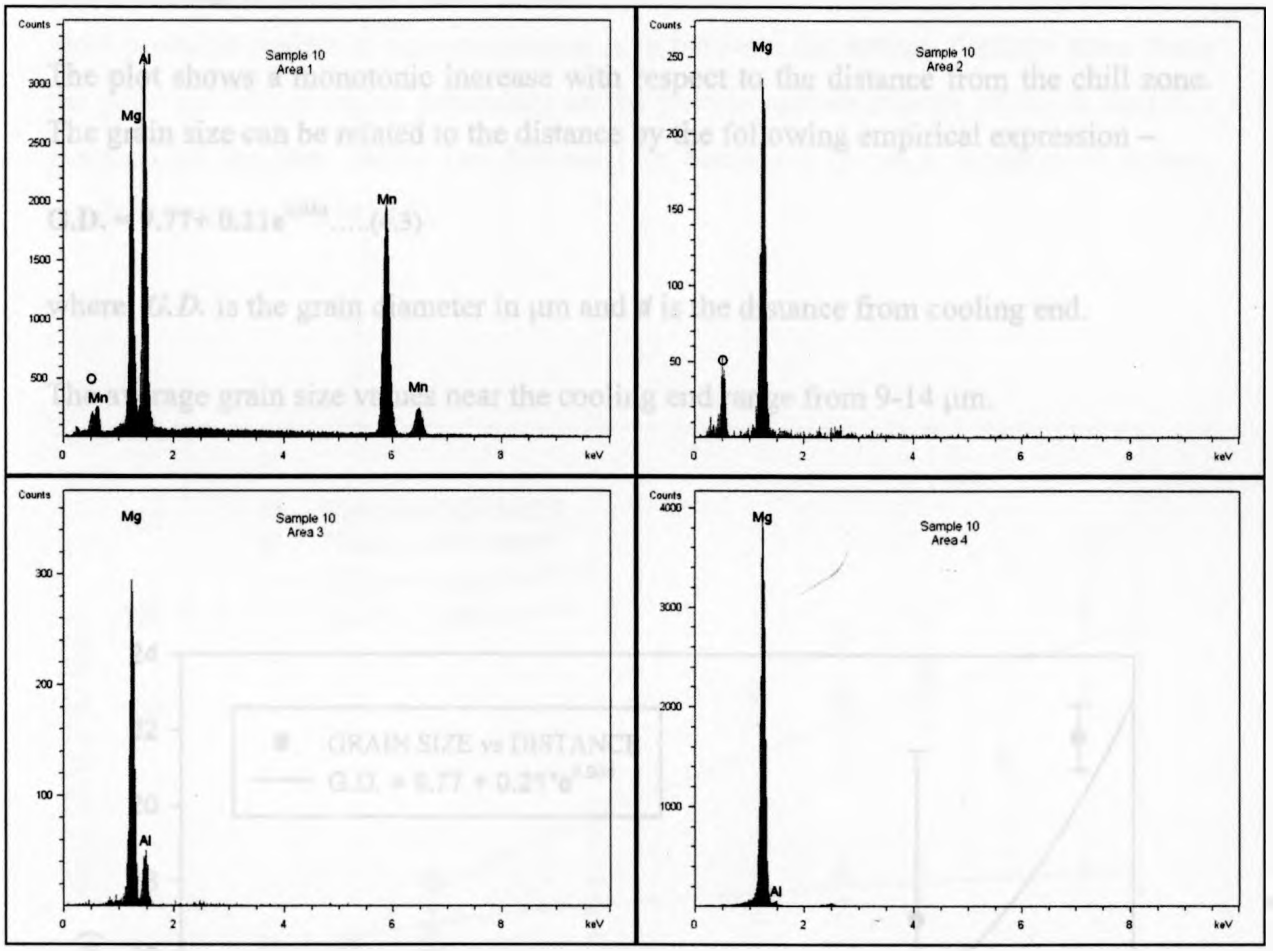

Figure 4.11 EDX spectrum for specimen 10 (120mm from cooling end): The area numbers shown in the graphs represent the corresponding selected areas in the SEM micrograph in Figure 4.10.

Table 4.1 EDX elemental composition table.

AM60B (SAMPLE LOCATION – 120mm)	O (wt %)	Mg (wt %)	Al (wt %)	Mn (wt %)
AREA #1	5.3	21.6	29.0	44.2
AREA #2	50.5	49.6		
AREA #3		68.2	31.8	
AREA #4		95.7	4.3	

4.1.2.2 Grain size analysis

The optical micrographs were analyzed for the grain size distribution along the length of the casting, as shown in Figure 4.12.

The plot shows a monotonic increase with respect to the distance from the chill zone. The grain size can be related to the distance by the following empirical expression –

$$\mathbf{G.D. = 9.77 + 0.21e^{0.03d}} \quad \text{.....(4.3)}$$

where, ***G.D.*** is the grain diameter in μm and ***d*** is the distance from cooling end.

The average grain size values near the cooling end range from 9-14 μm.

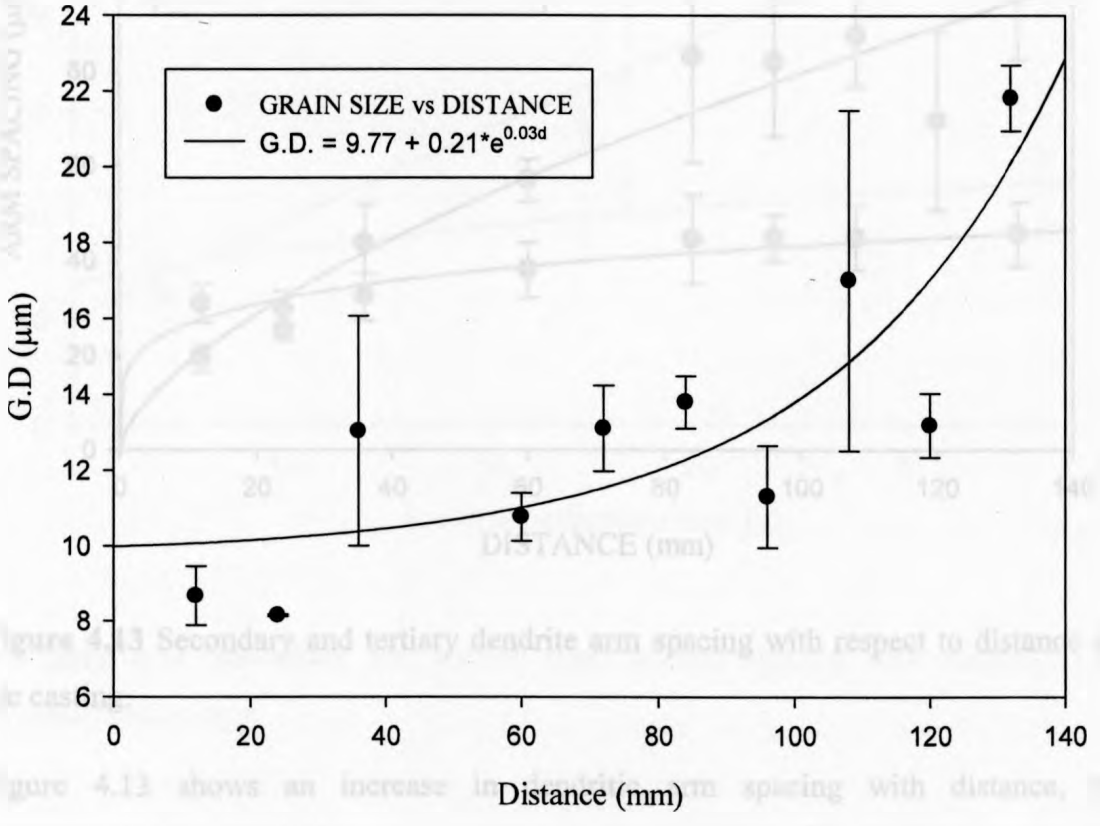

Figure 4.12 Grain size with respect to distance along casting.

4.1.2.3 Arm spacing analysis

The variation of dendrite arm spacing was also studied as a function of the process parameters. It is important to understand the variation of dendrite arm spacing, as the most probable region of pore nucleation is in between the tertiary dendrite arms. Now the pore stability is highly dependent on the bubble surface energy, which in turn is a function of the pore radius (as discussed in Section 2.7) i.e. a function of tertiary dendrite arm spacing [63,66].

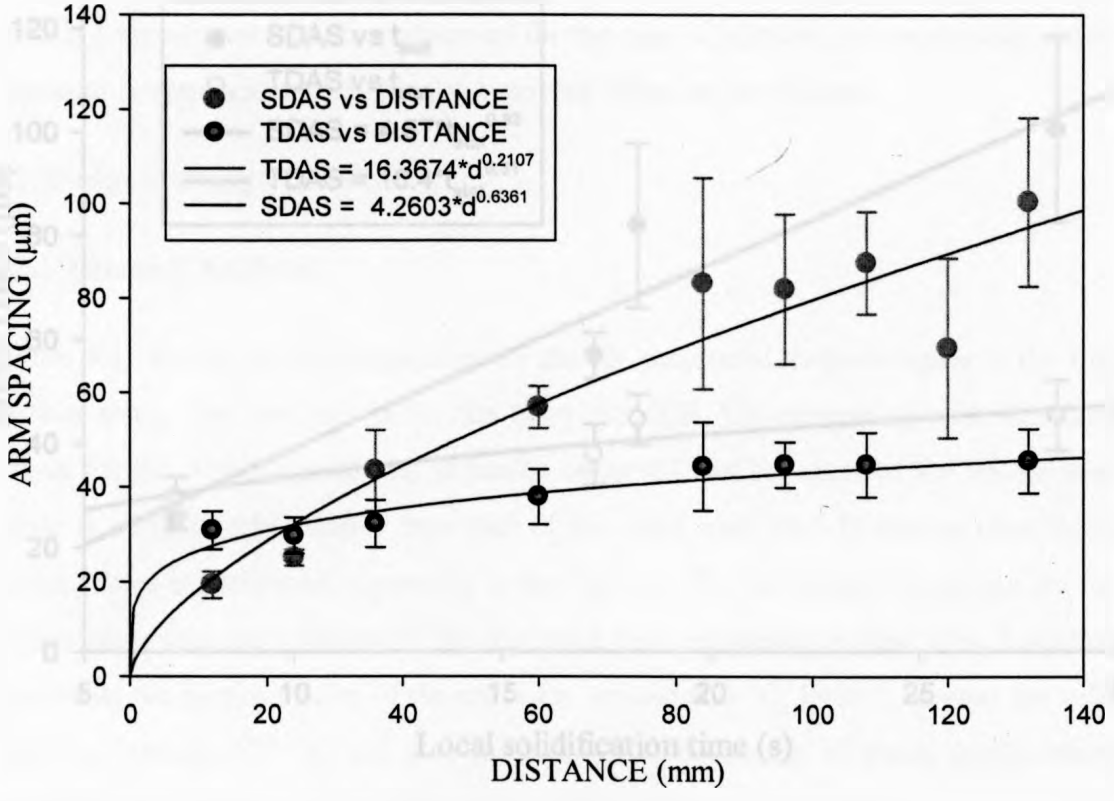

Figure 4.13 Secondary and tertiary dendrite arm spacing with respect to distance along the casting.

Figure 4.13 shows an increase in dendritic arm spacing with distance, thus corroborating the trend of grain coarsening as shown before. The dendritic arm spacing shows a power law increase with respect to distance from the cooling end. It can also be

observed that the rate of increase of secondary dendrite arm spacing (***SDAS***) is greater than that of the tertiary dendrite arm spacing (***TDAS***).

According to the plot SDAS and TDAS can be expressed empirically as

$$\mathbf{TDAS = 16.3674d^{0.21}} \quad .....(4.4)$$

$$\mathbf{SDAS = 4.2603d^{0.64}} \quad .....(4.5)$$

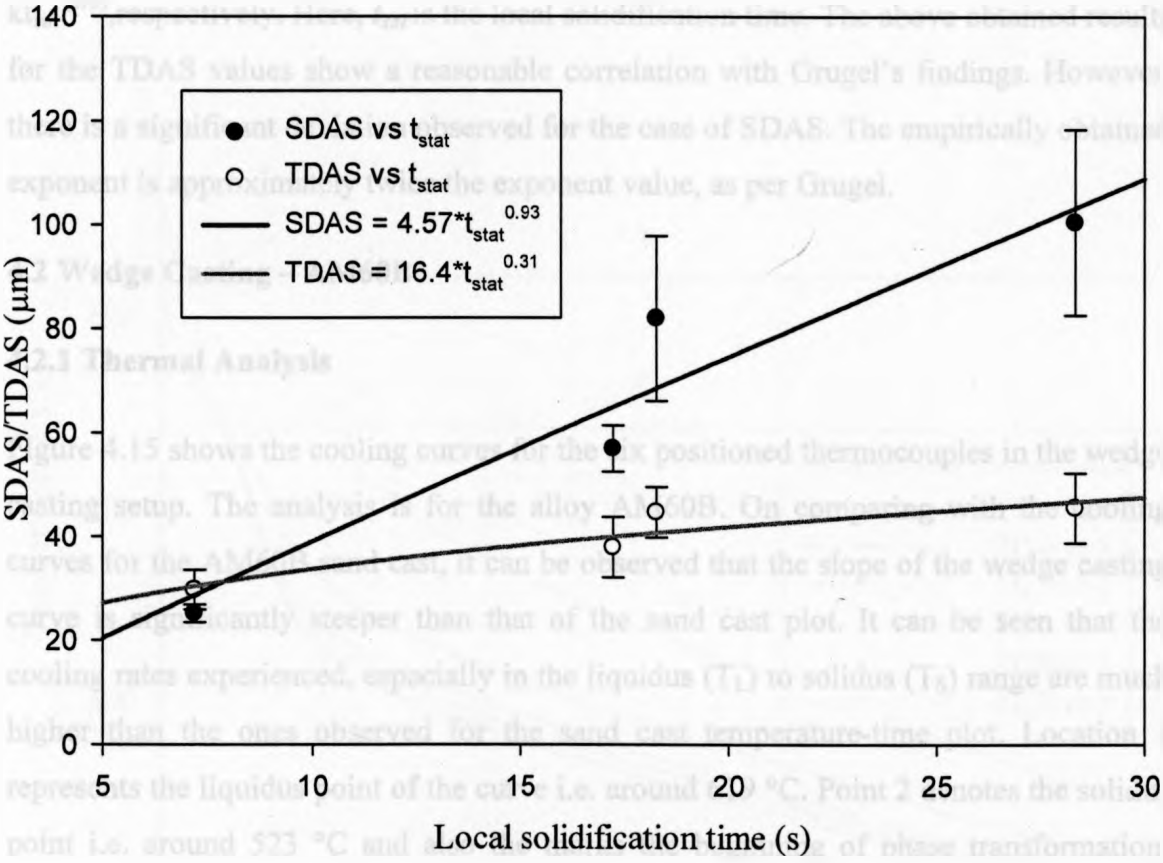

Figure 4.14 Secondary and tertiary dendrite arm spacing with respect to local solidification time.

Figure 4.14 shows the dependence of SDAS and TDAS on local solidification time. The local solidification time can be expressed as $t_{stat} = (T_L - T_S)/R$ where, R is the cooling rate (°C/s). Arm spacing can be empirically expressed as a function of solidification time as:

$$\mathbf{TDAS = 16.4 t_{stat}^{0.31}} \quad \text{..... (4.6)}$$

$$\mathbf{SDAS = 4.57 t_{stat}^{0.93}} \quad \text{.....(4.7)}$$

According to Grugel [50], the variation of secondary and tertiary dendrite arm spacing with respect to the local solidification time are given as SDAS = $kt_{sol}^{(1/2)}$ and TDAS = $kt_{sol}^{(1/3)}$,respectively. Here, t_{sol} is the local solidification time. The above obtained results for the TDAS values show a reasonable correlation with Grugel's findings. However, there is a significant deviation observed for the case of SDAS. The empirically obtained exponent is approximately twice the exponent value, as per Grugel.

4.2 Wedge Casting – AM60B

4.2.1 Thermal Analysis

Figure 4.15 shows the cooling curves for the six positioned thermocouples in the wedge casting setup. The analysis is for the alloy AM60B. On comparing with the cooling curves for the AM60B sand cast, it can be observed that the slope of the wedge casting curve is significantly steeper than that of the sand cast plot. It can be seen that the cooling rates experienced, especially in the liquidus (T_L) to solidus (T_S) range are much higher than the ones observed for the sand cast temperature-time plot. Location 1 represents the liquidus point of the curve i.e. around 619 °C. Point 2 denotes the solidus point i.e. around 523 °C and also the marks the beginning of phase transformation, wherein the nucleation of the intermetallic phase; $Mg_{17}Al_{12}$ takes place.

For thermocouple 1 (TC 1), primary phase or α-Mg phase dendrite nucleation is observed at temperatures around 620 °C. As the heat extraction process continues, the dendritic arms grow further into the liquid and branching takes place. Due to the high cooling rates experienced in this range, there is not enough time for dendritic "coarsening" to occur. Thus we observe sharp and fine dendritic arms, with secondary

and tertiary branching. The region between 620 °C to 520 °C is designated as the freezing range of the alloy. At around 520 °C, precipitation of intermetallic phases commences [76].

A similar explanation can be provided for the cooling curves observed for the other thermocouples. Another major observation from the plot is an unexpected increase in cooling rate on moving from thermocouple 1 to thermocouple 3, followed by a decreasing trend.

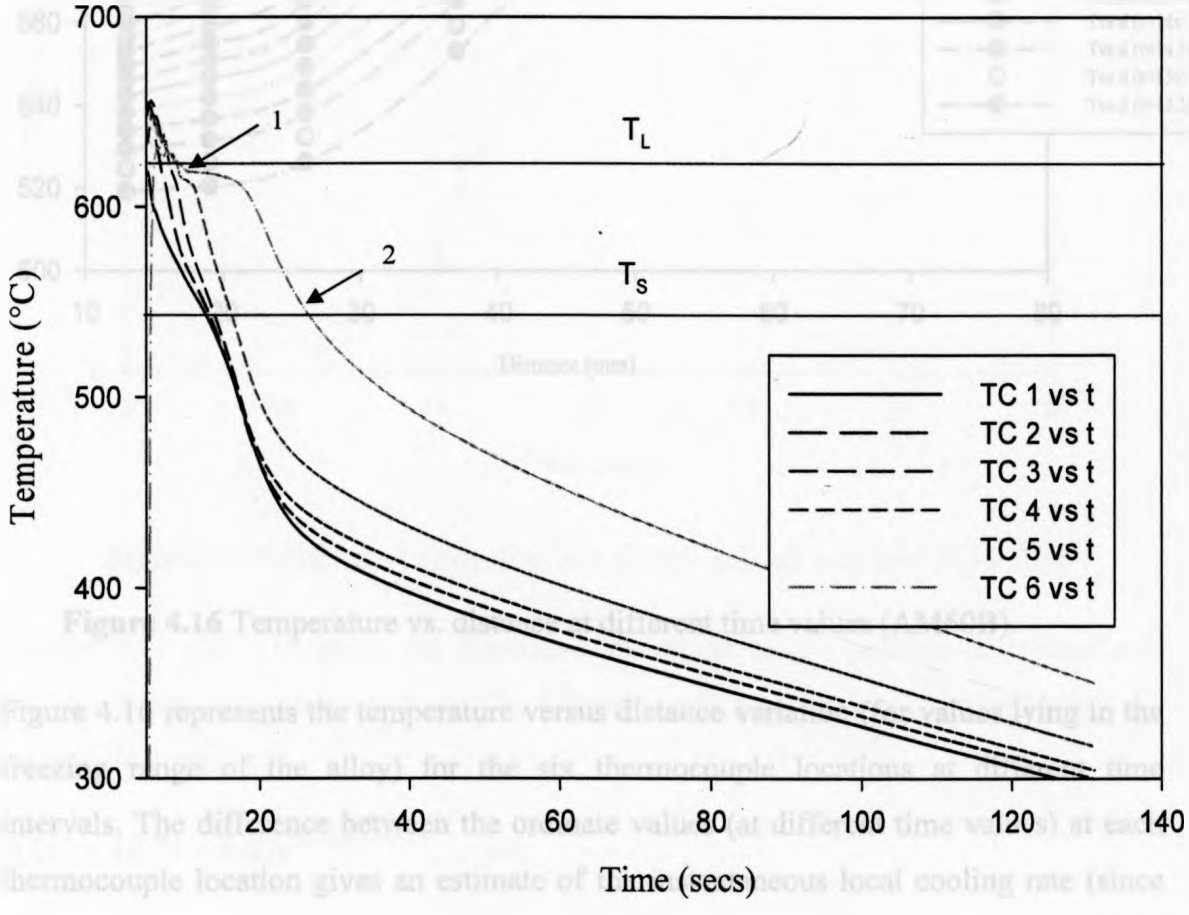

Figure 4.15 Temperature-time curves at different thermocouple locations (AM60B).

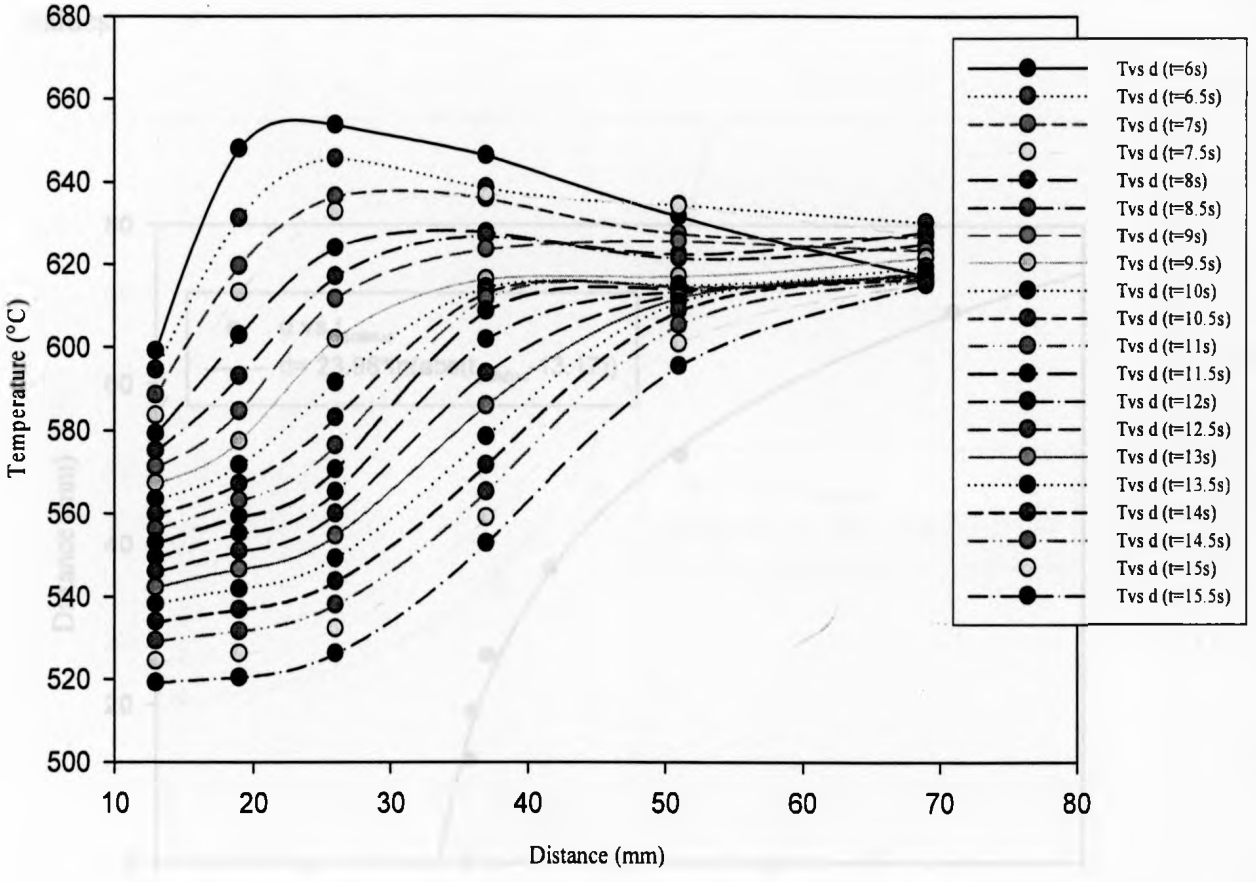

Figure 4.16 Temperature vs. distance at different time values (AM60B).

Figure 4.16 represents the temperature versus distance variation (for values lying in the freezing range of the alloy) for the six thermocouple locations at different time intervals. The difference between the ordinate values (at different time values) at each thermocouple location gives an estimate of the instantaneous local cooling rate (since the temperature values are recorded at regular time intervals). For thermocouple 1, it can be observed that the rate of cooling is more or less uniform, with points being almost equidistant. On moving to thermocouples 2 and 3, the separation between the initial ordinate values is considerable, depicting high cooling rates. However, at longer

times, the spacing becomes smaller and the distribution is more crowded. Similarly, thermocouples 4 to 6 show a gradual reduction in the separation between the ordinate values.

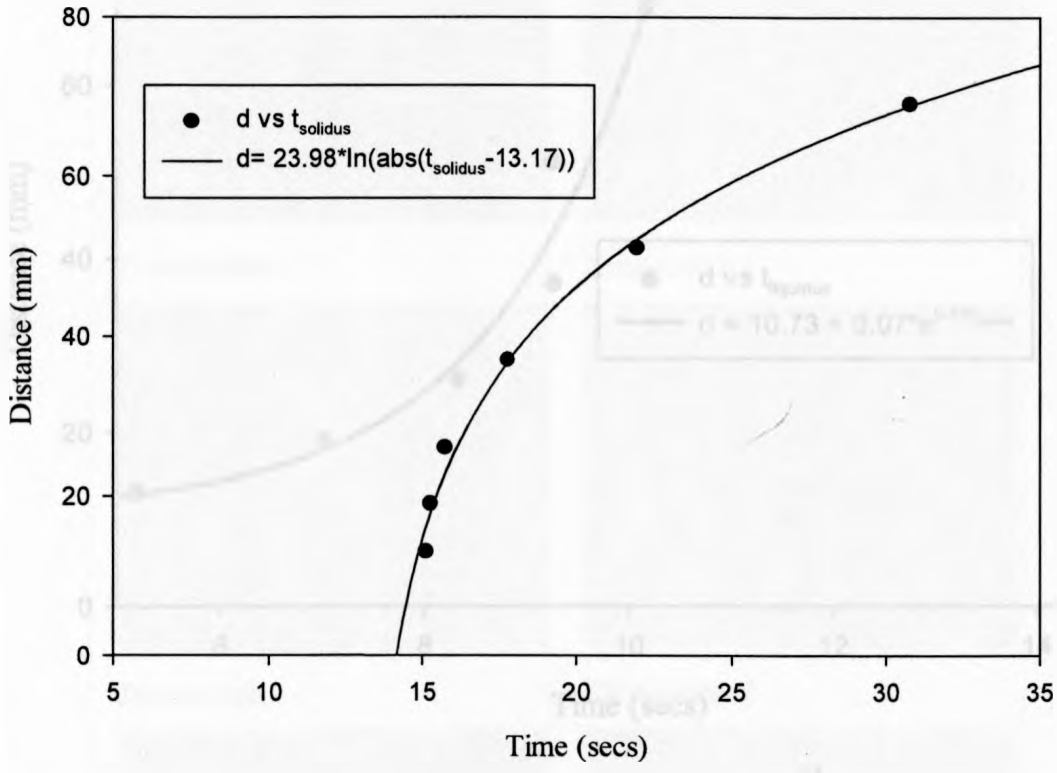

Figure 4.17 Distance versus time plot for the solidus interface (AM60B).

Figures 4.17 and 4.18 show the respective variations of the position of solidus and liquidus fronts with respect to time. The following relations can be established based on the obtained curves.

$$\mathbf{d(T_L) = 10.73 + 0.07e^{0.66t(liquidus)}} \quad \text{..... (4.8)}$$

$$\mathbf{d(T_S) = 23.98Ln\ (abs(t_{solidus}-13.17))} \quad \text{..... (4.9)}$$

where, $d\ (T_{L,S})$ = Position (in millimeters) of the liquid, solid front respectively and t = time in seconds

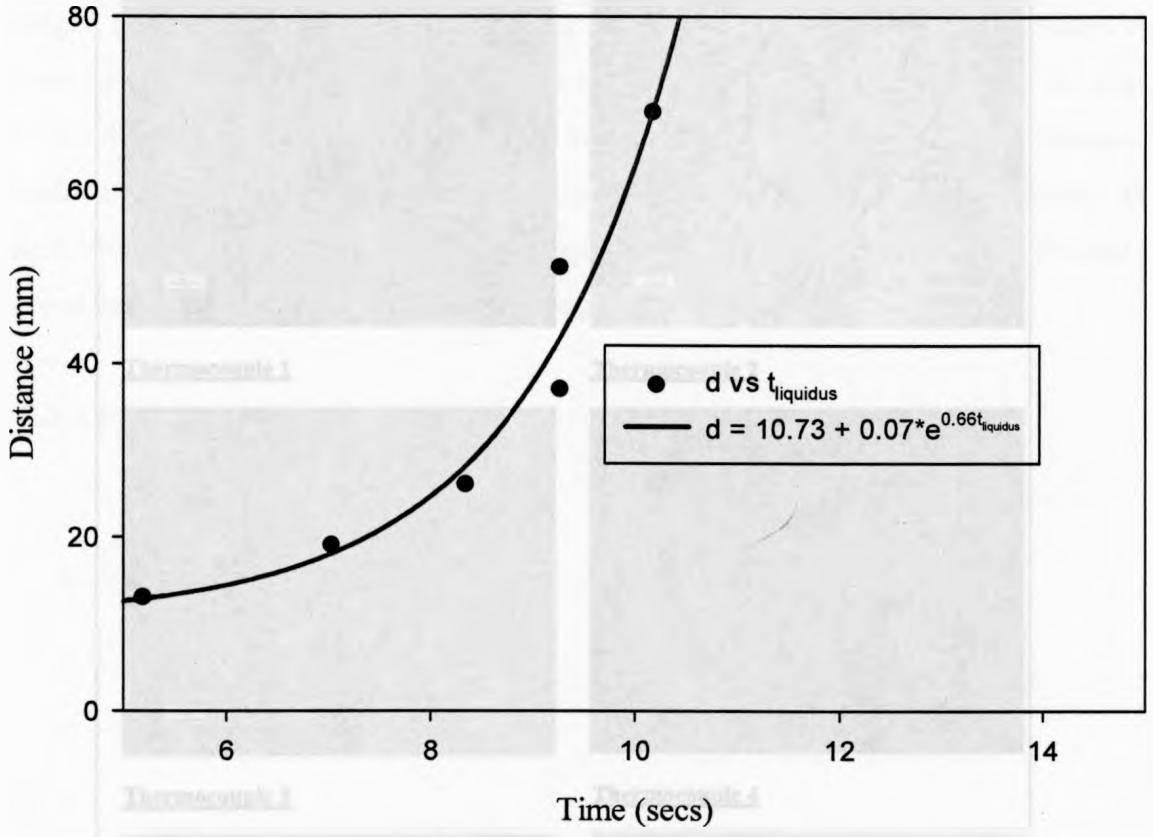

Figure 4.18 Distance versus time plot for the liquidus interface (AM60B).

4.2.2 Microstructural Analysis

This section will discuss the microstructural observations for the AM60B wedge casting. Figure 4.19 shows the microstructural profile along the casting, from the tip to the base of the wedge. At the tip of the wedge, it is observed that an equiaxed dendritic network with intermetallic ($Mg_{17}Al_{12}$) precipitates distributed uniformly in the inter-dendritic zone. The precipitates surround the dendrites, mainly constituting the primary or α-Mg phase. This microstructural feature is denoted as coring.

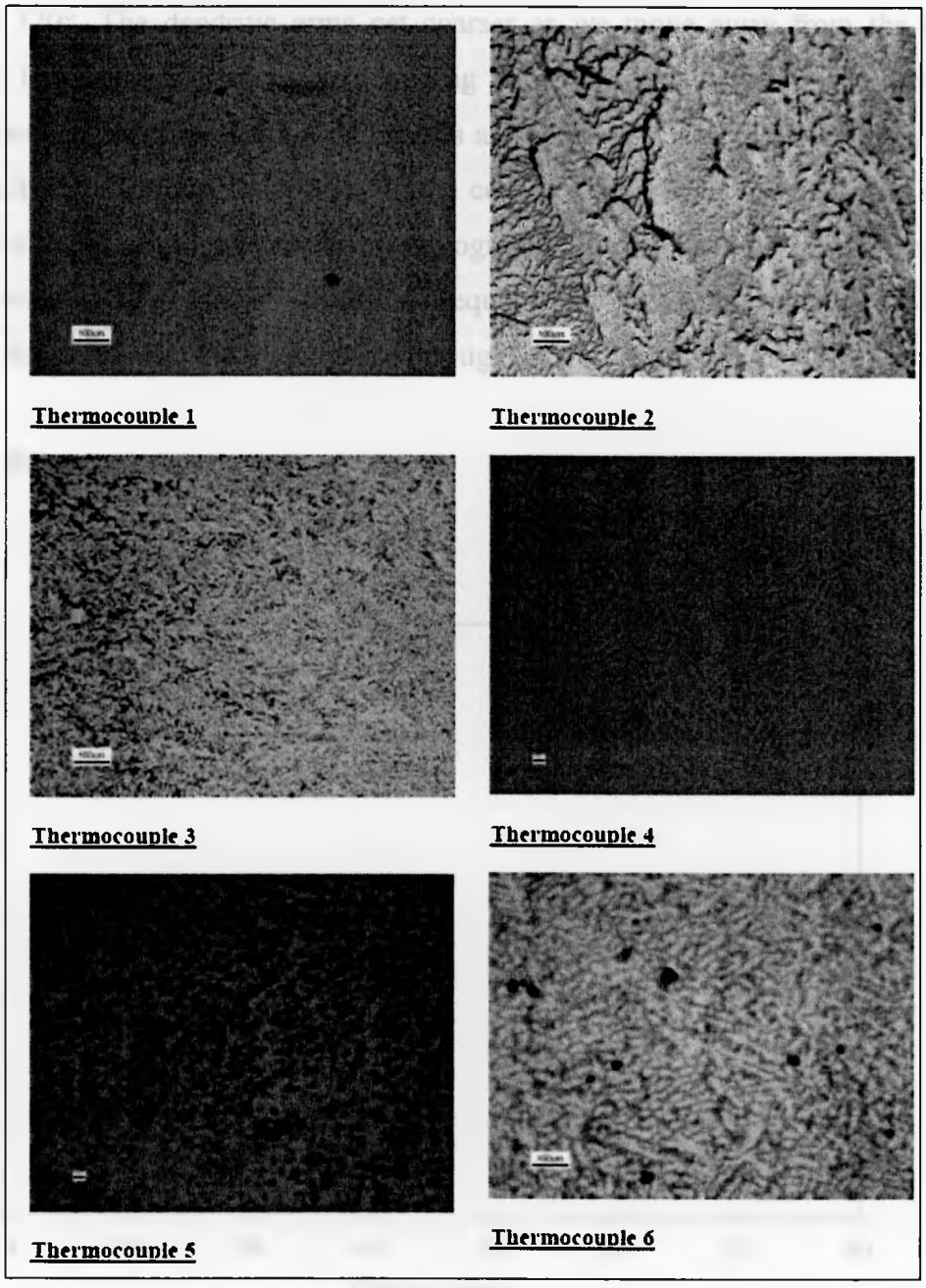

Figure 4.19 Metallographic structures at different thermocouple locations (AM60B).

Moving further towards the base of the casting, there is a sudden profusion in dendritic growth. Dendrites grow at roughly at an angle of 45° to the horizontal. Since, the angle of the wedge is 30°, the angle of dendritic growth with respect to the mold walls is around 120°. The dendritic arms get coarser as we move away from the tip of the wedge. The average dendritic arm spacing increases as the cooling rate increases. At lower cooling areas two structural regions are observed viz. a dendritic array all along the mold walls and a cellular array in the central region of the casting. The secondary dendrites shoot out along the six crystallographic directions. Hence, by symmetry the angle between the secondary dendrites is equal to 60°.The amount of eutectic formed is almost negligible and the major phase throughout the casting is alpha Mg.

4.2.2.1 Porosity analysis

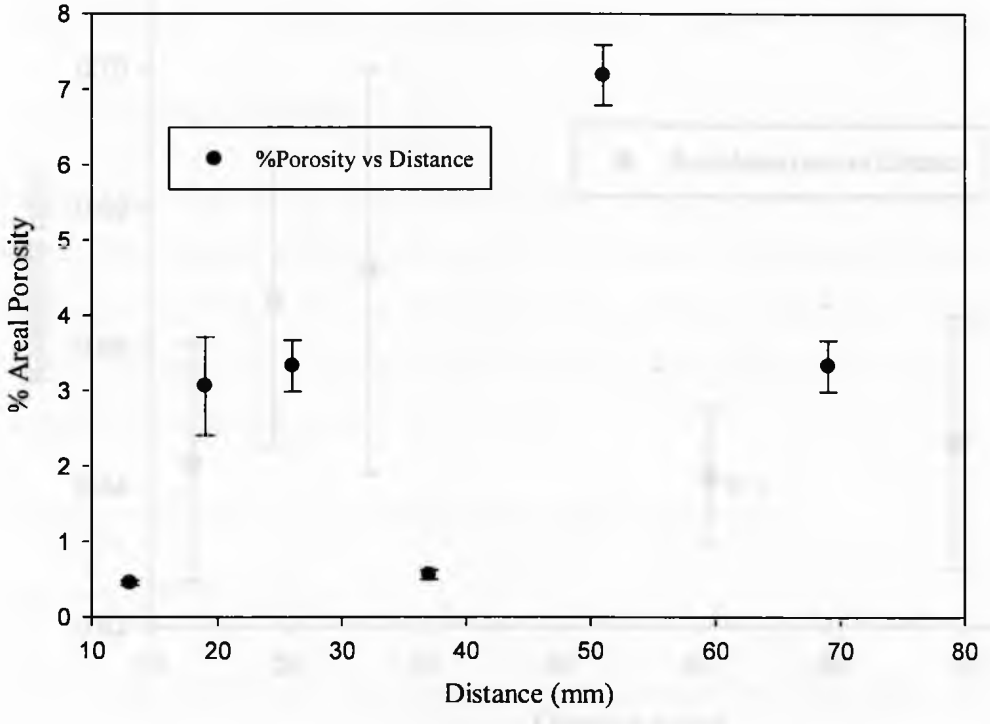

Figure 4.20 Areal porosity plotted as a function of distance along casting for AM60B wedge cast.

Figure 4.20 shows the variation of porosity with distance for AM60B alloy under wedge casting conditions. The plot shows a similar bimodal distribution as observed during the step shaped sand casting analysis.

On analyzing the relationship between the pore roundness factor and distance from the cooling end(Figure 4.21), it can be observed that in the region near the 5th thermocouple there is a reduction in the pore roundness ratio. Higher roundness ratio infers pores have a higher sphericity, implying a higher share of gas porosity, while low roundness ratios imply the presence of mainly shrinkage porosity. This indicates that the porosity in this region is mostly a combination of shrinkage type and gas induced shrinkage porosity.

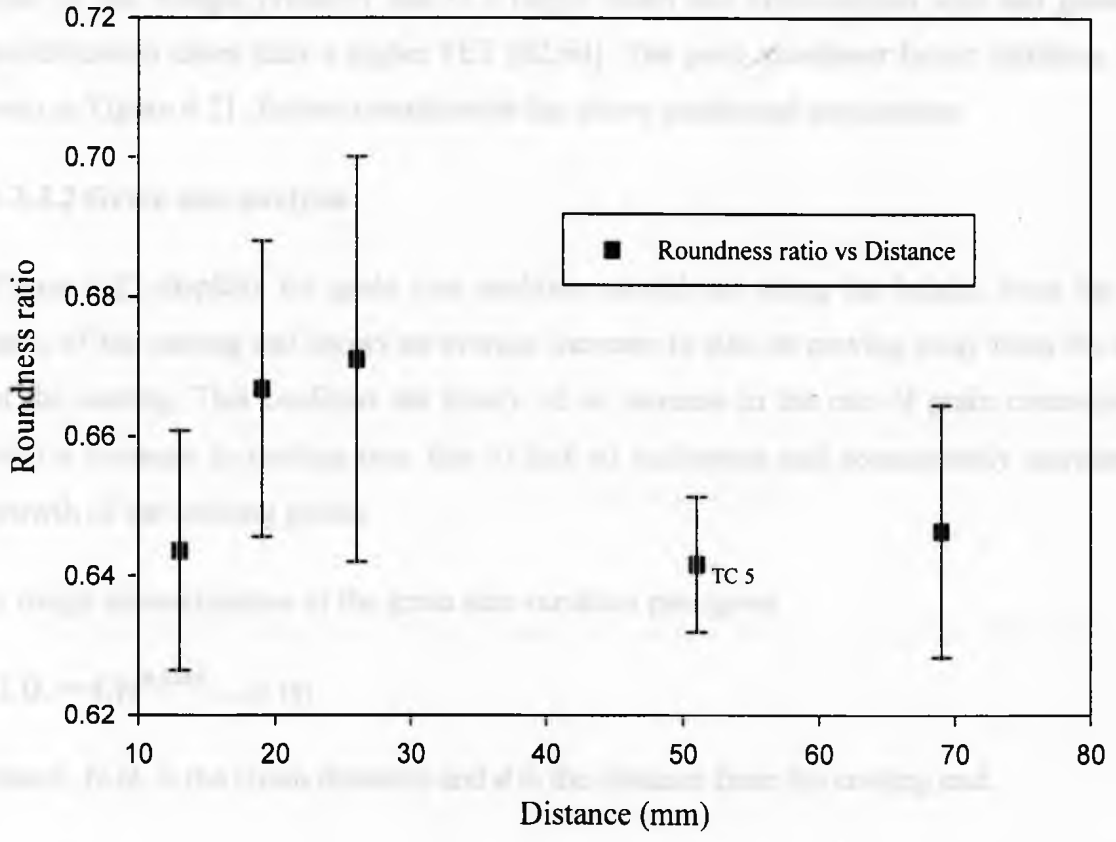

Figure 4.21 Roundness ratio varying as a function of distance along casting for AM60B.

The probable cause for the observed trend could be attributed to the progressive widening of the wedge. Near the tip of the wedge, the local solidification times are low and the gradient values are high, thus leading to a high feeding pressure and consequently enhanced feeding in the pasty/mushy region (higher FEP) [62,64]. However near the 5th thermocouple there is a sudden rise in the porosity levels. This behavior could be attributed to the restricted feeding from the base. As the dendritic front grows, the shape of the front becomes parabolic with the interface along the edges moving faster. Thus, the dendrite branches engulf the region from all the sides, leading to the liquid being trapped in between. This area, with highly restricted feeding is full of pores once the solidification is complete. The nature of porosity is of mainly shrinkage type. On moving further upwards towards the base there is again a drastic reduction in the porosity fraction. This effect can be contributed to the abundant feeding near the base of the wedge, probably due to a larger width and cross-section area and greater solidification times thus a higher FET [62,64]. The pore roundness factor variation, as seen in Figure 4.21, further corroborates the above mentioned explanation.

4.2.2.2 Grain size analysis

Figure 4.22 displays the grain size analysis carried out along the height, from tip to base, of the casting and shows an average increase in size on moving away from the tip of the casting. This confirms the theory of an increase in the rate of grain coarsening with a decrease in cooling rate, due to lack of nucleation and consequently increased growth of the existing grains.

A rough approximation of the grain size variation plot gives

$$\mathbf{G.D. = 4.7e^{0.024d}} \quad .....(4.10)$$

where, ***G.D.*** is the Grain diameter and ***d*** is the distance from the cooling end.

The above expression clearly depicts the nature of grain coarsening. At regions near the cooling end the rate of grain coarsening is gradual. However, as the distance from the cooling end increases, the grain coarsening rate becomes more and more rapid.

The average grain sizes at the tip of the wedge casting range from 6-12 μm.

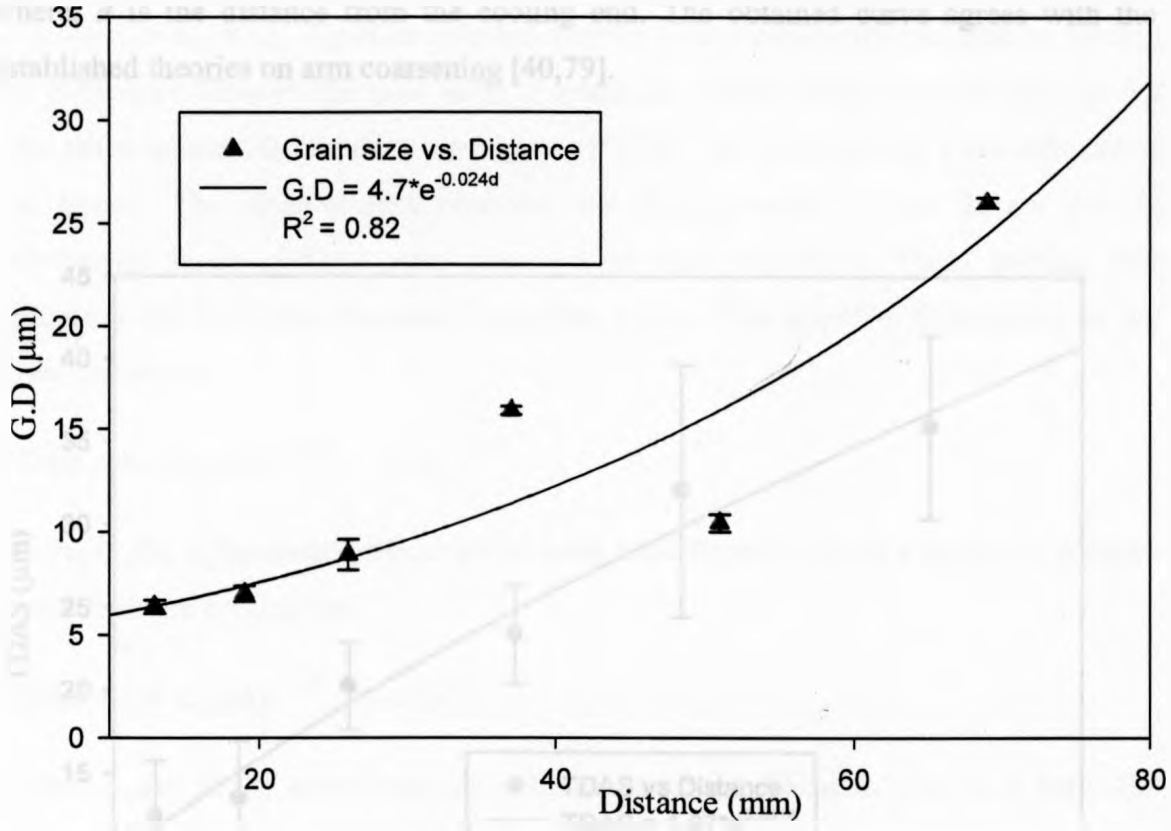

Figure 4.22 Grain size with respect to distance along casting for AM60B wedge cast.

4.2.2.3 Arm spacing analysis

Figure 4.23 shows the variation of tertiary dendrite arm spacing (TDAS) with distance from the tip of casting. The variation can be expressed by the following power law expression, given as:

$$\mathbf{TDAS = 1.97d^{0.6914}} \quad \text{..... (4.11)}$$

where, ***d*** is the distance from the cooling end. The obtained curve agrees with the established theories on arm coarsening [40,79].

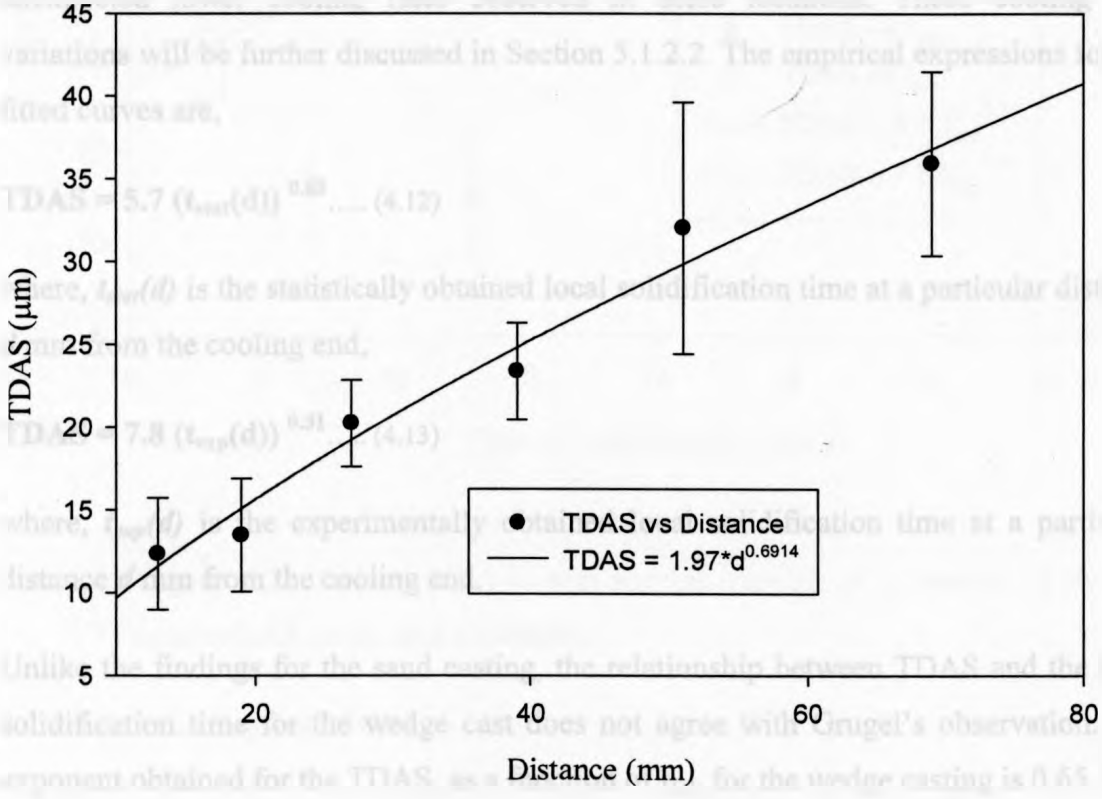

Figure 4.23 Tertiary dendrite arm spacing plotted as a function of distance along casting for AM60B wedge cast.

Thus, on moving away from the wedge tip we observe a coarsening of the dendritic arms. From the micrographs, the following transition trend can be observed in the

dendritic morphology at the interface. With an increase in the distance from the tip of the casting, we see the progression

Fine dendrites → Coarse dendrites →Cellular array [80]

TDAS can also be expressed as a function of the local solidification time. Figure 4.24 shows the variation of tertiary dendrite arm spacing with respect to the local solidification time. As mentioned previously, the local solidification time can be expressed as $t_{stat} = (T_L - T_S)/R$ or obtained directly from the experimental data by finding the difference between the time taken to reach the solidus temperature $(t\ (T_S))$and the time taken to reach the liquidus temperature $(t\ (T_L))$. The plots provide a fair estimate of the trends. The disagreement observed for thermocouples 1 and 2, are due to unexpected lower cooling rates observed in these locations. These cooling rate variations will be further discussed in Section 5.1.2.2. The empirical expressions for the fitted curves are,

$$\mathbf{TDAS = 5.7\ (t_{stat}(d))^{0.65}} \quad \text{..... (4.12)}$$

where, $t_{stat}(d)$ is the statistically obtained local solidification time at a particular distance d mm from the cooling end,

$$\mathbf{TDAS = 7.8\ (t_{exp}(d))^{0.51}} \quad \text{..... (4.13)}$$

where, $t_{exp}(d)$ is the experimentally obtained local solidification time at a particular distance d mm from the cooling end.

Unlike the findings for the sand casting, the relationship between TDAS and the local solidification time for the wedge cast does not agree with Grugel's observation. The exponent obtained for the TDAS, as a function of t_{sol}, for the wedge casting is 0.65. This value is twice the exponent value obtained in Grugel's results [50]. This deviation is probably due to the solidification pattern in the wedge casting being not perfectly directional in nature. Unlike the step-shaped casting, the continuous widening of the wedge leads to the involvement of a non-directional solidification component.

On moving from thermocouple 1 to thermocouple 6, the average measured tertiary dendrite arm spacing values were observed ranging from 10-40 μm.

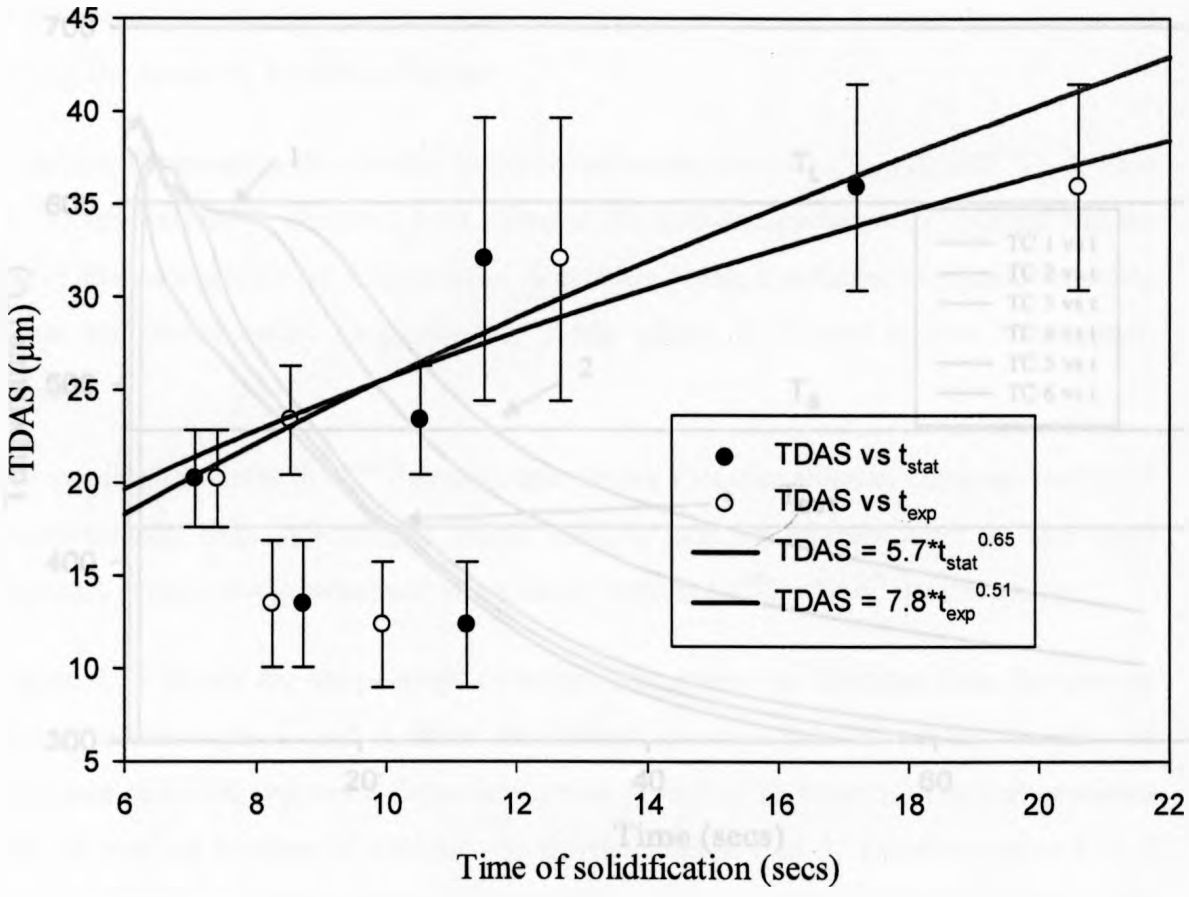

Figure 4.24 Tertiary dendrite arm spacing varying as a function of the local solidification time (AM60B).

4.3 Wedge Casting – AZ91D

4.3.1 Thermal Analysis

A similar analysis of process parameters was carried out for AZ91D to understand the effect of these parameters on the casting process. Figure 4.25 represents the variation of temperature with time at each thermocouple location. The portion of curve above point 1 is referred to as the "superheat" zone.

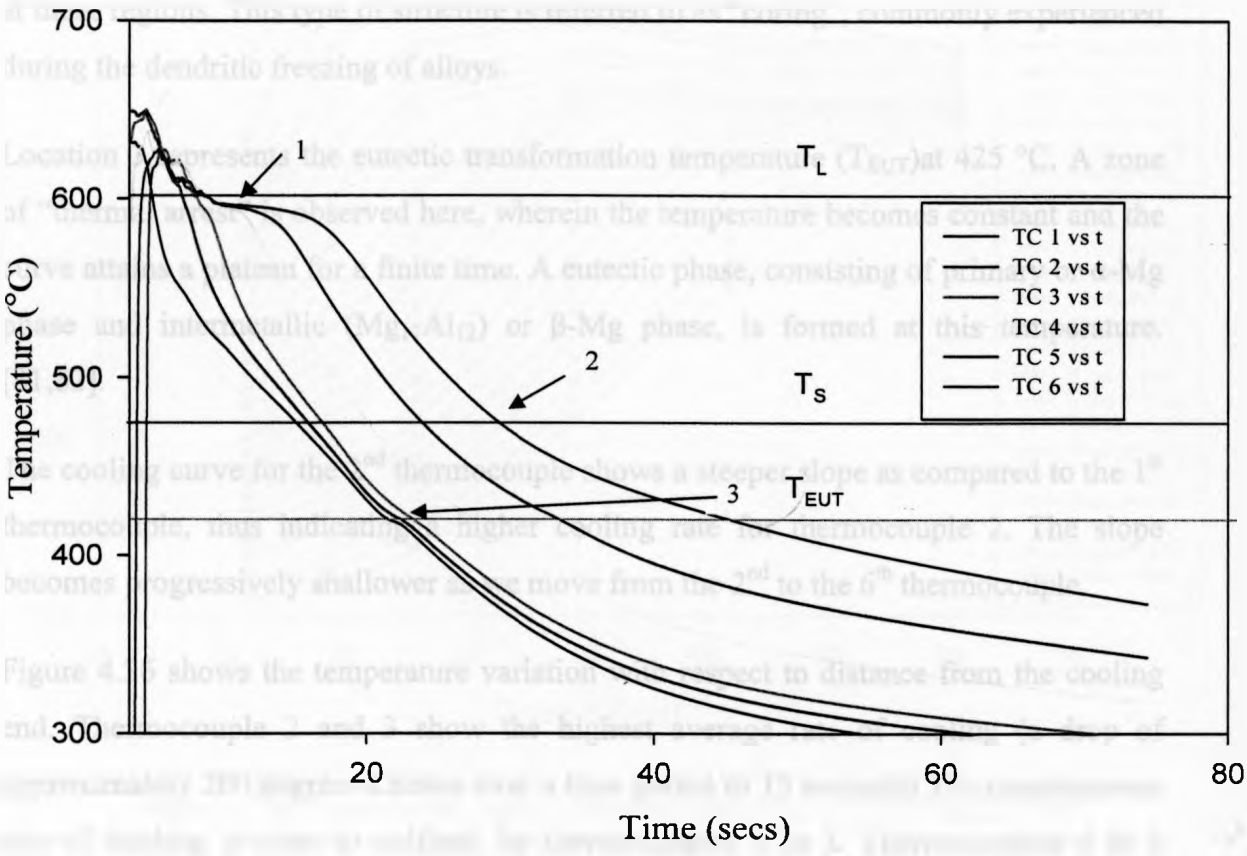

Figure 4.25 Temperature-time curves at different thermocouples (AZ91D).

Point 1 denotes the liquidus temperature (T_L), i.e., 601 °C. As discussed previously, this zone marks the initiation of the nucleation and growth of primary phase or α-Mg phase. The α-Mg phase starts as equiaxed grains and gradually changes to a dendritic structure (equiaxed →columnar → cellular) on moving away from the wedge tip, due to progressive reduction in the rate of cooling.

Location 2 represents the solidus temperature (T_S), i.e., 475 °C and is also the temperature at which the intermetallic precipitates nucleate around the edges of the α-

Mg dendrite arms. During solidification of dendrites, the arms grow in an outward fashion, rejecting solute as they develop into branched network. This leads to solute segregation near the edges of the arms. Thus, the center of the arm is low in solute content whereas the edges are rich in solute, hence the precipitation of the intermetallics at these regions. This type of structure is referred to as "coring", commonly experienced during the dendritic freezing of alloys.

Location 3 represents the eutectic transformation temperature (T_{EUT})at 425 °C. A zone of "thermal arrest" is observed here, wherein the temperature becomes constant and the curve attains a plateau for a finite time. A eutectic phase, consisting of primary or α-Mg phase and intermetallic ($Mg_{17}Al_{12}$) or β-Mg phase, is formed at this temperature. [81,82].

The cooling curve for the 2nd thermocouple shows a steeper slope as compared to the 1st thermocouple, thus indicating a higher cooling rate for thermocouple 2. The slope becomes progressively shallower as we move from the 2nd to the 6th thermocouple.

Figure 4.26 shows the temperature variation with respect to distance from the cooling end. Thermocouple 2 and 3 show the highest average rate of cooling (a drop of approximately 200 degrees Celsius over a time period of 13 seconds).The instantaneous rate of cooling is close to uniform for thermocouples 1 to 3. Thermocouples 4 to 6 initially show a large spacing between the ordinate values, which decrease with increasing time value.

To understand the characteristics the mushy zone and its motion during the solidification process, it is important to study the variation of interface velocity as a function a distance and time. Figures 4.27 and 4.28 show the variation of the liquidus and solidus fronts as functions of time.

The position of the liquidus front is a monotonically increasing function of time. The following relationship between distance and time can be established by empirical analysis of the experimental data:

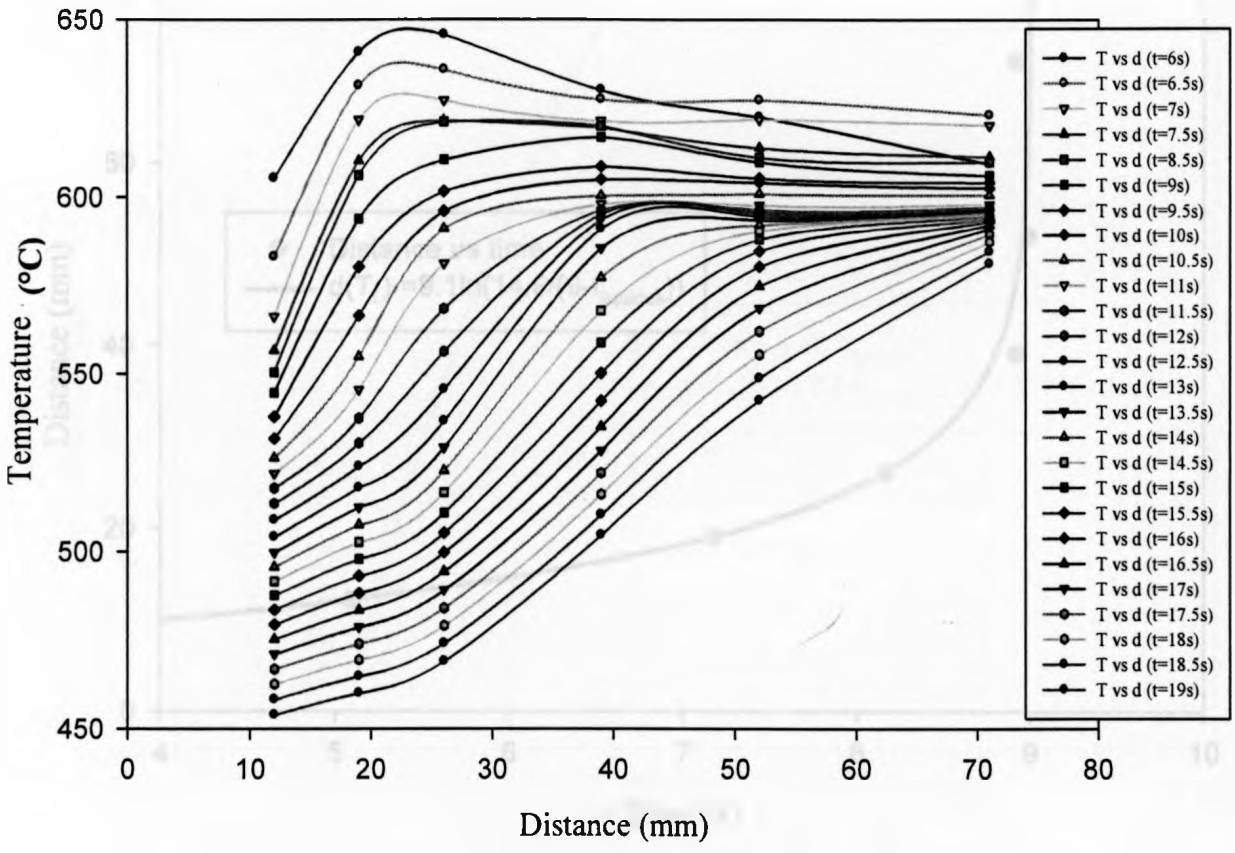

Figure 4.26 Temperature versus distance curves for AZ91D wedge cast.

$$d(T_L) = 9.1\ln(14.9/(9-t_{liquidus})) \quad \text{..... (4.14)}$$

where, $t_{liquidus}$ is the time to reach the liquidus temperature at any distance d from the wedge tip.

Differentiating the above equation with respect to time provides with the liquidus front velocity. Similarly, we can obtain plots representing variation of time against solidus front as shown below.

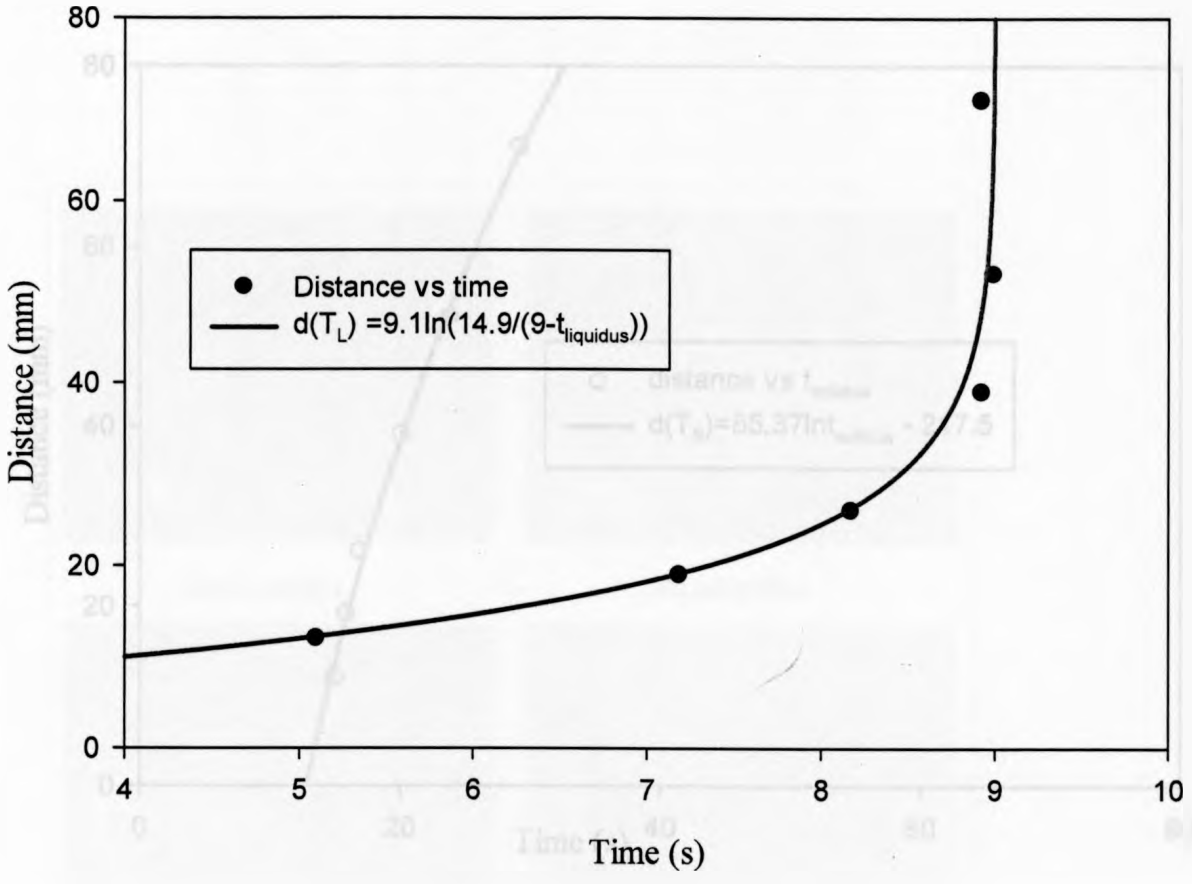

Figure 4.27 Distance versus time plot for the liquidus interface for AZ91D.

The position of the solidus front as a function of time can be represented graphically as shown in figure. The plot shown is a monotonically increasing, exhibiting a logarithmic nature. The curve can be described by the empirical relationship

$$\mathbf{d(T_S) = 85.37ln(t_{solidus}) - 217.5} \ldots\ldots (4.15)$$

where, $t_{solidus}$ is the time taken to reach the solidus temperature at a distance d from the cooling end.

On differentiating the above mentioned equation with respect to time, we obtain the solidus front velocity as a function of distance.

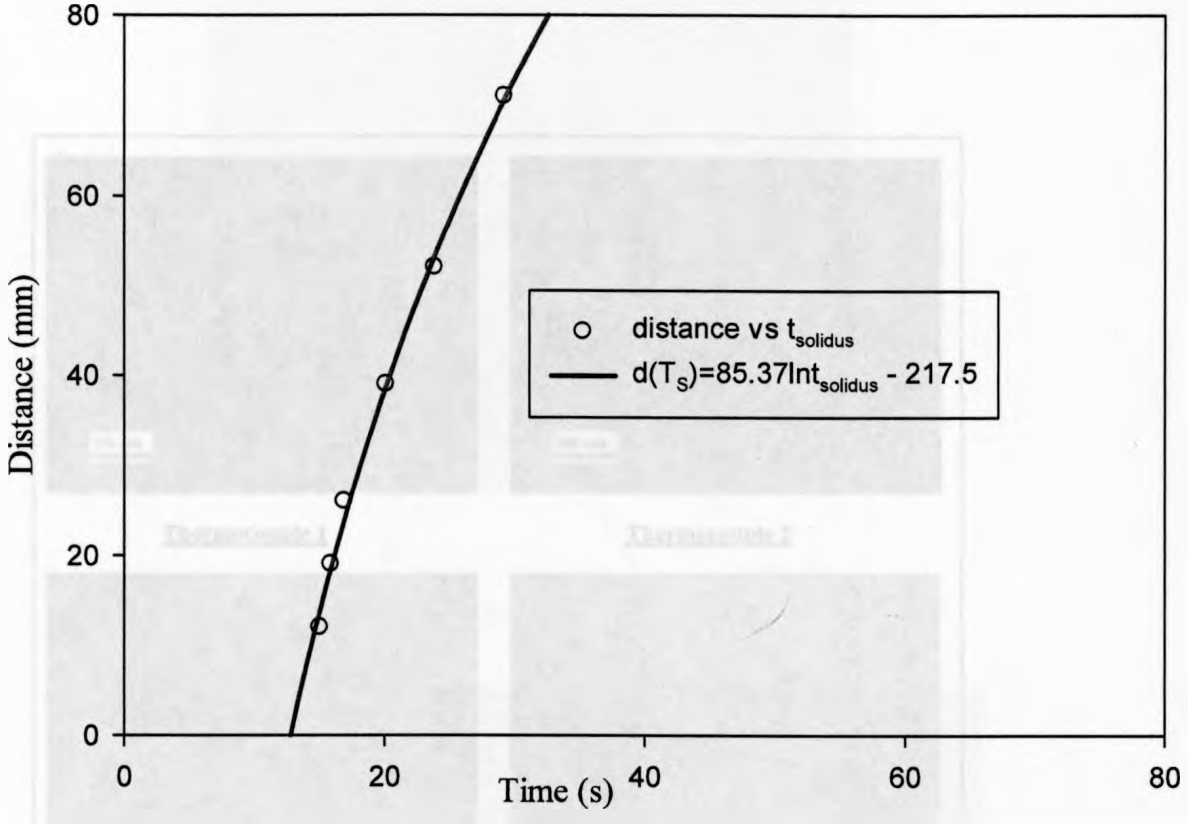

Figure 4.28 Distance vs. time plot for the solidus interface for AZ91D.

4.3.2 Microstructural Analysis

Figure 4.29 presents the microstructural profile for the AZ91D wedge casting. At the tip of the wedge we obtained equiaxed grain structures with a minimal amount of dendritic growth. There is a large amount of inter-metallic precipitation, which is surrounded by the eutectic phase embedded in an alpha Magnesium matrix.

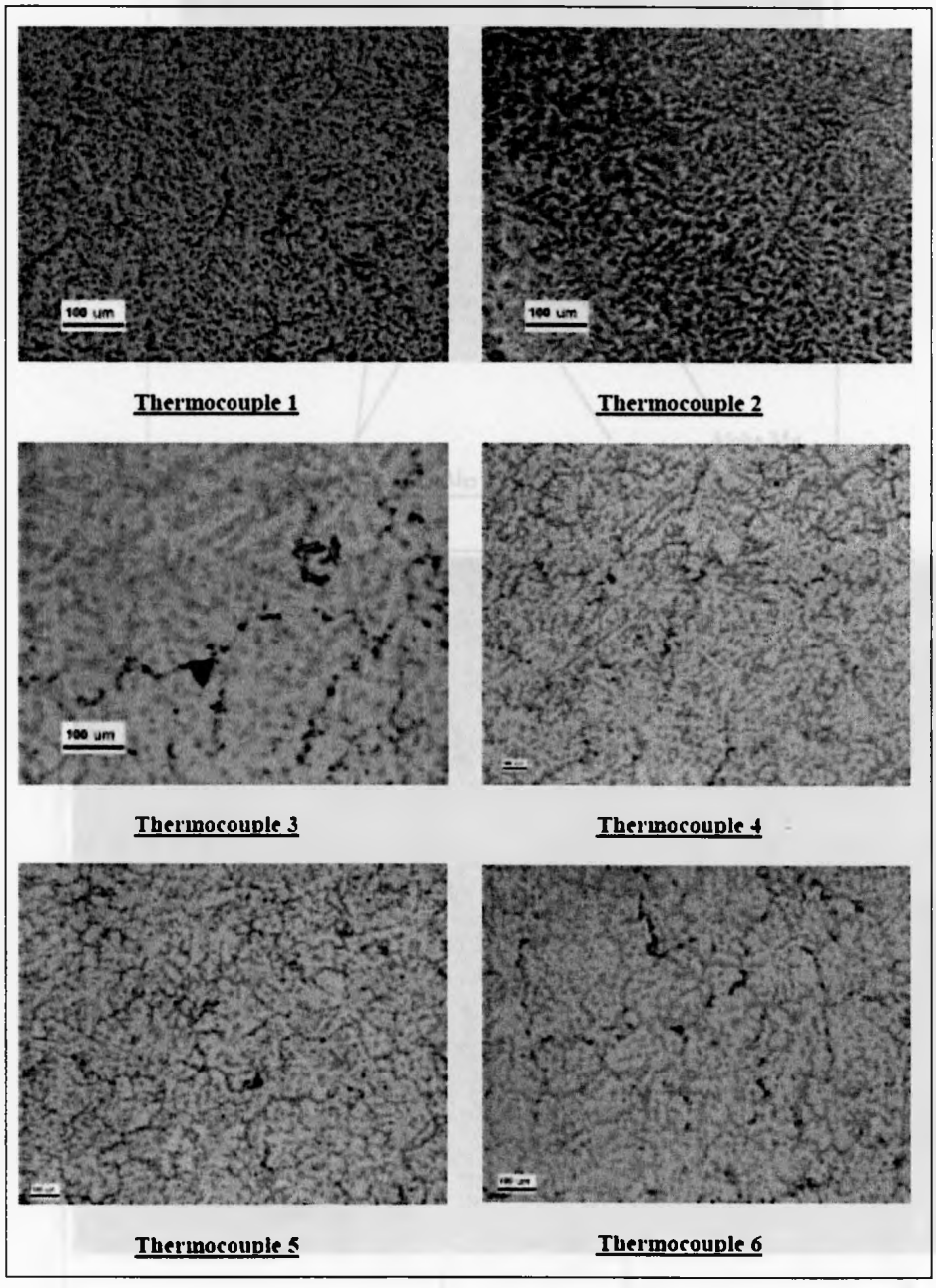

Figure 4.29 Metallographic structures at different thermocouple locations.

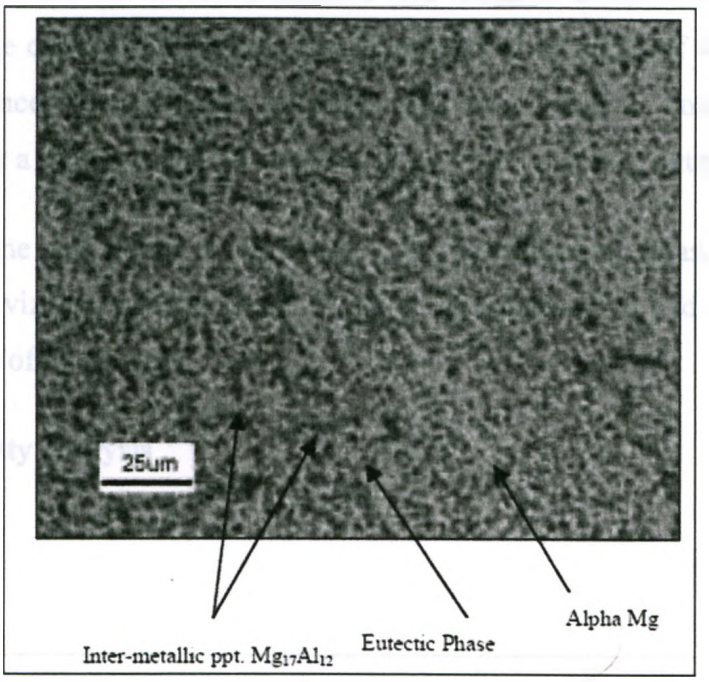

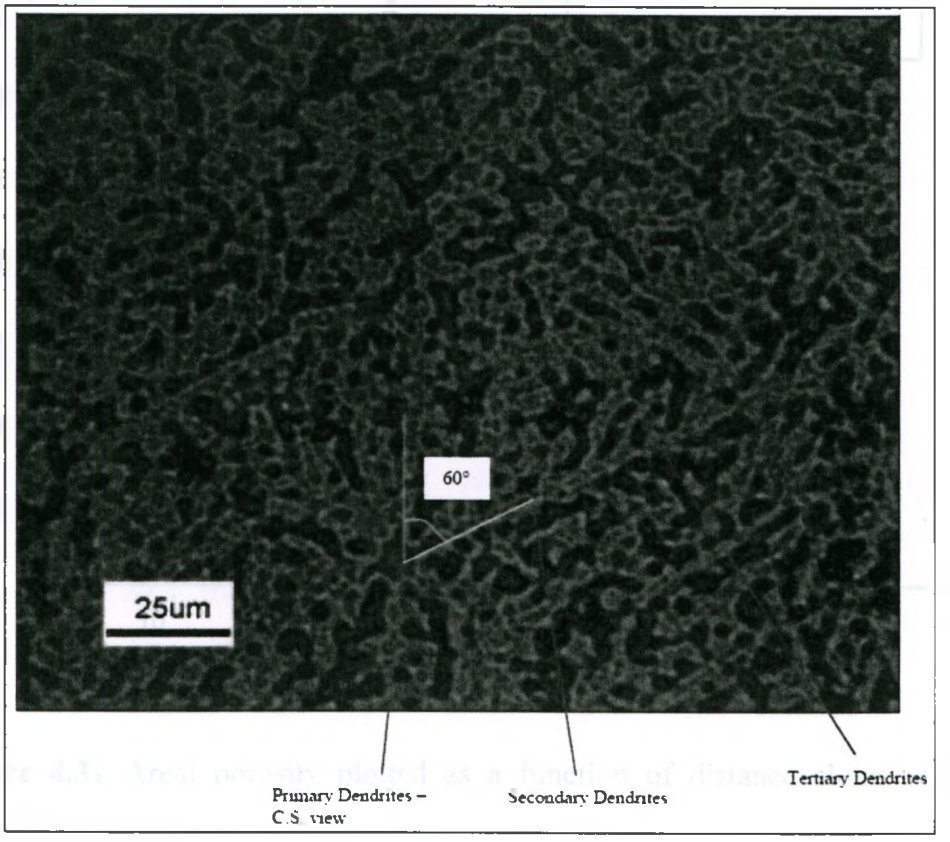

Figure 4.30 Divorced eutectic phases and dendrite morphology in AZ91D wedge cast.

As we proceed toward the base of the wedge, there is an increase in dendritic growth. Figure 4.30 shows the divorced eutectic and dendrite morphologies observed in the AZ91D wedge casting. Dendrites grow at roughly at an angle of 45° to the horizontal. As the distance from the tip increases the arms become coarser. The arms are surrounded by a high concentration of solute in form of Al-Mg eutectic phases.

As found in the case of the AM60B alloy, at lower cooling areas, 2 structural regions are observed viz. a dendritic array all along the mold walls and cellular array in the central region of the casting.

4.3.2.1 Porosity analysis

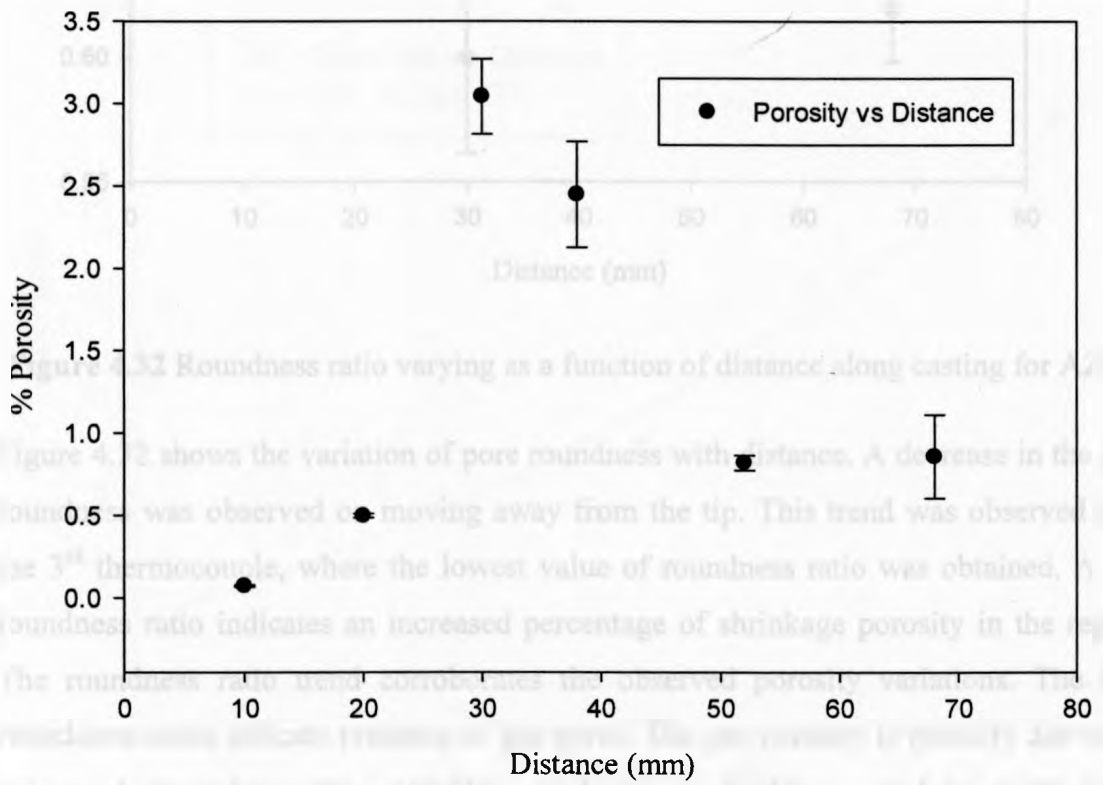

Figure 4.31 Areal porosity plotted as a function of distance along casting for AZ91D wedge cast.

Figure 4.31 represents the variation of porosity with distance from the tip. A significant increase in the porosity, upto a distance of 30mm from the wedge tip, is observed.

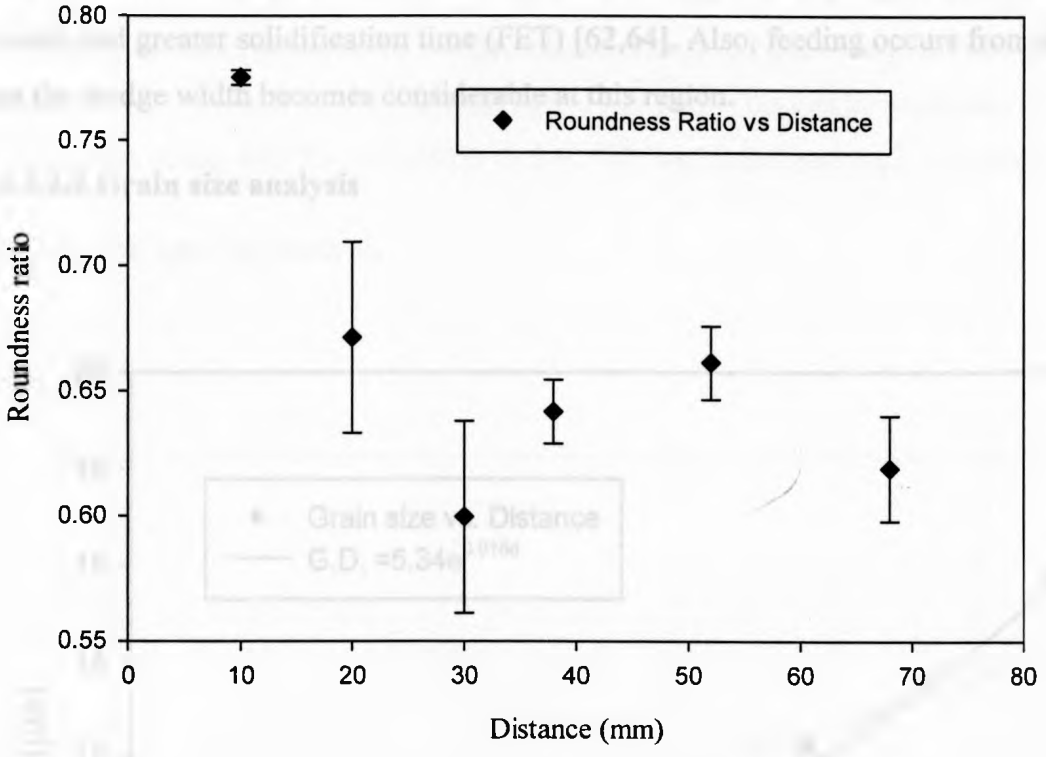

Figure 4.32 Roundness ratio varying as a function of distance along casting for AZ91D.

Figure 4.32 shows the variation of pore roundness with distance. A decrease in the pore roundness was observed on moving away from the tip. This trend was observed until the 3rd thermocouple, where the lowest value of roundness ratio was obtained. A low roundness ratio indicates an increased percentage of shrinkage porosity in the region. The roundness ratio trend corroborates the observed porosity variations. The high roundness ratios indicate presence of gas pores. The gas porosity is possibly due to the entrapped gases during the mold filling or due to gas bubbles created due to the liquid metal turbulence during the filling process. The possible cause for this observed trend is similar to that discussed for the AM60 alloy. Figures 4.31 and 4.32 imply that the solidification front, which is parabolic in shape, chokes off the feeding near the 3rd thermocouple due to excessive dendritic branching from the sides. Thus, there is a pool

of liquid trapped in the region, which leads to formation of shrinkage porosity (thus lower roundness ratio in this region). On moving further towards the base (i.e. along the 4th and 5th thermocouples) of the wedge, the porosity values reduce drastically with a slight increase in the value during the transition from the 5th to 6th thermocouple. This can be attributed to an enhanced feeding from the top, due to a larger volume of liquid metal and greater solidification time (FET) [62,64]. Also, feeding occurs from sideways as the wedge width becomes considerable at this region.

4.3.2.2 Grain size analysis

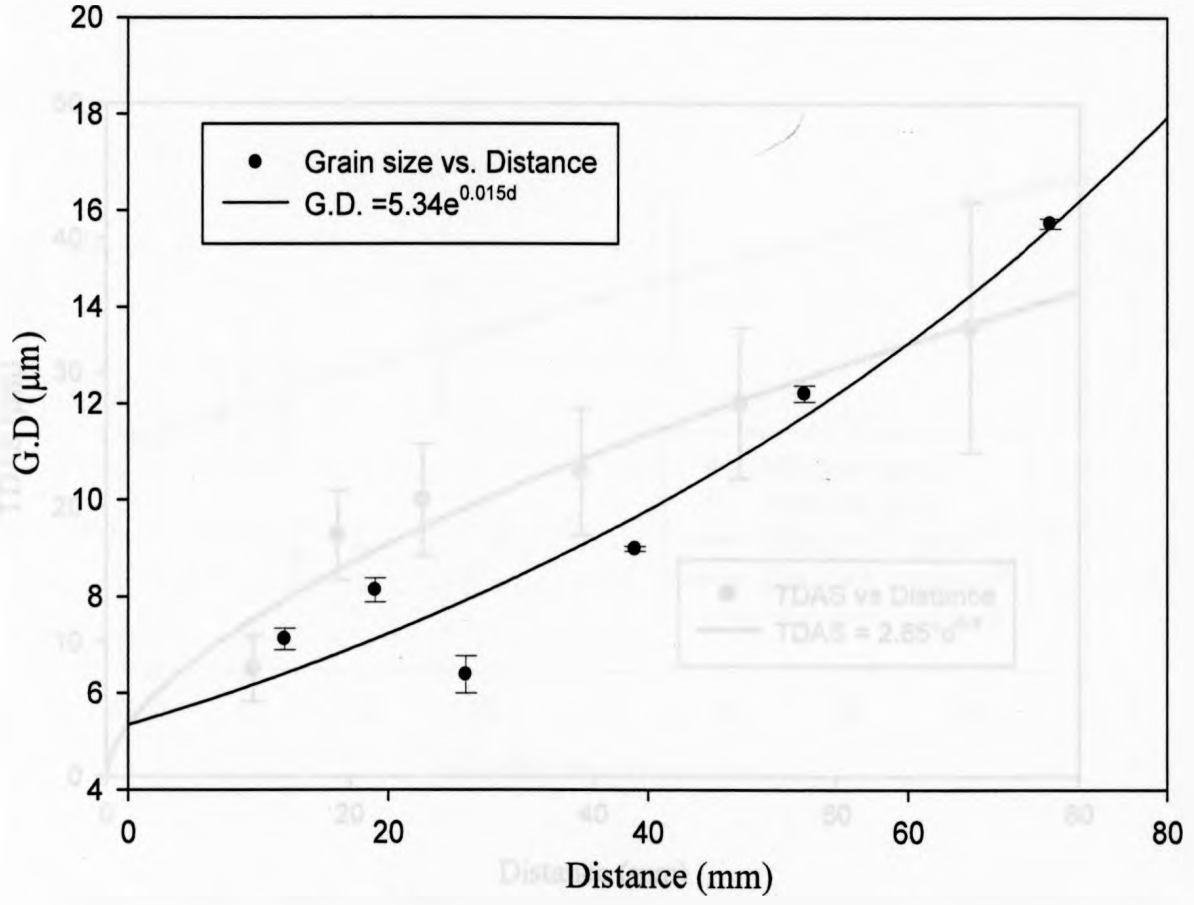

Figure 4.33 Grain size with respect to distance along casting for AZ91D wedge cast.

Figure 4.33 shows the variation of grain size with distance from the wedge tip. The values roughly fit to the following empirical expression, given below.

$$G.D = 4.19e^{0.016d} \quad \text{..... (4.16)}$$

where, ***G.D*** is the grain diameter and ***d*** is the distance from the cooling end. The average grain size, at the tip of wedge, ranged from 5-10 μm. The grain size values are comparatively smaller than those observed in AM60B. This can be attributed to a higher Al content, along with Zn, in AZ91D (8.5-9.5%), which leads to grain refinement [83].

4.3.2.3 Arm spacing analysis

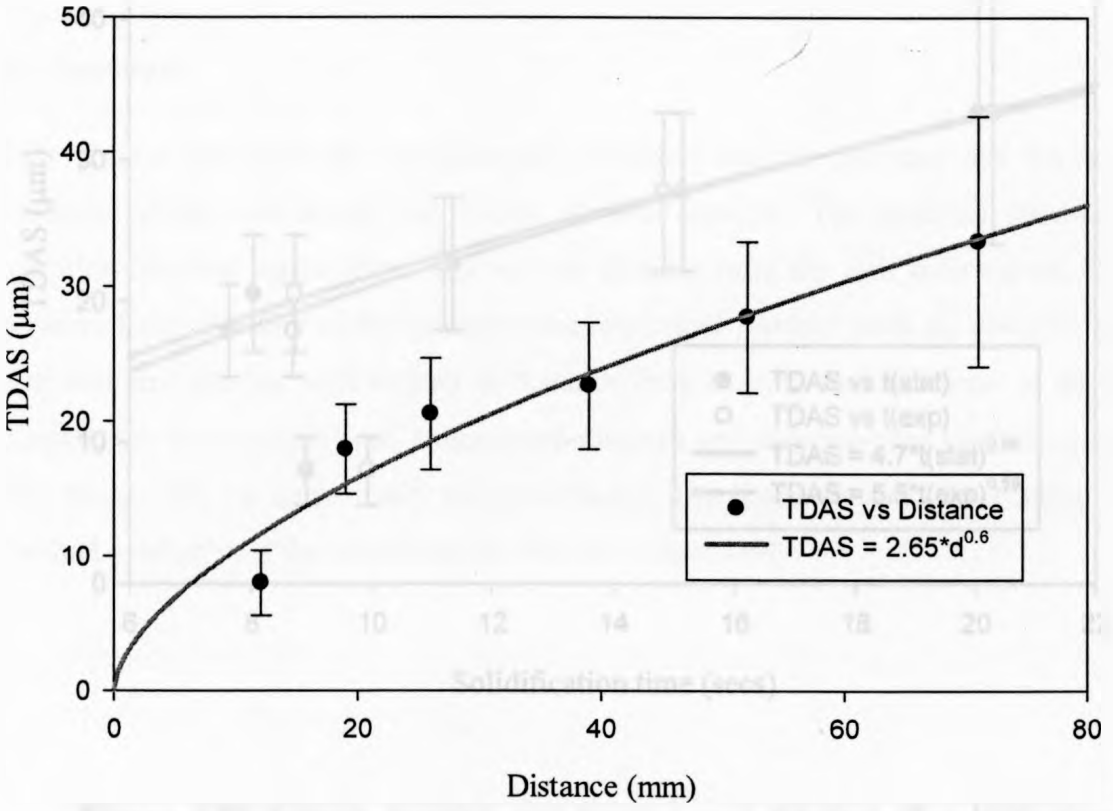

Figure 4.34 Tertiary dendrite arm spacing as a function of distance along casting (AZ91D).

Tertiary dendrite arm spacing (TDAS) was also plotted as functions of distance and local solidification time (Figure 4.34 and 4.35). It is observed that TDAS has a power law dependency on the distance from the wedge tip, as described by the following empirical relationship

$$\mathbf{TDAS = 2.65d^{0.6}} \quad \text{..... (4.17)}$$

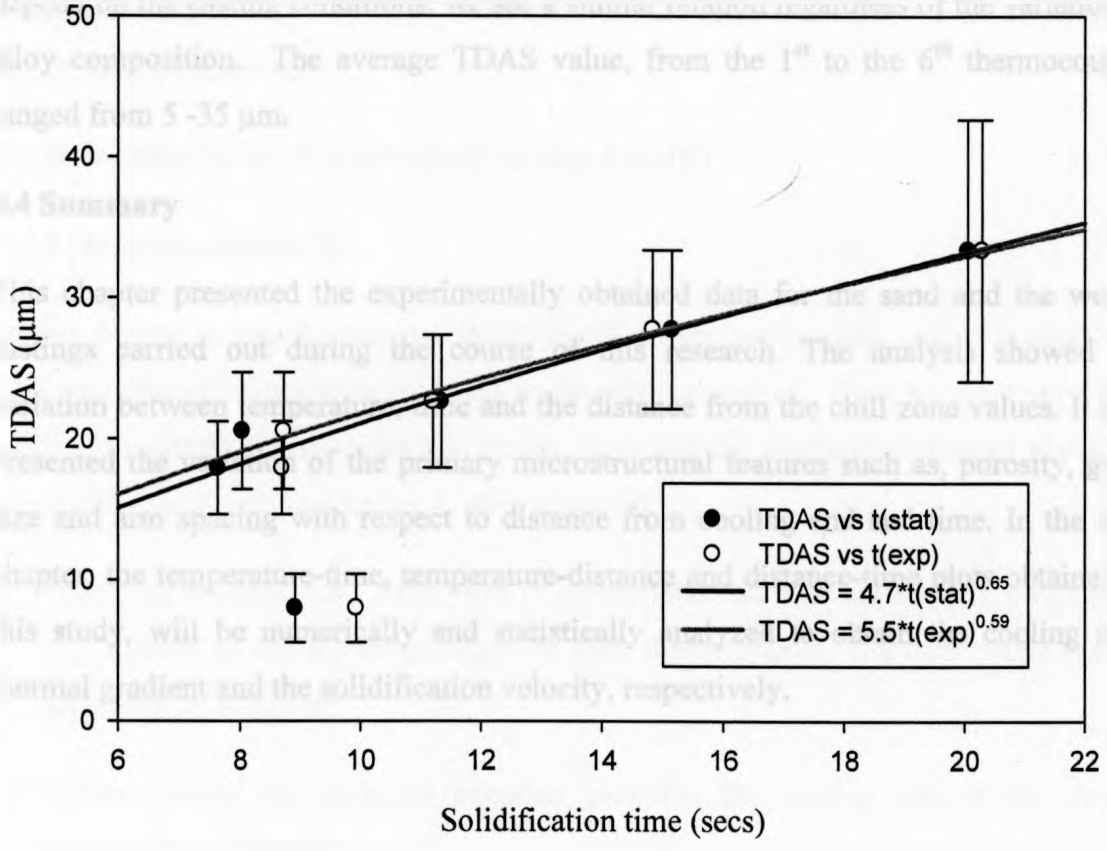

Figure 4.35 Tertiary dendrite arm spacing as a function of solidification time (AZ91D).

TDAS shows an increase with solidification time (Figure 4.34). The deviations observed for the 1st thermocouple, were due to lower cooling rates observed in the

region. The probable explanation for this has been provided in Section 5.1.2.2. The relation between TDAS and solidification time is empirically equivalent to an increasing power law curve.

$$\mathbf{TDAS = 4.7(t\text{-}stat)^{0.65}} \quad \text{... (4.18)}$$

$$\mathbf{TDAS = 5.5(t\text{-}exp)^{0.59}} \quad \text{... (4.18)}$$

The above relationship is similar to that obtained for the AM60B wedge casting. This corroborates Fleming's theory of dendrite coarsening, being entirely dependent on the rate of heat extraction or rate of cooling [47]. Since the cooling rate will primarily depend on the casting conditions, we see a similar relation regardless of the variation in alloy composition. The average TDAS value, from the 1st to the 6th thermocouple, ranged from 5 -35 μm.

4.4 Summary

This chapter presented the experimentally obtained data for the sand and the wedge castings carried out during the course of this research. The analysis showed the variation between temperature, time and the distance from the chill zone values. It also presented the variation of the primary microstructural features such as, porosity, grain size and arm spacing with respect to distance from cooling end and time. In the next chapter, the temperature-time, temperature-distance and distance-time plots obtained in this study, will be numerically and statistically analyzed to obtain the cooling rate, thermal gradient and the solidification velocity, respectively.

Chapter 5

Analysis of Process variables

An effective control of the process parameters is important to improve the resultant solidification microstructure and properties of a given casting. This chapter presents the numerical and statistical analysis methods applied to calculate the process parameters from the temperature-time, temperature-distance and distance-time curves shown in Chapter 4.This also discusses the variation of the process variables as a function of the distance and time variables. These obtained trends will be correlated with the microstructural features, so as to understand the dependence of the as-cast structure on the process parameters.

5.1 Determination and Analysis of Cooling rate (R)

5.1.1 Determination of R

In this section, a step-by-step procedure to obtain the cooling rate values is described. The temperature values were recorded at discrete time values. These temperature values were then plotted against time and curves depicting the continuous thermal history of the casting, as shown in Chapter 4, were obtained.

1. Using the thermocouple data, plots of temperature vs. time are created, ranging from the liquidus to solidus temperature for each thermocouple. The data points are fit to an empirical equation.

2. Differentiating the obtained equation provides the cooling rate at the different thermocouple locations.

3. The statistical average local cooling rate (***R_{stat}*/*R-stat***) can be represented as:

$$R_{stat} = \int_{t_i}^{t_f} \frac{R}{(t_f - t_i)} dt$$

where, t_f is the time in seconds to reach the solidus temperature and t_i is the time in seconds to reach the liquidus temperature.

4. The numerical values of the cooling rate can be obtained by calculating the instantaneous local cooling rate from the temperature-time data, using the following equation:

$$R_{inst.} = -\frac{T_{i+1} - T_i}{t_{i+1} - t_i}$$

The numerical average of the $R_{inst.}$ values give the numerical average local cooling rate –***R-num***

5. These cooling rate values can be plotted against the thermocouple distance values to obtain the cooling profile along the casting.

5.1.2 Analysis of R

The content presented here describes the variation of the cooling rate values as functions of distance along casting, wedge height and wedge width.

5.1.2.1 Sand casting – AM60B

Figure 5.1 presents a plot of average local cooling rate with respect to distance. The cooling rate shows a monotonic decrease with respect to increasing distance values. The relationship can be empirically fitted to an exponentially decreasing trend, as shown in Equation (5.1) and (5.2).

$$\textbf{R-num} = 15.54e^{-0.011d} \quad \text{.....(5.1)}$$

$$\textbf{R-stat} = 16.49e^{-0.013d} \quad \text{.....(5.2)}$$

where, ***R-num*** and ***R-stat*** are the numerically and statistically calculated values of local cooling rate and ***d*** is the distance from the cooling end in mm. At the chill end, the average R values reach as high as 16-17 °C/s.

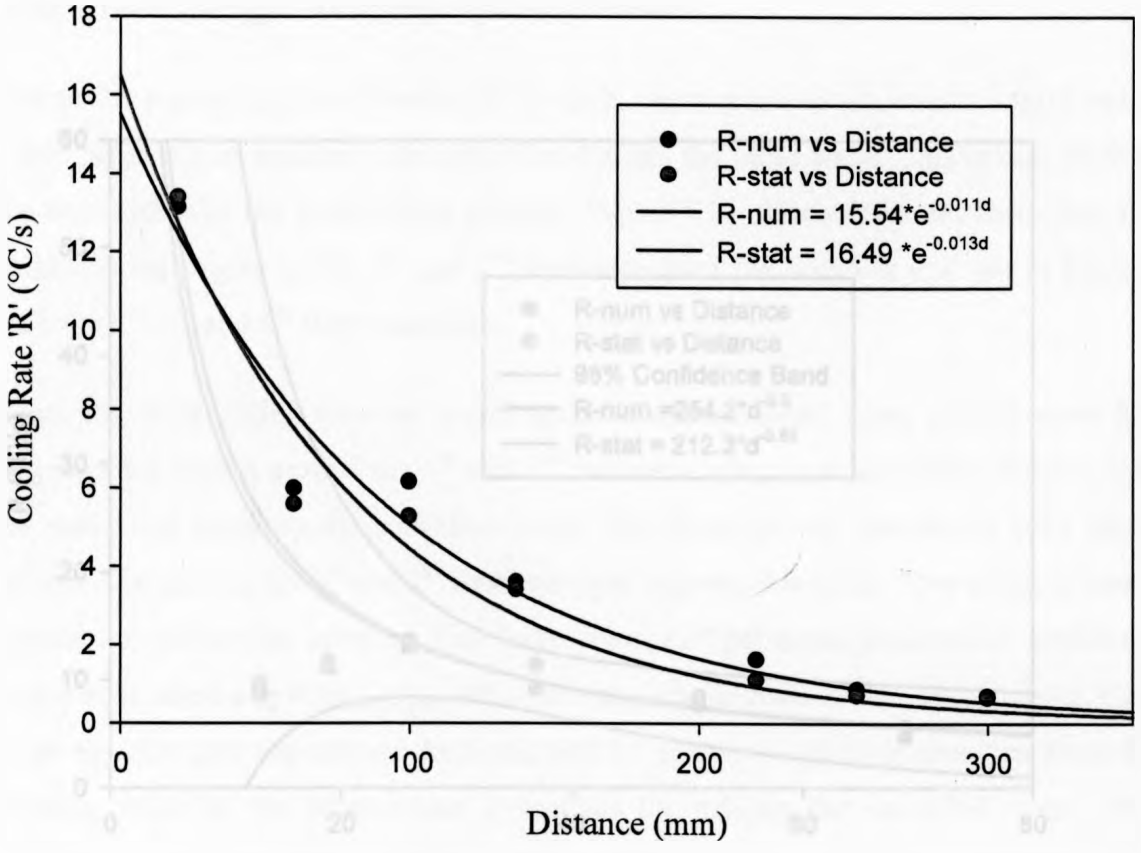

Figure 5.1 Cooling rate with respect to distance along casting.

5.1.2.2 Wedge casting – AM60B

Figure5.2 shows the variation of average local rate of cooling with distance from the cooling end for the AM60B wedge casting.

The plot shows a good fit for thermocouples 3 to 6. The fitted curves give the empirical relationships

R-numerical = $254.2x^{-0.9}$..... (5.3)

R-statistical = $212.3x^{-0.85}$..... (5.4)

where, ***R*** is the Cooling rate (°C/s).

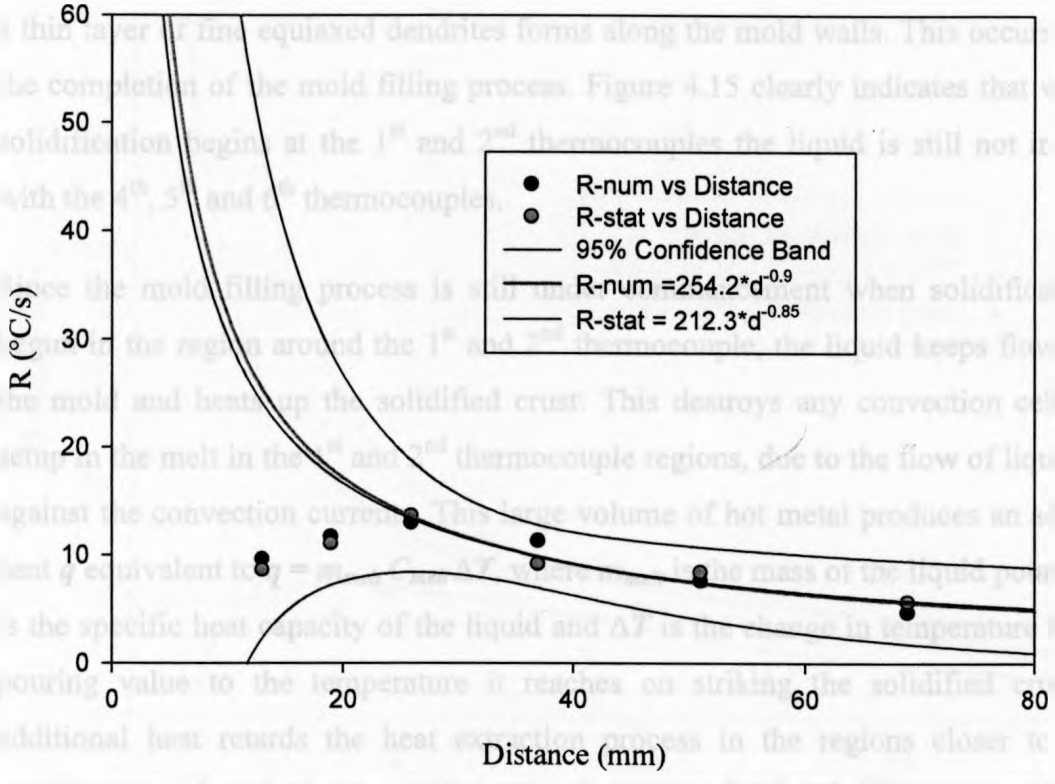

Figure 5.2 Cooling rate as a function of distance (AM60B).

The observed deviations for the 1st and 2nd thermocouples are possibly due to two reasons: a) experimental artefacts involved in recording temperature values by the thermocouple due to delay in thermocouple response and b) the effect of mold filling. At the 1st thermocouple location, we observe a cooling rate of around 8.5 °C/s. On moving away from the cooling end the cooling rate increases progressively for the 2nd and the 3rd thermocouples from 11 °C/s to 13.6 °C/s. This variation can be attributed to the changing shape of the solidification front.

The interface has a nearly parabolic shape with an increasing latusrectum [71], with increasing distance from the cooling end. Thus, the interface velocity is higher along

the edges than in the center of the casting. When the liquid hits the wedge tip, a high surface area to volume ratio (—→) and a divergent heat flow provides very high cooling rates leading to extremely rapid solidification.

Due to the immediate solidification of the melt, coming in contact with the mold walls, a thin layer of fine equiaxed dendrites forms along the mold walls. This occurs prior to the completion of the mold filling process. Figure 4.15 clearly indicates that when the solidification begins at the 1st and 2nd thermocouples the liquid is still not in contact with the 4th, 5th and 6th thermocouples.

Since the mold filling process is still under commencement when solidification has begun in the region around the 1st and 2nd thermocouple, the liquid keeps flowing into the mold and heats up the solidified crust. This destroys any convection cells being setup in the melt in the 1st and 2nd thermocouple regions, due to the flow of liquid metal against the convection currents. This large volume of hot metal produces an additional heat q equivalent to $q = m_{melt} C_{melt} \Delta T$, where m_{melt} is the mass of the liquid poured, C_{melt} is the specific heat capacity of the liquid and ΔT is the change in temperature from the pouring value to the temperature it reaches on striking the solidified crust. This additional heat retards the heat extraction process in the regions closer to the tip considerably. A rise in the cooling rate on moving from the 1stthermocouple to the 3rdthermocouple could be primarily attributed to the relative reduction in the m_{melt}, thus lesser heat generation and relatively lower retardation to heat extraction.

As the filling commences further and liquid level rises, the front also moves towards the base of the casting. Therefore, in the region around the 4th thermocouple we observe a significant increase in the volume of liquid metal (due to considerable widening of the wedge) and a lower surface area to volume ratio.

Also, the fraction of the melt surface area exposed to the steel walls increases, which extracts heat at a much slower rate (thermal conductivity of steel at room temperature is 16W/(m.K)) than the regions in contact with the water-cooled copper (401 W/(m.K))

[84]. Thus, the net rate of heat extraction drops down considerably, with distance, on moving from the 3rd thermocouple to the 6th thermocouple.

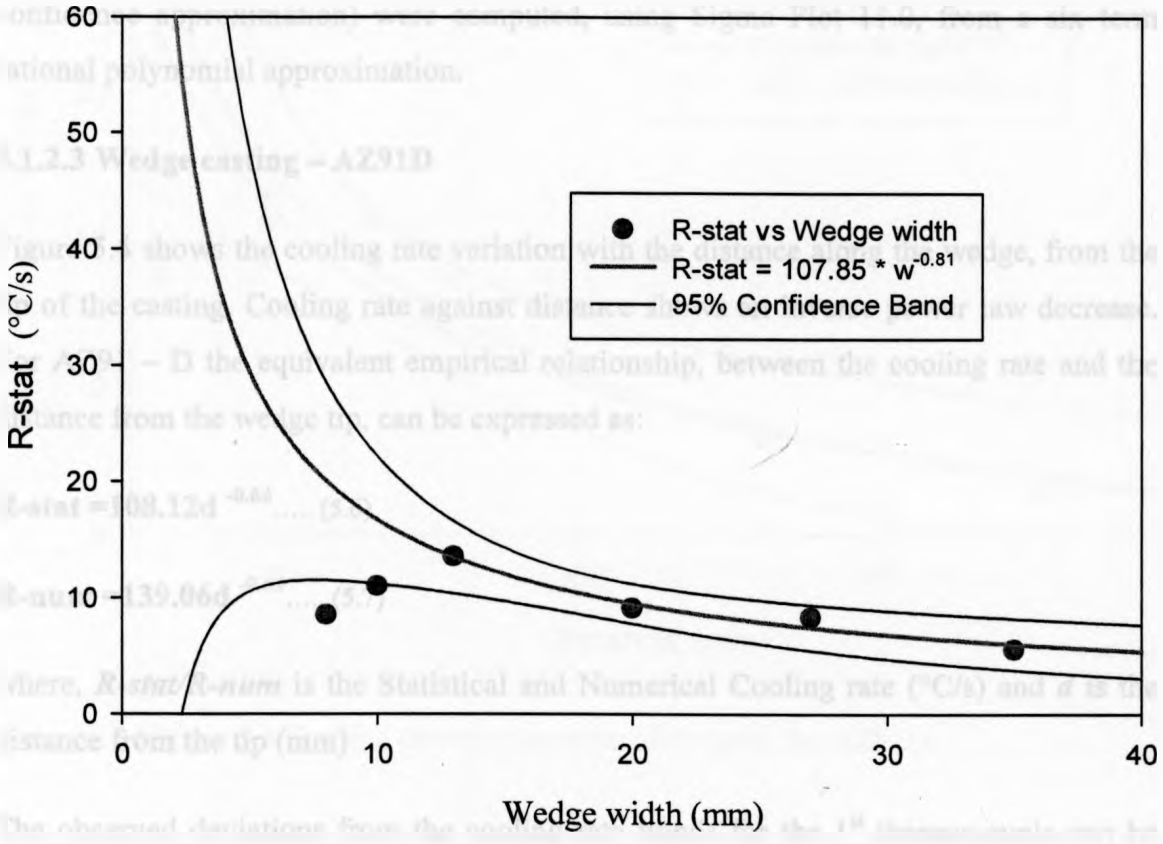

Figure 5.3 Cooling rate as a function of wedge width (AM60B).

Figure 5.3 shows the variation of cooling rate with respect to the width of the wedge. The relationship follows an inverse power law expression. An approximate fit of the experimental data provides us with the following empirical equation.

$$\left\{\frac{dT}{dt}\right\}_{\text{statistical}} = 107.85w^{-0.81} \quad \text{..... (5.5)}$$

where, w is the wedge width

The plots representing the cooling rate variation as a function of distance along the casting and wedge width indicate extremely high rates of cooling at the wedge tip. Both the plots show a singularity at the point $x \rightarrow 0^+$ i.e. $f(0) = \lim_{x \to 0} f(x) \rightarrow +\infty$. The confidence intervals shown in Figures 5.2 and 5.3 were calculated using the *t*-test method. The '*t*' value and the standard normal percentile equivalent '*z*' (z=1.96 for 95% confidence approximation) were computed, using Sigma Plot 11.0, from a six term rational polynomial approximation.

5.1.2.3 Wedge casting – AZ91D

Figure 5.4 shows the cooling rate variation with the distance along the wedge, from the tip of the casting. Cooling rate against distance shows an inverse power law decrease. For AZ91 – D the equivalent empirical relationship, between the cooling rate and the distance from the wedge tip, can be expressed as:

$$\textbf{R-stat} = 108.12 d^{-0.64} \quad \text{..... (5.6)}$$

$$\textbf{R-num} = 139.06 d^{-0.69} \quad \text{..... (5.7)}$$

where, ***R-stat/R-num*** is the Statistical and Numerical Cooling rate (°C/s) and ***d*** is the distance from the tip (mm)

The observed deviations from the cooling rate trends for the 1st thermocouple can be explained by the same effect as predicted for the cooling rate variations in the AM60B wedge casting.

As in case of the AM60B analysis, the dependence of the cooling rate on the wedge width was also observed. Figure 5.5 shows the effect of the wedge width on the average local cooling rate. The plot represented a trend similar to that of AM60B. The curve shows an inverse power law relationship between the two variables. It can be described by the below given empirical expressions:

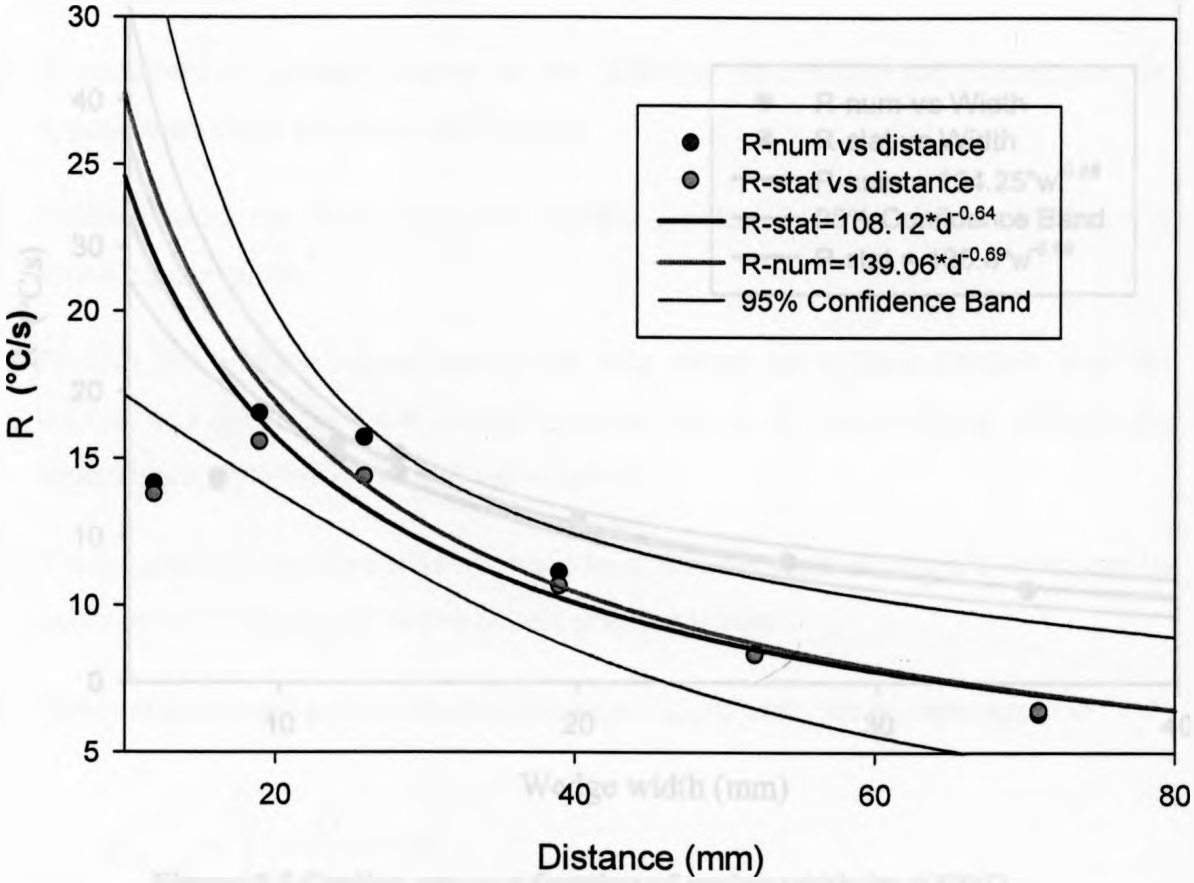

Figure 5.4 Cooling rate as a function of distance for AZ91D.

R-num = $154.25w^{-0.85}$..... (5.8)

R-stat = $135.6w^{-0.69}$..... (5.9)

where, w is the width of the wedge (mm).

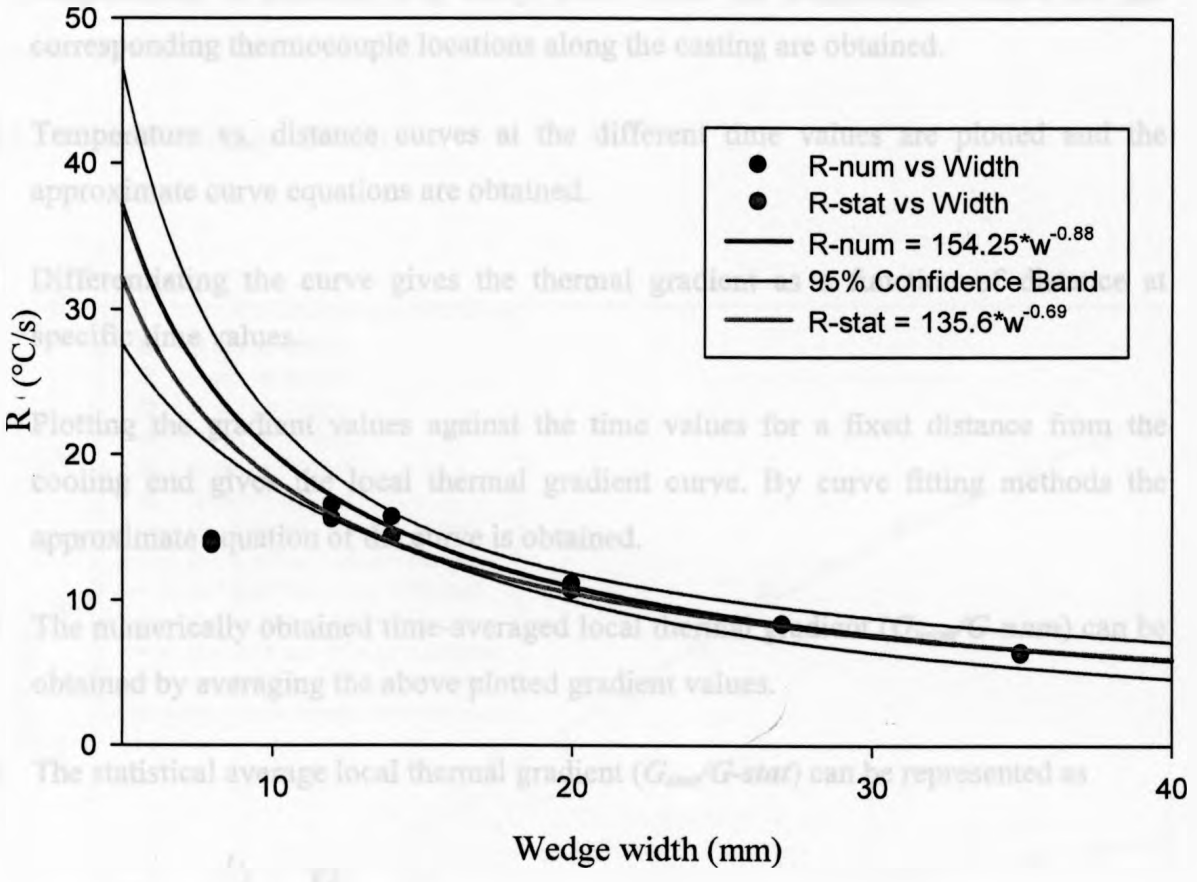

Figure 5.5 Cooling rate as a function of wedge width for AZ91D.

As observed in case of AM60B wedge cast, we see a singularity in the cooling rate trends near the wedge tip and the values approach to infinity. Thus, extremely high cooling rates are experienced near the wedge tip.

5.2 Determination and Analysis of Thermal gradient (G)

5.2.1 Determination of G

This section presents the numerical methodology applied to obtain the average local thermal gradient values.

1. From the temperature – time data, for the given number of thermocouples positioned in the casting, a range of data values lying between the liquidus and solidus

temperatures is selected. For every time value the temperature values for the corresponding thermocouple locations along the casting are obtained.

2. Temperature vs. distance curves at the different time values are plotted and the approximate curve equations are obtained.

3. Differentiating the curve gives the thermal gradient as a function of distance at specific time values.

4. Plotting the gradient values against the time values for a fixed distance from the cooling end gives the local thermal gradient curve. By curve fitting methods the approximate equation of the curve is obtained.

5. The numerically obtained time-averaged local thermal gradient (***G_{num}*/G-num**) can be obtained by averaging the above plotted gradient values.

6. The statistical average local thermal gradient (***G_{stat}*/G-stat**) can be represented as

$$G_{stat} = \int_{t_i}^{t_f} \frac{G}{(t_f - t_i)} dt$$

where, t_f is the time in seconds to reach solidus temperature and t_i is the time in seconds to reach liquidus temperature

7. These values were compared with the numerical average of the local thermal gradient values.

8. The maximum and minimum values of the local thermal gradient can also be determined from the G vs. time plot, by obtaining the G values corresponding to t_f and t_i, respectively.

5.2.2 Analysis of G

The variation of thermal gradient values, as functions of distance from cooling end and time are presented in this section.

5.2.2.1 Sand casting- AM60B

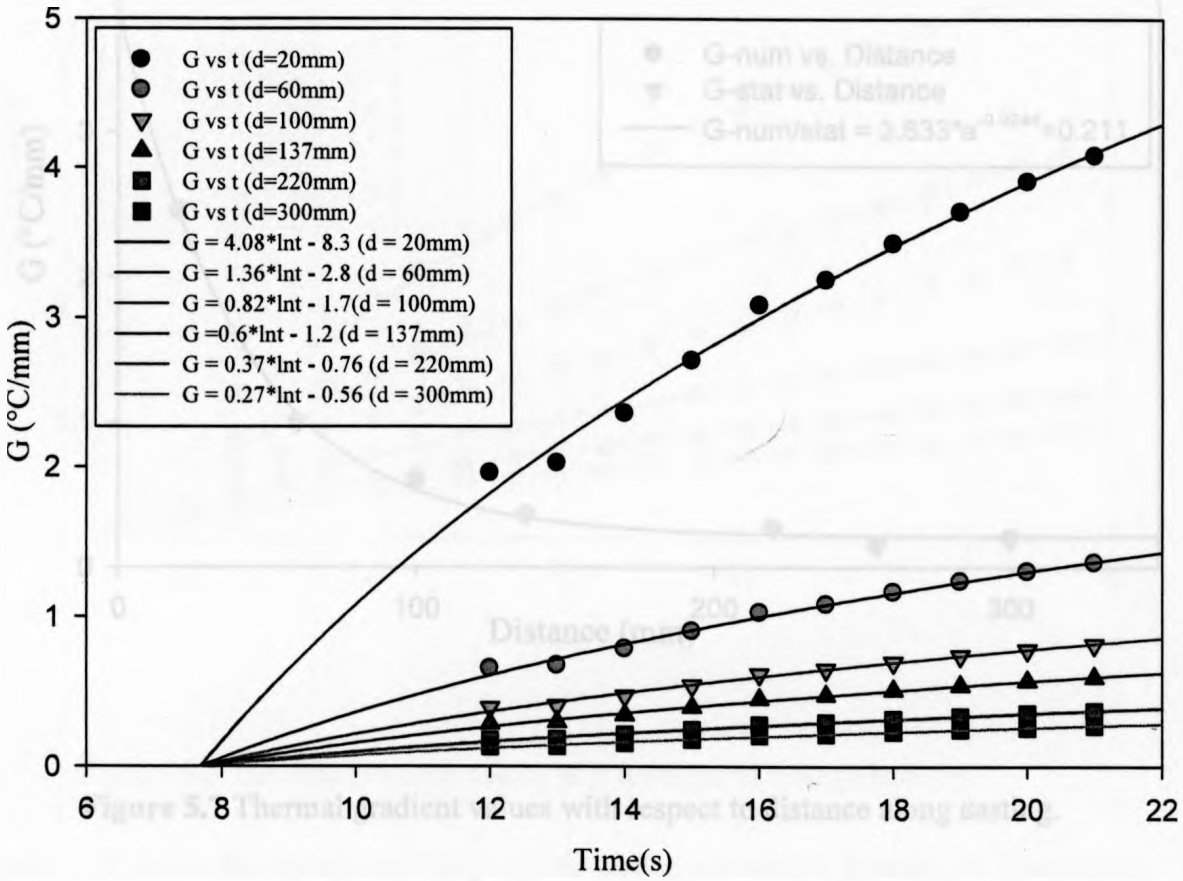

Figure 5.6 Thermal gradient values as a function of time (AM60B Sand casting).

Figure 5.6 shows the variation of the local thermal gradient as a function of time (in the freezing range). The instantaneous local thermal gradient is a monotonically increasing logarithmic curve with time. Thus, the local thermal gradient increases with time as the temperature drops from the liquidus point to the solidus point. The above plot is based on two main assumptions: a) the metal in mold exists in a mushy state; b) mold filling and solidification are two independent processes.

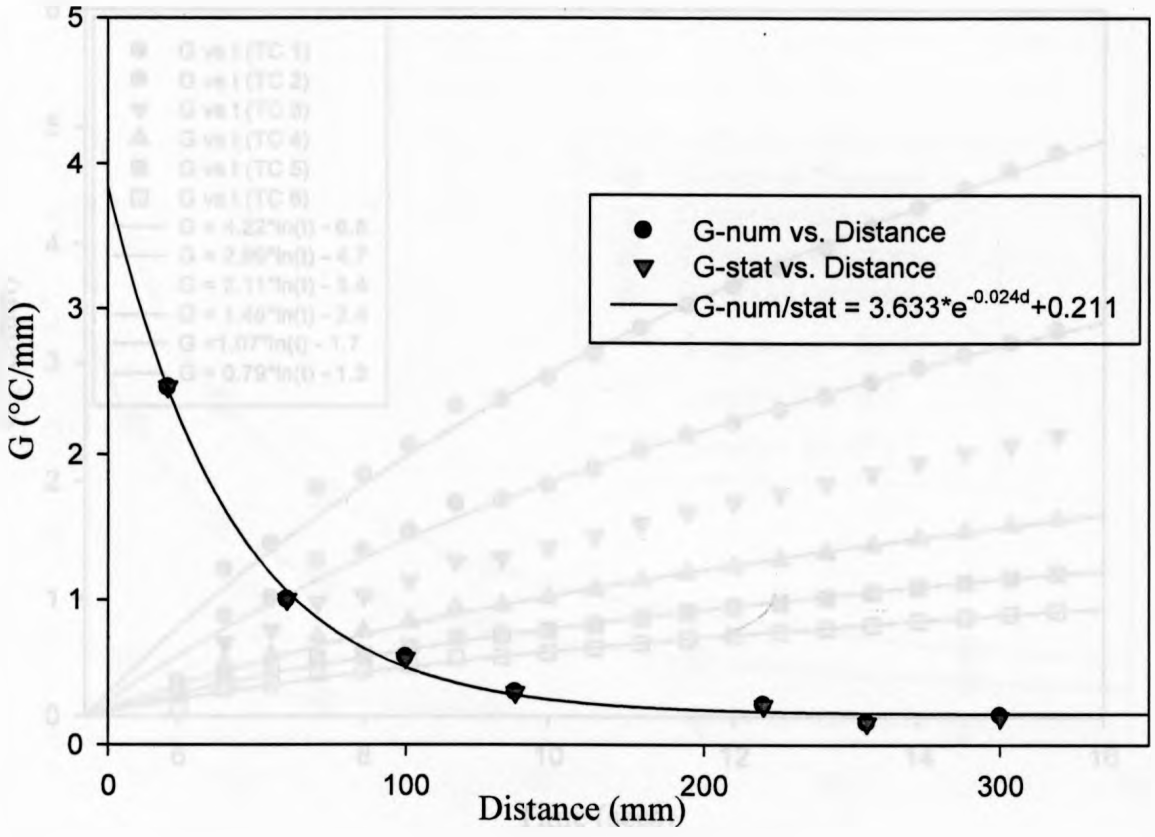

Figure 5.7 Thermal gradient values with respect to distance along casting.

Figure 5.7 represents the variation of the thermal gradient as a function of the distance from the cooling end. The thermal gradient was observed to decay exponentially with distance from the chill zone. The curve can be described by,

$$\textbf{G-stat/num} = \mathbf{3.633e^{-0.024d} + 0.211} \ldots\ldots (5.10)$$

where, ***G-stat/G-num*** is the statistical/numerical local thermal gradient.

The average gradient values, near the copper chill, are around 3.8-3.9 °C /mm

5.2.2.2Wedge casting- AM60B

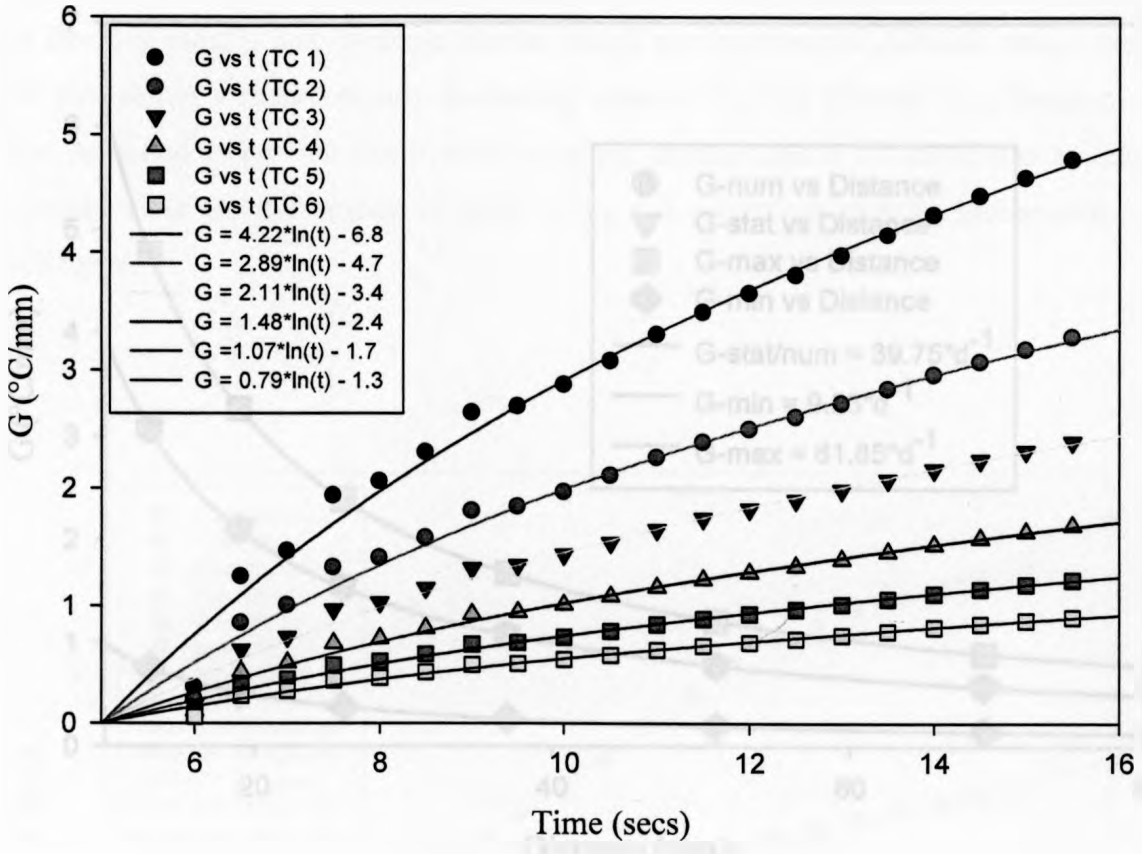

Figure 5.8 Thermal gradient values as a function of time (AM60B).

Figure 5.8 shows the variation of the local thermal gradient as a function of time values (in the freezing range) for the wedge casting. The variation of instantaneous local thermal gradient with time is a monotonically increasing logarithmic curve. Thus, the local thermal gradient increases with time as the temperature drops from the liquidus point to the solidus point. As mentioned for the sand casting, the above plot is based on two main assumptions: a) the metal in mold exists in a mushy state; b) mold filling and solidification are two independent processes.

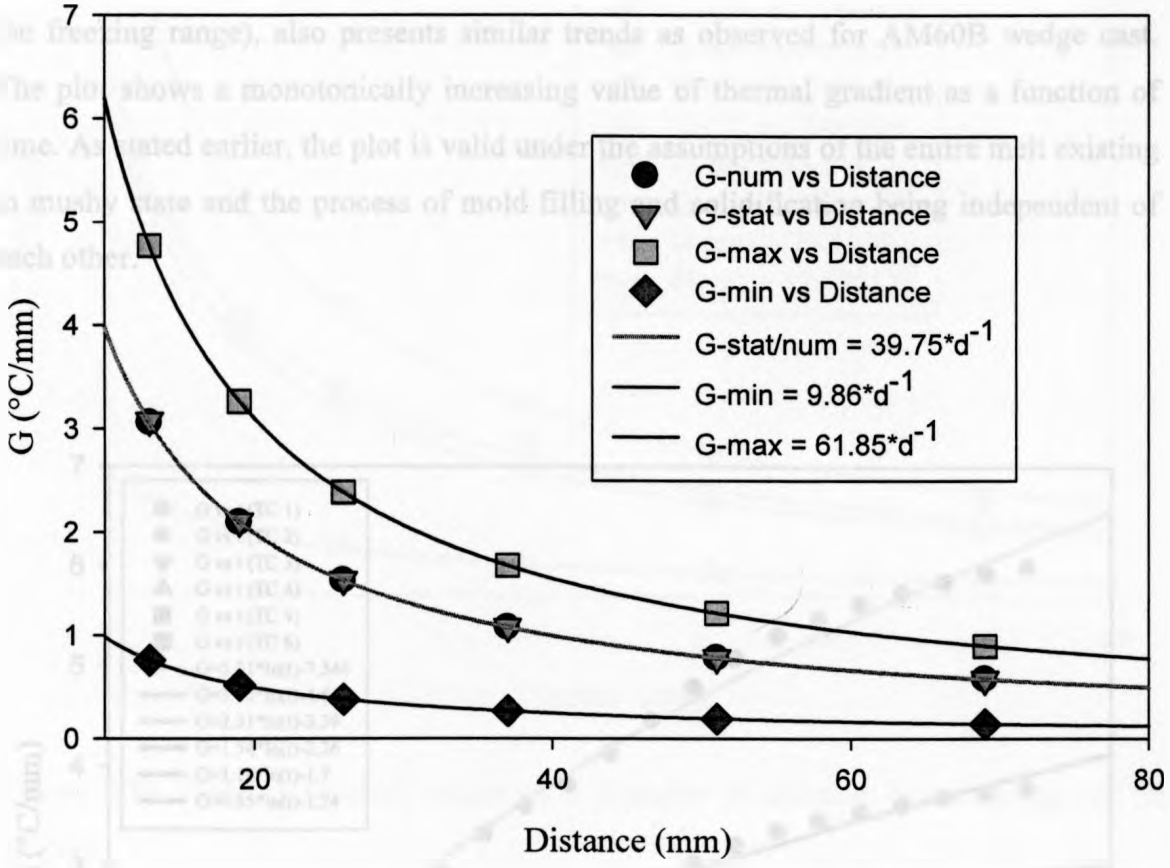

Figure 5.9 Thermal gradient values as a function of distance for AM60B wedge cast.

Figure 5.9shows the dependence of time-averaged local thermal gradient over the distance along the casting. The plot shows a monotonically decreasing curve that follows an inverse power law relationship. The variation can be empirically described by the below mentioned empirical equation. The curves describing maximum and minimum local thermal gradient bound the average gradient as shown in the plot.

$$\textbf{G-stat/num} = 39.75d^{-1} \quad \text{..... (5.11)}$$

where, **G-stat/num** is the statistical/numerical average local thermal gradient.

At d=0 the value of G is undefined, thus indicating that extremely high thermal gradients are expected near the wedge tip.

5.2.2.3 Wedge casting- AZ91D

Figure 5.10, showing the variation of instantaneous local thermal gradient with time (in the freezing range), also presents similar trends as observed for AM60B wedge cast. The plot shows a monotonically increasing value of thermal gradient as a function of time. As stated earlier, the plot is valid under the assumptions of the entire melt existing in mushy state and the process of mold filling and solidification being independent of each other.

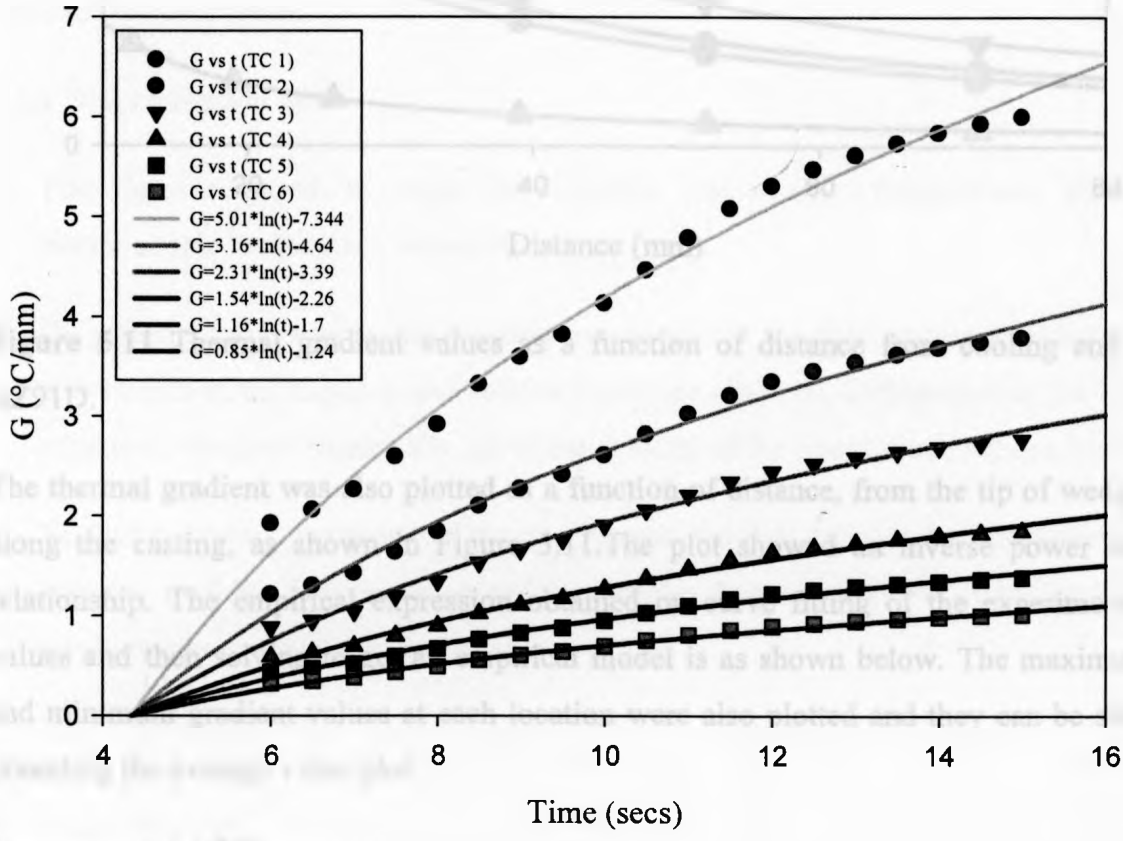

Figure 5.10 Thermal gradient values as a function of time for AZ91D (at different thermocouple locations).

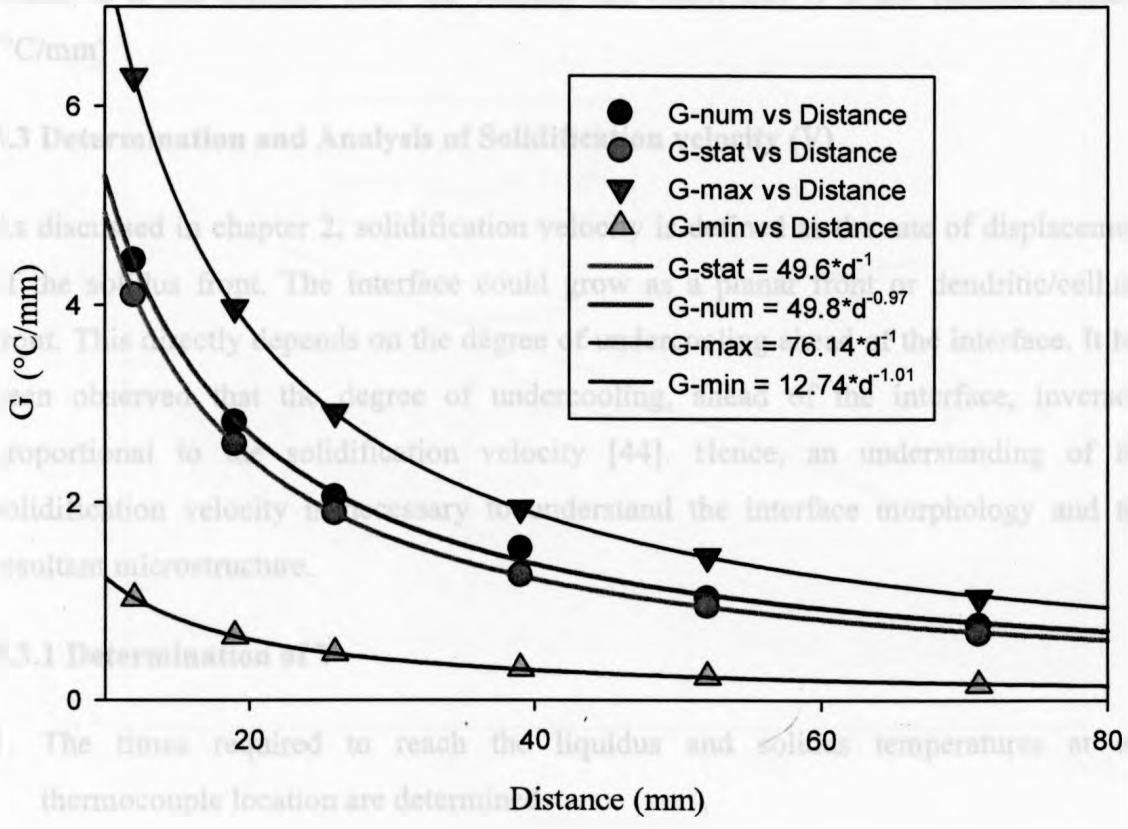

Figure 5.11 Thermal gradient values as a function of distance from cooling end for AZ91D.

The thermal gradient was also plotted as a function of distance, from the tip of wedge, along the casting, as shown in Figure 5.11.The plot showed an inverse power law relationship. The empirical expression obtained on curve fitting of the experimental values and then solving to get an empirical model is as shown below. The maximum and minimum gradient values at each location were also plotted and they can be seen bounding the average value plot.

$$\mathbf{G\text{-}num = 49.8d^{-0.97}} \quad \text{..... (5.12)}$$

$$\mathbf{G\text{-}stat = 49.6d^{-1}} \quad \text{..... (5.13)}$$

$$\mathbf{G\text{-}max = 76.14d^{-1}} \quad \text{..... (5.14)}$$

$$\mathbf{G\text{-}min = 12.74d^{-1.01}} \quad \text{..... (5.15)}$$

where, ***d*** is the distance from the cooling end (mm) and ***G*** is the thermal gradient (°C/mm)

5.3 Determination and Analysis of Solidification velocity (V)

As discussed in chapter 2, solidification velocity is defined as the rate of displacement of the solidus front. The interface could grow as a planar front or dendritic/cellular front. This directly depends on the degree of undercooling ahead of the interface. It has been observed that the degree of undercooling, ahead of the interface, inversely proportional to the solidification velocity [44]. Hence, an understanding of the solidification velocity is necessary to understand the interface morphology and the resultant microstructure.

5.3.1 Determination of V

1. The times required to reach the liquidus and solidus temperatures at each thermocouple location are determined.

2. On plotting the thermocouple location values against the time, curves describing the movements of the liquidus and solidus fronts are obtained. Differentiating the curve equations, obtained empirically, gives the velocity of the liquidus and solidus fronts.

3. To find the velocity at center of the mushy zone, the first derivative of the differential between liquidus front equation and the solidus front equation is determined. The resultant curves are plotted and analyzed.

5.3.2Analysis of V

This section discusses the variation of the solidus and liquidus fronts for the sand and the wedge castings. It describes the prevalent mushy zone characteristics and their effect on feeding.

5.3.2.1 Sand casting – AM60B

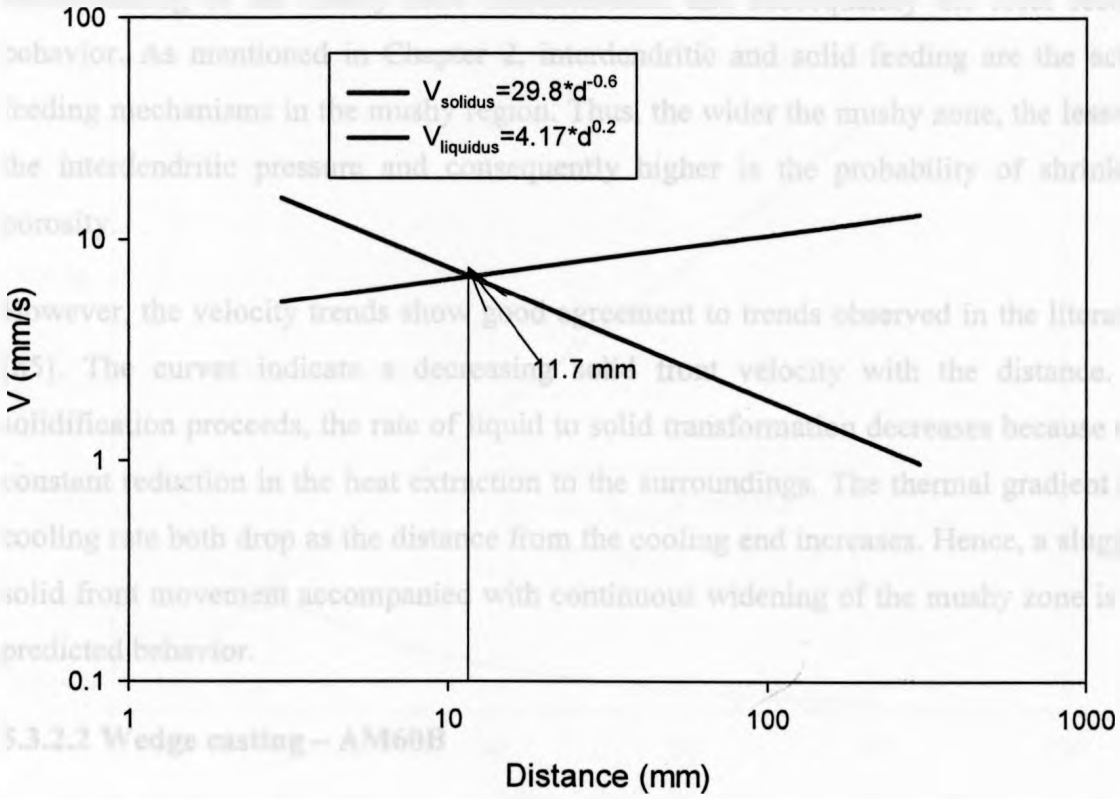

Figure 5.12 Solidus and liquidus velocity as a function of distance.

Figure 5.12 shows the variation of solidus and liquidus velocity as functions of distance. The solidus and liquidus front velocities can be described by

$$V_{solidus} = 29.8d^{-0.8} \quad .....(5.16)$$

$$V_{liquidus} = 4.17d^{0.2} \quad .....(5.17)$$

The separation between the data points lying on the liquidus front and solidus front velocity plots show a gradual yet consistent increase with increasing the distance values. This signifies the widening of the mushy zone as the distance from the cooling end increases. The solid front velocity decreases from 4.9 mm/s (at 20mm from chill)) to 0.97 mm/s (300mm from chill), whereas the liquidus front velocity shows very gradual variations, increasing from 7.6mm/s to 13 mm/s from thermocouple 1 to thermocouple 7. On extrapolating, the curves meet at 11.7 mm. This signifies the

location where the rate of change of mushy zone width is zero. This provides a better understanding of the mushy zone characteristics and subsequently the local feeding behavior. As mentioned in Chapter 2, interdendritic and solid feeding are the active feeding mechanisms in the mushy region. Thus, the wider the mushy zone, the lesser is the interdendritic pressure and consequently higher is the probability of shrinkage porosity.

However, the velocity trends show good agreement to trends observed in the literature [85]. The curves indicate a decreasing solid front velocity with the distance. As solidification proceeds, the rate of liquid to solid transformation decreases because of a constant reduction in the heat extraction to the surroundings. The thermal gradient and cooling rate both drop as the distance from the cooling end increases. Hence, a sluggish solid front movement accompanied with continuous widening of the mushy zone is the predicted behavior.

5.3.2.2 Wedge casting – AM60B

Figure 5.13 shows the variation of solidus and liquidus velocity with respect to the distance from the cooling end. The interface width changes as the solidification proceeds from the wedge tip to the base of the casting. It undergoes continuous compositional variations and phase transformations throughout the solidification process.

At any time t_o, the interface will consist of a solid boundary and a liquid boundary bounding a mushy zone in between. The plot indicates that as solidification proceeds, the solidus front velocity decreases, whereas the liquidus front velocity continues on an increasing trend. Therefore, a constant increase in the width of the mushy zone is observed. Initially, it is observed that the rate of change of mushy zone width is negative.

The instantaneous velocity of the liquidus reaches values around 50 mm/s at the region around thermocouple 6 and the velocity of the solidus comes down to values ranging between 0.9-1.3 mm/s at the same region.

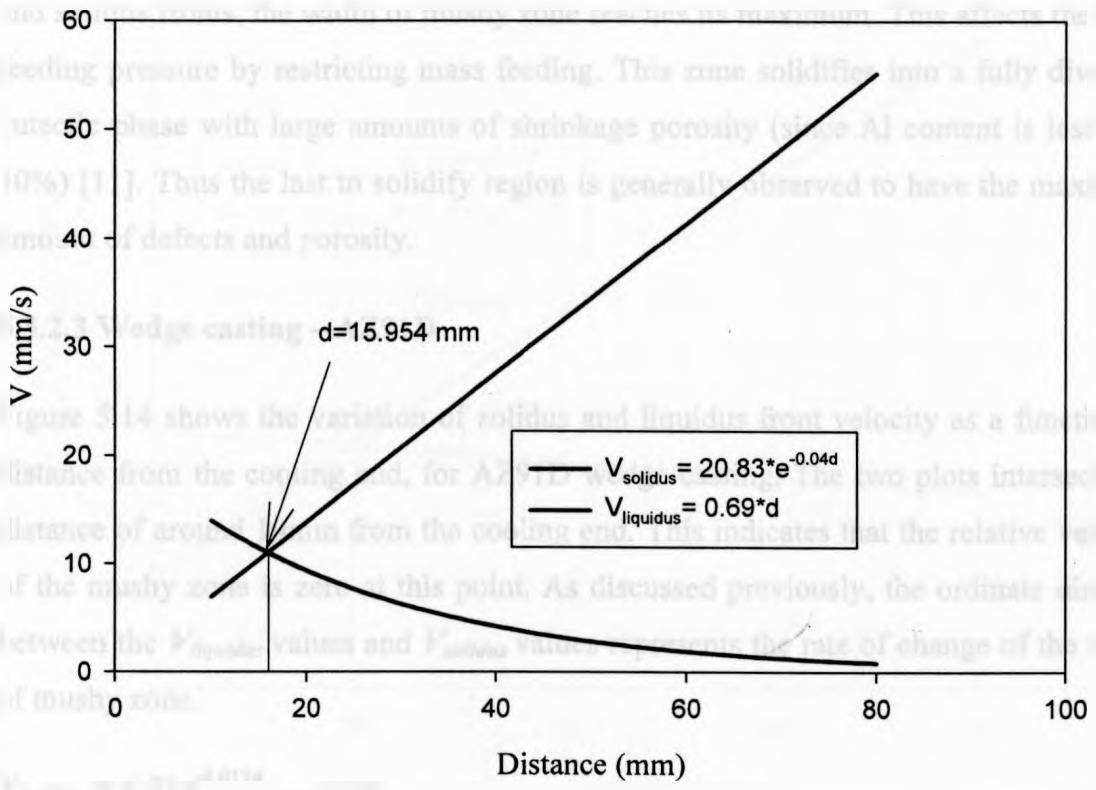

Figure 5.13 Solidus and liquidus front velocity as a function of distance for AM60B.

The distance between the points lying on V (liquidus) and V (solidus) represent the rate of change of width of the mushy zone. It can be seen that roughly at d (distance from the wedge tip) 16mm the rate of change of mushy zone width is zero.

The plot also indicates a linear variation of liquidus front velocity with distance but an exponentially decreasing curve for the case of solidus front velocity is given by

$$V_{liquidus} = 0.69d \quad \text{..... (5.18)}$$

$$V_{solidus} = 20.38e^{-0.04d} \quad \text{.... (5.19)}$$

where, V is the growth rate in mm/s and d is the distance from the cooling end (mm).

The maximum value of the solidus velocity is at the tip i.e. V (solidus) = 20.83 mm/s. At this point the value of liquidus velocity is zero. On moving towards the base

(d=140mm) the value of solidus velocity reduces to a value 0.08 mm/s while that of liquidus velocity becomes 96.6 mm/s. At such high differences between the liquidus and solidus fronts, the width of mushy zone reaches its maximum. This affects the local feeding pressure by restricting mass feeding. This zone solidifies into a fully divorced eutectic phase with large amounts of shrinkage porosity (since Al content is less than 10%) [11]. Thus the last to solidify region is generally observed to have the maximum amount of defects and porosity.

5.3.2.3 Wedge casting – AZ91D

Figure 5.14 shows the variation of solidus and liquidus front velocity as a function of distance from the cooling end, for AZ91D wedge casting. The two plots intersect at a distance of around 19mm from the cooling end. This indicates that the relative velocity of the mushy zone is zero at this point. As discussed previously, the ordinate distance between the $V_{liquidus}$ values and $V_{solidus}$ values represents the rate of change of the width of mushy zone.

$$V_{solidus} = 6.51e^{-0.012d} \quad \text{..... (5.20)}$$

$$V_{liquidus} = 0.6e^{0.11d} \quad \text{..... (5.21)}$$

The above equations describe the variation of solidus and liquidus front velocity with respect to distance from the cooling end, respectively. At the tip of the casting the solidus front velocity is about 6.5mm/s and the liquidus front velocity is only 0.6 mm/s. The width of the mushy zone becomes considerably large near the base of the wedge. With the remaining of the casting existing in a liquid-solid phase, there is a significant reduction in the feeding pressure. Thus the zone near the base is expected to be a sink for most of the casting defects and should exhibit the maximum amount of shrinkage porosity. Due to the continuous solute rejection during the solidification process from the tip to base, we have a high solute content (Al,Zn) at this end, leading to formation of partially divorced eutectic structures along with a very small percentage of granular eutectic phases.

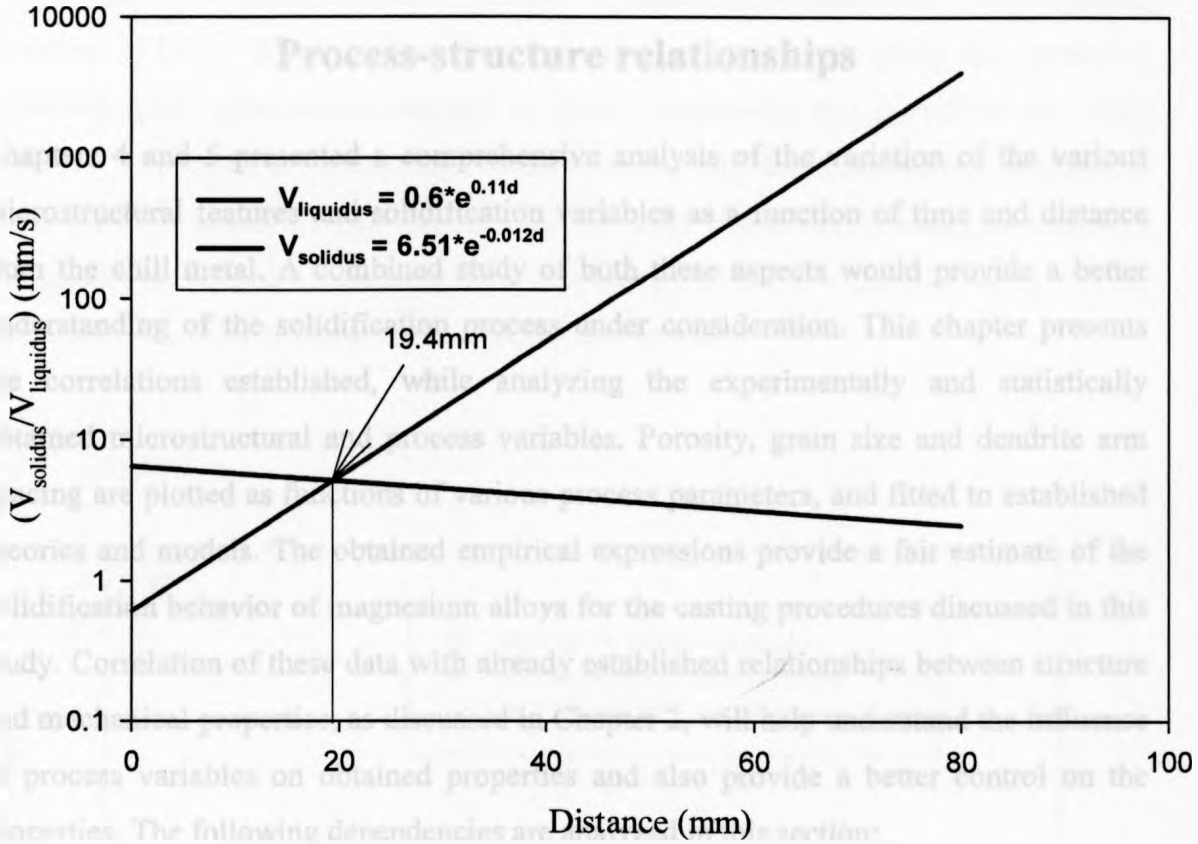

Figure 5.14 Liquidus and solidus velocity with respect to distance for AZ91D.

5.4 Summary

This chapter discussed the variation of the process parameters along the casting, presenting empirical expressions to describe their dependence on the distance along the casting. In the next chapter, these trends will be correlated with the microstructural variations to establish definite process-structure relationships.

Chapter 6

Process-structure relationships

Chapters 4 and 5 presented a comprehensive analysis of the variation of the various microstructural features and solidification variables as a function of time and distance from the chill metal. A combined study of both these aspects would provide a better understanding of the solidification process under consideration. This chapter presents the correlations established, while analyzing the experimentally and statistically obtained microstructural and process variables. Porosity, grain size and dendrite arm spacing are plotted as functions of various process parameters, and fitted to established theories and models. The obtained empirical expressions provide a fair estimate of the solidification behavior of magnesium alloys for the casting procedures discussed in this study. Correlation of these data with already established relationships between structure and mechanical properties, as discussed in Chapter 2, will help understand the influence of process variables on obtained properties and also provide a better control on the properties. The following dependencies are analyzed in this section:

1. Grain size as a function of the cooling rate, thermal gradient, solidification velocity and Niyama criteria.

2. Dendrite arm spacing as a function of the cooling rate, thermal gradient and solidification velocity.

3. Porosity as a function of the Niyama criteria and the feeding efficiency parameter

6.1 Sand casting-AM60B

Figures6.1 and 6.2 show the relative variation of the structural features and parameters affecting the solidification process as a function of distance from the cooling end. Comparing the plots indicates a coarsening grain size behavior with decreasing values of process variables. Both the secondary and tertiary dendrite arm spacing show a progressive increase with decrease in the cooling rate, thermal gradient and solidification velocity [86]. Such a dependency can be explained by the theory of arm

"coarsening", as described in Chapter 2, which states that the rate of heat extraction (i.e. cooling rate and thermal gradient) is the sole influencing parameter for arm spacing variation [47,87]. When the cooling rate is low, the arms along the preferred crystallographic orientations continue to grow, suppressing the growth of the other branches. The initial arms shooting out are very fine and fragile, eventually coarsening while growing further into the liquid. Thus the arms, which stop growing, re-melt into the liquid, consequently increasing the arm spacing due to a low rate of cooling. On the other hand, the ones growing become bigger and coarser.

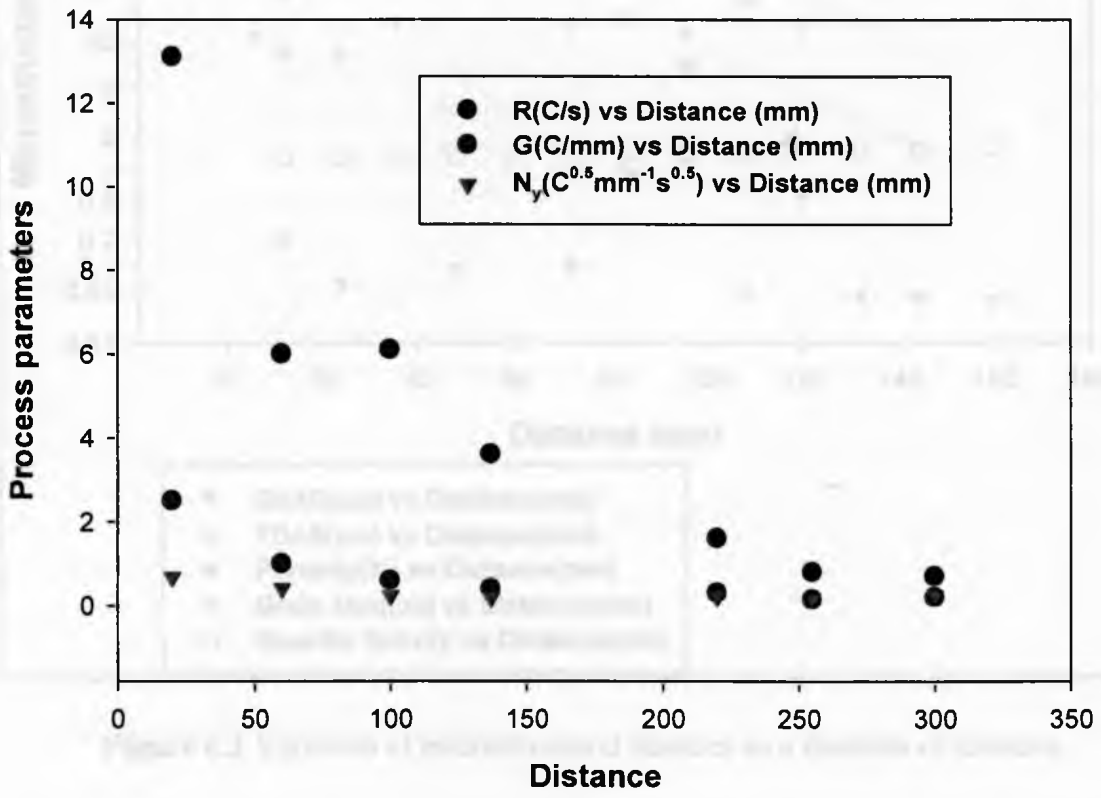

Figure 6.1 Variation of process parameters as a function of distance.

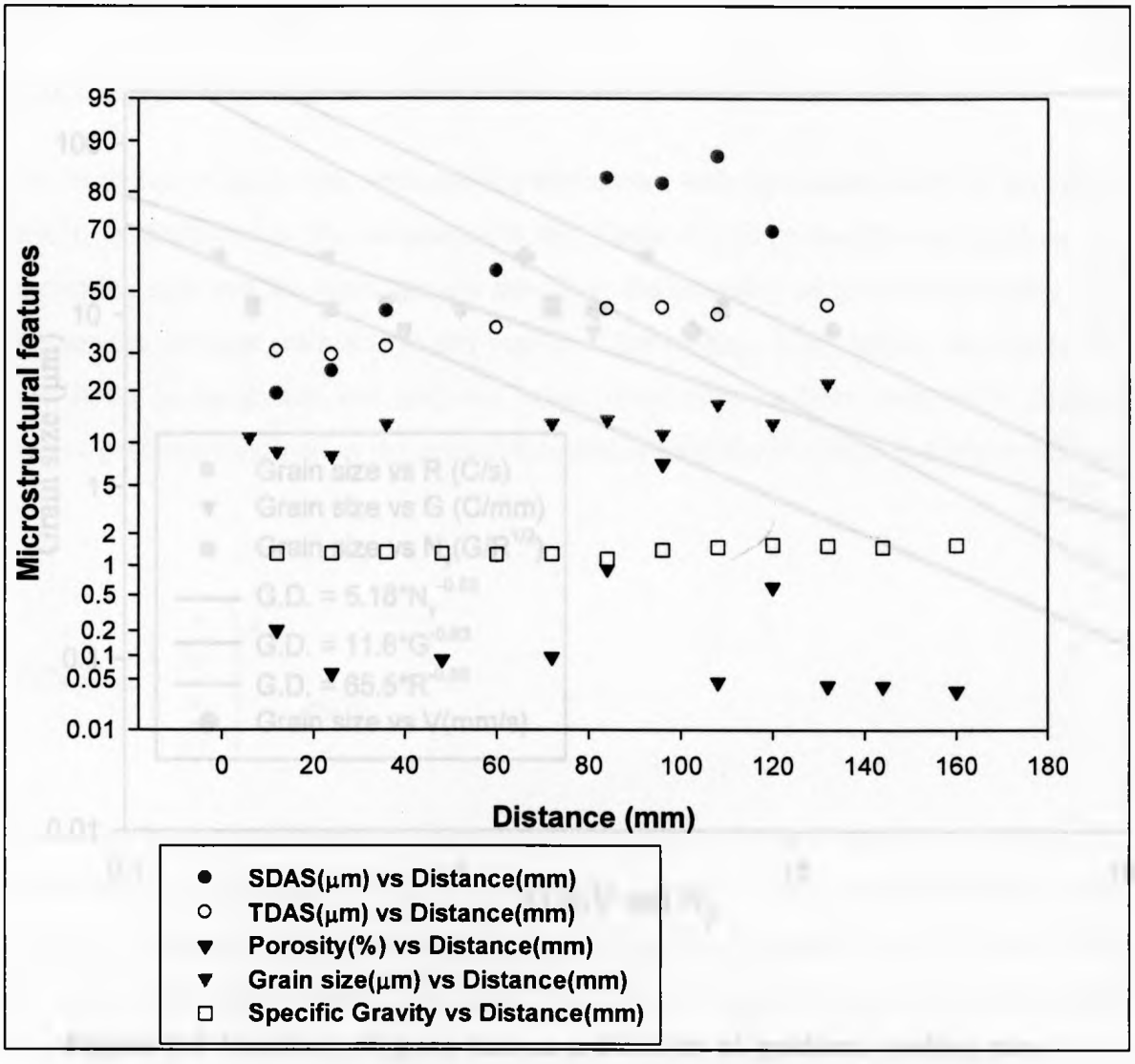

Figure 6.2 Variation of microstructural features as a function of distance.

6.1.1 Grain size vs. Process variables

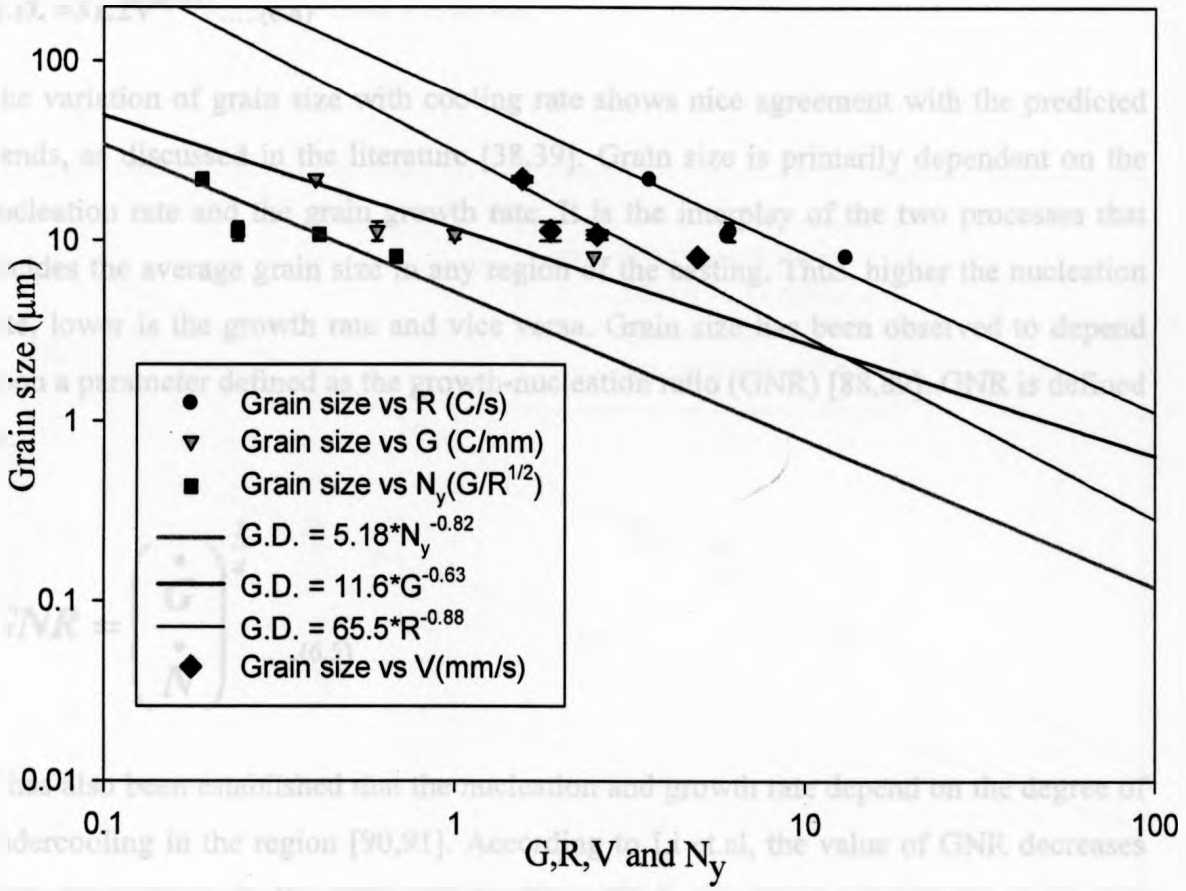

Figure 6.3 Variation of grain size as a function of gradient, cooling rate, solidification velocity and Niyama.

The grain size showed a nearly monotonic increase with distance along the casting. The average trend has been shown to have an exponential nature for this particular type of casting. Figure 6.3 presents the variation of grain size as a function of thermal gradient, cooling rate, growth velocity and the Niyama criterion. It shows an inverse power law dependency with respect to the above mentioned parameters. The curves on empirical fitting give the following expressions (Equations (6.1)-(6.4)):

$$G.D. = 65.5R^{-0.88} \quad .....(6.1)$$

$$G.D. = 11.6G^{-0.63} \quad .....(6.2)$$

$$G.D. = 5.18N_y^{-0.82} \quad .....(6.3)$$

$$G.D. = 31.2V^{-1.02} \quad .....(6.4)$$

The variation of grain size with cooling rate shows nice agreement with the predicted trends, as discussed in the literature [38,39]. Grain size is primarily dependent on the nucleation rate and the grain growth rate. It is the interplay of the two processes that decides the average grain size in any region of the casting. Thus, higher the nucleation rate, lower is the growth rate and vice versa. Grain size has been observed to depend upon a parameter defined as the growth-nucleation ratio (GNR) [88,89]. GNR is defined as:

$$GNR = \left(\frac{\dot{G}}{\dot{N}} \right)^{\frac{1}{4}} \quad .....(6.5)$$

It has also been established that the nucleation and growth rate depend on the degree of undercooling in the region [90,91]. According to Li et.al, the value of GNR decreases with the increase in the melt undercooling. They also proposed that the grain size increases as the value of GNR increases [91]. Thus, the grain size will decrease as the undercooling increases. The degree of undercooling ahead of the solid-liquid interface is directly proportional to G and inversely proportional to the solidification velocity (Equation (3.19)).

$\Delta T \alpha G/V$.....(6.6) [92,93]

On studying the influence of G, V and R (See appendix) on each other, it was observed that the parameters are interdependent. Therefore, the individual influence of G and V on the degree of undercooling is still subject to argument. Hence, the grain size cannot be confirmed to vary as independent functions of G and V as seen in Figure 6.3.

However, the combined effect should significantly influence the resultant grain size. According to Quested and Greer [94], the grain size is independent of G and V for a constant R. Hence, its dependency on the solidification variables, though more pronounced than porosity, is not completely clear.

6.1.2Arm spacing vs. Process variables

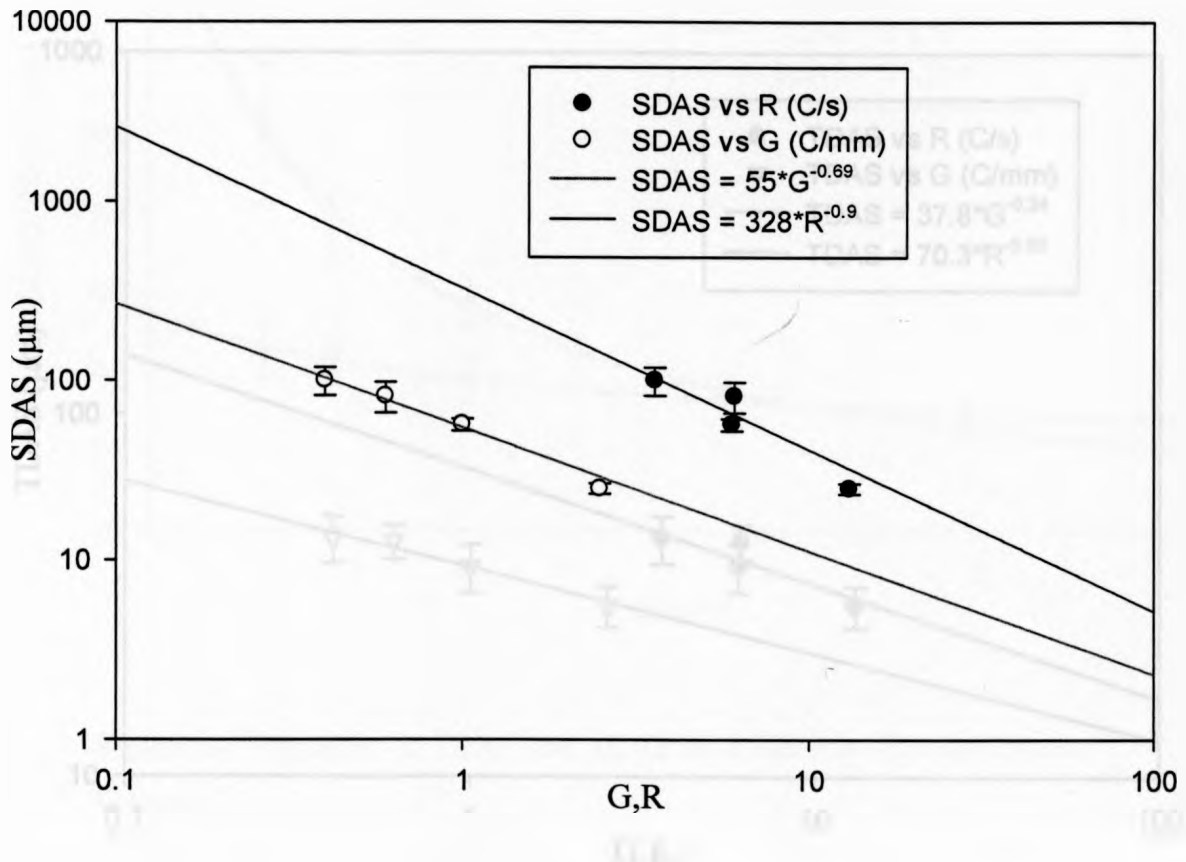

Figure 6.4 Variation of SDAS as a function of gradient and cooling rate.

Figure 6.4 shows the variation of SDAS with respect to cooling rate and thermal gradient. It is observed to vary inversely with both the parameters. This correlates well with the above explanation given for dendritic arm coarsening. The empirical relations between SDAS and G and R are given as

$$\mathbf{SDAS = 328R^{-0.9}} \quad .....(6.7)$$

$$\mathbf{SDAS = 55G^{-0.69}} \quad \text{.....(6.8)}$$

where, ***SDAS*** is the secondary dendrite arm spacing and ***G*** and ***R*** are the thermal gradient (°C/mm) and the cooling rate (°C/s), respectively.

Similar relations are observed in Figure 6.5, which presents the variation of TDAS as a function of G and R.

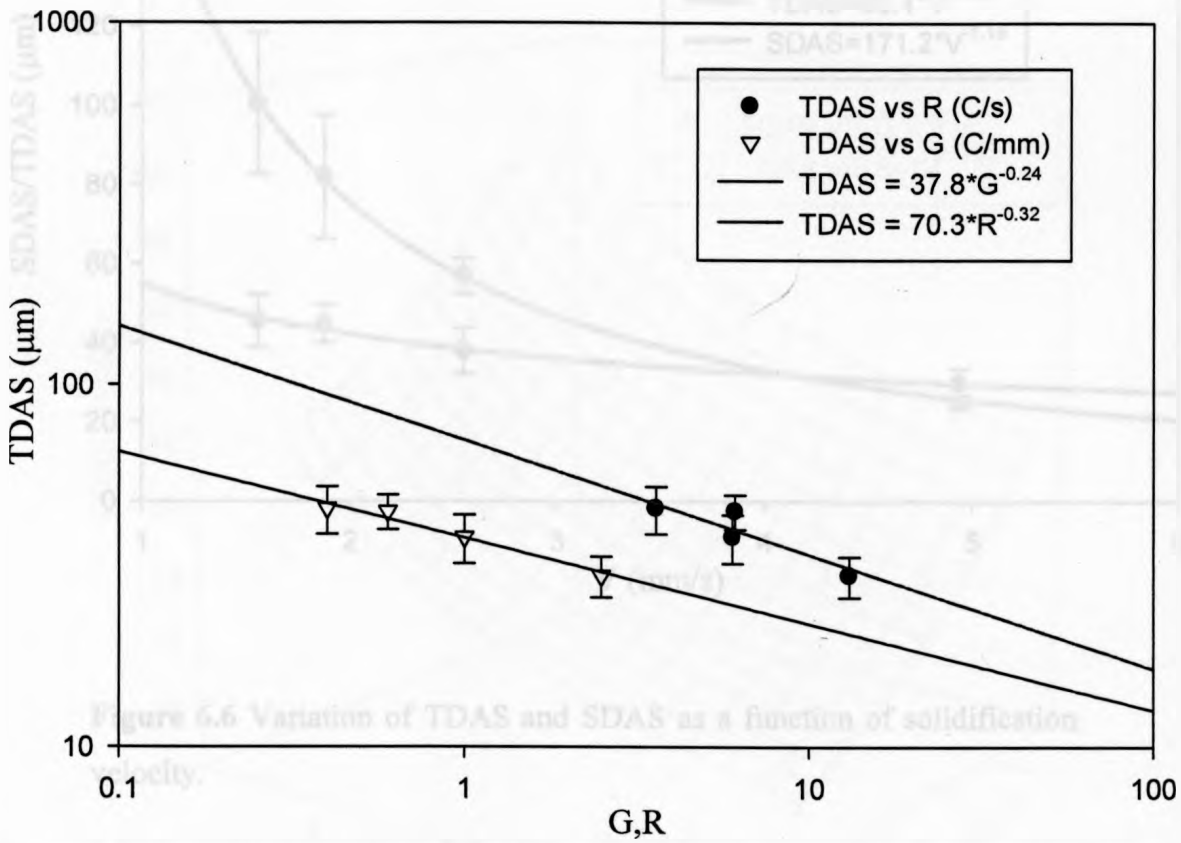

Figure 6.5 Variation of TDAS as a function of gradient and cooling rate.

The empirical relations between TDAS and G and R are given as

$$\mathbf{TDAS = 70.3R^{-0.32}} \quad \text{.....(6.9)}$$

$$\mathbf{TDAS = 37.8G^{-0.24}} \quad \text{.....(6.10)}$$

where, ***TDAS*** is the tertiary dendrite arm spacing and ***G*** and ***R*** are the thermal gradient (°C/mm) and the cooling rate (°C/s), respectively.

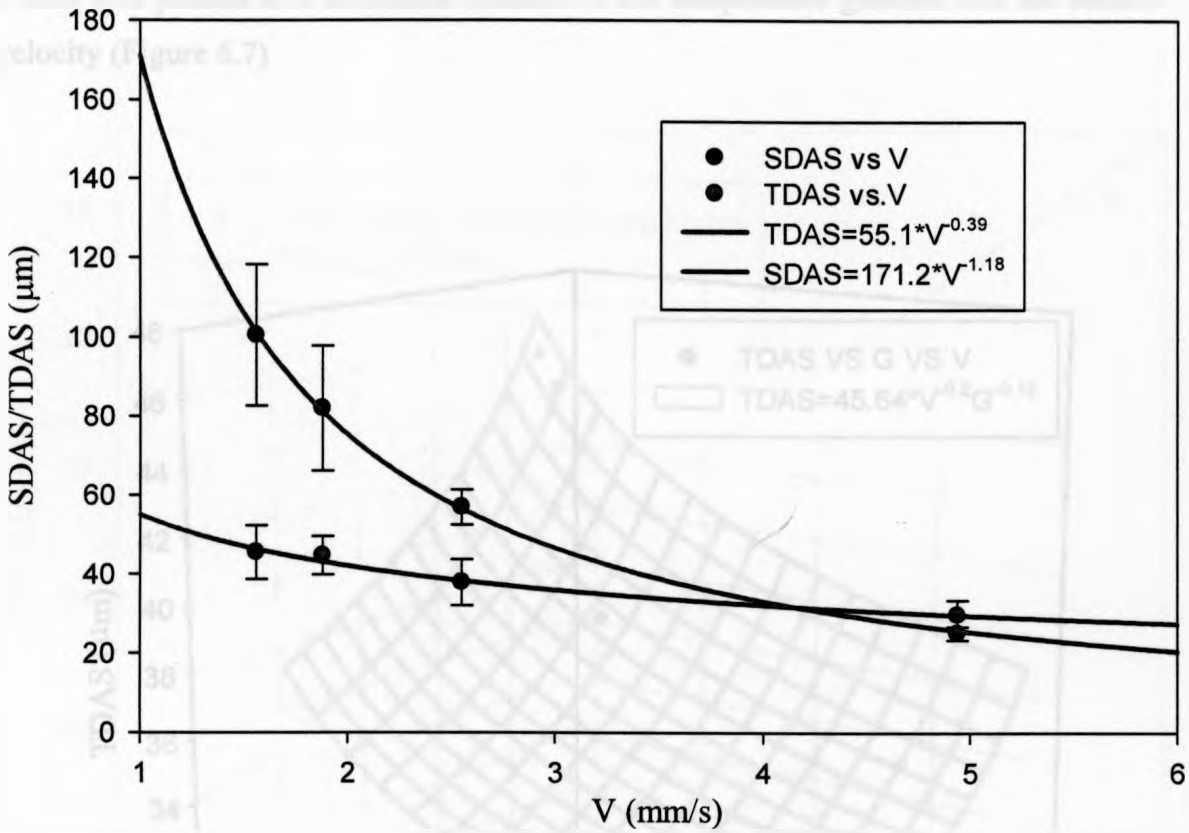

Figure 6.6 Variation of TDAS and SDAS as a function of solidification velocity.

Figure 6.6 shows the variation of SDAS and TDAS with respect to the solidification velocity. The obtained plots, when empirically fitted, showed inverse power law trends [86]. The relationship between SDAS and TDAS with solidification velocity can be expressed as:

$$\mathbf{SDAS = 171.2V^{-1.18}} \quad \text{.....(6.11)}$$

$$\mathbf{TDAS = 55.1V^{-0.39}} \quad \text{.....(6.12)}$$

where, V is the solidus growth velocity in mm/s. These results agree with the findings of Hunt-Lu and Kurz-Fisher [51-53], who established that arm spacing varies as inverse powers of G and V.

TDAS was plotted as a combined function of the temperature gradient and the solidus velocity (Figure 6.7)

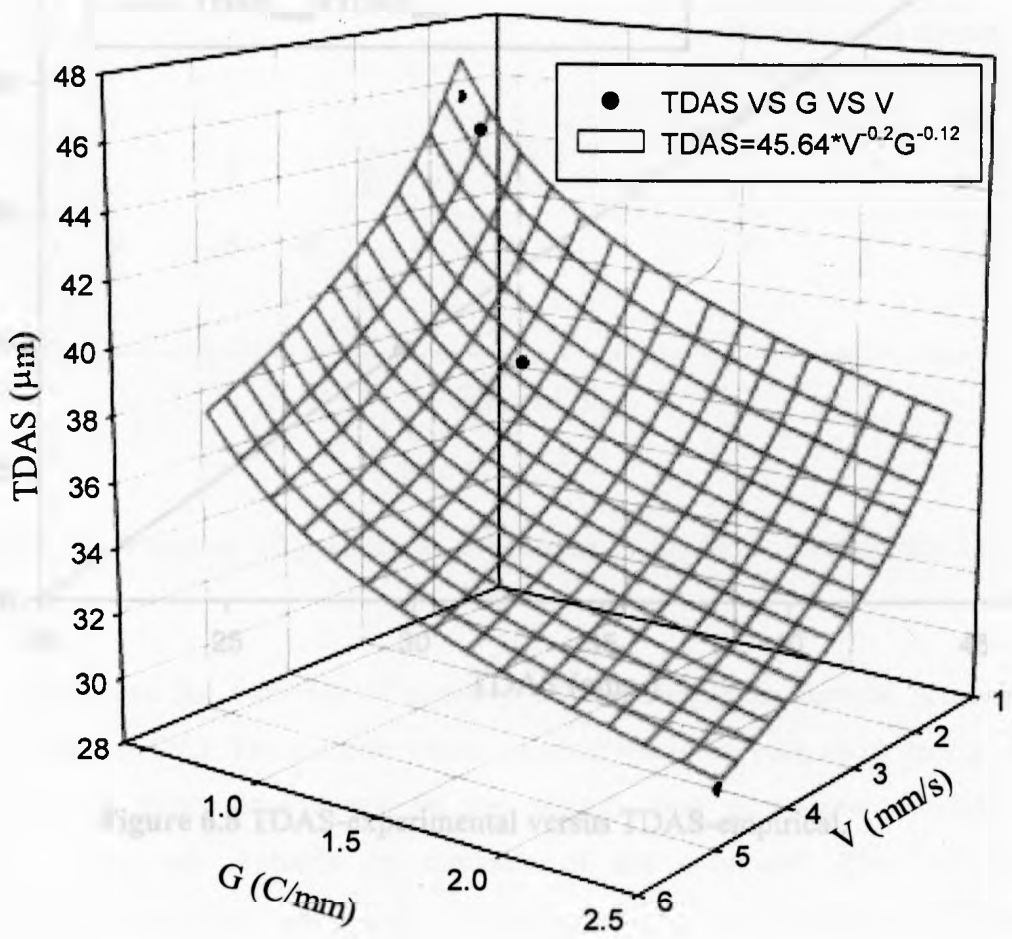

Figure 6.7 Variation of TDAS as a function of solidification velocity and gradient.

TDAS can be expressed as a combined function of G and V, as shown in Figure 6.7, as:

$$\mathbf{TDAS = 45.64G^{-0.12}V^{-0.2}} \quad .....(6.13)$$

This agrees with the previously established theories showing the dependence of arm spacing on gradient and growth velocity [51-53]. The empirical model and the experimental values show good correlation (Figure 6.8), hence further validating the predicted model.

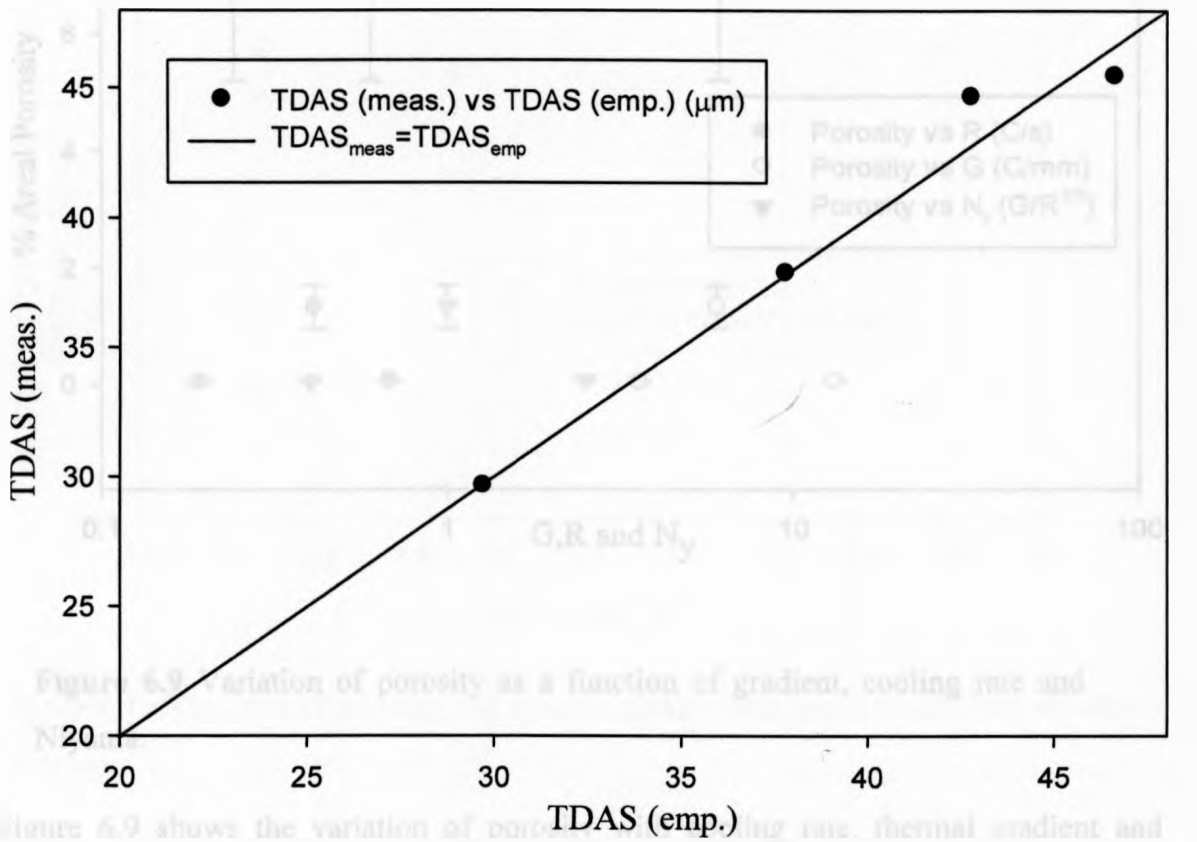

Figure 6.8 TDAS-experimental versus TDAS-empirical.

6.1.3 Porosity vs. Process variables

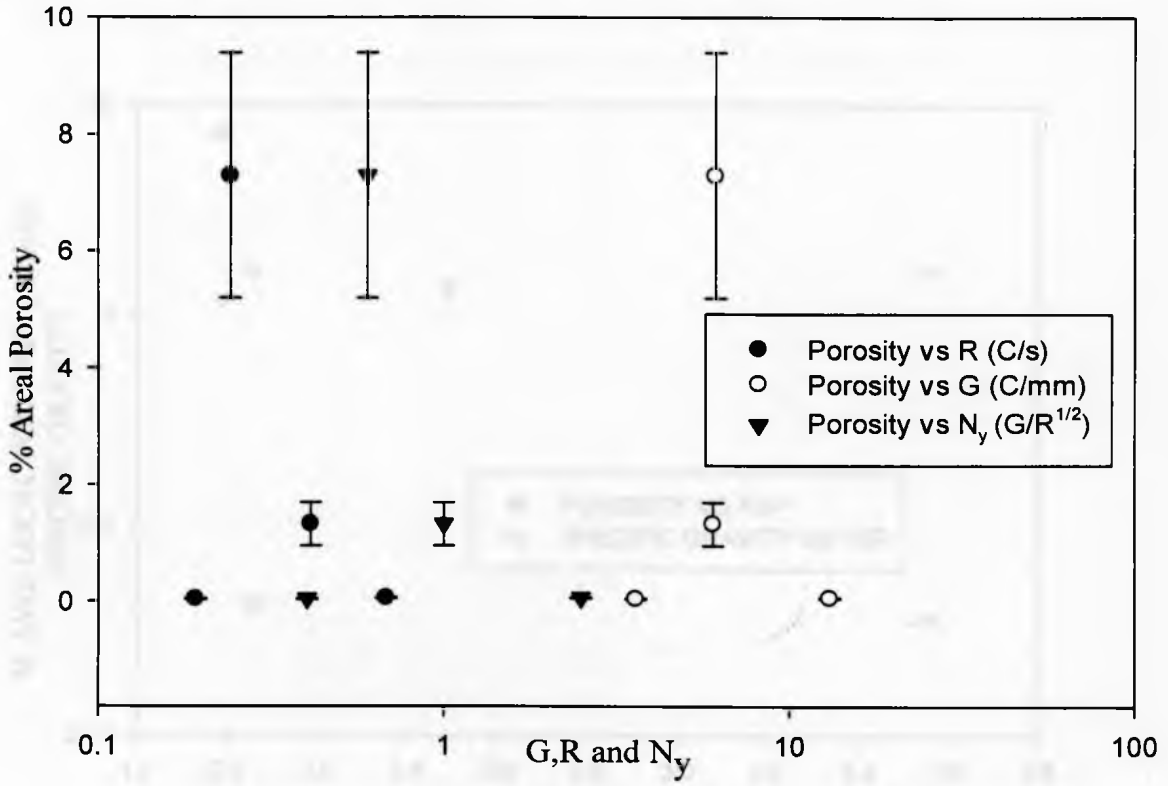

Figure 6.9 Variation of porosity as a function of gradient, cooling rate and Niyama.

Figure 6.9 shows the variation of porosity with cooling rate, thermal gradient and Niyama criterion (N_y). The porosity trends, as observed in the plot, show no significant indications of direct dependency on the solidification parameters (cooling rate, gradient). They are probably an outcome of the combined effect of various solidification parameters, along with alloy composition and microstructural features. Both the density plot and the porosity trend showed agreement with each other. In the above case, it was also observed that the Niyama criterion was not a good measure to quantify porosity in the casting. To further understand the factors influencing porosity, it was plotted with respect to the feeding efficiency parameter. Figure 6.10 shows the variation of porosity and specific gravity against the feeding efficiency parameter (*FEP*). It shows that with increasing values of *FEP*, a reduction in the porosity and an

increase in specific gravity are observed. These results indicate that the feeding efficiency is an important factor influencing the average local porosity.

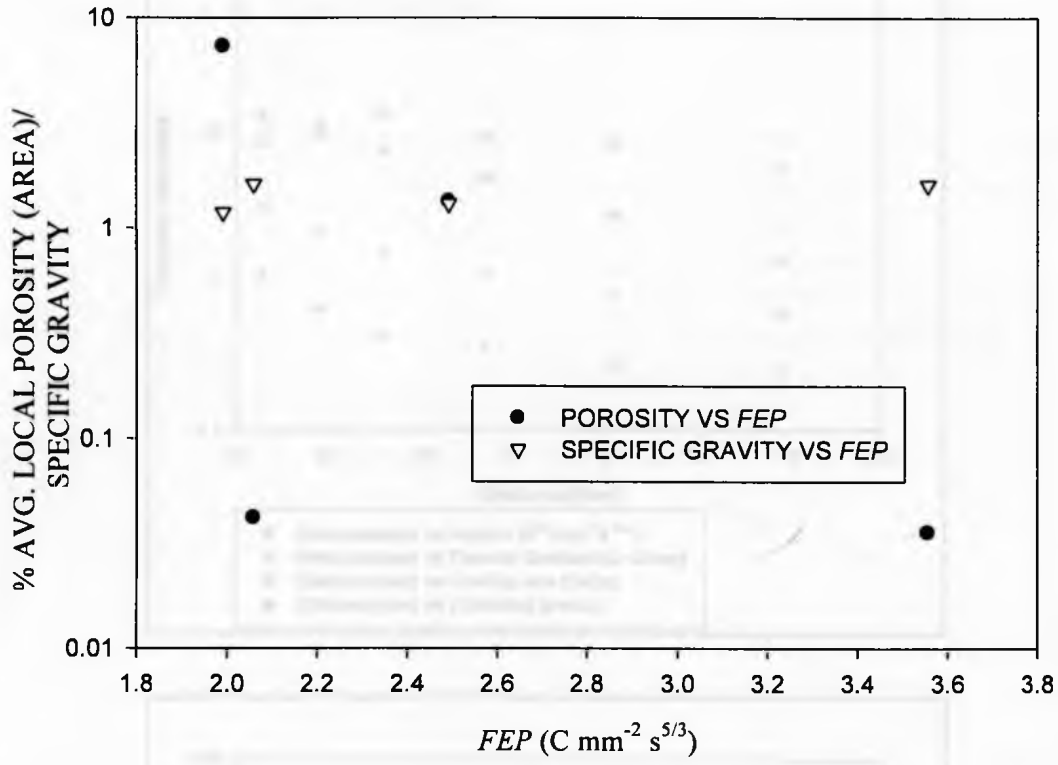

Figure 6.10 Variation of porosity and specific gravity with respect to feeding efficiency parameter.

A metallographic study of the casting indicated that the majority of porosity resembled shrinkage type and a few were gas induced shrinkage type. However, there was a negligible presence of purely gas pores throughout the cross-section of casting. This can be attributed to the casting shape. The analysis was carried out along the first step of the casting which can be assumed as thin long plate. Hence, the flow of liquid would be close to perfectly laminar in this region. Thus, there would be a very low probability of entrained gases.

6.2 Wedge casting-AM60B

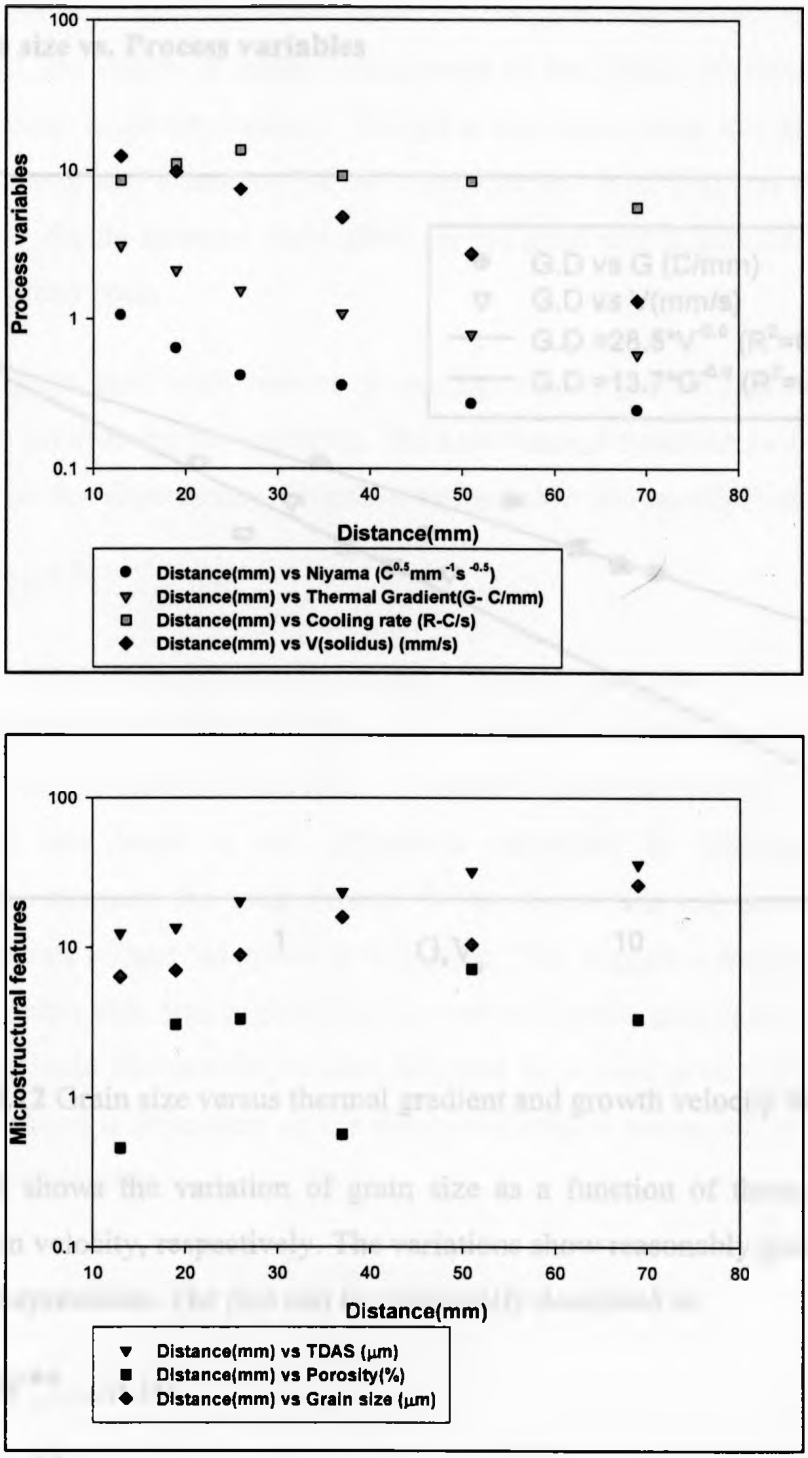

Figure 6.11 Process and Microstructural parameters as a function of distance for AM60B.

Figure 6.11 shows the dependence of process variables and microstructural features as a function of distance. Average grain size and arm spacing values show a steady increase with distance, whereas the G, $V_{solidus}$, R and Niyama values show a steady decrease.

6.2.1 Grain size vs. Process variables

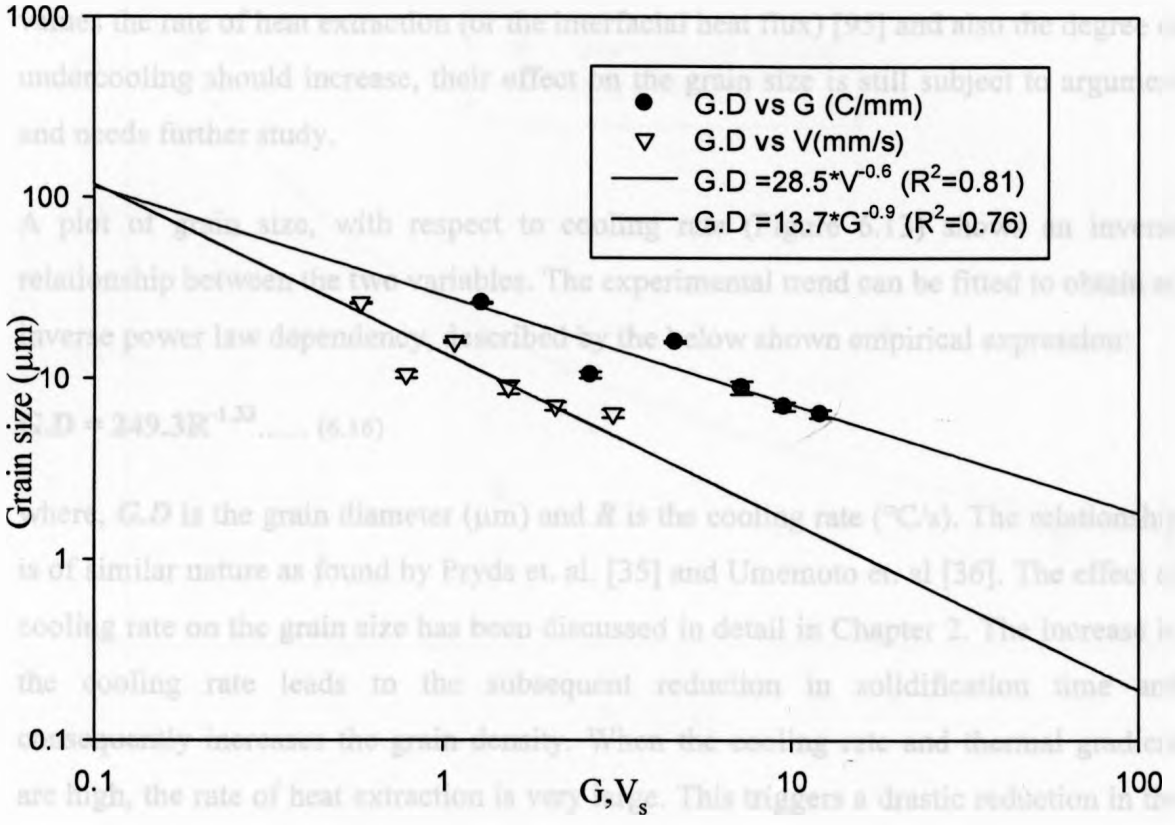

Figure 6.12 Grain size versus thermal gradient and growth velocity for AM60B.

Figure 6.12 shows the variation of grain size as a function of thermal gradient and solidification velocity, respectively. The variations show reasonably good fits to inverse power law expressions. The plot can be empirically described as:

$$\mathbf{G.D = 28.5V^{-0.6}} \quad \text{..... (6.14)}$$

$$\mathbf{G.D = 13.7G^{-0.9}} \quad \text{..... (6.15)}$$

where, ***G.D*** is the grain diameter (μm) and ***G*** is the thermal gradient (°C/s). The variation of grain size with thermal gradient and solidification velocity as independent parameters has not been given much attention, in the presently available literature. Hence, it is difficult to confirm their effect on the grain size. However, as discussed in section 6.1.1, the degree of undercooling ahead of the solidus interface depends on the ratio of gradient to growth velocity. Though it can be proposed that at higher G and V values the rate of heat extraction (or the interfacial heat flux) [95] and also the degree of undercooling should increase, their effect on the grain size is still subject to argument and needs further study.

A plot of grain size, with respect to cooling rate (Figure 6.13) shows an inverse relationship between the two variables. The experimental trend can be fitted to obtain an inverse power law dependency, described by the below shown empirical expression:

$$\mathbf{G.D = 249.3R^{-1.33}} \quad \text{..... (6.16)}$$

where, ***G.D*** is the grain diameter (μm) and ***R*** is the cooling rate (°C/s). The relationship is of similar nature as found by Pryds et. al. [35] and Umemoto et. al [36]. The effect of cooling rate on the grain size has been discussed in detail in Chapter 2. The increase in the cooling rate leads to the subsequent reduction in solidification time and consequently increases the grain density. When the cooling rate and thermal gradient are high, the rate of heat extraction is very large. This triggers a drastic reduction in the melt temperature at a rate, higher than the rate of transformation at equilibrium. This gives rise to large undercooling values followed by a rapid grain nucleation rate. The rate of nucleation is dependent on the number of critical nuclei, which is a function of the undercooling value.

$$n^* \propto e^{-\Delta G^*} \text{ and } \Delta G^* \propto \left(\frac{1}{\Delta T^2}\right) \quad \text{..... (6.17)}$$

$$\Rightarrow n^* \propto e^{-\left(\frac{1}{\Delta T^2}\right)}$$

where, n* is the number of critical nuclei per second, ΔG* is the nucleation free energy and ΔT is the undercooling value (°C). Grain size also shows an inverse proportionality

when plotted against the Niyama criterion. Figure 6.14 shows the variation of grain size with respect to Niyama criterion.

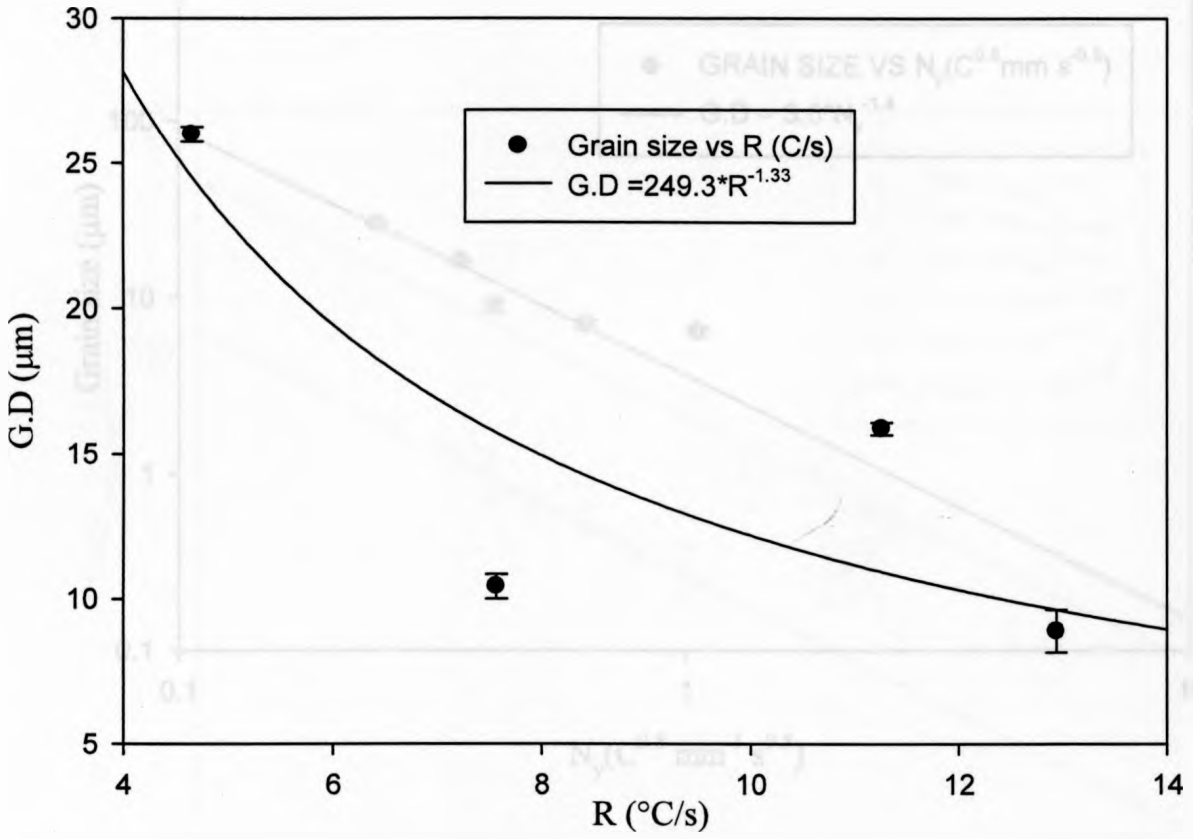

Figure 6.13 Grain size versus cooling rate for AM60B.

$$\mathbf{G.D = 3.6N_y^{-1.4}} \ldots\ldots (6.18)$$

where, ***G.D*** is the grain diameter (µm) and N_y is the Niyama criterion ($°C^{0.5}$ mm $s^{-0.5}$)

The variation of grain size with the Niyama value also shows an inverse power law dependency as seen in the case of cooling rate. The Niyama values range in between 1.1 to 0.2 as we move from thermocouple 1 to thermocouple 6. The influence of Niyama values on grain size can be primarily attributed to the effect of cooling rate on grain size and the interdependence of G, V and R (see the Appendix).

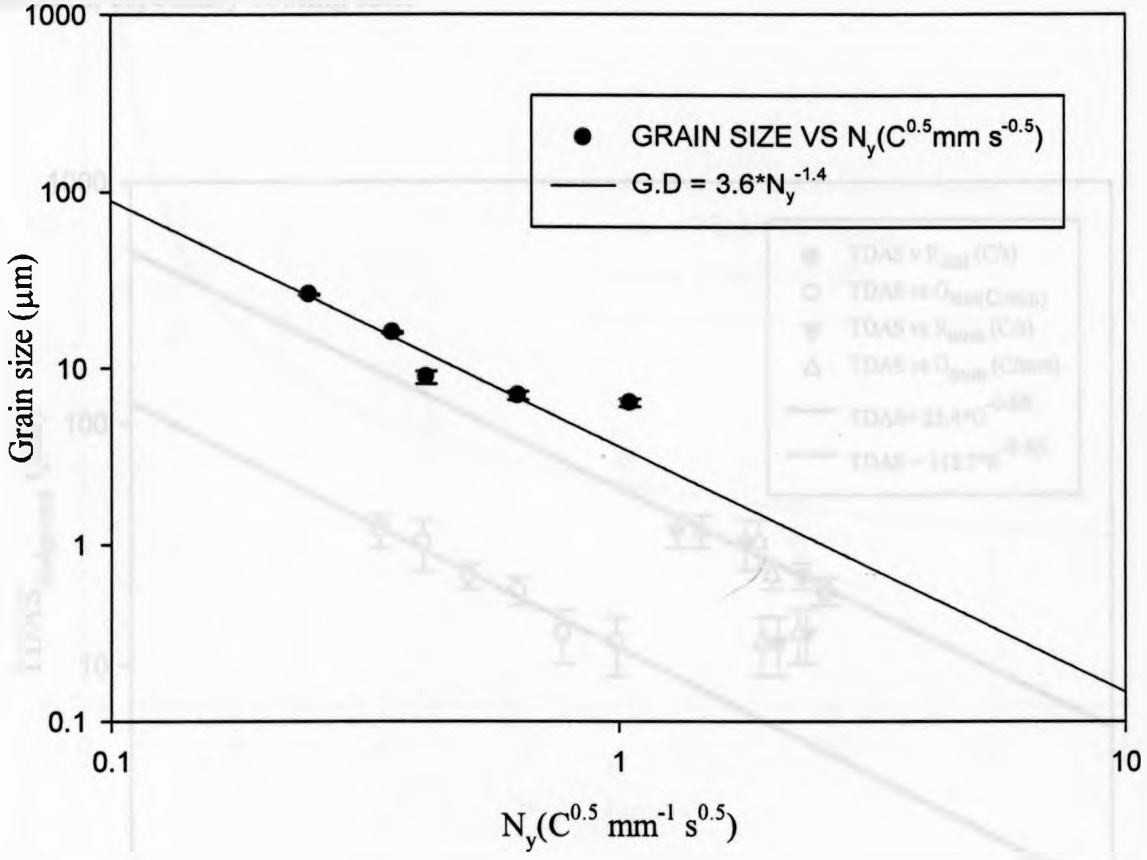

Figure 6.14 Grain size versus Niyama for AM60B.

6.2.2 Arm spacing vs. Process variables

The dendrite arm spacing has been observed to show strong dependence on the process parameters, especially cooling rate.

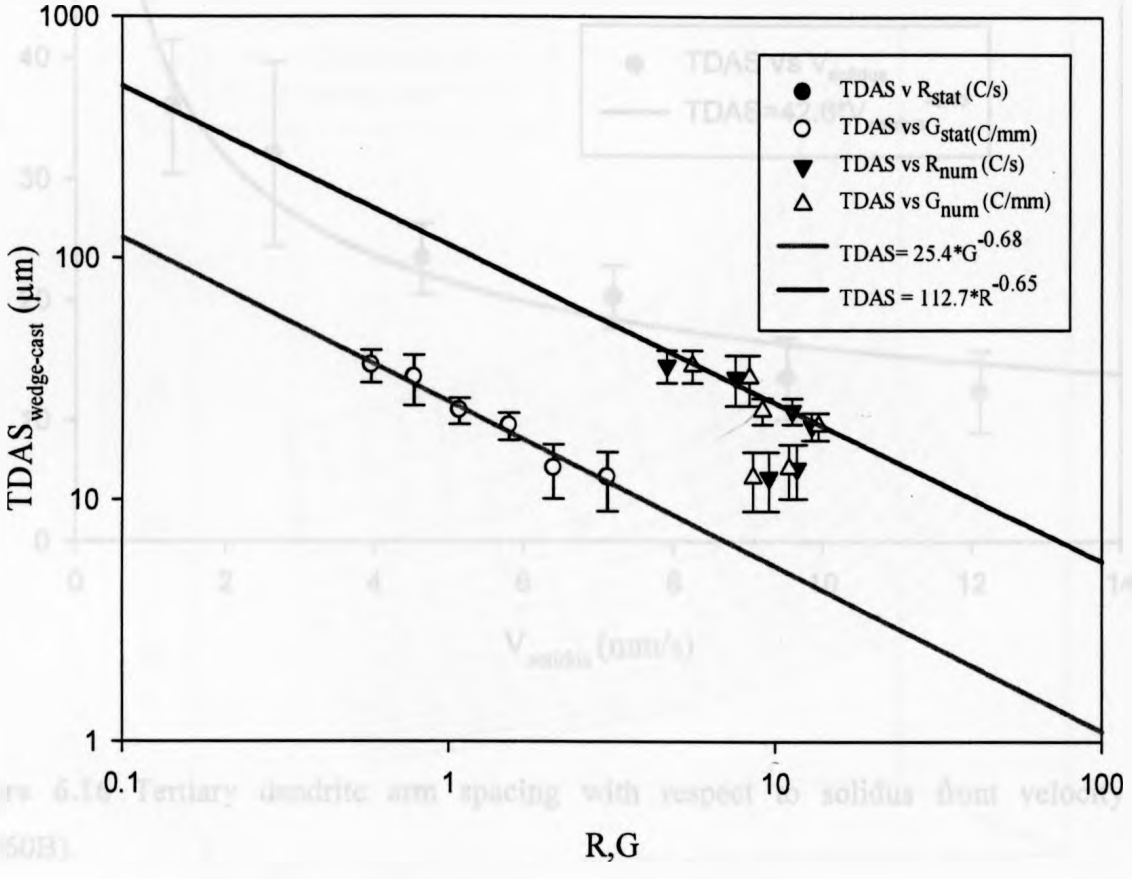

Figure 6.15 Tertiary dendrite arm spacing with respect to cooling rate and thermal gradient for AM60B.

Figure 6.15 represents the variation of tertiary dendrite arm spacing as a function of cooling rate and thermal gradient. The following empirical equations were obtained.

$$\mathbf{TDAS = 112.7R^{-0.65}} \quad \text{.....(6.19)}$$

$$\mathbf{TDAS = 25.4G^{-0.68}} \quad \text{.....(6.20)}$$

where, ***TDAS*** is the tertiary dendrite arm spacing (μm)

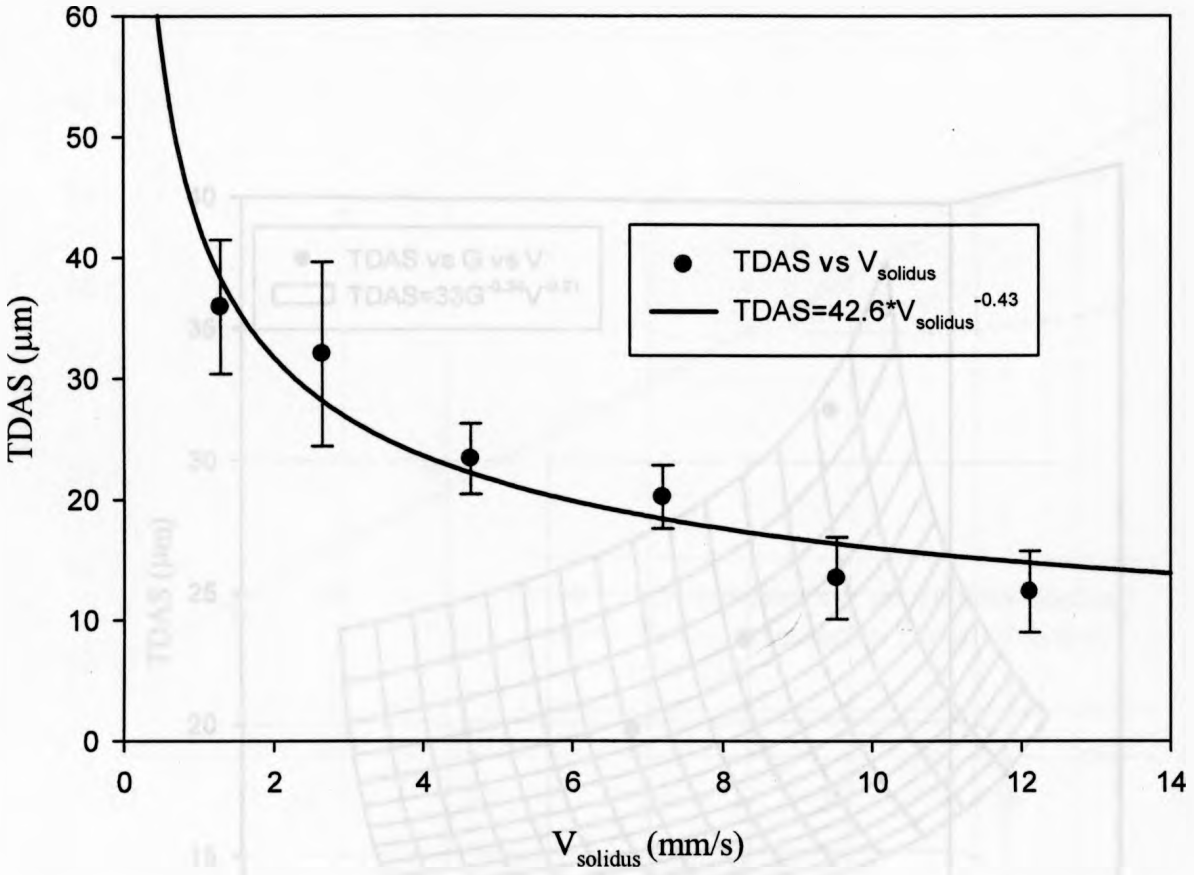

Figure 6.16 Tertiary dendrite arm spacing with respect to solidus front velocity (AM60B).

$$\mathbf{TDAS = 42.6V_{solidus}^{-0.43}} \quad .....(6.21)$$

Figure 6.16 presents the variation of TDAS with the solidification velocity. The variation of TDAS as a function of growth velocity also represents an inverse power law dependency, similar to the trends seen for arm spacing with respect to cooling rate and thermal gradient. The results show good agreement with the previously established trends between arm spacing and solidification velocity [51-53, 96]

TDAS can also be represented as a compound function of both G and R (Figure 6.17), as proposed by Hunt, Lu et.al, and Kurz-Fisher [51-53].

$$\mathbf{TDAS}_{\mathbf{empirical}} = 33G^{-0.34}V^{-0.21} \quad .....(6.22)$$

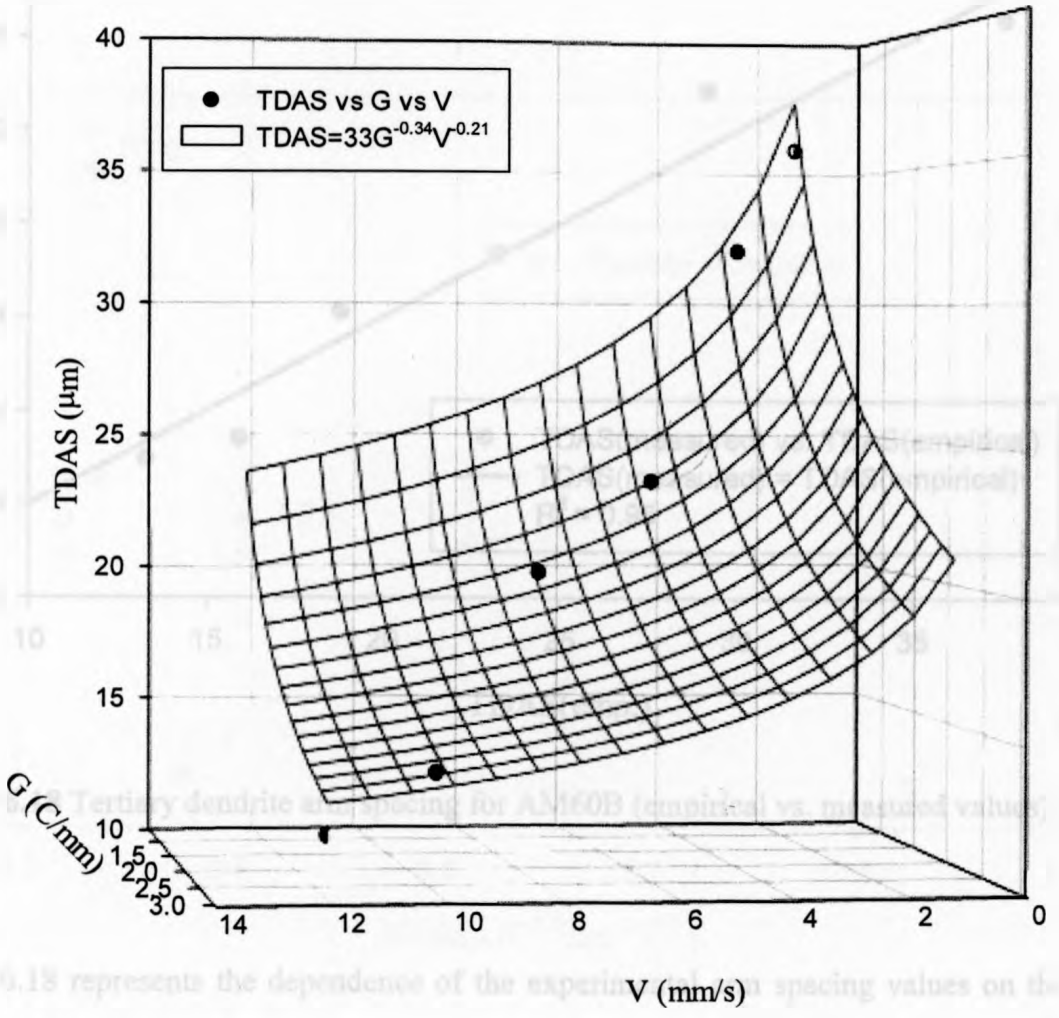

Figure 6.17 Tertiary dendrite arm spacing as function of gradient and growth velocity for AM60B.

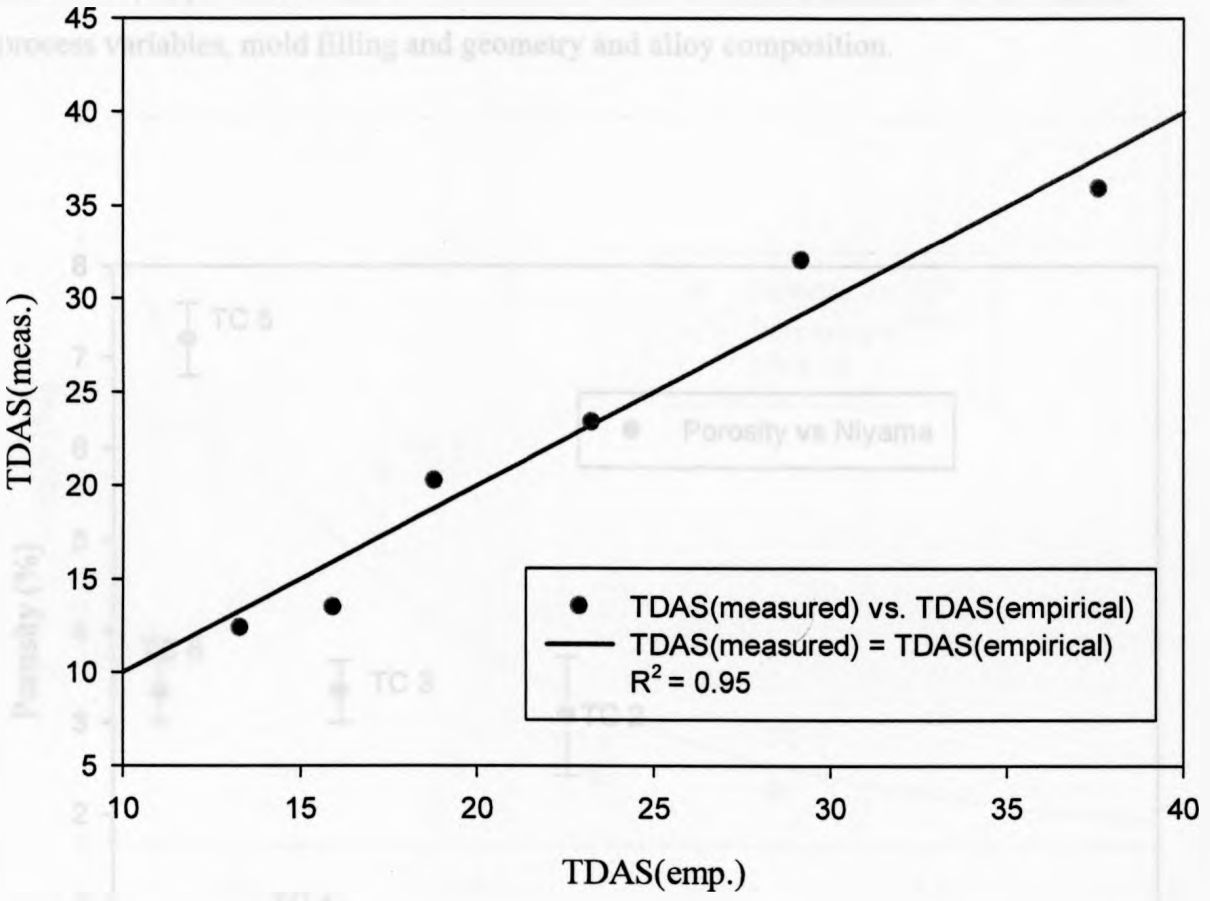

Figure 6.18 Tertiary dendrite arm spacing for AM60B (empirical vs. measured values).

Figure 6.18 represents the dependence of the experimental arm spacing values on the empirical data. The trends show an extremely good fit, which corroborates the predicted nature of dependence of tertiary dendrite arm spacing on the product of inverse powers of thermal gradient and the growth velocity.

6.2.3 Porosity vs. Process variables

The observed porosity trends are an outcome of the combined influence of the various process variables, mold filling and geometry and alloy composition.

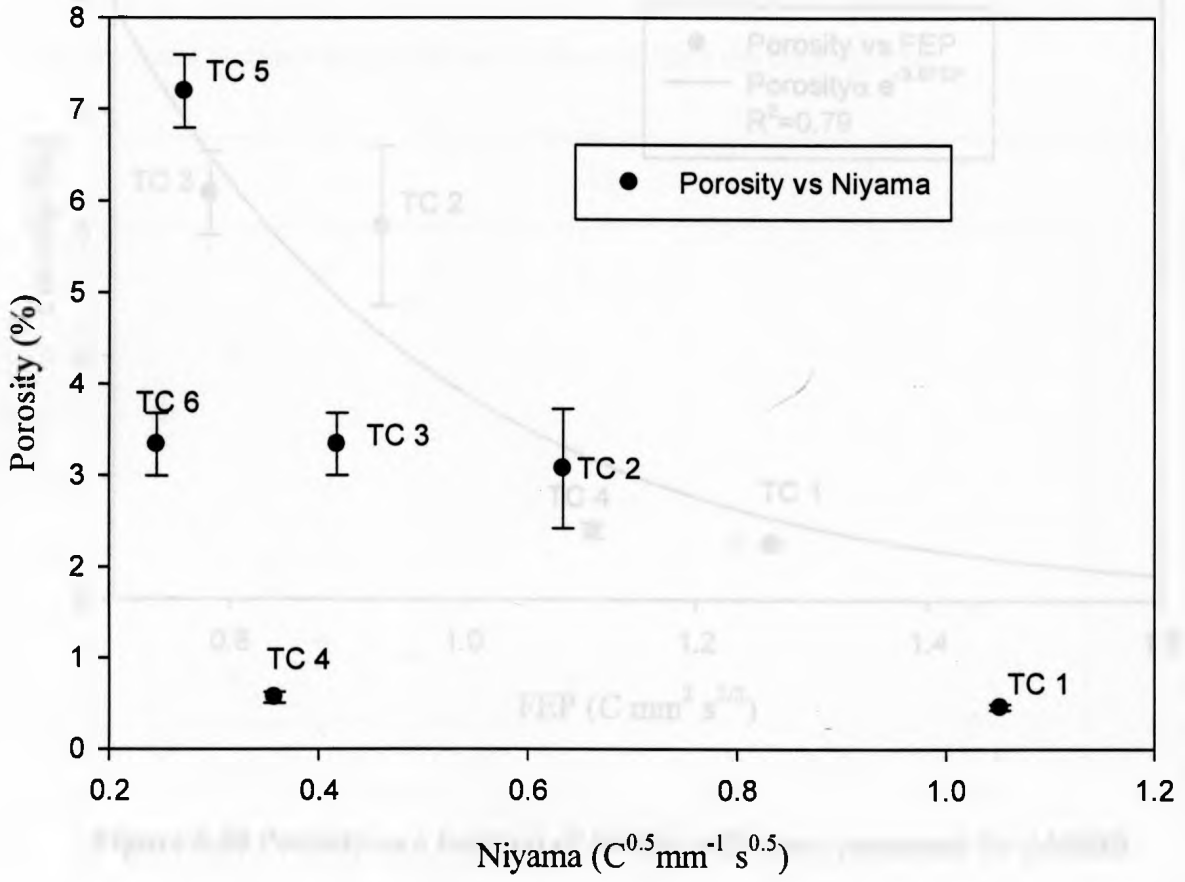

Figure 6.19 Porosity versus Niyama criteria for AM60B.

Figure 6.19 shows the variation of porosity with respect to Niyama values. The trends show a good agreement with the Niyama prediction methods, upto the 5th thermocouple (Porosity = 7.2%). Feeding has been observed to be the prime phenomenon to influence porosity distribution over a casting. Hence, the parameters affecting the feeding efficiency must show a strong effect on the porosity trends. As proposed by Lee, Chang et.al. [62], the feeding efficiency parameter (*FEP*) is defined as:

$$FEP = \frac{G * t^{2/3}}{V} \quad \text{.....(6.23)}$$

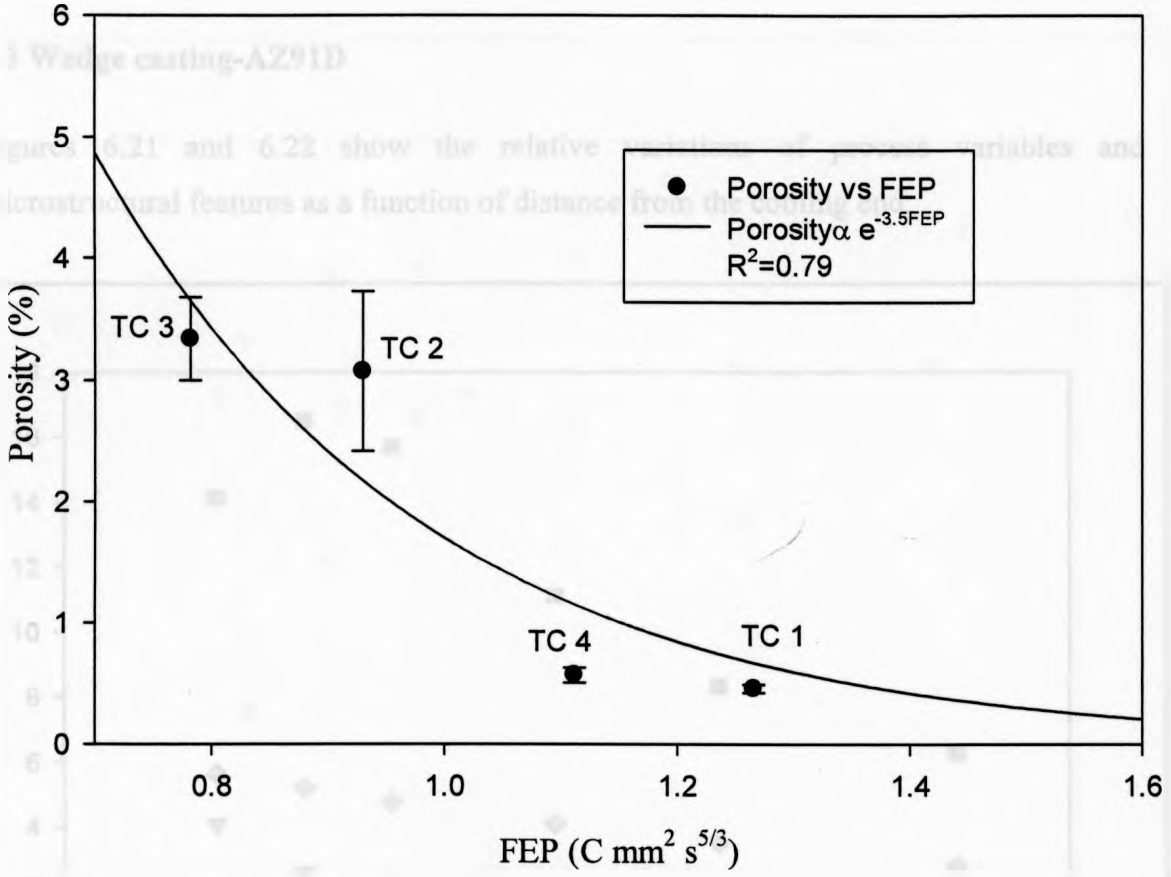

Figure 6.20 Porosity as a function of feeding efficiency parameter for AM60B.

The *FEP* (Figure 6.20) proves to be a considerably effective porosity prediction parameter up till the 4th thermocouple. However, it did not present agreeable values for the 5th and the 6th thermocouples, wherein the *FEP* values are as high as 1.5 and 3.0, respectively. It should be noted that *FEP* can only account for the shrinkage porosity in the region.

The complete efficiency of both the Niyama criterion and the *FEP* can be realized only if the effect of mold filling technique and the rate of metal filling on the solidification process are considered. Figure 4.19 showed a considerable amount of gas porosity in

the regions near the 5th and 6th thermocouple. This also indicates that the nature of porosity is mixture of gas and shrinkage around the 5th and 6th thermocouples. This might be the probable explanation behind the disagreement between the porosity and *FEP* values in these regions.

6.3 Wedge casting-AZ91D

Figures 6.21 and 6.22 show the relative variations of process variables and microstructural features as a function of distance from the cooling end.

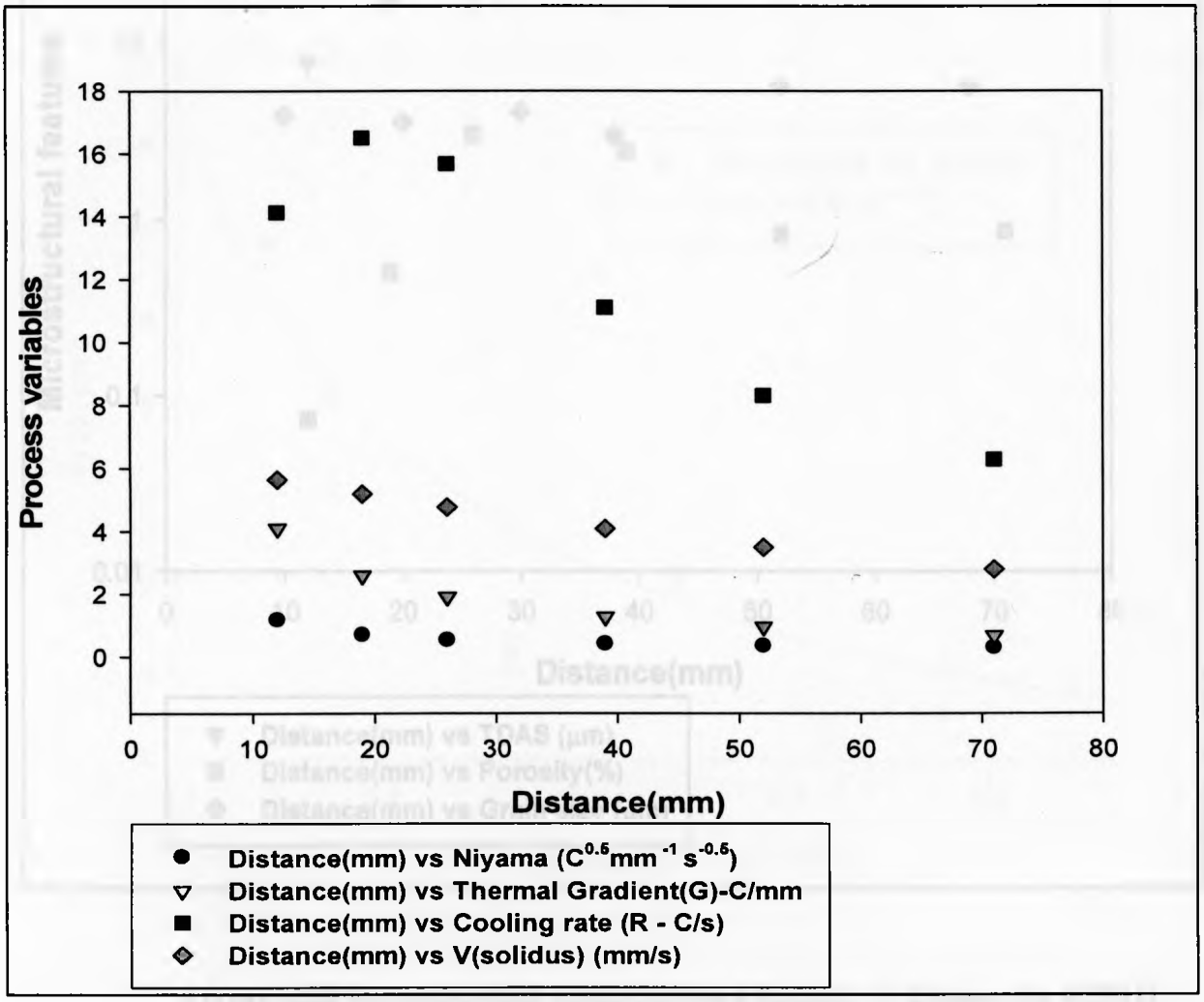

Figure 6.21 Process parameters as a function of distance for AZ91D.

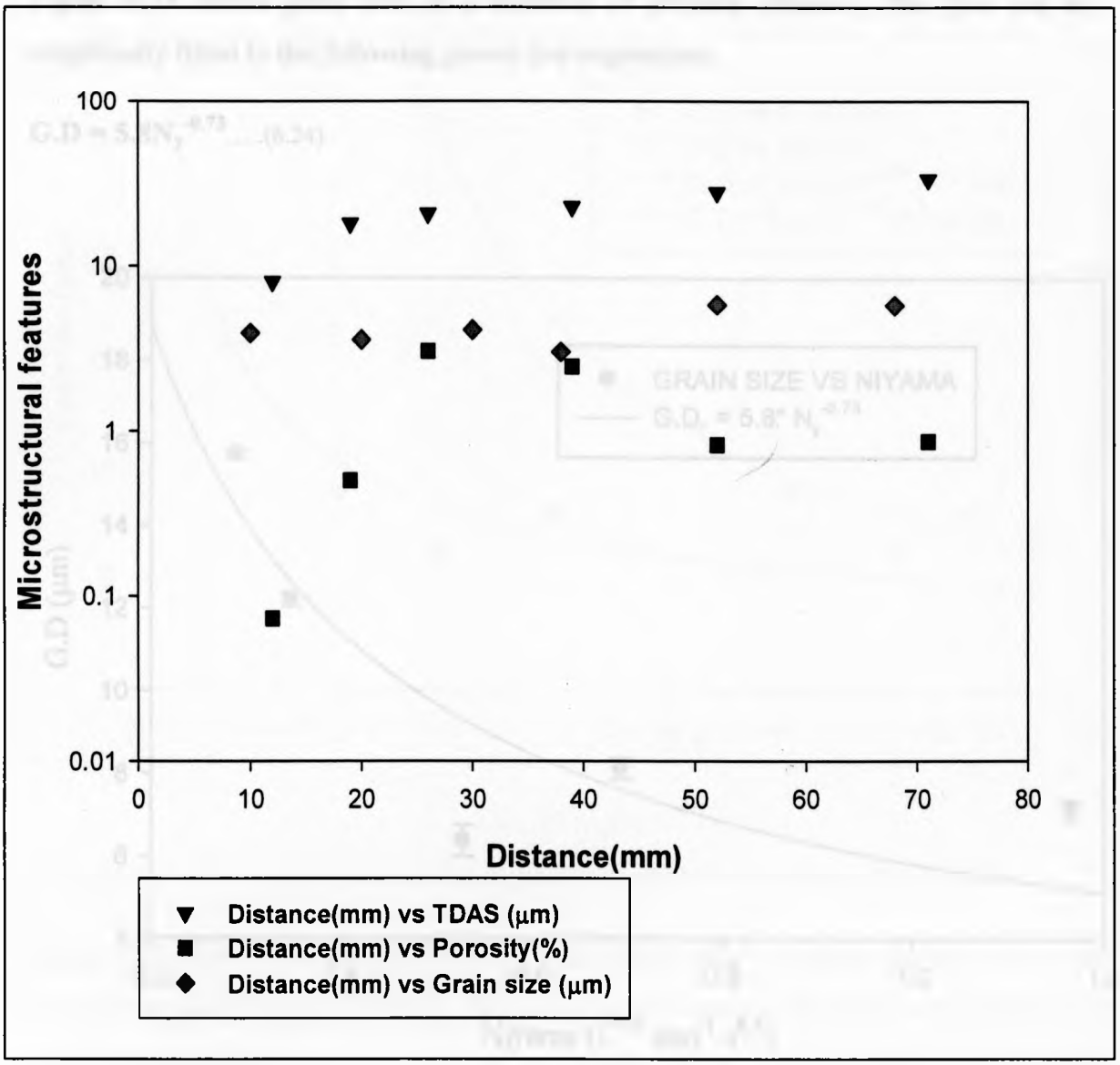

Figure 6.22 Microstructural parameters as a function of distance for AZ91D.

G, V and R values (Figure 6.21 and 6.22) show a steady decrease with increasing grain size and arm spacing values as a function of distance from the cooling end.

6.3.1 Grain size vs. Process variables

Figure 6.23 shows grain size as a function of Niyama criterion. The plot can be empirically fitted to the following power law expression:

$$\mathbf{G.D = 5.8N_y^{-0.73}} \quad .....(6.24)$$

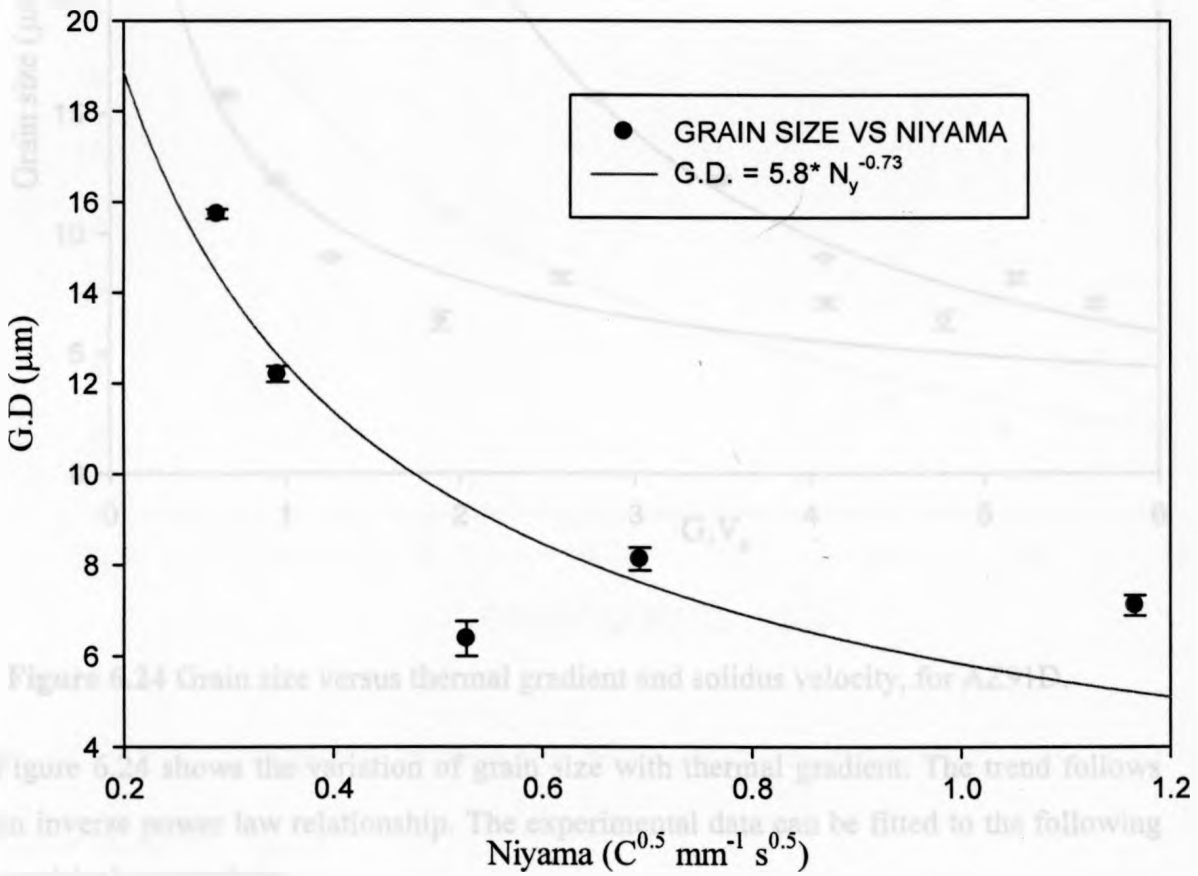

Figure 6.23 Grain size versus Niyama for AZ91D.

where, ***G.D*** is the grain size in µm and N_y represents the Niyama criterion ($C^{0.5}$mm $s^{0.5}$). However, the overall average trend shows a reduction in grain size with increase in

Niyama values. The Niyama values for the casting range from 0.2 to 1.2, on moving towards the tip of the wedge.

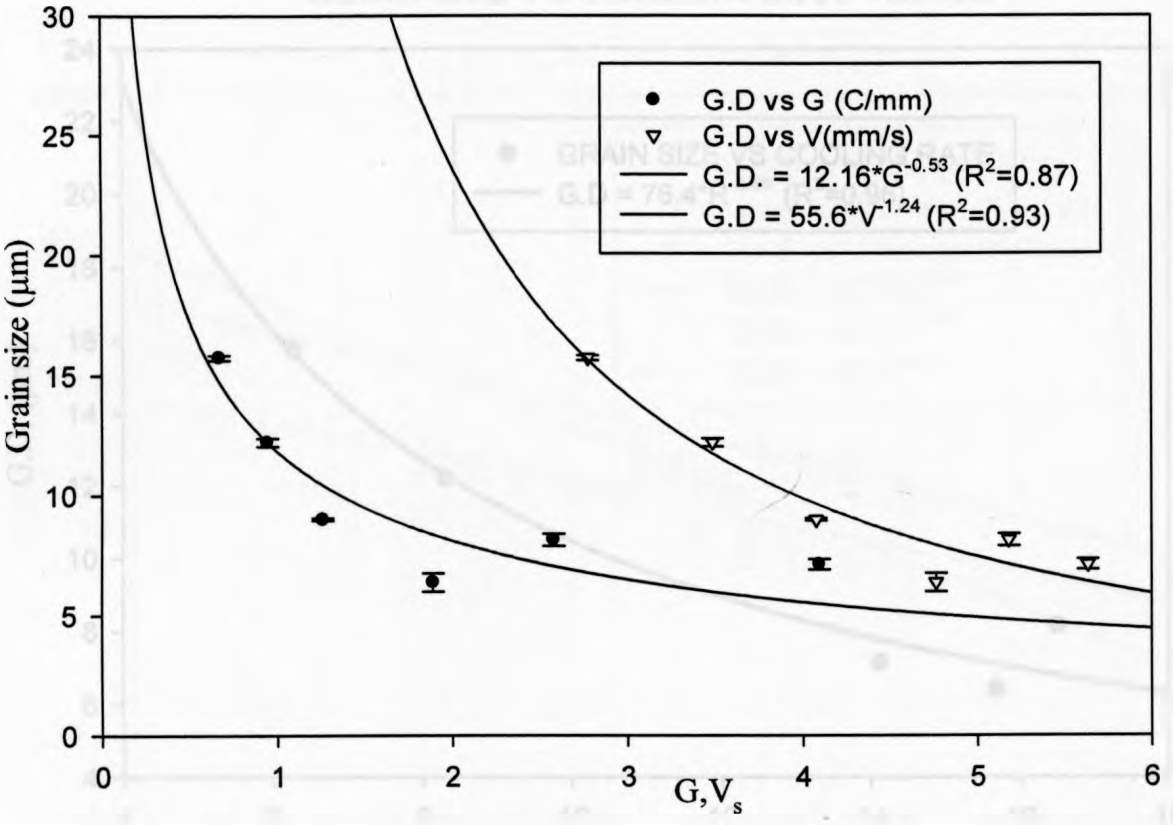

Figure 6.24 Grain size versus thermal gradient and solidus velocity, for AZ91D.

Figure 6.24 shows the variation of grain size with thermal gradient. The trend follows an inverse power law relationship. The experimental data can be fitted to the following empirical expressions:

$$G.D = 12.16G^{-0.53} \quad .....(6.25)$$

$$G.D = 55.6V^{-1.24} \quad .....(6.26)$$

where, ***G.D*** is the grain size in μm and ***G*** is the thermal gradient in °C/mm. The observed trend is similar to that for AM60B

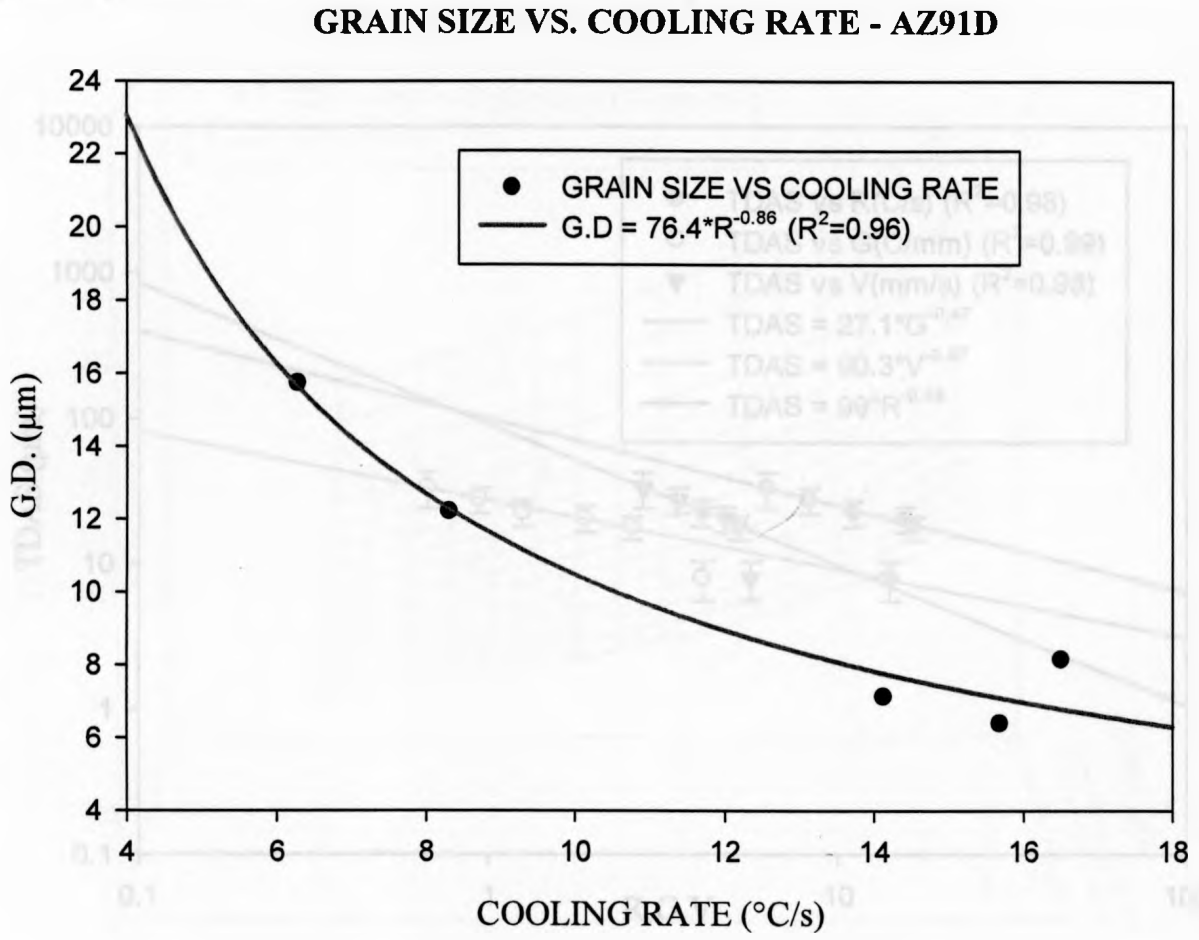

Figure 6.25 Grain size versus cooling rate for AZ91D.

$$G.D = 76.4R^{-0.86} \quad .....(6.27)$$

where, ***G.D*** is grain size in μm and ***R*** is the cooling rate in °C/s

The reduction in cooling rate should lead to increase in the grain size due to lower undercooling and longer solidification times, leading to grain coarsening. The relationship between grain size and cooling rate, as shown in Figure 6.25, is of an inverse power law nature. The trend can be described by the above mentioned equation.

6.3.2 Arm spacing vs. Process variables

As seen for AM60B, dendrite arm spacing for AZ91D shows similar trends with respect to the process parameters. Figure 6.26 shows the variation of TDAS as a function of process parameters.

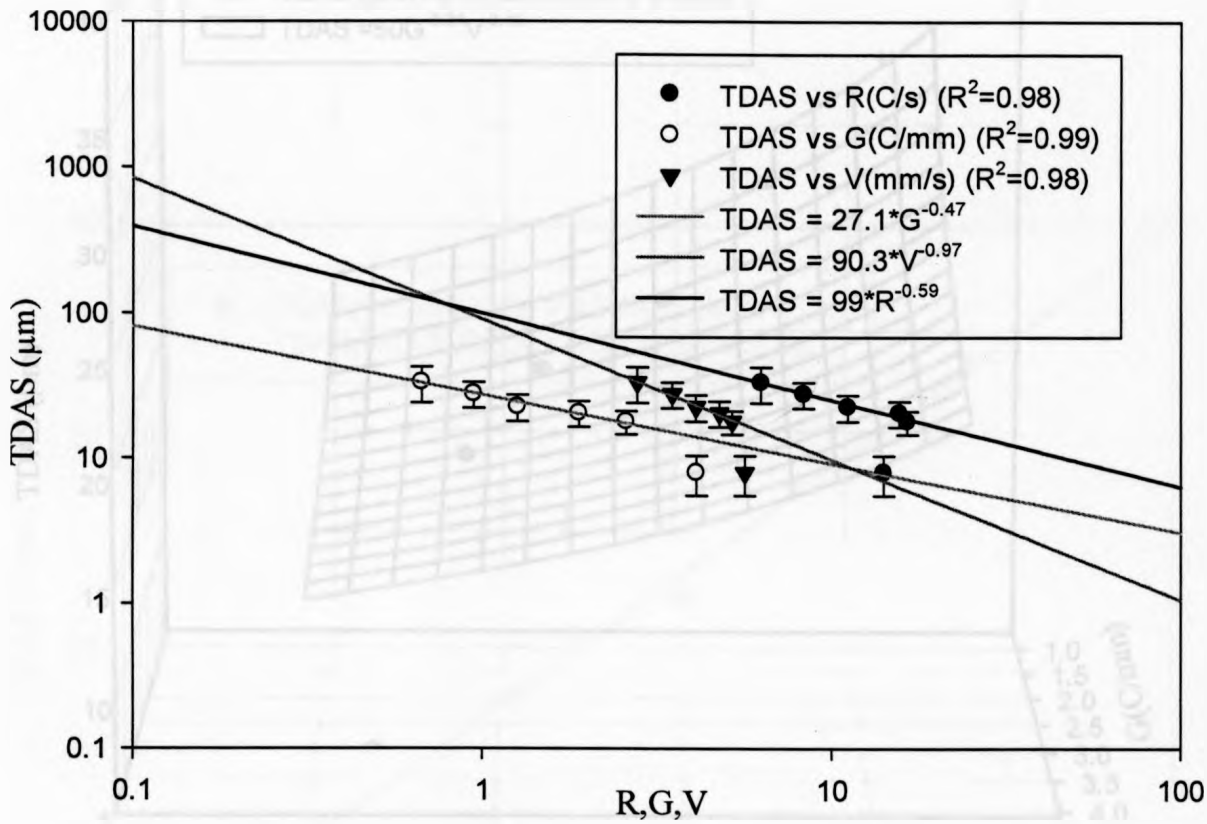

Figure 6.26 Tertiary dendrite arm spacing with respect to cooling rate, thermal gradient and growth velocity for AZ91D.

$$\mathbf{TDAS = 99R^{-0.59}} \quad .....(6.28)$$

$$\mathbf{TDAS = 27.1G^{-0.47}} \quad .....(6.29)$$

$$\mathbf{TDAS = 90.3V^{-0.97}} \quad .....(6.30)$$

where, ***R*** is the cooling rate (°C/s), ***G*** is the thermal gradient (°C/mm), ***V*** is the solidus velocity (mm/s) and ***TDAS*** is the tertiary dendrite arm spacing in μm.

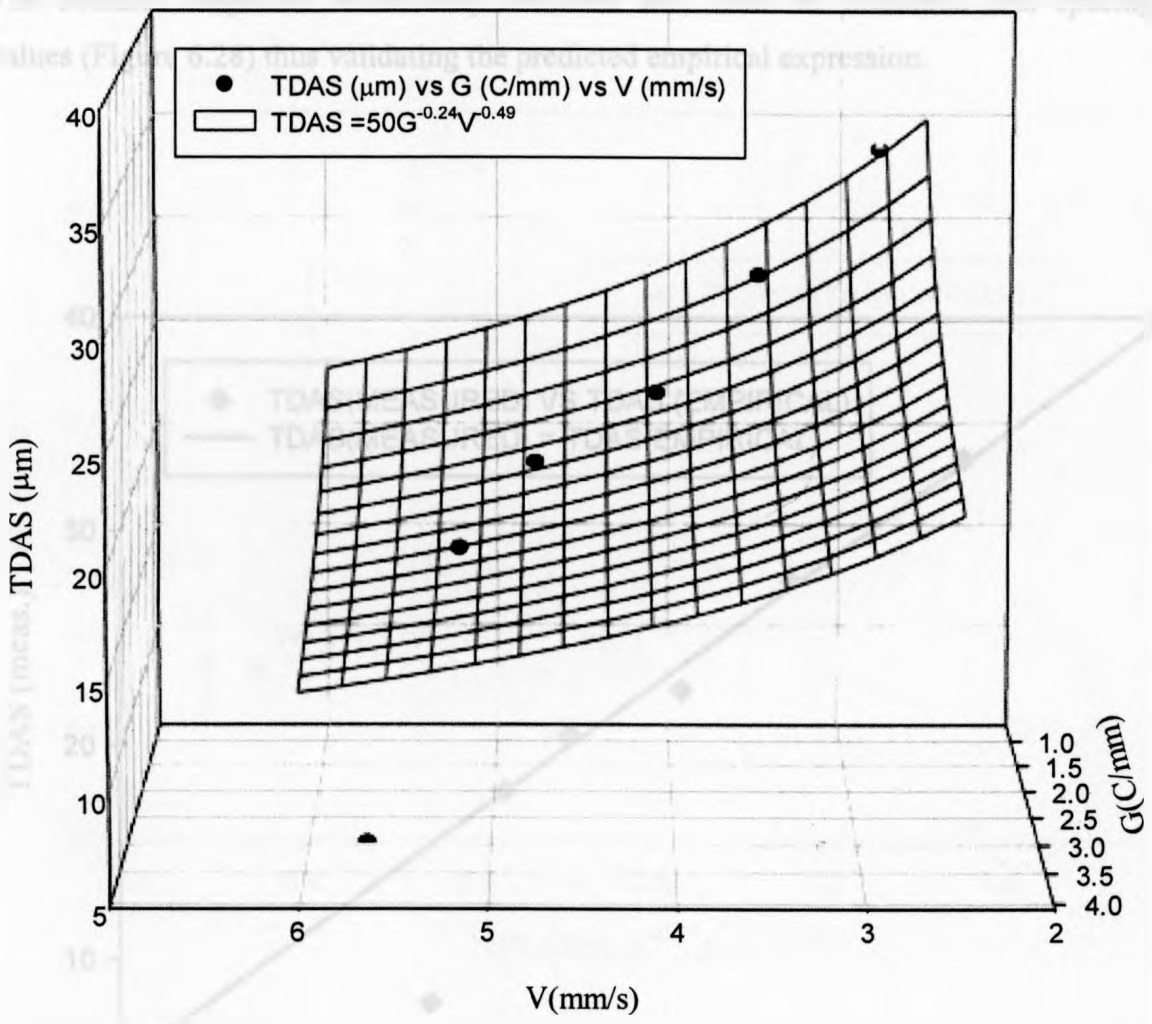

Figure 6.27 Tertiary dendrite arm spacing as a function of gradient and growth velocity for AZ91D.

The dendrite arm spacing, as predicted, shows inverse power law dependencies with respect to G, V and R. Also, the arm spacing values can be represented as a compound

function of G and V (Figure 6.27), thus satisfying the models established by Hunt, Lu et. al. and Kurz-Fisher[51-53].

$$\mathbf{TDAS_{empirical} = 50G^{-0.24}V^{-0.49}} \quad .....(6.31)$$

The obtained empirical relationship confirms well with the measured arm spacing values (Figure 6.28) thus validating the predicted empirical expression.

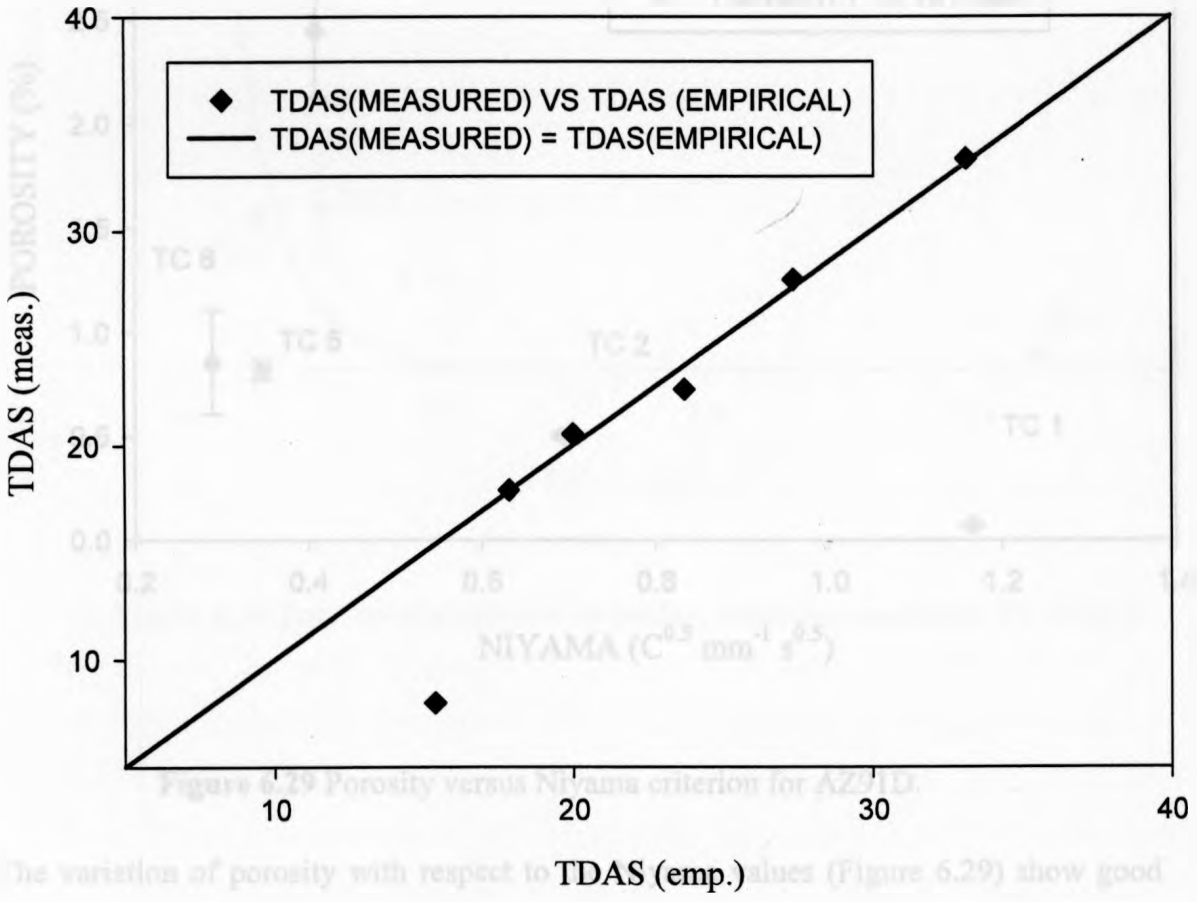

Figure 6.28 Tertiary dendrite arm spacing for AZ91D (empirical vs. measured values).

6.3.3 Porosity vs. Process variables

The variation of porosity, as observed in AM60, does not represent any direct dependencies on the process parameters but instead seems to be an outcome of a number of influencing factors.

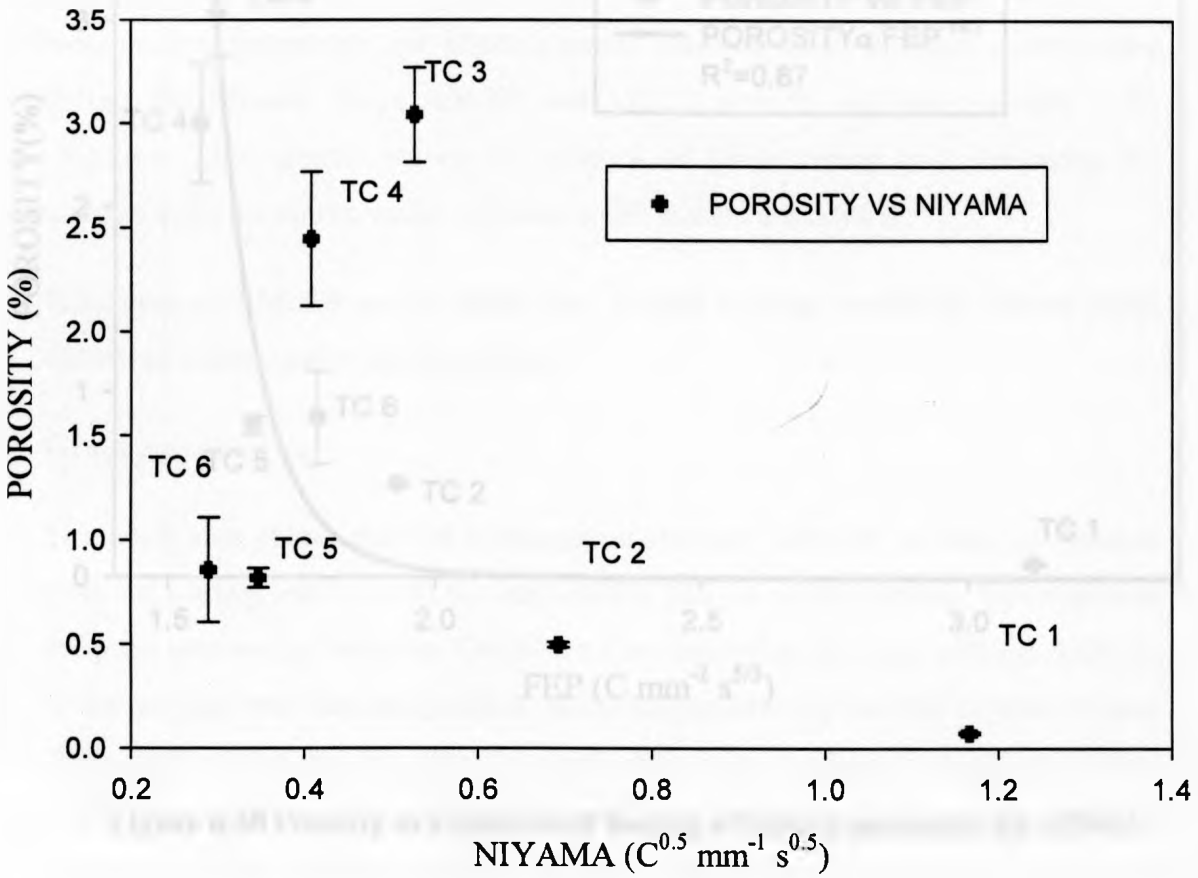

Figure 6.29 Porosity versus Niyama criterion for AZ91D.

The variation of porosity with respect to the Niyama values (Figure 6.29) show good agreement to the expected trends till the 4th thermocouple (porosity is around 2.5%). However, the porosity values for the 5th and the 6th thermocouple do not follow the expected trends as expected from Niyama values. Another plot, wherein porosity is studied as function of the feeding efficiency parameter (Figure 6.30) shows reasonably agreeable values.

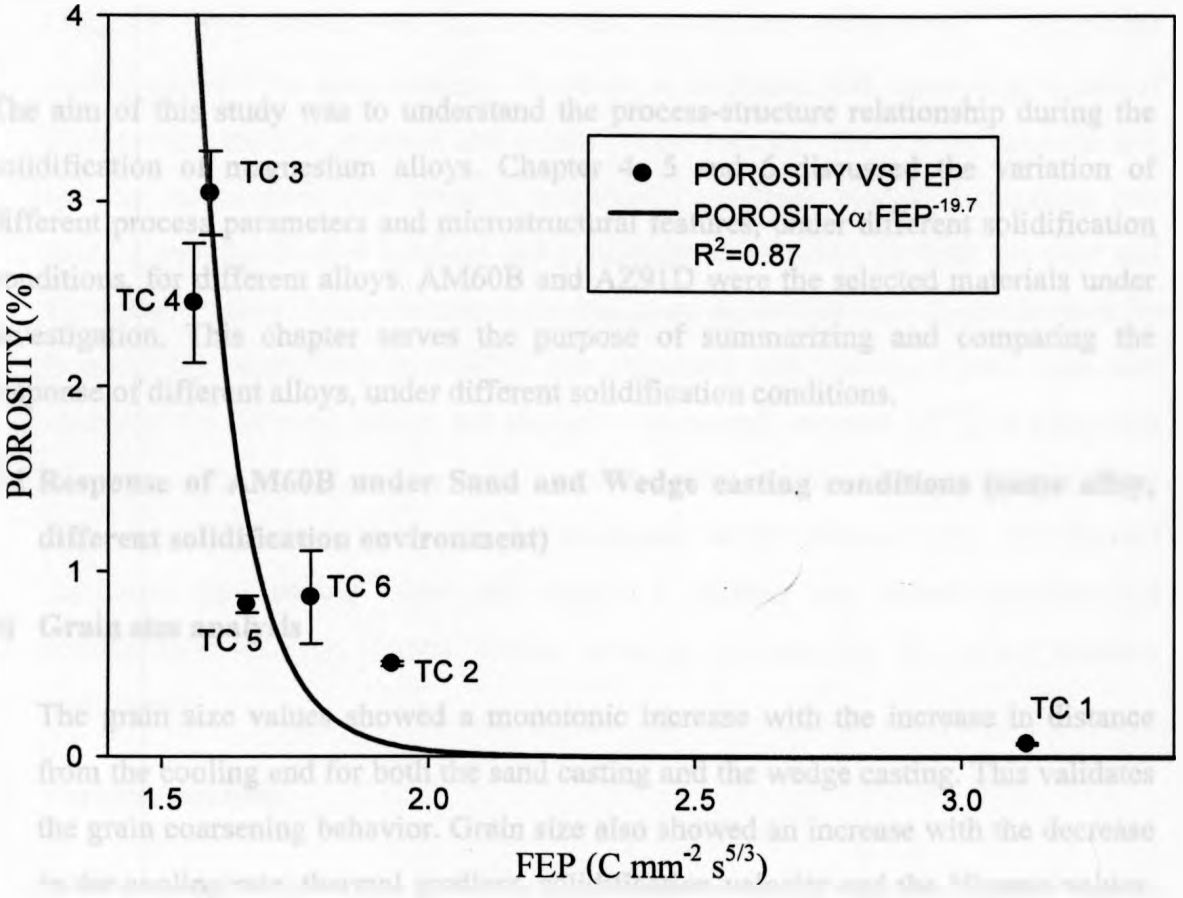

Figure 6.30 Porosity as a function of feeding efficiency parameter for AZ91D.

Chapter 7

Summary and Conclusions

The aim of this study was to understand the process-structure relationship during the solidification of magnesium alloys. Chapter 4, 5 and 6 discussed the variation of different process parameters and microstructural features, under different solidification conditions, for different alloys. AM60B and AZ91D were the selected materials under investigation. This chapter serves the purpose of summarizing and comparing the response of different alloys, under different solidification conditions.

7.1 Response of AM60B under Sand and Wedge casting conditions (same alloy, different solidification environment)

a) Grain size analysis

The grain size values showed a monotonic increase with the increase in distance from the cooling end for both the sand casting and the wedge casting. This validates the grain coarsening behavior. Grain size also showed an increase with the decrease in the cooling rate, thermal gradient, solidification velocity and the Niyama values. Grain size values, for the both the sand and wedge castings, showed an inverse power law variation with respect to cooling rate, thermal gradient, solidification velocity and the Niyama criterion. However, the experimental grain size values presented a relatively better fit with the cooling rate data than the other parameters. The thermal gradient and solidification velocity, even though they show a good fit, cannot be confirmed as individually affecting the grain size. The interdependence of the cooling rate, gradient and growth velocity (See the Appendix) also needs to be considered, while reaching further conclusions. Grain size values also showed a good agreement with the Niyama trends. This indicates that it is the combined influence of the process variables, which affects the resultant grain size.

b) Dendrite Arm Spacing

Tertiary dendrite arm spacing increased monotonically with local solidification time ($t_{stat}^{0.31}$ for sand casting and $t_{stat}^{0.65}$ for wedge casting) and distance ($d^{0.69}$ for wedge casting and $d^{0.21}$ for sand casting). However, it decreases with increasing values of cooling rate, thermal gradient and solidification velocity. The tertiary dendrite arm spacing values were also fitted to empirically predicted models, expressing arm spacing as a function of gradient and solidification velocity, for both the sand and the wedge casting. The expressions showed good agreement with the predictions by Hunt-Lu and Kurz Fisher [45-47]. The secondary arm spacing values were also measured for the sand casting and showed a monotonic increase ($d^{0.63}$) as a function of distance from the cooling end. Thus, the arm spacing is found to vary as a function of distance, which can be expressed as d^x ($0<x<1$). The variation of secondary arm spacing values with respect to cooling rate, thermal gradient and solidification velocity, showed similar trends as observed for the tertiary dendrite arm spacing.

c) Porosity analysis

Porosity did not show any direct dependency on any of the process variables. It is generally an outcome of the combined influence of various process parameters. However, as proposed in literature and related texts, feeding is a major influencing factor. The rate of feeding is mainly governed by thermal gradient. Hence, both porosity prediction criteria proposed in the literature have gradient as the dominant term. Porosity showed a bimodal distribution for both the casting conditions. In case of the sand casting, porosity and the Niyama values did not show any agreement whatsoever. However, the porosity values displayed a decreasing trend with increasing *FEP* values. Contrastingly for the wedge casting, it did show agreement with the Niyama criterion upto the 5th thermocouple (porosity = 7.2%). Porosity, for the wedge casting, was also plotted against the feeding efficiency parameter. It showed decent agreement till the 4th thermocouple, varying inversely with respect to *FEP*.

Table 7.1 Structure-process relationships chart for AM60B, showing the various empirically obtained relationships between different variables.

SOLIDIFICATION OF AM60B: STRUCTURE-PROCESS RELATIONSHIPS CHART		PROCESS VARIABLES				
		R (°C/s)	**G** (°C/mm)	**V** (mm/s)	N_y ($C^{0.5}$ $mm^{-1}s^{0.5}$)	**d** (mm)
MICROSTRUCTURAL FEATURES: SAND CASTING	**G.D.** (μm)	$R^{-0.88}$	$G^{-0.63}$	$V^{-1.02}$	$N_y^{-0.82}$	$e^{0.033d}$
	SDAS (μm)	$R^{-0.9}$	$G^{-0.69}$	$V^{-1.18}$	---	$d^{0.63}$
	TDAS (μm)	$R^{-0.32}$	$G^{-0.24}$	$V^{-0.39}$	---	$d^{0.21}$
	Porosity (%)	---	---	---	---	---
MICROSTRUCTURAL FEATURES: WEDGE CASTING	**G.D.** (μm)	$R^{-1.33}$	$G^{-0.9}$	$V^{-0.6}$	$N_y^{-1.4}$	$e^{0.024d}$
	TDAS (μm)	$R^{-0.65}$	$G^{-0.68}$	$V^{-0.43}$	---	$d^{0.69}$
	Porosity (%)	---	---	---	---	---

Table 7.1 shows the various empirically obtained relationships between structural features and the process parameters. Table 7.2 shows the various empirically obtained models describing TDAS as functions of G and V for the sand and the wedge castings.

Table 7.2 Comparison of TDAS as an empirical function of G and V.

HUNT-LU/KURZ – FISHER MODEL	TERTIARY DENDRITE ARM SPACING					
	AM60B: SAND CAST		AM60B: WEDGE CAST		AZ91D: WEDGE CAST	
TDAS α $G^{-a}V^{-b}$	a	b	a	b	a	b
	-0.12	*-0.2*	*-0.34*	*-0.21*	*-0.24*	*-0.49*

7.2 Response of AM60B and AZ91D under Wedge casting conditions (different alloy, same solidification environment)

a) Grain size analysis

Grain size values increased monotonically as a function of distance from the cooling end. The average grain size values are lower for AZ91D than AM60B. This is due to higher Al content in AZ91D, leading to more effective grain refinement. Grain size values, for both AM60B and AZ91D, showed an increase with decreasing Niyama values. They also showed inverse power law variations with respect to cooling rate, thermal gradient and solidification velocity.

b) Dendrite arm spacing

The arm spacing values, as expected, showed an increase with increasing distance, ***d*** from tip of wedge and time of solidification, t_{stat}. The tertiary dendrite arm spacing values are observed to vary as, $\mathbf{d}^{0.69}$ for AM60B and $\mathbf{d}^{0.6}$for AZ91D. Similarly, TDAS is proportional to $\mathbf{t}_{stat}^{0.65}$ for both AM60B and AZ91D. TDAS shows an inverse dependence on the cooling rate for both the alloys ($\mathbf{R}^{-0.65}$ and $\mathbf{R}^{-0.6}$ for AM60B and AZ91D, respectively). These results correlate well with the hypothesis of arm spacing varying primarily as a function of cooling rate. The variation of arm spacing, as a function of thermal gradient and solidification velocity, also showed an

inverse power law relationship; with AM60B varying as linear functions of $G^{-0.68}$ and $V^{-0.43}$, while AZ91D being proportional to $G^{-0.47}$ and $V^{-0.97}$. The Hunt-Lu/Kurz-Fisher prediction model when applied to the wedge cast alloys, gave the following relations:

$$TDAS_{empirical} = 33*G^{-0.34}V^{-0.21} \text{ (AM60B)}$$

$$TDAS_{empirical} = 50*G^{-0.24}V^{-0.49} \text{ (AZ91D)}$$

Table 7.3 Structure-process relationships chart for the wedge casting analysis, showing the various empirically obtained relationships between different variables.

WEDGE CASTING ANALYSIS: STRUCTURE-PROCESS RELATIONSHIPS CHART		PROCESS VARIABLES				
		R (°C/s)	G (°C/mm)	V (mm/s)	N_y ($C^{0.5}$ $mm^{-1}s^{0.5}$)	d (mm)
MICROSTRUCTURAL FEATURES: AZ91D	G.D. (μm)	$R^{-0.86}$	$G^{-0.53}$	$V^{-1.24}$	$N_y^{-0.73}$	$e^{0.015d}$
	TDAS (μm)	$R^{-0.6}$	$G^{-0.47}$	$V^{-0.97}$	---	$d^{0.6}$
	Porosity (%)	---	---	---	---	---
MICROSTRUCTURAL FEATURES: AM60B	G.D. (μm)	$R^{-1.33}$	$G^{-0.9}$	$V^{-0.6}$	$N_y^{-1.4}$	$e^{0.024d}$
	TDAS (μm)	$R^{-0.65}$	$G^{-0.68}$	$V^{-0.43}$	---	$d^{0.69}$
	Porosity (%)	---	---	---	---	---

Table 7.4 Structure-process relationships chart for the sand and the wedge casting analysis, showing the empirical relations between TDAS and solidification time, and between porosity and *FEP*.

SOLIDIFICATION ANALYSIS: STRUCTURE-PROCESS RELATIONSHIPS CHART		PROCESS VARIABLES	
		FEP ($C\ mm^{-2}\ s^{5/3}$)	t_{stat} (s)
AM60B	**SDAS** (μm)	---	$t^{0.93}$
	TDAS (μm)	---	$t^{0.31}$
	Porosity (%)	inversely proportional	---
AZ91D	**TDAS** (μm)	---	$t^{0.65}$
	Porosity (%)	$FEP^{-19.7}$	---
AM60B	**TDAS** (μm)	---	$t^{0.65}$
	Porosity (%)	$FEP^{-3.2}$	---

c) Porosity analysis

Porosity values showed good agreement with Niyama criterion, upto the 5th thermocouple and the 4th thermocouple for AM60B and AZ91D, respectively. When plotted against the feeding efficiency parameter (FEP), the AM60B alloy showed an

inverse dependence till the 4th thermocouple. On the other hand, the porosity and FEP values for the AZ91D alloy agreed well with the predicted trends.

Table 7.3 and 7.4 present a comparative study of the structure-process relationships between the various solidification variables.

7.3 Future work

In the case of commercial castings, due to complex mold geometries, the various process variables are influenced by each other. Hence, the individual effects of various process parameters on the microstructural features cannot be determined accurately. Also, it is necessary to simulate directional solidification conditions to have a better understanding of the dependence of dendrite arm spacing on the process variables. Therefore, to completely understand the influence of each process variable on the resultant microstructure, it is required to carry out a study where each parameter can be varied keeping the other variables fixed. This is especially required to study the independent effects of gradient and solidification velocity on the various structural features. The most suitable technique for the same is the Bridgman-Stockbarger solidification method [97,98]. This provides the advantage of varying both the solidification velocity and the temperature gradient, individually. It will also provide an oxygen free atmosphere during the melting and solidification process, by incorporation of argon atmosphere or vacuum. The rate of cooling is slower and more controlled. This will lead to better correlations between the microstructure and the equilibrium phase diagrams. Apart from all these advantages, it will provide a more comprehensive study of the structure-process relationships by varying each parameter keeping the others fixed, thus generating data over a range of solidification conditions. These experimental values can then be compared and fitted to the already obtained results from the sand and the wedge castings, to understand the general trends and variations of microstructure with the process variables.

Appendix

Figures 8.1-8.3 represent the observed interdependencies between G, V and R for the sand casting and the wedge casting experiments.

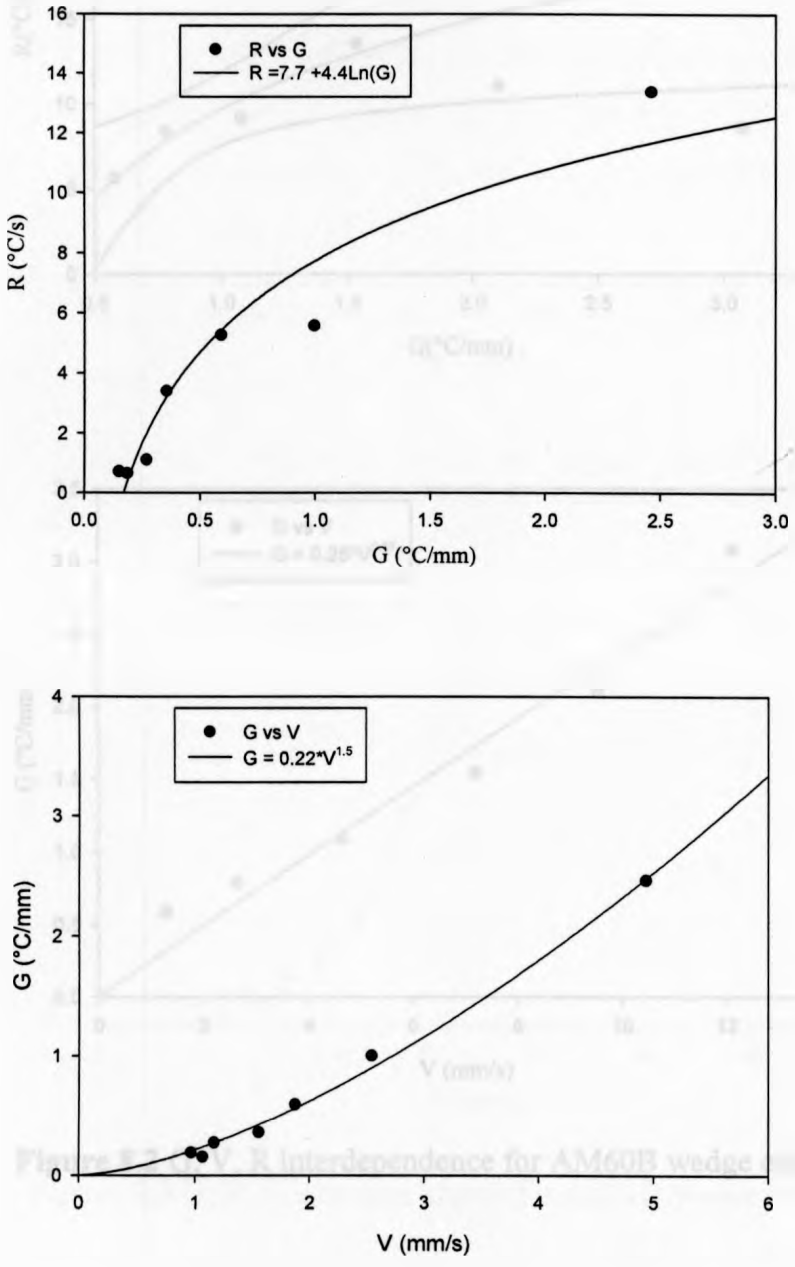

Figure 8.1 G, V, R interdependence for sand casting.

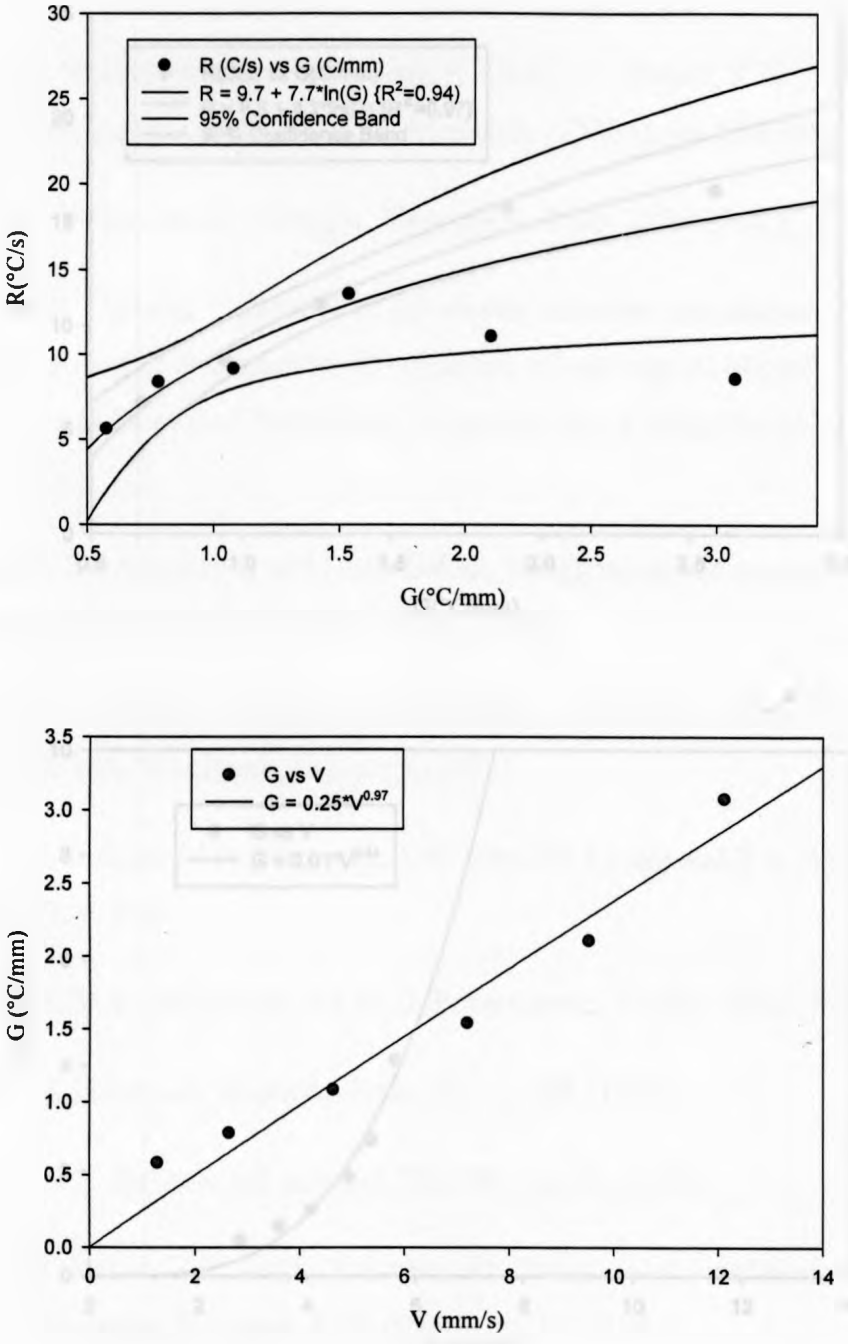

Figure 8.2 G, V, R interdependence for AM60B wedge casting.

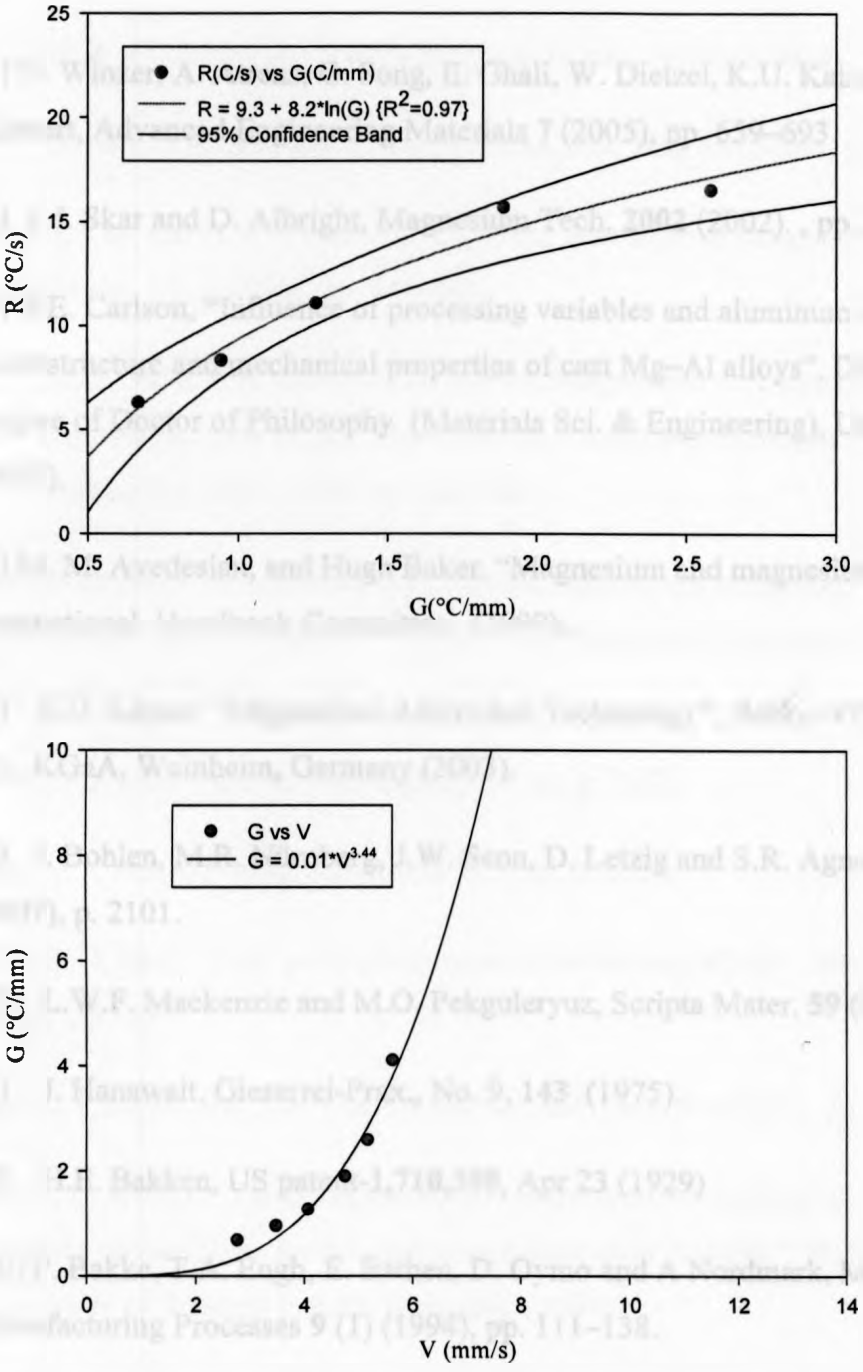

Figure 8.3 G, V, R interdependence for AZ91D wedge casting.

References

[1] N. Winzer, A. Atrens, G. Song, E. Ghali, W. Dietzel, K.U. Kainer, N. Hort and C. Blawert, Advanced Engineering Materials **7** (2005), pp. 659–693.

[2] J. I. Skar and D. Albright, Magnesium Tech. **2002** (2002). , pp. 255–261.

[3] B.E. Carlson, "Influence of processing variables and aluminum content on the microstructure and mechanical properties of cast Mg–Al alloys", Dissertation for the Degree of Doctor of Philosophy (Materials Sci. & Engineering), University of Michigan, (1997).

[4] M. M. Avedesian, and Hugh Baker. "Magnesium and magnesium alloys", ASM International. Handbook Committee, (1999).

[5] K.U. Kainer, "Magnesium Alloys and Technology", Wiley–VCH Verlag GmbH and Co., KGaA, Weinheim, Germany (2003).

[6] J. Bohlen, M.R. Nürnberg, J.W. Senn, D. Letzig and S.R. Agnew, Acta Mater. **55** (2007), p. 2101.

[7] L.W.F. Mackenzie and M.O. Pekguleryuz, Scripta Mater. **59** (2008), p. 665.

[8] J. Hanawalt. Gieserrei-Prax., No. 9, **143** (1975).

[9] H.E. Bakken, US patent-**1,710,398**, Apr 23 (1929)

[10] P. Bakke, T.A. Engh, E. Bathen, D. Oymo and A Nordmark, Materials and Manufacturing Processes **9** (1) (1994), pp. 111–138.

[11] A.K. Dahle, Y.C. Lee, M.D. Nave, P.L. Schaffer and D.H. StJohn, J Light Met **1** (2001), p. 61.

[12] E. Scheil Z. Metallk. **42** (1942), p. 70.

[13] B. E. Carlson. Advanced Engineering Materials, **3** (2001), pp. 245–247.

[14] J.H. Perepezko and W.J. Boettinger, Mater. Res. Soc. Symp. Proc. 19, **223** (1983)

[15] Web reference - http://www.magnesium.com /w3/data-bank

[16] Q. Han, B.K. Kad and S. Viswanathan, Phil Mag **84** (2004), pp. 3843–3860.

[17] A. Luo and G.W. Lorimer (Ed.), Third International Magnesium Conference, Manchester, UK, (1996), pp. 449-464.

[18] M.D. Nave, A.K. Dahle, D.H. StJohn, Magnesium technology 2000, in: H.I. Kaplan, J.N. Hryn, B.B. Clow (Eds.), The Minerals, Metals and Materials Society (TMS), Warrendale, PA, USA, 2000, pp. 233-242.

[19] M.D. Nave, A.K. Dahle, D.H. StJohn, Magnesium technology 2000, in: H.I. Kaplan, J.N. Hryn, B.B. Clow (Eds.), The Minerals, Metals and Materials Society (TMS), Warrendale, PA, USA, 2000, pp. 243-250.

[20] E. O. Hall, Proc. R. Soc. B,**B64**, (1951), p. 747.

[21] N. J. Petch, J. Iron Steel Inst.,**174**, (1953), p. 25.

[22] E. O. Hall, 'Yield point phenomena in metals and alloys', New York, NY, Plenum Press, (1970)

[23] D.J. Lloyd, and S.A. Court, Mat. Sci. and Tech.,**19**,(2003), pp. 1349-1354

[24] J. P. Weiler, "The development of comprehensive material models of the structure-property relationships for die-cast magnesium alloy AM60B", Ph.D. Thesis Dissertation, University of Western Ontario (Canada), (2009)

[25] W. P. Sequeira, G. L. Dunlop, M. T. Murray. In Proceedings of the 3rd International Magnesium Conference, G.W. Lorimer (ed.). Manchester, UK: The Institute of Metals,(1996), pp. 63-73

[26] R.E. Spear and G.R. Gardner AFS Trans. **71** (1963), p. 209.

[27] G. R. Armstrong and H. Jones, Proc. of Int. Conf. on Solidification and Cast Metals (ed., P. Beeley), The Metals Society, Sheffield (1977), p. 454,

[28] K. Mizuno, E. Fan, S. Furutani, S. Yokota, and T. Fukusako, J. Jpn. Inst. Light Metal , **46**, (1996), p.55.

[29] C.D. Lee and K.S. Shin, Met. Mater. Int. **9** (2003), pp. 21–27.

[30] C.H. Cáceres, Scripta Metall. Mater. **32** (1995), pp. 1851–1856.

[31] M.K. Surappa, E. Blank and J.C. Jaquet, Scripta Metall. **20** (1986), pp. 1281–1286.

[32] A.M. Gokhale and G.R. Patel, TMS Annual Meeting: Proceedings of TMS 2002 Annual Meeting: Automotive Alloys and Aluminum Sheet and Plate Rolling and Finishing Technology Symposia, vol. **1**, (2002), pp. 65–73.

[33] S.E. Offerman, N.H. van Dijk, J. Sietsma, S. Grigull, E.M. Lauridsen and L. Marguilies et al., Science **298** (2002), pp. 1003-1005.

[34] D. Kashchiev, A. Borissova, R. B. Hammond, K. J. Roberts, J. Phys. Chem. B **114** (16), (2010), pp. 5441-5446

[35] C. Zener. J. Appl. Phys. 20, **950** (1949).

[36] Y.C. Lee, A.K. Dahle, D.H. StJohn, Metal. Mater. Trans A **31**, (2000), p. 2895

[37] R.T. Wood, "The Foundryman", (1953), pp. 98-99 and 256-61.

[38] M. Umemoto, Z.H. Guo and I. Tamura, Mater. Sci. Technol. **3** (1987), p. 249.

[39] N.H. Pryds and X. Huang, Metall. Mater Trans A **31A** (2000), pp. 3155–3166.

[40] T.Z. Kattamis and M.C. Flemings, Trans. AIME 236 (1966), pp. 1523–1532.

[41] Weisstein, Eric W. "Gradient.", Math World-- A Wolfram Web Resource. http://mathworld.wolfram.com/Gradient.html

[42] J.W. Martin, "Concise encyclopedia of the structure of materials", Elsevier, Oxford (2006), p. 149.

[43] H. Biloni and W.J. Boettinger: "Solidification, in Physical Metallurgy", 4th. eds. R.W. Cahn and P. Haasen. Elsevier Science BV, Switzerland, (1996), pp. 670.

[44] R.E. Reed-Hill and R. Abbaschain, "Physical Metallurgy Principles", (3rd edn. ed.). PWS-KENT, Boston (1992).

[45] Bruce Chalmers, Trans. AIME, **200** (1954), p. 519

[46] D.M. Stefanescu. "Science and engineering of casting solidification", Kluwer Academic/Plenum Publishers, New York (NY) (2002).

[47]M.C. Flemings, Metall. Trans., vol. **5**, (1974), pp. 2121–34

[48] J.D. Zhu, S.L. Cockcroft and D.M. Maijer, Metall. Mater. Trans. A **37** (2006), pp. 1075–1085.

[49] F. Sá, O.L. Rocha, C.A Siqueira, and A. Garcia, Mater. Sci. Eng. A **373**, 131 (2004)

[50] R.N. Grugel, J. Mater. Sci. **28** (1993), pp. 677–683.

[51] J.D. Hunt and S.Z. Lu, Metall. Mater. Trans. A **27**, (1996), p. 611

[52] W. Kurz and J.D. Fisher Acta Metall. **29** (1981), pp. 11–20.

[53] W. Kurz and J.D. Fisher In: "Fundamentals of Solidification", Trans Tech Public, Switzerland (1992), pp. 85–90.

[54] J.P. Anson and J.E. Gruzleski, Mater. Char. **43** (1999), pp. 319–335.

[55] S.G. Lee, Arun M. Gokhale. [J]. Scripta Materialia **55**, (2006), pp. 387–390.

[56] P.D. Lee, A. Chirazi and D. See, J Light Metal **1** (2001), pp. 15–30.

[57] E. Niyama, T. Uchida, M. Morikawa and S. Saito. AFS Cast Met. Res. J., vol. **7**, (1982), pp. 52–63.

[58] N. Chvorinov. Giesserei **27** (1940), pp. 177-186.

[59] E. Niyama, T. Uchida, M. Morikawa, and S. Saito, AFS Int. Cast Met. J., vol. **6**, (1981), pp. 16–22.

[60] C. Carlson and C. Beckermann: Metall. Mater. Trans. A, vol. **40A**, (2009), pp. 163–75.

[61] K.D. Carlson and C. Beckermann, Proc. 62nd SFSA Technical and Operating Conference, Chicago, Illinois, (2008).

[62] Y.W. Lee, E. Chang, and C.F. Chieu. Metall. Trans. B, vol. **21B**, (1990), pp. 715–22.

[63] D.R. Poirier, Metall Trans. B, vol. **18B**, (1987), pp. 245–55.

[64] S.D. Pathak and O. Prabhakar, AFS Trans., vol. 92, (1984), pp. 671–80.

[65] K. Kubo, R.D. Pehlke, AFS Trans. **94** (1986), pp. 753-766.

[66] T.S. Piwonka and M.C. Flemings, Trans. Metall. Soc. A.I.M.E. **236**, (1966), pp. 1157-1165.

[67] A.S. Sabau and S. Viswanathan. Light Metals, TMS, Warrendale, PA, (2000), pp. 597–602.

[68] G.K. Sigworth, C. Wang, Met. Trans. B **24** (1993), p. 349.

[69] H. Jacobi and K. Schwerdtfeger, Metall. Trans. A **7**(1975), pp. 811-820.

[70] H. Jacobi, "Crystallization of Steel" in Information Symposium, Casting and Solidification of Steel, Commission of the European Communities, IPC Science and Technology Press, Ltd., Guildford, Surrey, England, vol. 1,(1977), p. 111.

[71] Y. He, A. Javaid, E. Essadiqi, M. Shehata. Canadian Metallurgical Quarterly, Vol **48**(2), (2009), pp. 145-155

[72] T.V. Padfield, "Metallography and Microstructures", Materials Park, OH: ASM International, Vol. **9**, (2004), pp. 801-815

[73] J. M. Tartaglia, J. H. Howard, R. E. Swartz, and R. L. Bentz, Jr., JOM 53:11, (2001)

[74] G. V. Voort, "Metallography of Magnesium and its Alloys", Buehler, Vol. 4, Issue 2, Tech. Note. 42

[75] Nature, Volume 156, Issue 3969, (1945), pp. 614.

[76] W. Kasprzak, J.H. Sokolowski, M. Sahoo, L.A. DobrzaĔski. Journal of Achievements in Materials and Manufacturing Engineering, **28**(2), (2008), pp. 131-138.

[77] S. T. Kao, E. Chang and Y.W. Lee, Mat. Trans., JIM 35:9 (1994), pp. 632-639

[78] P. Cao, M. Qian and D.H. StJohn, Scripta Mater. 54 (2006), p. 1853.

[79] D. Ruvalcaba, R.H. Mathiesen, D.G. Eskin, L. Arnberg, and L. Katgerman: Metall. Mater. Trans. B, vol. **40**B, (2009), pp. 312-16.

[80] S. Lu, J.D. Hunt and W. Kurz, Acta. Metall. Mater. **42** (1994), p. 1653.

[81] M.N. Khan, M. Aljarrah, J.T. Wood and M. Medraj. Journal of Materials Research, (2011), Available on CJO doi:10.1557/jmr.2011.24

[82] D. Mirković, J. Gröbner, and R. Schmid-Fetzer, "Solidification curves of AZ-magnesium alloys determined by DSC experiments and heat-transfer model (DSC-HTM)", in Proceedings of the 6th International Conference Magnesium Alloys and Their Application, Wolfsburg, (2003), pp. 842–847.

[83] D.H. StJohn, M. Qian, M.A. Easton, P. Cao and Z. Hildebrand, Metall. Mater. Trans. A **36** (2005), p. 1669

[84] F. Cverna, editor. ASM ready reference: "Thermal properties of metals". ASM International – The Materials Information Society, (2002)

[85] P.K. Rohatgi, K. Pasciak, S. Ray, C.S. Narendranath and A. Sachdeva, J. Mater. Sci. **29** (1994), p. 5357.

[86] E. Cadirli and M. Gündüz, J. Mater. Sci. **35** (2000), pp. 3837–3848.

[87] Flemings M.C., Behavior of metal alloys in the semi-solid state, Metall. Trans. A **22**(5), (1991), p. 957.

[88] F. Liu. Ph.D. Thesis. Northwestern Polytechnical University, (2001).

[89] H. Hu,: Proceedings of the Metallurgical Treatises, ed. by T. K. Tien and J. F. Eliot, The Metallurgical Society, AIME, (1981) p. 385.

[90] J.H. Perepezko, Mater. Sci. Eng. **65** (1984), pp. 125–135.

[91] F. Liu, R. Kirchheim, G. Yang, Journal of Materials Science, vol. **39**, issue 5, (2004), pp. 1871-1873

[92] W. Kurz, B. Giovanola and R. Trivedi Acta Met **34** (1986), p. 823

[93] R. Trivedi, J. Crystal Growth, vol. **49**, (1980), pp. 219–32.

[94]T.E. Quested and A.L. Greer, Acta Mater **53** (2005), p. 4643.

[95] M.A. Gafur, M.N. Haque and K.N. Prabhu, J. Mater. Process. Technol. **133** (2003), pp. 257–265.

[96]L. Li, R.A. Overfelt: J. Mater. Sci., vol. **37**, (2002), pp. 3521–32

[97] P. W. Bridgman, U. S. Patent Number 1,793,672. (1931)

[98] C.E. Chang and W.R. Wilcox, J. Crystal Growth **21** (1974), p. 135.